IN-TYRE STRAIN SENSING OF SMALL NON-PRESSURISED TYRES FOR MOBILE ROBOTIC APPLICATIONS

A Thesis submitted by

Ali Farooq Lutfi Lutfi

MSc Mechatronics Engineering

For the award of

Doctor of Philosophy

2019

Abstract

Small non-pressurised tyres are widely utilised for wheeled mobile robots. They possess several merits that justify their feasibility compared to pressurised tyres for small mobile vehicles. These tyres are relatively low cost, require less maintenance, and provide better traction. In addition, they can operate in harsh roads since they are invulnerable to punctures.

This research investigates the possibility of building a low-cost tyre deformation sensing system inside these tyres. In-tyre sensing provides direct and accurate measurements of the tyre-ground contact. The in-tyre measurements are analysed in this research to conclude features that are used to estimate the condition of the tyre and its surrounding. These features are employed to detect slip/spin incidents, identify obstacles, discriminate surfaces, and estimate the tyre's properties, i.e., the forces, contact patch dimensions, angular velocity, and camber angle.

The novelty in this thesis is the aspect of addressing the in-tyre sensing for non-pressurised tyres. An in-tyre strain sensing system is designed and installed on the inner surface of the tyre. The strain profiles acquired from this system through static and dynamic tests are described and analysed.

Static tests were conducted on a custom-designed bench-top rig to evaluate the performance of the sensing system during slip incidents. These tests showed that the slip caused oscillations between two values in the strain reading. Dynamic tests were conducted on a second specially built bench-top rig to examine the in-tyre strain measurements for spin detection, obstacle identification, surface discrimination, and mechanical properties estimation. Spin incidents were indirectly detected utilising a cue in the strain waveforms. The waveforms contain a distinguishing segment that indicates reaching the track's end on the rig. The spin was detected by calculating the

number of the tyre's revolutions relative to the beginning of this segment. In terms of obstacle identification, the shape of the strain waveform and the values of the strain were employed to detect hitting or passing over an obstacle. For surface identification, the results showed that the sensing system can indicate traversing rough surfaces. When the tyre moved from the control surface to a rough surface on the rig, the strain values increased considerably. The percentages of increase in strain values for three of the rough surfaces were 24.98 %, 51.20 %, and 52.13 %. The change in strain was much smaller when the tyre moved from the control surface to a smooth or liquid surface on the rig. The change in strain was between 1.73 % - 3.22 % for smooth surfaces and less than 1 % for liquid surfaces. Features were extracted from the strain profiles to estimate the tyre's forces in three directions, the contact patch centre and length, the angular velocity, and the camber angle. Since the strain profiles of the non-pressurised tyres have not been previously modelled, the estimation models for pneumatic car tyres were utilised in this thesis. The estimations of the tyre's mechanical properties by these models showed reasonable results. These results also showed that the estimation accuracy could be improved in the future by addressing the dynamic deformations of the non-pressurised tyres.

The results were verified qualitatively utilising the readings of the motor's current sensor in the dynamic tests. Similar variations were evidently observed in the measurements of the strain sensors and the current sensor. In addition, the angular velocity estimations from the strain profiles were validated using the encoder's measurements. The strain sensors provide acceptable estimations where the error was 3.98 %.

The proposed in-tyre strain sensing system can be utilised to complement the sensing modules in small mobile platforms. The features extracted from the measurements of this system can be employed to develop efficient control, localisation, and navigation systems.

Certification of Thesis

This Thesis is entirely the work of Ali Farooq Lutfi Lutfi except where otherwise acknowledged. The work is original and has not previously been submitted for any other award, except where acknowledged.

Principal Supervisor: Dr Tobias Low

Associate Supervisor: Dr Andrew Maxwell

Student and supervisors signatures of endorsement are held at the University.

Acknowledgements

I would like to express my deep appreciation and gratitude to my principal supervisor Dr Tobias Low for the invaluable guidance, instructive discussions, and support throughout my PhD study. Without his encouragement, this thesis would not have been completed. I would also like to express my sincere thanks and gratitude to my associate supervisor Dr Andrew Maxwell for his support, guidance, and constructive suggestions during this study. I appreciate his help in designing and printing the 3D parts for the rig used in the static tests.

I would like to thank Dr Richard Landers for helping me in building the data acquisition system for the dynamic tests. I would like to acknowledge the technical staff in USQ for their support, especially Mr Chris Galligan, Mr Brian Aston, Mr Oliver Kinder, Mr Terry Byrne, Mr Graham Holmes, Mr Adrian Blokland, and Mr Mohan Trada. I would like to express my sincere thanks to Associate Dean (Research and Research Training) Professor Thiru Aravinthan for his support. I would like to thank Mrs Juanita Ryan, Mrs Kathryn Schmacker, and Ms Pranjali Dabadi from the Graduate Research School for their support. I would like to gratefully acknowledge the contribution from the Australian Commonwealth Government through the Research Training Program (RTP) in supporting this research.

I would like to thank the Ministry of Higher Education and Scientific Research and the University of Technology in Baghdad, Iraq for funding my PhD scholarship.

Finally, I am genuinely grateful to my mother, father, sisters, and brother for their encouragement and support. My special thanks and gratitude are to my wife Marwah for her unconditional support, encouragement, and love. Thanks to my daughters Mayar and Malak for their love and encouragement.

ALI FAROOQ LUTFI LUTFI

Contents

List of Figures

List of Tables

Notation

F_x	Tyre longitudinal force
F_y	Tyre lateral force
F_z	Tyre vertical force (wheel load)
I	Current
K_m	Motor torque constant
M_x	Overturning moment
M_y	Rolling resistance moment
M_z	Aligning moment
r	Tyre's effective rolling radius
T	Torque
V	Tyre's linear speed
α	Sideslip angle (slip angle)
γ	Camber angle
K	Longitudinal slip ratio
ω	Tyre's angular velocity

Acronyms &Abbreviations

3D	Three Dimensional
ABS	Anti-lock Brake Systems
ABS	Acrylonitrile Butadiene Styrene
AGV	Autonomous Ground Vehicles
CCD	Charge-Coupled Device
DAQ	Data Acquisition
DFT	Discrete Fourier Transform
EKF	Extended Kalman Filter
ESC	Electronic Stability Control
GPS	Global Positioning System
HS	High rotational Speed
IMU	Inertial Measurement Unit
INS	Inertial Navigation System
IR	Infrared
KF	Kalman Filter
LED	Light-Emitting Diode

LS	Low rotational Speed
MS	Medium rotational Speed
NI	National Instruments
PLA	Polylactic Acid
PSD	Position Sensitive Diode
PVDF	Polyvinylidene Fluoride
Rad.	Radian
RMS	Root Mean Square
RPM	Revolution Per Minute
SAE	Society of Automotive Engineers
SAW	Surface Acoustic Wave
Sec.	Second
SLAM	Simultaneous Localisation and Mapping
STC	Self-temperature Compensation
SVM	Support Vector Machine
TC	Traction Control
TPMS	Tyre Pressure Monitoring Systems
TREAD	Transportation, Recall, Enhancement, Accountability, and Documentation
UHMWPE	Ultra-high Molecular Weight Polyethylene

Chapter 1

Introduction

1.1 In-tyre sensory systems for small non-pressurised tyres

Tyre characteristics play a significant role in vehicle dynamics because the tyres produce all forces and moments experienced by the vehicle, excluding the gravity and aerodynamic forces (Tuononen 2008). In order to estimate these quantities, a tyre being converted into a sensing unit can outperform other solutions in terms of direct detection of variations, high robustness, and close proximity to the interface area (Braghin et al. 2006). Erdogan et al. (2011) suggested that tyre sensors can deliver reliable readings even under normal steady-state driving which is generally not the case with the vehicle's on-board sensors such as steering angle sensors, engine torque sensors, and wheel speed sensors. Furthermore, Pohl et al. (1999) reported that tyre sensors can help understand the tyre-ground contact phenomena. This is a crucial factor when assessing a control system's ability to accelerate, decelerate, and steer a vehicle.

Both the automotive and robotics realms have witnessed a number of publications that included the concept of directly measuring the contact parameters using in-tyre sensors. In pertinent literature, this aspect seems to be mainly spurred by the objective of improving the vehicle's control systems. In robotics, for example, "tactile wheels" were introduced to enable a mobile robot to detect obstacles in its vicinity while traversing rough terrains (Lauria et al. 2002). Using this additional input, the robot's controller could adapt the rover's locomotion to climb the sensed obstacles. Moreover, boosting the controllers of planetary exploration rovers with measured contact

parameters, such as normal stress distribution and wheel sinking depth in loose soil, has also been studied (Nagatani et al. 2009; Iizuka et al. 2014).

Regarding automotive control systems, the term “Intelligent tyres/Smart tyres” has drawn the attention of many researchers. These tyres are equipped with sensors to measure thermal and mechanical parameters (Pohl et al. 1999). The researchers have been investigating the promising potentials and expected outcomes of these intelligent tyres. Firstly, the measurements provided by the intelligent tyres can accelerate the development of current control strategies particularly to improve active safety systems (Singh et al. 2012). In addition, Braghin et al. (2006) argued that even for the quantities that cannot be measured directly at present, their estimation procedure becomes faster and more accurate with the introduction of intelligent tyres. Namely, these quantities are friction coefficients, tyre forces, slip ratio, and slip angle (Tuononen 2008). The accurate estimations of these variables enhance the performance of the control systems.

A high number of research projects exists for the use of intelligent tyres in the automotive field. In contrast, only a small number of contributions in the area of in-tyre sensing are identified in the robotic field. In particular, compared to the majority of researchers who have addressed the instrumentation of rigid wheels for a special type of mobile robots, very few researchers have examined the in-tyre sensing for small rubber tyres. More specifically, only one study was identified for examining the utilisation of a sensing system inside non-pressurised tyres (Lauria et al. 2002). However, this system estimates the deformation of the tyre’s inner surface indirectly through non-contacting infrared sensors installed on the wheel inside the tyre. One possible reason for this lack of research in the area of in-tyre sensing for the non-pressurised tyres is the expectation that the deformations in these tyres are high in level and contain many variations. Hence, it could have been anticipated that it is difficult to exploit the measurements of these deformations. However, these non-pressurised tyres are widely used in small to medium-sized mobile robots. Therefore, studying the possibility and the feasibility of installing a sensing system in these tyres should be greatly extended. This is one of the key goals for the research presented herein.

When designing an in-tyre sensing system for small non-pressurised tyres, a number of constraints must be taken into consideration. Most importantly, these tyres are

normally low-cost; thus, it is preferable to employ inexpensive sensors to design the sensory system. In addition, these tyres are normally made of a thin layer of rubber solely. As a result, it cannot adopt sensing systems that require a degree of destructive modifications such as cutting the tyre to embed a sensor (Zhang et al. 2013). It also cannot hold systems that might weaken its structure or affects its rotation like those systems that involve creating a hole to pass a part of the sensor from inside to outside the tyre (Ise et al. 2017). Moreover, foam inserts can be installed inside these non-pressurised tyres (Ray et al. 2009). Thus, it is not practical to mount the sensors on the rim inside the tyre as it would be difficult to monitor the deformations of the foam inserts. This means that designing a sensing system that is based on contacting sensors attached to the tyre produces a more generalised sensing solution for this type of tyres. Furthermore, because of the limited space inside these tyres, the size of the sensors or of the components of the sensing system should be as small as possible.

The measurements acquired from the in-tyre sensors can be utilised to determine wheel slip, identify contact surfaces, detect obstacles, and estimate the tyre's mechanical parameters.

1.2 Wheel slip

Wheel slip can be simply defined as the difference between a vehicle's velocity and its wheels' angular velocity (Changfang Chen et al. 2013). It arises when the wheels' translational velocity vectors work in different directions. This situation occurs because of an uneven ground surface or different wheel velocities. Wheel slip also happens when a wheel torque is producing high traction for the vehicle on the traversed surface (Xu et al. 2011). According to the following equation, the tyre's longitudinal slip ratio is given as the difference between the tyre linear speed and the tyre angular velocity (Yang 2011):

$$K(\%) = \left(\frac{r\omega}{V} - 1\right) \times 100 \tag{1.1}$$

where:

r = Tyre's effective rolling radius (m).

ω = Tyre's angular velocity (rad./sec.)

V = Tyre's linear speed (m/sec.)

For both robots and cars, wheel slip represents a determinant factor in a number of applications. Regarding wheeled mobile robots, odometric solutions may seriously deteriorate during wheel slip incidents. In these cases, the wheel encoders cannot differentiate between a mobile robot that is proceeding normally in its planned path and one whose motion is being affected by wheel slippage (Heewon & Jae-Bok 2013). Since the odometric measurements represent an essential element in most mobile robot localisation methods (Ojeda et al. 2006; Ward & Iagnemma 2008; Jung et al. 2013), accounting for the effect of the slip on the accuracy of these measurements will in turn results in more efficient localisation systems. In addition, taking wheel slip into consideration is a crucial element in developing efficient path planning algorithms which, for example, avoid slippery surfaces (Ward & Iagnemma 2008). Moreover, wheel slip estimation is a key component in enhancing various control systems such as traction control and stability control (Song et al. 2008). Wheel slip also affects the navigation of the mobile robot and hinders its performance in target chasing and obstacle avoidance (Sidek & Sarkar 2013). Furthermore, as wheel slip does not usually contribute to the robot's motion in the desired path, it is regarded as a form of energy loss (Xu et al. 2011). Thus, wheel slip estimation can result in an overall reduction of the robot's energy consumption (Reina et al. 2006).

In the automotive literature, the relationship between the wheel slip and the tyre-road friction has been investigated for various applications. For example, Chankyu et al. (2004) estimated the maximum tyre-road friction coefficient for different driving scenarios utilising the friction coefficient-slip curve. Additionally, wheel slip is an important parameter in several active safety systems such as anti-lock brake systems (ABS), electronic stability control (ESC), traction control (TC), and advanced driver assistance systems for lane-keeping or collision avoidance (Miller et al. 2001; Ergen et al. 2009).

Conventional wheel slip estimation methods are based on sensors such as accelerometers (Ward & Iagnemma 2007), gyroscopes (Ojeda et al. 2004), IMU (Yi et al. 2007; Baffet et al. 2009; Yi et al. 2009) , and optical cameras (Reina et al. 2008; Song et al. 2008; Song et al. 2009; Heewon & Jae-Bok 2013). These sensors were mounted on different locations on the body of the vehicle. To interpret the indirect measurements collected by these sensors about the tyre-ground dynamic events, a number of mathematical projections from one coordinate system to another as well as imprecise mathematical models are required (Krier et al. 2014).

Furthermore, some of the issues encountered with cameras, which are a dominant sensor for slip detection in mobile robots, are the necessity of identifying traceable features as well as the known pitfalls of cameras such as illumination problems and image motion blur (Ward & Iagnemma 2008; Heewon & Jae-Bok 2013). However, due to the developing sensor technologies, it is now possible to embed various types of micro-sensors directly in the tyre to measure different tyre-ground quantities (Palmer et al. 2002).

It is argued that a significant improvement to wheel slip estimation approaches could be achieved utilising measurements from in-tyre sensory systems. These systems can provide direct measurements about the current operating condition of the tyre and contact surface (Tuononen & Hartikainen 2008; Yang et al. 2013). These measurements can be employed to develop accurate wheel slip detection techniques. Figure 1.1 shows a comparison of two levels of measurements that can be utilised for wheel slip estimations, indirect using an on-board sensor and direct using an in-tyre sensor. A combination of these direct and indirect sensors could also be utilised in the future to develop reliable estimation systems of the wheel slip.

(a) On-board camera (Song et al. 2008).

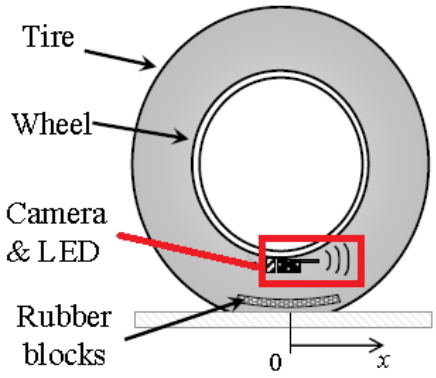

(b) In-tyre camera (Matsuzaki et al. 2012).

Figure 1.1: Two measurement levels for wheel slip estimation (example).

1.3 Surface identification

Surface identification is an important factor in improving the mobility of wheeled robots in unstructured environments (Giguere & Dudek 2011). The ability to identify the surface allows the mobile robot to navigate safely and autonomously over unknown, rough or soft, terrains (Brooks et al. 2005; Park et al. 2012). Terrain variations can negatively affect the performance of the mobile robot; however, knowledge about the traversed surfaces helps the robot to efficiently accomplish the task (Collins & Coyle 2008). Terrain classification allows the robot to adapt its control and path planning strategies according to the terrain type (Brooks et al. 2005; Manduchi et al. 2005). For instance, terrain information can be employed to avoid untraversable regions or to adjust the robot's speed over the terrain. Consequently, this

leads to minimizing the robot's power consumption, maximizing wheel traction, or building better mapping and localisation algorithms (Halatci et al. 2008; Giguere & Dudek 2011).

Surface identification is particularly valuable in designing efficient control and planning systems for off-road autonomous ground vehicles (AGV) (Collins & Coyle 2008; Khaleghian & Taheri 2017). These vehicles are proposed to perform various missions such as military operations, search and rescue tasks, environmental monitoring, planetary exploration, and agricultural applications (Manduchi et al. 2005; Collins & Coyle 2008). Knowledge about the surface will help the vehicles in determining the optimum route towards a desired goal or properly tuning the vehicle's controller to account for the terrain (Manduchi et al. 2005; Collins & Coyle 2008).

Surface identification is presented in previous research in three forms. First, the form of identifying road condition, i.e. dry, icy, wet, snowy, etc. Second, the form of identifying features in road surfaces such as roughness and friction potential. Third, the form of surface classification, for example, asphalt, concrete, grass, sand, cement, ice, etc. (Armstrong et al. 2015; Niskanen & Tuononen 2015; Khaleghian & Taheri 2017; Lee & Taheri 2017).

Based on the type of the utilised sensors' data, the surface identification methods can be divided into two main groups; vision-based methods and vehicle's response-based methods. Visual techniques detect the surface using images obtained from cameras or laser range finders. Response-based methods rely on sensing external and internal terrain-dependent physical changes such as wheel sinking, wheel slip, induced sounds, or the more commonly utilised, vehicle vibrations. Currently, both of these methods have limitations (Collins & Coyle 2008). Vision-based methods can easily be disturbed by static or dynamic objects on the surface such as leaves or a thin layer of dust (Collins & Coyle 2008). In addition, visual techniques are affected by variations in illumination as well as atmospheric conditions like fog (Brooks & Iagnemma 2005; Giguere & Dudek 2011; Park et al. 2012). Furthermore, vision-based methods usually depend on sensing the covering of the surface which in some cases may not be the surface of interest that holds the vehicle's weight as in the case of soil covered by grass (Brooks & Iagnemma 2005). Similarly, a negative point about the response-based method is that the surface signature acquired by interpreting the vehicle's

reaction changes if the vehicle runs at different speeds. To address this issue, numerous experiments need to be conducted to train the surface identification system with a large number of speeds. Additionally, current response-based systems cannot detect the surface under each wheel in case the vehicle traverses multiple terrains simultaneously, e.g., when the wheels on one side of the vehicle are on-road while the wheels on the other side are off-road (Collins & Coyle 2008).

It is assumed that utilising the in-tyre sensing for surface identification can overcome the limitations of the previously presented methods. The in-tyre sensing is not greatly distorted by overlaying objects or materials. It is immune to lighting and atmospheric effects. The measurements of the in-tyre sensors correspond to the texture of the real surface that carries the robot. The in-tyre sensing systems can be developed to be robust against changes in speeds. These systems can be used for surface identification by day and night. They can also identify the surface under each tyre if the robot's tyres move over different surfaces. In addition, the tactile sensing of the surface with the in-tyre sensors can provide subtle measurements that reflect the mechanical properties of the surfaces and thereby produces a more discriminative approach for surface identification. The disadvantage is that this in-tyre tactile sensing can only be used to identify the surface that the robot is currently traversing (Halatci et al. 2008). However, this tactile sensing of the current surface is still valuable for enhancing the robot's mobility and control system. For instance, once the tyres touch a new surface, the in-tyre sensors will provide the tactile information to the controller so that it can accordingly adjust the driving and steering mechanisms. Consequently, the robot will be able to proceed efficiently in its path on this surface. Alternatively, the tactile sensing can be used to provide a detailed description of the surface to train other terrain identification systems (Giguere & Dudek 2011). Thus, the in-tyre sensing can complement other surface identification systems to enable the robot to more accurately determine the surfaces both underneath and in front of the tyres.

1.4 Obstacle detection

The task of obstacle detection has been extensively investigated in robotic applications. The majority of the obstacle detection techniques were designed for structured environments and cannot work properly under unknown situations. The reason is that these techniques are based on some prior assumptions about the condition, such as the presence of a flat ground surface. This approach is referred to as the “flat world” assumption. For unstructured environments, this approach cannot be adopted without introducing additional data processing steps as well as computational and storage requirements (Manduchi et al. 2005).

Geometric features extracted from the data obtained using stereo cameras or range finders have been widely utilised for obstacle detection. These features are employed to detect the obstacles within a common framework that is based on identifying changes in elevation from the ground plane (Halatci et al. 2008). This approach can be easily implemented if the surface in front of the vehicle is flat because any object protruding from the ground plane will be defined as an obstacle. However, in challenging roads such as uneven dirt roads some objects do not necessarily represent real obstacles in the path of the robot. Examples of such objects are small bumps or compressible vegetation such as tall grass. These can be easily negotiated by, for example, moving with a slower speed. Another difficulty for using these standard detection methods in challenging roads is the potential existence of negative obstacles such as holes and grooves (Manduchi et al. 2005).

Several benefits are predicted for using the in-tyre sensing for obstacle detection. First, obstacle detection using in-tyre tactile sensing does not require relying on the assumption that the terrain should be modelled as a planar surface. Thereby, it does not need elevation information about the traversed surfaces. Thus, it can be concluded that using intelligent tyres for obstacle detection can work in unknown environments without adding external load to the processing algorithm. In addition, the in-tyre sensing can provide information not only about the geometry but also about the nature of the obstacles, for example, hard, soft, compressible, slippery, brittle, etc. The robot can then use these precise details to determine if the obstacles can be easily crossed without affecting the robot’s mobility or damaging environmental features of interest

in exploration or monitoring missions. Moreover, it can identify bumps, holes and other irregularities in the surface (Giguere & Dudek 2011). Furthermore, it can sense obstacles even if they are hidden by other details in the scene. These estimations of obstacles can improve the mobility of the robot when crossing through new regions by continuously regulating the driving and steering mechanisms. They can also help in building a detailed traversability map for a given area. Such a map can then be used by the path planning system for future missions in that area to decide the best path in terms of minimizing the power consumption, efficiently accomplishing the task, or avoiding vehicle's damage (Manduchi et al. 2005; Armstrong et al. 2015).

1.5 Tyre's terminology and axis system

The Society of Automotive Engineers (SAE) has introduced the coordinate system shown in Figure 1.2 to define the tyre's working conditions and its force/moment system (Gillespie 1992). The origin of this coordinate system is fixed to the centre of the tyre's footprint. The x-axis is the intersection between the tyre plane and the ground plane. The z-axis is perpendicular to the ground plane. The y-axis is in the ground plane and is perpendicular to both the x and the z-axes (Jazar 2017). The axes x, y, and z correspond respectively to the tyre's longitudinal, lateral, and vertical directions (Yang 2011). The forces and moments that are delivered to the tyre as a result of the tyre-ground interactions are located at the centre of the tyre's footprint. These forces and moments comprise three-dimensional components (Jazar 2017). The components of the force along the x, y, and z-axes are respectively the tyre longitudinal force (F_x), the tyre lateral force (F_y), and the tyre vertical force (F_z) (Yang 2011). F_x is the force component that is parallel to the intersection of the tyre plane and the ground plane. F_y is the force component that is normal to the intersection of the tyre plane and the ground plane. F_x and F_y are tangents to the ground. F_z is normal to the ground plane. The moments about the x, y, and z-axes are respectively the overturning moment (M_x), the rolling resistance moment (M_y), and the aligning moment (M_z). These moments act on the tyre in the same direction and plane as the forces in the respective axes (Gillespie 1992).

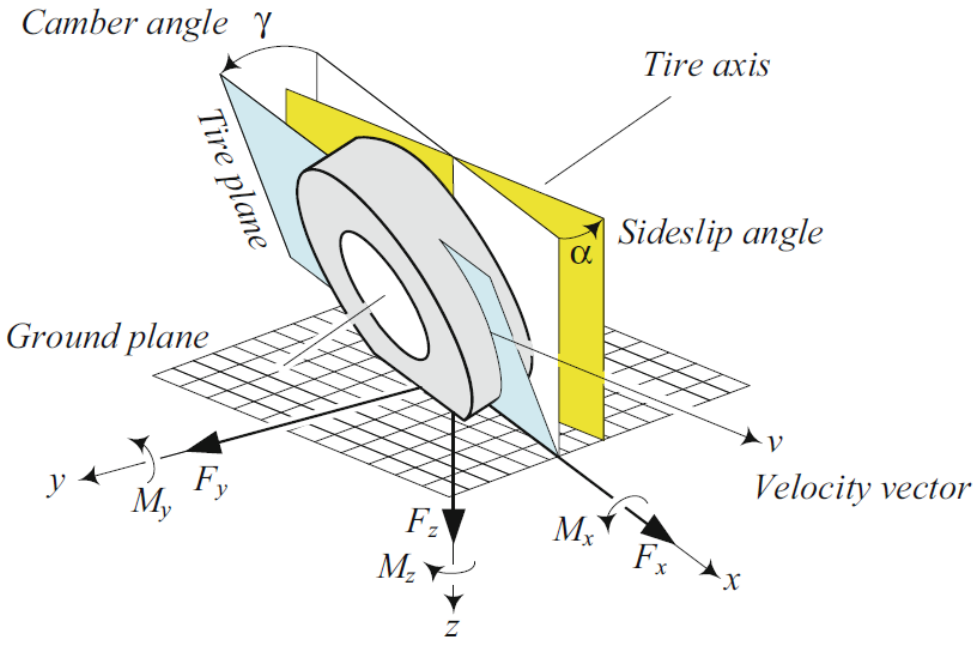

Figure 1.2: Tyre coordinate system (Jazar 2017).

The tyre orientation is defined by two angles called the camber angle (γ) and the sideslip angle (slip angle) (α) (Jazar 2017). The camber angle, shown in Figure 1.3a, is the angle between the tyre plane and the x-z plane (Yang 2011). In other words, the camber angle is the angle between the tyre plane and the vertical axis (Gillespie 1992). The slip angle, shown in Figure 1.3b, is the angle between the intersection of the tyre plane with the ground plane and the tyre’s velocity vector (Yang 2011). This means that the slip angle is the angle between the direction of the tyre’s heading and the direction of the tyre’s travel (Gillespie 1992).

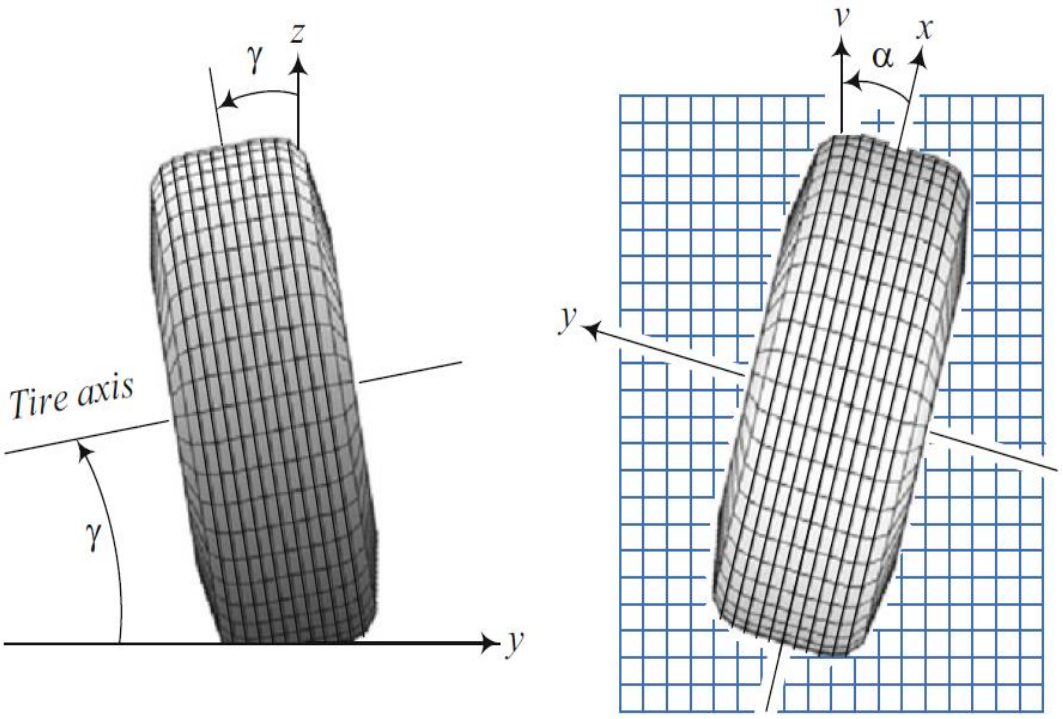

(a) Front view of a tyre illustrating the camber angle.

(b) Top view of a tyre illustrating the slip angle.

Figure 1.3: Camber and slip angles (Jazar 2017).

1.6 Research problem

Wheeled vehicles are widely used in various applications including industrial, agricultural, and personal (Wang et al. 2012). Besides the rigid wheels that are typically used for planetary exploration rovers (Sutoh et al. 2010; Iizuka et al. 2014), rubber tyres are largely used in wheeled vehicles. More specifically, small non-pressurised tyres are commonly utilised for wheeled mobile robots. Compared to pressurised tyres, these tyres are relatively low-cost, less susceptible to punctures (Ju et al. 2012), can hold more weight, and require less maintenance (Ju et al. 2012). Additionally, they are better in gripping the road, traversing rough terrains, and absorbing shocks. Thus, it is feasible to use these tyres in small-wheeled platforms. Robots equipped with this type of tyres can be deployed for both indoor and outdoor activities (Ray et al. 2009).

To obtain precise, direct, and real-time tactile measurements of the tyre-ground contact, an in-tyre strain sensing system that continuously monitors tyre deformations in both longitudinal and lateral directions is proposed. This sensing system is anticipated to help develop a clearer understanding of the tyre-ground interactions and their corresponding phenomena. However, due to the associated technical and analytical challenges, the in-tyre sensing for small non-pressurised tyres has been introduced only once in previous research. A key factor when designing a sensing system for these tyres is to adopt low-cost elements since it is impractical to embed high-cost components inside these low-cost tyres. This research will exploit the in-tyre measurements to estimate the tyre's mechanical properties, detect tyre slip, differentiate surfaces, and identify obstacles.

Previous work on the in-tyre strain sensing was designated for pneumatic car tyres. This research will investigate the possibility of utilising the models used to describe the strain measurements of pneumatic car tyres in the case of small non-pressurised tyres. These models will relate the in-tyre strain measurements to the tyre's mechanical properties such as the forces, the contact patch centre and length, the angular velocity, and the camber angle (Yang 2011).

Wheel slip has significant impacts on odometric accuracy as well as overall power consumption in wheeled mobile robots (Reina et al. 2006). In addition, wheel slip represents a vital factor in traction control, stability control, and braking control in both robots and cars (Reina et al. 2006; Song et al. 2008; Matsuzaki et al. 2012). Utilising the readings of the in-tyre sensors for slip detection is predicted to surpass the traditionally used methods for two reasons. First, it relies on direct measurements of the tyre-ground interface area, which is the area of interest in terms of estimating the slip. This means that fewer transformations, assumptions, and approximations, and thereby fewer uncertainties are involved when employing these measurements for slip estimation. Second, it simplifies the process of slip detection as it requires less knowledge about the vehicle's dynamics. The slip will be detected by solely analysing the readings of the in-tyre sensors and identifying significant features and variations in the measurements.

Surface identification and obstacle detection represent two important components of environment sensing for autonomous wheeled vehicles (Manduchi et al. 2005). While

visual information is commonly used to identify the surface that the wheeled vehicle is about to traverse or is currently traversing (Brooks & Iagnemma 2005), a degree of uncertainty should be expected. The known limitations of vision-based sensors such as the requirement of proper illumination and reflections contribute to this outcome (Brooks & Iagnemma 2005; Giguere & Dudek 2011; Park et al. 2012). In addition, static and dynamic obstacles in the scene may interfere and cause false predictions about the nature of the surface. Furthermore, even for cameras mounted as close as possible to the tyre-road contact surface, inaccurate estimations might arise because of misleading images of the surface's material. The reason is that images of different surfaces might indicate very similar features in terms of colour, texture, and/or appearance. For instance, the camera would not be able to differentiate between carpet and vinyl that have a look-alike appearance or between a surface when it is clean and when it is covered with a thin layer of liquid or dust. Although the images of the surfaces in these examples can be quite similar, they might result in different levels of gripping, slipping, and/or traction of the vehicles' tyres. Moreover, there might be a problem of blurry images caused by the mechanical vibrations when the vehicle travels across a harsh or rugged surface or when the vehicle runs at high speeds. Regarding obstacle detection, the current methods rely on prior assumptions about the scene in front of the vehicle, cannot indicate whether the sensed obstacles represent a hazard in the vehicle's path, and are not capable of detecting the obstacles when they are below the ground plane or hidden by other elements (Manduchi et al. 2005). For all these reasons, tyre sensors are an alternative sensing solution for surface identification and obstacle detection. The tyre sensors can provide tactile information about the traversed surfaces and the present obstacles from the only direct link between the vehicle and the contact surface.

From the above discussion, the following research questions emerge:

1- Is it possible to measure the strain in the primary directions for non-pressurised tyres using standard low-cost strain gauges?

2- Can the models that are used to relate the information from the in-tyre strain profiles to the tyre mechanical properties such as forces, contact patch centre

and length, angular velocity, and camber angle, in standard pressurised car tyres be utilised for small non-pressurised tyres?

3- Can the in-tyre strain information indicate slip/spin incidents, obstacle presences, or traversing different surfaces?

1.7 Research aim and objectives

The aim of this research is to develop a low-cost in-tyre sensing system for small non-pressurised tyres. The measurements acquired by this system will be analysed to gain a better perception of the tyre's environment by indicating slip/spin incidents, identifying traversed surfaces, and detecting obstacles. In addition, these readings will be utilised to derive the tyre's mechanical properties such as the forces in three directions, the contact patch length and centre, the angular velocity, and the camber angle.

The objectives of this study are:

1- Identify an appropriate sensing method, choosing suitable sensors, and suggesting the best design for the sensor system for small non-pressurised tyres.

2- Build low-cost testing platforms to acquire the data in static and dynamic tests.

3- Extract features from the in-tyre strain measurements to detect slip/spin, identify obstacles, differentiate surfaces, and to estimate the forces, contact patch variables, tyre's angular velocity, and tyre's camber angle.

4- Conduct static tests to determine whether the sensors' readings can indicate slip incidents. A second reason for carrying out the static tests is to build a comprehensive understanding of the sensors' response by constructing strain profiles for different values of vertical and longitudinal forces.

5- Conduct dynamic tests to evaluate the performance of the in-tyre strain sensors in the case of a rotating tyre. The readings that are collected in these dynamic tests will be utilised to investigate the possibility of detecting spin, identifying obstacles, differentiating surfaces, and estimating the tyre forces, contact patch variables, angular velocity, and camber angle.

1.8 Research contributions

The contributions of this research are as follows:

1- Designing an in-tyre sensing system to directly measure the strain for small non-pressurised tyres utilising off-the-shelf sensors. No previous research has addressed and investigated direct strain sensing for non-pressurised tyres.

2- All slip estimation methods that utilised in-tyre sensors were designed for automotive cars; however, this research will investigate the potential of applying the concepts of intelligent tyres to explicitly estimate wheel slip for mobile robots. The measurements of the in-tyre sensors will be examined to extract strain features and/or variations that indicate the occurrence of slip incidents.

3- Utilising the in-tyre strain measurements for surface identification. Although the idea of using measurements from in-tyre sensors for surface identification has been previously introduced, the measurements used were either the acceleration or deflection of the tyre.

4- Investigating the use of the in-tyre strain measurements for obstacle detection.

1.9 Thesis outline

This thesis is organised as follows:

- Chapter 2 presents the literature review of the related studies in the field of this work. It reviews the different in-tyre sensing systems and their measured variables and purposes in both the robotic and the automotive fields. Surface identification and obstacle detection utilising in-tyre sensing are closely examined. Wheel slip estimation methods that are based on the in-tyre sensors as well as the on-board sensors are also presented.

- Chapter 3 shows the experimental setup of the work. It first introduces the components utilised to build the sensing system. These components are the sensors, the tyres, the materials used for the installation, and the DAQ system. The footprint tests conducted to study the contact patch for the tyre used herein are presented. The analysis of the results of the footprint tests that is used to design the sensing system is demonstrated. The chapter also describes the two bench-top rigs designed to conduct the tests. The experimental setup for the static and dynamic tests is also described.

- Chapter 4 explains the initial steps for analysing the readings of the sensors in the static tests. These readings are filtered and used to build strain profiles. The chapter then illustrates the first steps for processing the readings of the sensors collected in the dynamic tests. The strain profiles acquired from the sensors are described in detail.

- Chapter 5 examines the measurements of the in-tyre sensors for the slip, spin, and obstacle detection. Features extracted from the sensors' readings in the static tests are utilised to investigate slip detection. The results of the dynamic tests are used to study the potential of spin and obstacle detection.

- Chapter 6 investigates the ability to identify the contact surfaces utilising the measurements of the in-tyre sensors. It also presents a study of using the frequency content of the strain measurements for surface identification.

- Chapter 7 examines the relationships between the in-tyre strain measurements and the tyre's properties. These measurements are used to estimate the forces in three directions, the contact patch length and centre, the tyre's angular velocity, and the tyre's camber angle.

- Chapter 8 discusses the achievement of the research objectives. It also reports the research's findings and suggests potential future work and applications.

Chapter 3- Chapter 8 only show an example subset of the work. For full data set and examples, please see the attached files.

Chapter 2

Literature Review

Small non-pressurised tyres are commonly used in small-wheeled mobile platforms. Equipping such tyres with sensors helps in providing the controller of these platforms with information about the tyre and the traversed environment.

The literature in the area of in-tyre sensing and its applications for small non-pressurised tyres can be divided into three main sections. Firstly, in-tyre sensing systems where the focus is on the development and design of in-tyre sensors. Secondly, surface identification and obstacle detection using in-tyre sensing. Thirdly, wheel slip estimation methods that are developed utilising the in-tyre sensors and the on-board sensors. Figure 2.1 shows the topics of the literature review presented in this chapter.

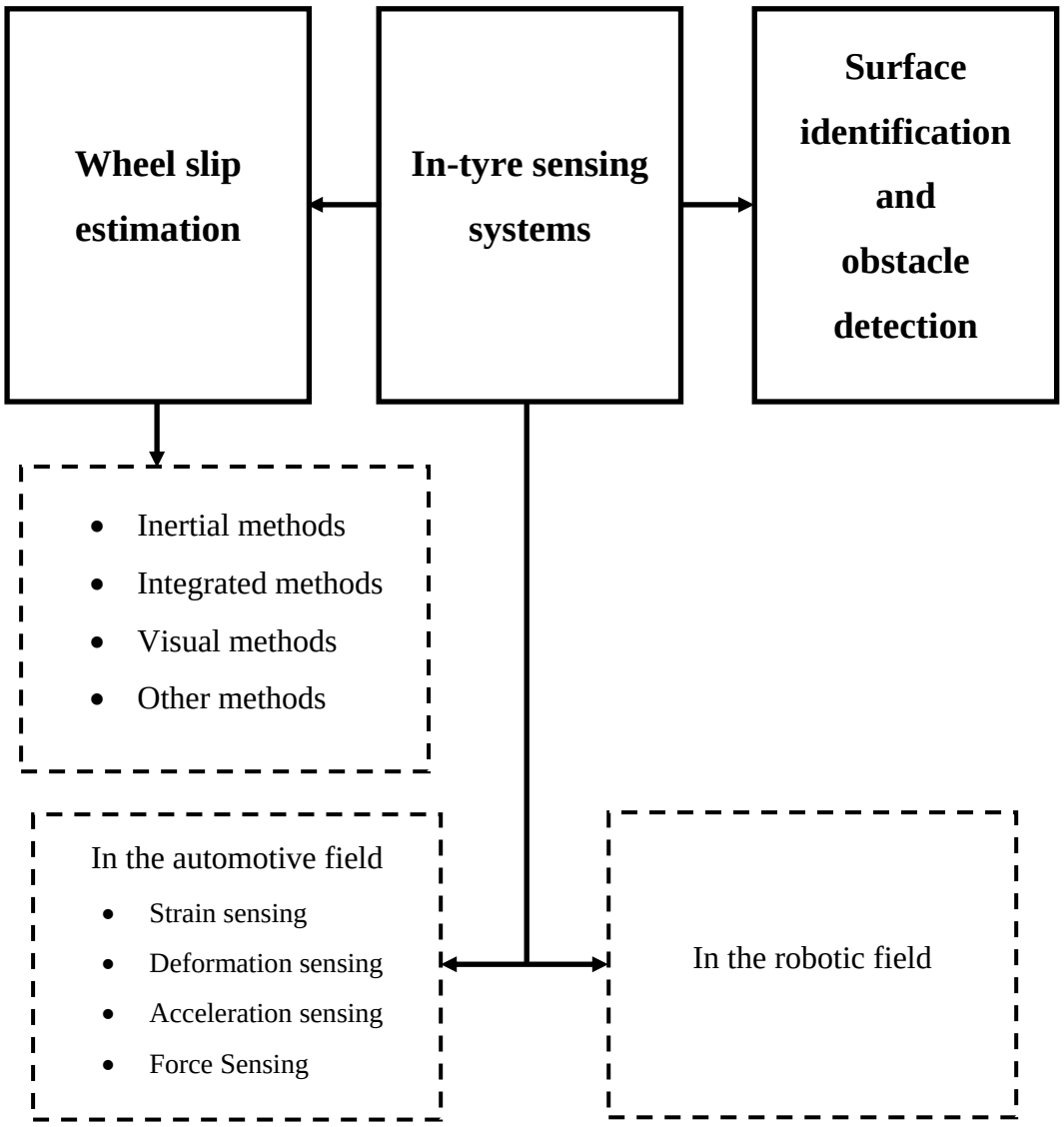

Figure 2.1: The topics of the literature review (the solid boxes represent the main sections and the dashed boxes represent the subsections).

2.1 In-tyre sensing systems

This section will review the designs of the tyre sensing systems that were suggested to measure tyre's strain, deformation, acceleration, and force. Based on the wheel size as well as the wheel and the tyre's materials, a general classification into robotic and automotive subsections will be presented.

2.1.1 In the robotic field

For wheeled mobile robots, only a few in-wheel sensing systems were identified. These systems can be divided into two classes: sensory systems for wheel deflection and sensory systems for tyre rubber deformation. In both classes, the sensing systems were dedicated to collect measurements only in the longitudinal direction of motion. The designs in the first class aim at developing direct wheel-ground contact sensing modules particularly for planetary rovers. To develop these sensing systems, the sensors were placed in four different positions. First, on a rigid wheel's grousers (Iizuka et al. 2014). Second, between a rigid wheel's lugs (Nagatani et al. 2009; Sutoh et al. 2010). Third, on a stationary frame fixed to a flexible metallic wheel (Krebs et al. 2008; Krebs et al. 2010; Xu et al. 2011). Fourth, on an l-shaped structure attached to a rigid wheel's inner circumference (Senatore et al. 2012; Jayakumar et al. 2014; Senatore & Iagnemma 2014). In these designs, three types of sensors were utilised: strain gauges (Senatore et al. 2012; Iizuka et al. 2014; Jayakumar et al. 2014; Senatore & Iagnemma 2014), Infrared (IR) (Krebs et al. 2008; Krebs et al. 2010; Xu et al. 2011), and pressure sensors (Nagatani et al. 2009; Sutoh et al. 2010). The sensory systems were proposed to improve the wheel-ground traction models and the control systems through accurate estimations of various traversability aspects. The first aspect was detecting contact angles and estimating sinking on loose soil (Iizuka et al. 2014). The second aspect was detecting ground obstacles in rough terrains (Krebs et al. 2008; Krebs et al. 2010; Xu et al. 2011). The third aspect was measuring normal and shear stresses and estimating traction forces on deformable soils (Nagatani et al. 2009; Sutoh et al. 2010; Senatore et al. 2012; Jayakumar et al. 2014; Senatore & Iagnemma 2014). Regarding wheel type and service conditions, this class is neither relevant nor applicable for the specifications of the proposed research. As was presented, these designs were developed for rigid wheels and cannot be used on rubber tyres. Furthermore, they were specially built for planetary rovers. These rovers traverse either loose soil or rugged terrains with a very low-speed motion. These sensing systems have not been tested on mobile robots running on normal ground surfaces with high speeds.

The second class of the sensing systems in the robotic field was built for rubber tyres. Lauria et al. (2002) and Lamon and Siegwart (2005) used tactile wheels where an array

of IR sensors was mounted on the wheel hub inside low-pressure tyres. The IR sensors measure the tyre's deformations. These sensors were used to provide an online estimation of wheel-ground contact points. This estimation was used to improve the ability of obstacle climbing for rugged lands' exploration rovers (Figure 2.2a). For ground robots, Yi (2008) and Yi and Tseng (2008) placed two specially designed piezoelectric sensors on the inner surface of a skid-steered mobile robot's pneumatic tyre (Figure 2.2b). These sensors measure the deformation of the tyre's rubber tread. Analytical models were presented to describe the sensors' outputs and obtain the wheel-ground friction information. Recently, some researchers investigated the use of in-tyre sensing for surface identification. Khaleghian and Taheri (2017) fixed a three-axis accelerometer to the inner surface of a robot's pneumatic tyre. The power of the radial acceleration measured by this accelerometer was used as one of the inputs to a fuzzy logic system. This fuzzy algorithm categorises the contacting surfaces into four main groups: asphalt, concrete, grass, and sand. Armstrong et al. (2015) placed piezoelectric film sensors on the inner surface of the tread and the sidewall of a tube-type pneumatic tyre. The films were positioned between the inner tube and the tyre, where the pressurised tube was used to secure the sensors to their positions. The sensors were used to measure the deflections of the tyre. The researchers used the amplitude and width of the signals of these sensors to classify the traversed surfaces. However, the authors stated that their method of placing the sensors inside the tyre was challenging. They reported that inserting and inflating the tube caused the sensors to move from their desired locations. Additionally, their preliminary results indicate that further investigation needs to be conducted. This investigation must address both the required tests and the suggested data analysis algorithm.

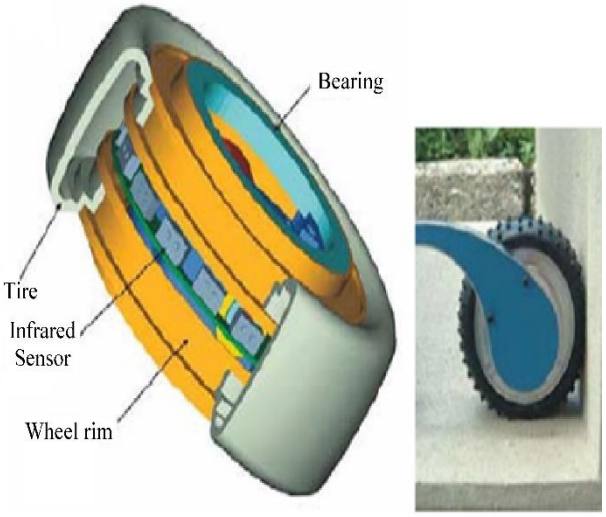

(a) Tactile wheel for a rough terrain rover (Lauria et al. 2002).

(b) In-tyre sensors for a small-scale robot's tyre (Yi 2008).

Figure 2.2: Examples of tyre rubber's deformation sensing systems for mobile robots.

2.1.2 In the automotive field

Road safety concerns have been necessitating equipping car tyres with sensing abilities to monitor both the road and tyre conditions (Matsuzaki & Todoroki 2008a). In the field of intelligent tyres, Tyre Pressure Monitoring Systems (TPMS) were the first outcomes of the research effort that has been offered commercially. The primary task of TPMS is to monitor the tyre's inflation pressure and temperature (APOLLO

Consortium 2003). In 2002, the United States of America issued the so-called Transportation, Recall, Enhancement, Accountability, and Documentation (TREAD) act. This act has made the installation of TPMS mandatory to warn the drivers when the tyre is under-inflated. This legislation has significantly encouraged the development of the in-tyre sensing systems (APOLLO Consortium 2003; Matsuzaki & Todoroki 2008b; Yang 2011). Therefore, intelligent tyres were the backbone of numerous publications in the automotive field. The various advanced sensor designs can be divided into strain, deflection, acceleration, and force sensing systems.

There are several specifications required to develop a feasible tyre sensor system. Firstly, if the sensor is to be attached directly to the tyre inner surface, the sensor material should be flexible enough to follow the tyre rubber's elastic characteristics (D'Alessandro et al. 2012). This ensures that the sensor captures the actual local tyre deformations without any external disturbances (Matsuzaki & Todoroki 2005). This compatibility is also required to avoid adhesion failure. Secondly, the sensor must be lightweight in order not to add mechanical loads on the tyre (D'Alessandro et al. 2012). Third, it has to tolerate harsh operating conditions such as high accelerations and shocks (Daimler 2005). Fourth, integrating such systems must not interfere with the vehicle's primary tasks like braking and handling (Braghin et al. 2006). Lastly, the cost and manufacturing complexity are preferred to be as low as possible (D'Alessandro et al. 2012).

2.1.2.1 Strain sensing

A number of benefits have promoted the use of tyre strain measurements. Tyre strain measurements are not affected by wheel rotational velocities (Daimler 2005). Therefore, readings that are more robust as compared to acceleration sensing are obtained. It also helps leverage the so-called tyre health monitoring since measured strains can directly justify various tyre defects (Moffitt et al. 2009). In addition, in-tyre strain sensing systems can improve the vehicles' modern control systems (Matsuzaki & Todoroki 2007). Due to the significant importance and outcomes of direct tyre strain monitoring, a considerable number of strain sensing systems are observed.

The tyre's strain measurements are captured through contacting sensors. Direct measurements are acquired with contacting sensors (Moffitt et al. 2009). In addition, from a signal processing perspective, direct strain data are easier to analyse. This is because the strain sensor measures tyre deformations only in its vicinity (Moffitt et al. 2009). At the same time, these sensors must meet critical requirements such as material compatibility with tyre rubber and high durability (Matsuzaki & Todoroki 2008b).

The in-tyre strain sensing depends on a strain sensor mounted directly on the tyre inner surface (Palmer et al. 2002; Daimler 2005; Matsuzaki & Todoroki 2007; Matsuzaki et al. 2008) or embedded in the tyre rubber (Palmer et al. 2002).

To develop the strain sensing systems, resistive (Yang 2011), piezoelectric (Daimler 2005), and fibre optic (Palmer et al. 2002) sensing technologies were utilised. However, Matsuzaki and Todoroki (2008b) had argued that strain sensors developed with these technologies are made of high stiffness and low elongation materials. Thus, attaching such sensors directly on the tyre rubber might disturb the deformation measurements. Moreover, the durability and robustness of these sensors to withstand the hard-working conditions inside the tyres must be further investigated (Daimler 2005; Moffitt et al. 2009). To overcome this problem, they introduced three different sensing solutions based on capacitive changes. The solutions were a flexible patch-type sensor (Matsuzaki & Todoroki 2007), a rubber-based sensor manufactured with photolithography (Matsuzaki et al. 2008), or a self-sensing technique where the tyre structure works as a sensor (Sergio et al. 2003; Todoroki et al. 2003a, 2003b; Matsuzaki & Todoroki 2005). The last solution requires no attached sensors as can be seen in Figure 2.3. The adjacent steel wires embedded in the tyre belt are utilised as electric conductors between which a dielectric element, rubber, exists. Thus, this structure serves as an electric capacitor. Compared to the strain sensing with attached sensors, the advantage of using the tyre structure as a sensing component is that the sensor's de-bonding can be avoided. This issue might occur because of a stiffness difference between the tyre rubber and the contacting sensor's material (Matsuzaki & Todoroki 2008b). However, Green (2011) pointed out that this sensing technique can be difficult to implement. It requires a delicate operation of extracting the steel wires from the condensed tyre layers without affecting the tyre structure's integrity.

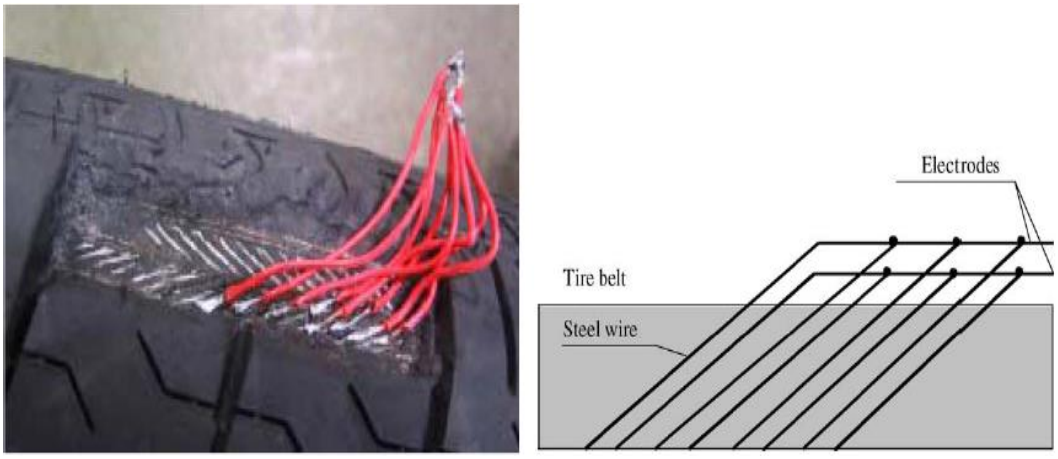

Figure 2.3: Utilising tyre steel wires for strain sensing by monitoring capacitance changes (Matsuzaki & Todoroki 2006).

The strain sensors can be placed on the tyre inner surface longitudinally or laterally to detect strain changes in the respective direction. Therefore, they were deployed to measure tyre deformations in the longitudinal direction only (Matsuzaki & Todoroki 2007; Matsuzaki et al. 2008). Furthermore, two strain sensors mounted on two different locations can be oriented to separately measure the longitudinal and lateral strains (Palmer et al. 2002; Daimler 2005; Yang et al. 2013).

Measured strain profiles can be analysed to determine three-dimensional forces (Daimler 2005; Yang 2011), slip ratio (Matsuzaki & Todoroki 2008a), tyre-road friction coefficient (Palmer et al. 2002; Matsuzaki & Todoroki 2008a), tyre rotational speed, tyre inflation pressure, and tyre lateral force under different slip angles and camber angles (Yang 2011).

2.1.2.2 Deformation (Deflection) sensing

Tyre deflections are commonly measured by non-contacting sensors. Non-contacting tyre sensors are preferable since they usually need no major tyre structure modifications (Moffitt et al. 2009). Therefore, these systems will not affect tyre primary tasks as well as tyre deformation measurements. On the other hand, the most important issues are the large sensor size and the need for complex processing algorithms to model the sensor's data (Moffitt et al. 2009). The term non-contacting is

used here to indicate deflection monitoring systems where the sensing component is not directly mounted on the tyre. Instead, the sensing element is attached to the wheel rim inside the tyre. It continuously captures the deformation of the opposite part of the tyre inner surface. All non-contacting deflection-sensing methods are based on optical sensors, but the use of an ultrasonic sensor was also noted.

Optical sensing techniques can meet the requirements of a tyre sensor system. They provide fast responses and repeatable results (Xiong & Tuononen 2014). Optical techniques can also withstand the dynamically-changing working conditions of the tyres owing to their high durability and robustness (Xiong & Tuononen 2014). Figure 2.4 shows an example of the optical-based deflection systems.

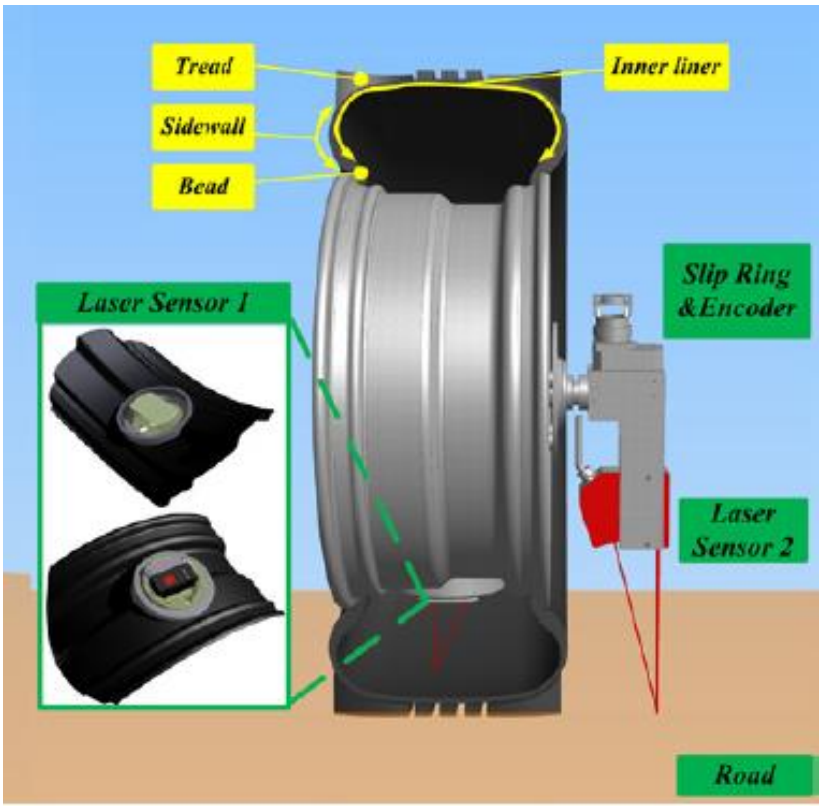

Figure 2.4: Laser-based tread deflection sensing system (Xiong & Tuononen 2014).

Three optical-based deformation systems were proposed. The first was developed utilising a position sensitive diode (PSD) on the rim and an IR diode on the tyre inner liner (Daimler 2005; Tuononen 2008; Naranjo et al. 2014). The deflection measurements were obtained by monitoring the displacement of a point in the inner

liner with respect to the rim. The second system deployed a charge-coupled device (CCD) camera (Matsuzaki et al. 2012). The tyre's deformations were extracted by processing image data for a modified inner tyre surface. The third sensing method relied on laser sensors (Xiong & Tuononen 2014). The measurements of two laser sensors placed inside and outside the tyre were integrated to measure the tread's deformations.

The optical sensing systems can deliver tyre deformation measurements in the radial direction. Therefore, they were used to estimate the deflected rolling radius (Naranjo et al. 2014) and the tread block vertical deformation (Xiong & Tuononen 2014). More importantly, optical systems can be deployed to measure tyre deformations in three directions; thus, three-dimensional contact forces could be estimated (Daimler 2005; Tuononen 2008; Matsuzaki et al. 2012).

Another type of sensors was utilised for non-contacting deflection measurements. Magori et al. (1998) placed an ultrasonic sensor on the wheel rim inside the tyre (Figure 2.5). This sensor measured the tyre's vertical deformations by monitoring the perpendicular distance between the rim and the tyre inner surface. Unlike optical sensing, the measurements' accuracy severely degraded across the contact patch because of echo attenuations caused by interferences of spurious signals.

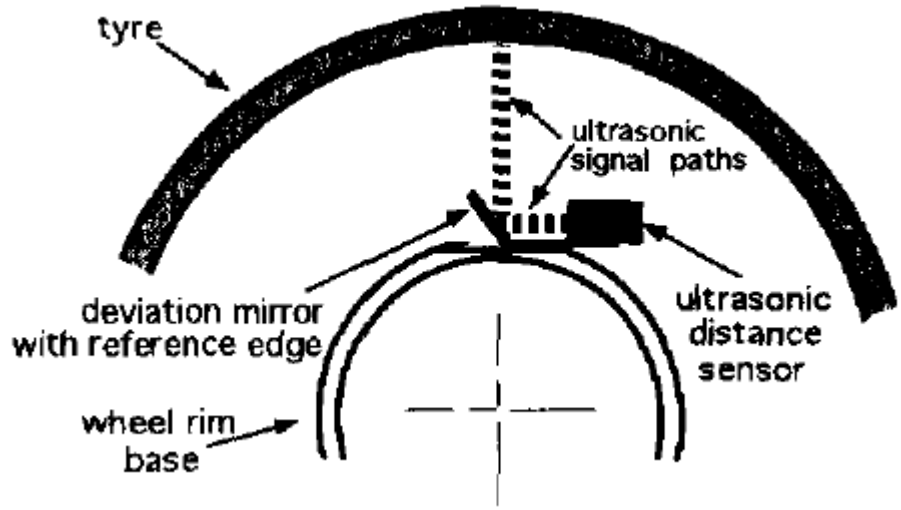

Figure 2.5: Deflection sensing system based on the ultrasonic sensor (Magori et al. 1998).

Another approach for non-contacting deflection sensing is based on sensors placed outside the tyre. The sidewall torsion sensor was introduced to measure the longitudinal and lateral sidewall deflections (APOLLO Consortium 2003). Two magnetised strips are embedded in the sidewall at two different diameters. The magnetic field from these strips was measured by two sensors mounted on the vehicle chassis. These measurements were used to estimate the corresponding force. A phase shift between the two signals measured by the sensors is proportional to the exerted longitudinal force. A difference in the field intensity measured by the two sensors is used to extract the applied lateral force. The second system in this approach measures the wheel's deflections using sensors mounted on the wheel. For instance, Gobbi et al. (2010) designed a smart sensing wheel that consisted of three spokes equipped with 12 strain gauges. The spokes were connected to an outer frame by means of a flexible joint. With this configuration, the three forces and the three moments exerted at the elastic tips were calculated. However, compared to in-tyre sensors, this approach requires two transformations in order to estimate the tyre-ground contact. The first transformation is from the chassis/wheel to the tyre and the second is from the tyre to the contact patch. As a result, low estimation resolution is obtained. In addition, dealing with more mechanical loads further complicates the problem. Moreover, there is the manufacturing difficulty for such a special tyre/wheel design.

Some designs were proposed to develop tyre deformation sensing based on measuring the tread block's deformation with contacting sensors. Breuer et al. (2000) instrumented a tyre tread block with a magnet and four position-detecting Hall sensors. The hall detectors monitored the embedded magnet's movements caused by the deflections of the tread block during tyre rotations. The deformations in x, y, and z directions were measured using this design. The sensors' measurements were employed to estimate the wheel load as well as the longitudinal and lateral contact forces. Evidently, a sophisticated manufacturing process was required to fit the sensor into the small space of one tread block of a car tyre. Other tread element's deformation sensing methods rely on a sensor equipped with a pin. The pin was inserted from the tyre inner surface into the tread block. For example, a passive surface acoustic wave (SAW) radio sensor instrumented with a lever was presented to measure the tread's deformation. The sensor's readings were used for estimating the tyre-road friction in the longitudinal direction of motion (Pohl et al. 1999). However, Sergio et al. (2003) suggested that the tyre deformation sensors that adopt a pin inserted into the tread block might produce inaccurate measurements. Movements of the pin in these sensors easily disturb the local deformations.

A unique contribution to the tyre's deformation sensing is introduced by Erdogan (2009). A piezoelectric tyre sensor was designed to measure the lateral sidewall deflection. The main principle was sensing the bending motion of a cantilever beam covered with polyvinylidene fluoride (PVDF) film. The tip of this beam was attached to the tyre edge near the rim since this part of the tyre encounters minimal deflection with respect to the rim. The second end of the beam was connected to a cylindrical element that is attached to the tyre inner surface. This cylinder caused low rigidity in longitudinal and radial directions and high rigidity in the lateral direction; therefore, the beam followed the lateral sidewall deflection only. From the measured lateral deflection profile, the slip angle was derived by applying a curve-fitting technique to the linear part existed in the initial portion. The lateral tyre force and the aligning moment were obtained from the deflection curve utilising a model that described the deflection profile inside the contact patch. A brush model used these estimated values for the slip angle, lateral force, and moment and provided the tyre-road friction coefficient (Erdogan et al. 2011). As mentioned, this sensor provided only lateral deformation measurements. Moreover, it would be challenging to build a smaller

version of this sensor for small tyres similar to the ones used in this research. It is also unknown whether a very shorter beam will generate strong signals to extract the lateral deflections.

2.1.2.3 Acceleration sensing

As can be seen in Table 2.1, several merits have encouraged the use of accelerometers as a basic component in many tyre-sensing systems. Accelerometers are small, lightweight, widely available, and well understood (Braghin et al. 2006; Ergen et al. 2009; Moffitt et al. 2009). Moreover, they can provide a robust performance to endure the sudden measurement peaks when passing through the tyre-road contact patch (Braghin et al. 2006; Ergen et al. 2009; Moffitt et al. 2009). Furthermore, three-axial accelerometers can give accelerations in radial, longitudinal, and lateral directions with a wide passband (Braghin et al. 2006).

The majority of the in-tyre sensing systems adopt an accelerometer attached to the tyre inner liner (Figure 2.6) (Daimler 2005; Braghin et al. 2006; Savaresi et al. 2008; Ergen et al. 2009; Hong et al. 2013; Cheli et al. 2014; Krier et al. 2014; Matsuzaki et al. 2014; Niskanen & Tuononen 2015). However, the potential of acquiring acceleration signals using an accelerometer embedded in the tyre tread was also investigated (Daimler 2005). Nevertheless, this tread sensor could not provide useful data due to the sensor-tyre relative motion throughout the contact patch.

One sensor was sufficient to deliver the required measurements (Daimler 2005; Savaresi et al. 2008; Ergen et al. 2009; Hong et al. 2013; Krier et al. 2014; Matsuzaki et al. 2014). To obtain higher resolutions, two (Cheli et al. 2014) and three (Braghin et al. 2006; Niskanen & Tuononen 2015) accelerometers were also used.

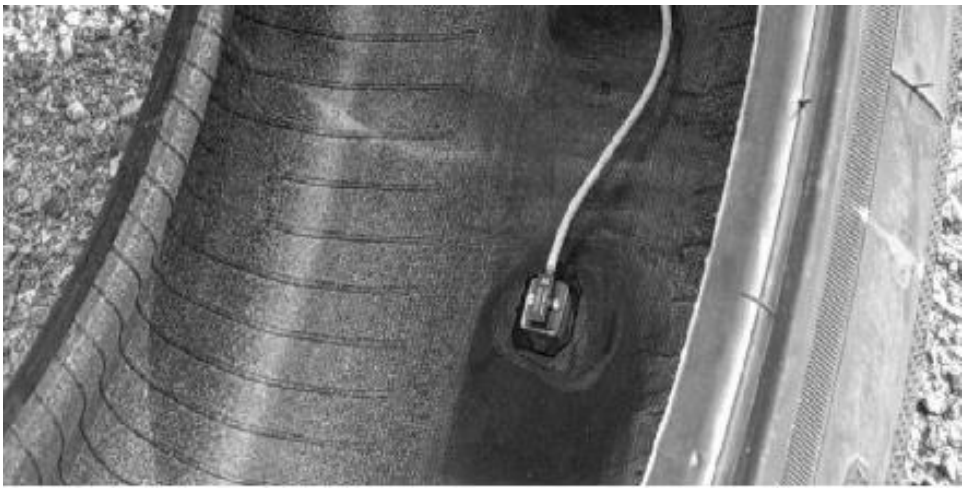

Figure 2.6: In-tyre accelerometer (Savaresi et al. 2008).

The accelerometer's readings were processed to derive the tyre-road contact forces. For this reason, most acceleration sensing systems were designed utilising three-axial accelerometer (Daimler 2005; Braghin et al. 2006; Ergen et al. 2009; Hong et al. 2013; Cheli et al. 2014; Matsuzaki et al. 2014; Niskanen & Tuononen 2015). These sensors could measure radial, longitudinal, and lateral acceleration profiles. Consequently, their signals can be analysed to estimate the three-dimensional contact forces (Braghin et al. 2006; Ergen et al. 2009; Cheli et al. 2014). The three-axial accelerometers can also be oriented to capture acceleration measurements only in one direction. For instance, Hong et al. (2013) measured lateral acceleration profiles to calculate lateral forces while Daimler (2005) used accelerometer measurement in the radial direction to determine vertical forces. Alternatively, a one-axial accelerometer can be employed to monitor acceleration signals in one direction. For example, Savaresi et al. (2008) and Krier et al. (2014) used the radial acceleration curves that were provided by a one-axis accelerometer to estimate longitudinal and vertical forces.

Measurements of the acceleration sensing systems were deployed to develop efficient estimation systems for longitudinal slip, wheel slip angle, vehicle sideslip angle, road surface's texture and condition, and tyre-road friction coefficient (Daimler 2005; Braghin et al. 2006; Ergen et al. 2009; Hong et al. 2013; Cheli et al. 2014; Matsuzaki et al. 2014; Niskanen & Tuononen 2014; Niskanen & Tuononen 2015).

Table 2.1 shows that despite the promising results obtained from the accelerometer-based systems, a number of challenges can be seen. Firstly, since the accelerometers record rotational and gravitational accelerations as well as vibration signals, it is crucial to develop a powerful algorithm to process the data. This algorithm must efficiently decouple these measurements and suppress unwanted readings to determine the desired parameters (Daimler 2005; Ergen et al. 2009; Moffitt et al. 2009). In addition, it is necessary to use an accelerometer with a high dynamic range. This compensates for the fact that the acceleration is proportional to the square of the wheel's angular velocity (Daimler 2005). Daimler (2005) suggested that the last issue could be negotiated by either considering it when designing the sensing system or integrating the acceleration signal with proper boundary conditions. Finally, heating induced by the tyre-road friction creates the problem of measurement sensitivity to temperature change. This problem should be addressed if the accelerometer is placed directly in the tyre tread (Moffitt et al. 2009).

2.1.2.4 Force sensing

For safe operation and reliable mobility of ground vehicles, direct measurement of tyre-road contact forces is valuable as it helps develop efficient control systems. In addition, it is possible to measure local forces in the contact patch with force sensors embedded in the tyres (Zhang et al. 2013). Therefore, a better understanding of complex dynamic events at the tyre-road interface such as slip and friction can be achieved (Zhang et al. 2012).

Only two force-sensing systems have been identified in the literature. Firstly, an elastic tactile sensor consisting of a cantilever (a whisker) attached to a circular base that carries three evenly spaced strain gauges was designed. The sensor was proposed to measure the tyre's vertical and horizontal forces as well as horizontal forces' directions (Ise et al. 2013). Experimental tests conducted with this sensor attached to a manipulator showed promising results. As shown in Figure 2.7, to install this sensor inside a car tyre, the elastic base was fixed to the tyre inner surface and the contacting part (the whisker) was passed through a hole in the tyre tread. For proper sensing, a specific distance between the end of this part and the surface of the tyre is an important factor. To validate the sensor's measurements, indoor tests were performed on a

custom-built test rig wherein the tyre fully slips on the contact surface. These tests showed that the measurements were disturbed by the tyre's deformations. To reduce this error, five correction constants were determined and introduced into the equations. Eventually, the sensor's readings were utilised to calculate the friction coefficient of the contact surface (Ise et al. 2017).

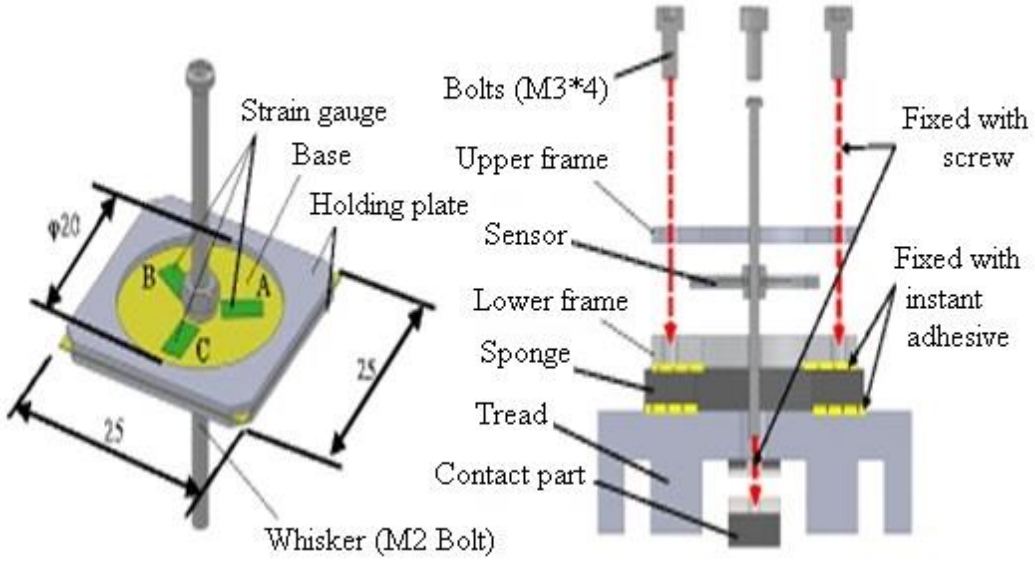

Figure 2.7: Tyre's force sensor built by Ise et al. (2017).

Zhang et al. (2012) and Zhang et al. (2013) developed the second force sensing system. It was based on a flexible pressure-sensitive electric conductive rubber sensor embedded inside the tyre rubber (Figure 2.8). They placed the sensor inside the contact patch of a motorcycle tyre. The sensor performance was tested during the stick to slip interactions. A beam-spring model utilised the internal pressures measured by the sensor to derive the local friction forces at the sensor position in three directions. The sensor was only sensitive to compressive pressures exerted perpendicularly on the sensor's cells. Therefore, an optimal positioning orientation was required to eliminate the tensile stresses potentially existing in the rubber layer. However, the authors stated that this was very challenging due to physical constraints.

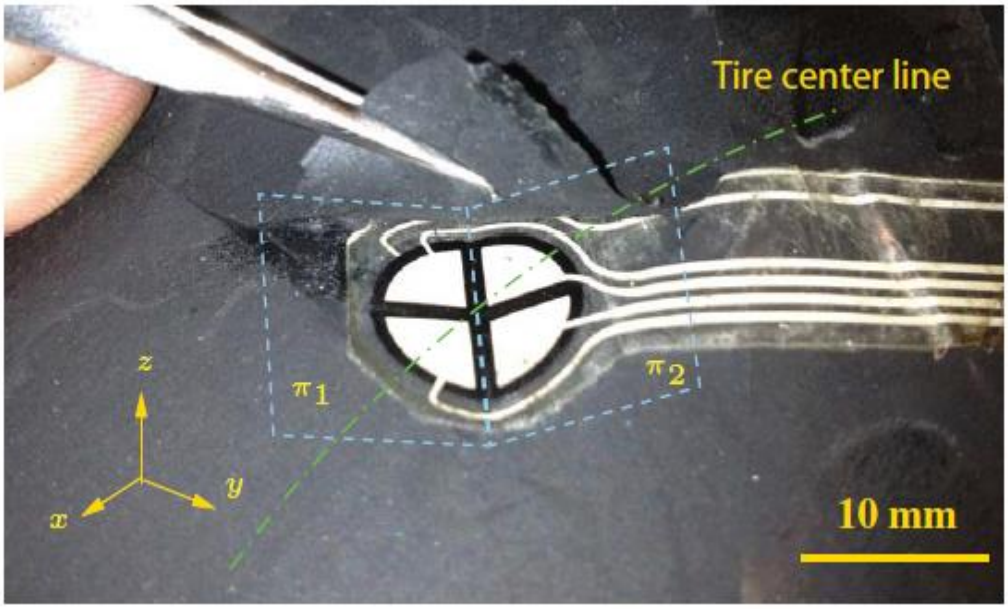

Figure 2.8: Tyre's force sensing system designed by Zhang et al. (2013).

Some negative points can be noted with force sensing systems. Zhang et al. (2013) stated that measuring contact forces at the tyre-road contact patch is challenging due to tyre rubber properties. Rubber is a viscous-elastic material and, hence, its deformations are described by a nonlinear stress-strain relationship and hysteresis (Pohl et al. 1999). Moreover, an accurate sensor model is essential to decouple the contact forces in longitudinal, lateral, and normal directions (Zhang et al. 2013). Lastly, it is evident that a strict installation procedure is crucial to ensure correct measurements.

Table 2.1 summarises the main advantages and disadvantages of the in-tyre sensing systems presented in the automotive field.

Table 2.1: Summary of tyre deformations' measurement systems in the automotive field.

Properties / **Sensing Systems**	**Advantages**	**Disadvantages**
Strain sensing systems	• Direct measurements. • Strain readings are not affected by the tyre's rotational velocity. • Strain data are easier to analyse.	• Must meet critical requirements such as material compatibility with tyre rubber and high durability.
Deformation sensing systems	• Do not require major modifications for the tyre structure. • Do not affect tyre primary tasks. • Do not disturb tyre deformation measurements.	• Large sensor size. • The need for complex data processing algorithms to model the sensor's data.
Acceleration sensing systems	• Accelerometers are small, lightweight, and well understood. • Can provide a robust performance to endure sudden measurement peaks when passing through the contact patch. • Three-axial accelerometers can give accelerations in radial, longitudinal, and lateral directions.	• A sophisticated data processing algorithm is crucial to decouple rotational and gravitational accelerations as well as vibration signals and suppress unwanted readings. • Acceleration measurements are affected by the wheel angular velocity. • Heating induced by tyre-road friction creates the problem of measurement sensitivity to temperature change for embedded sensors.
Force sensing systems	• Direct measurement of tyre-road contact forces is valuable as it helps develop efficient vehicle control systems. • Measuring local forces in the contact patch is possible.	• Require a sophisticated manufacturing process. • May produce inaccurate force measurements because of local disturbances for the deformations. • An optimal positioning orientation is needed which might not be achieved due to physical constraints. • Affected by tyre rubber properties. • An accurate sensor model is essential to decouple the contact forces in three directions.

2.2 Surface identification and obstacle detection using in-tyre sensing

The main sensors utilised for surface identification through in-tyre sensing are the accelerometers. Some researchers used the frequency content of the in-tyre acceleration signals to differentiate and classify the road surfaces (Matsuzaki et al. 2014; Niskanen & Tuononen 2015; Khaleghian & Taheri 2017). Other researchers utilised the root mean square (RMS) values of radial accelerations outside the tyre-road contact to identify the roughness of the road (Braghin et al. 2006). Niskanen and Tuononen (2014) studied the partial and full aquaplaning of car tyres by examining the shapes of the contact patch extracted from the in-tyre accelerometers.

Promising results were reported for using these in-tyre accelerometer-based methods for surface classification. Nevertheless, the main drawback of these methods was the dependence of acceleration on the tyre's angular velocity. Thus, to determine the validity of the proposed features extracted from the acceleration signals for the estimation process, it is indispensable to test these methods over a wide range of velocities (Lee & Taheri 2017).

A group of researchers had investigated the use of piezoelectric film sensors inside a robot's tyre for surface discrimination (Armstrong et al. 2015). They suggested that the amplitude and width of the sensor's measurements could be used as an indication of the road surface. However, their preliminary results implied that a more extensive study in terms of both experiments and analysis needs to be conducted. This should be done to verify the possibility of using this kind of sensors as well as the proposed algorithm for surface identification.

Another type of sensors was used to identify the condition of the road surface. Tuononen and Hartikainen (2008) utilised the tyre deflection measurements acquired by an optical sensing system. The main components of this system were a position sensitive diode (PSD) mounted on the wheel rim inside the tyre and a light-emitting diode (LED) attached to the tyre inner liner. The PSD monitored the position of the LED in x, y, and z directions. As a result, tyre deflections in longitudinal, lateral, and radial directions can be derived from the sensor's outputs. To differentiate between

wet and dry road surfaces, certain characteristics in the signals indicating the radial and the longitudinal deflections were compared. In particular, the peak's value and position in the average value curves as well as the value and shape in the standard deviation curves were utilised. It was also suggested that the standard deviation curves of these deflections could be employed to identify the start of the hydroplaning.

Regarding obstacle detection, the idea of using tyres equipped with sensors to detect obstacles has not been widely addressed in the robotic field and has never been presented in the automotive field. However, identifying objects, such as rocks, tree branches, etc., in the vehicle's roadway helps the controller to adjust the movement accordingly. The in-tyre sensing can provide tactile information about the true texture of these obstacles. This information can complement other sensors' readings, such as camera images, in building a better understanding of the traversed surfaces. For instance, the in-tyre sensor's data can be utilised to estimate how much slip would be introduced to the vehicle's motion when moving over particular objects. In addition, passing over or hitting some obstacles may cause mechanical vibration in the vehicle body. If the in-tyre sensors can provide indications that these vibrations exceed a predefined permissible level, then an appropriate control action could be consequently activated.

To the best of the author's knowledge, the only relevant work in the area of using tyre deformation sensing systems for obstacle detection was conducted by Lauria et al. (2002). They developed tactile wheels by placing a group of 16 IR sensors on the wheel hub to measure the deformation of the tyre inner surface. This sensing system was utilised to locate the contact points around the tyre's circumference to determine whether the tyre has hit an obstacle. This measurement was used by the controller to adjust the locomotion and enable the robot to climb the sensed obstacle. The researchers were only interested in estimating the contact points rather than acquiring continuous deformation profiles from the sensors. Furthermore, they tested this sensing system only on a special wheel. With this wheel, the sensors could be fixed on the hub, i.e., the sensors were not turning with the rim and tyre.

2.3 Wheel slip estimation methods

Slip detection has been investigated for various applications in robotics. For example, object manipulation where either avoiding or exploiting slip is required, object gripping and grasping, and biped walk stabilization (Holweg et al. 1996; Melchiorri 2000; Kaneko et al. 2005; Lincoln & Bamberg 2010; Teshigawara et al. 2010; Dao et al. 2011; Zhang & Liu 2012; Kawamura et al. 2013; Shirafuji & Hosoda 2014). For wheeled mobile platforms, many researchers have addressed wheel slip detection, which is in the focus of this study. In general, wheel slip estimation was used either to improve vehicle control systems (Miller et al. 2001; Anderson & Bevly 2004; Baffet et al. 2009; Changfang Chen et al. 2013), or to enhance position estimation techniques (Wada et al. 2000; Ojeda et al. 2006; Yi et al. 2007; Jung et al. 2013).

Table 2.2 illustrates the main wheel slip's estimation methods with a brief summary of their advantages and disadvantages. More details follow in the subsections below.

Table 2.2: Summary of wheel slip's estimation methods.

Properties / **Methods**	**Advantages**	**Disadvantages**
In-tyre measurements-based methods	• Direct tyre-road contact information. • No need for accurate vehicle models. • More accurate estimation.	• The challenge of selecting appropriate sensors that can endure the harsh environment inside the tyre and, at the same time, deliver meaningful measurements. • Technical difficulties of mounting sensors inside tyres.
Inertial measurements-based methods	• Autonomous. • Real-time navigation solutions.	• Accumulative errors.
Absolute measurements-based methods	• Accurate and consistent navigation solutions.	• Signal blockage and attenuation. • Slow update rates. • Necessity of data synchronization with other sensors. • Relatively expensive.
Integrated inertial-absolute measurements-based methods	• Continuous navigation solution • Robust estimations.	• High sensitivity to sensors and models uncertainties • Relatively expensive.
Visual measurements-based methods	• Real-time information on the entire surrounding environment. • Possibility of predicting slip beforehand. • Measurement errors at a specific point will not affect the upcoming readings.	• Necessity of identifying traceable features. • Illumination problems. • Image disturbances caused by dynamic obstacles. • Considerably expensive.

2.3.1 In-tyre measurements-based methods

The emergence of the intelligent tyres/smart wheels in the automotive field has tempted the researchers to investigate a new slip estimation method. This method uses direct tyre-road contact information measured with in-tyre sensors. It implies the challenge of selecting appropriate sensors with certain specifications. The sensors must endure the harsh environment inside the tyre and, at the same time, deliver meaningful measurements. This issue was discussed in more details in Section 2.1.2.

In this direct slip estimation method, four types of sensors were utilised to collect the data. The first type was capacitive strain sensors (Matsuzaki & Todoroki 2008a). The strain sensors were either a flexible patch-type sensor (Matsuzaki & Todoroki 2007) or a self-sensing sensor where the tyre itself becomes an electric condenser (Matsuzaki & Todoroki 2006). Secondly, a piezoelectric deflection sensor based on polyvinylidene fluoride (PVDF) was presented (Erdogan 2009; Erdogan et al. 2011). The third sensor was a three-axial accelerometer (Braghin et al. 2006; Ergen et al. 2009; Hong et al. 2013; Cheli et al. 2014). The fourth sensor was a pressure sensor (Zhang et al. 2013).

The estimation algorithms relied mainly on processing the tyre sensor's data to calculate the slip variables. Therefore, the longitudinal wheel slip was estimated by deriving the tyre's effective radius from circumferential strain profiles (Matsuzaki & Todoroki 2008a). Similarly, the tyre's slip angles were calculated through a line fitting to the linear part of the lateral deflection curve. This curve was obtained from either lateral deflection measurements (Erdogan 2009; Erdogan et al. 2011) or lateral acceleration signals (Hong et al. 2013). Cheli et al. (2014) used a model based-Extended Kalman Filter (EKF) to combine measurements from two in-tyre accelerometers with vehicle standard sensors to estimate vehicle sideslip angle.

As it was shown, the in-tyre measurements-based methods were developed to separately estimate either the longitudinal or the lateral wheel slip. However, Zhang et al. (2013) detected local slip onsets at the tyre sensor's location in both the longitudinal and lateral directions. They used the measurements of a flexible pressure-sensitive electric conductive rubber sensor. In addition, in-tyre acceleration signals were

analysed to derive several synthetic parameters related to calculating both the longitudinal wheel slip and the lateral slip angle (Braghin et al. 2006; Ergen et al. 2009).

With a slightly different level of sensor measurement's accuracy, Nam et al. (2013) proposed a method to estimate the sideslip angle for electric vehicles. They used a linearised lateral tyre model where the lateral forces were obtained directly from multi-sensing hub units.

2.3.2 Inertial measurements-based methods

Inertial sensors are self-contained positioning components that can provide real-time navigation solutions (Zhang 2003). Despite that, the inertial measurements can contain bias and noise errors. Integrating these measurements can lead to accumulative drifts in position and velocity estimations (Farrell & Barth 1999).

To correct these errors, the inertial data can be augmented with other measurements. In this section, the focus is on the correction techniques that do not require the use of external positioning measurements. These techniques depend on combining the inertial readings and the wheel speed's measurements for the slip estimation. The wheel slip was estimated through merging the sensors' measurements using either an extended Kalman filter (EKF) or a machine learning method. Under the first method, a model-based EKF was used to integrate the readings of the inertial measurement unit (IMU) and the wheel encoder. These readings were utilised to calculate the longitudinal wheel slip for a skid-steered mobile robot (Figure 2.9) (Yi et al. 2007; Yi et al. 2009). The same approach was enhanced with the steering angle's measurements to estimate vehicles' lateral slip angles (Baffet et al. 2009). For the machine learning method, Jung et al. (2013) and Ward and Iagnemma (2007) derived distinguishing features from the inertial and wheel speed measurements. They employed these features to recognise the longitudinal wheel slip's occurrences using a support vector machine (SVM) classifier. The two groups of researchers chose different number and types of features and tested the slip prediction method on indoor and outdoor mobile robots respectively. In addition, Ojeda et al. (2004) used fuzzy logic to fuse wheels'

encoder measurements with gyroscopic data. They deployed these readings to identify a situation when all wheels of a Mars rover slip in the longitudinal direction of motion.

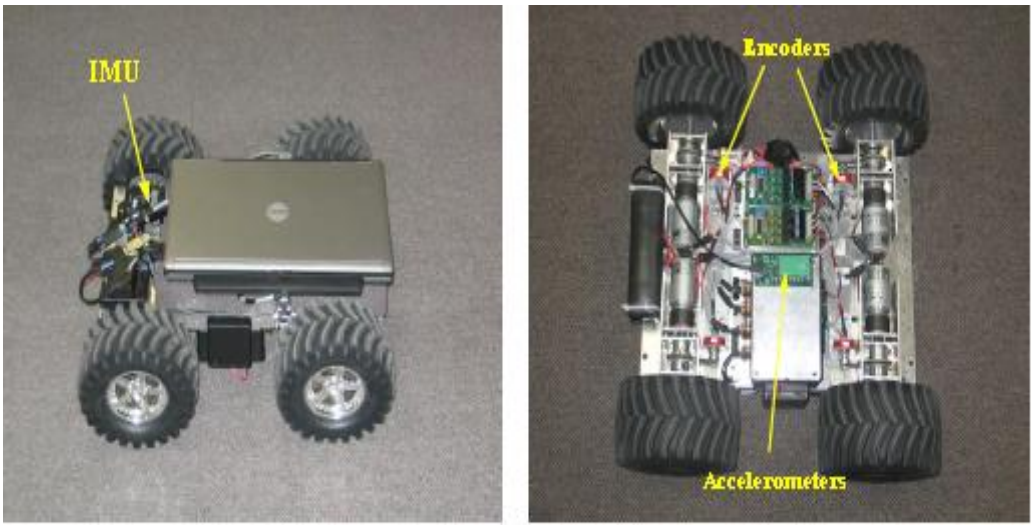

Figure 2.9: Inertial sensors utilised to estimate wheel slip for a skid-steered mobile robot (Yi et al. 2007).

Individual contributions in the field of estimating wheel slip using inertial data are also identified. For example, a nonlinear model-based observer was presented to determine the vehicle's longitudinal wheel slip theoretically. The observer used calculations of a parameter related to tyre-road contact (Changfang Chen et al. 2013). To develop this observer, the wheel's angular speeds, the wheel's steering angles, and the inertial measurements were all assumed to be known. In addition, Ward and Iagnemma (2007) briefly described a simple method to detect the longitudinal wheel slip for a rough-terrain rover. They suggested comparing the robot's body velocity obtained by integrating accelerometer readings to the wheel velocity derived from the encoder measurements.

2.3.3 Integrated inertial/absolute measurements-based methods

The global positioning system (GPS) can deliver consistent navigation solutions with high accuracy (Zhang 2003). Thus, the GPS combined with some of the vehicle standard sensors can be used to detect the wheel slip for outdoor applications. For example, Miller et al. (2001) integrated velocity measurements from the GPS and the wheel's speed sensor. They calculated the wheel slip ratio and the longitudinal force.

Then, they constructed the linear part of the longitudinal force-slip curve to improve the vehicle's control systems. Bevly et al. (2000) proposed a method to calculate longitudinal wheel slips, vehicle sideslip angles, and tyre sideslip angles. They used the GPS velocity measurements aided by wheel steering angle and wheel speed measurements. Expected estimation errors when employing this GPS-based approach are related to GPS signal blockage and attenuation (Zhang 2003), multi-path errors (Salycheva 2004), and GPS slow update rates (Daily & Bevly 2004). Moreover, there is a necessity of synchronising the data from the GPS and the wheel speed sensor if online slip estimation is intended (Miller et al. 2001).

Because of their complementary characteristics as positioning systems, the GPS and the inertial navigation system (INS) are often integrated. This integration produces more robust and accurate estimations as compared to either system in a standalone mode (Jwo et al. 2013). Such a combination has been explored for wheel slip estimation. A general scheme of estimating wheel slip utilising Kalman filter (KF) to merge inertial and absolute measurements can be noted in the literature. Commonly, lateral slip variables were estimated with this approach. Specifically, vehicle sideslip angles were determined using either a model based-KF (Anderson & Bevly 2004) or a kinematic KF (Wada et al. 2000; Ryu et al. 2002; Anderson & Bevly 2004). Among these algorithms, a distinguishing aspect of taking roll and pitch effects into consideration was presented by Ryu et al. (2002). The estimations of the vehicle sideslip angles were deployed to enhance the control systems (Anderson & Bevly 2004) and to improve position estimation systems (Wada et al. 2000). Conversely, the longitudinal wheel slip was detected using an EKF to capture mobile robots' immobilisation states on different terrains (Ward & Iagnemma 2008). Besides inertial and absolute measurements, wheel encoder readings were also employed in the filter framework (Wada et al. 2000; Ward & Iagnemma 2008).

Three drawbacks of this slip estimation method that integrates the inertial and absolute measurements using KF can be stated. The estimation is highly sensitive to uncertainties present in the sensors' readings and vehicle models (Piyabongkarn et al. 2009). In addition, Song et al. (2008) stated that the EKF may not produce accurate slip estimates if the vehicle's direction of travel is changed. In this case, the EKF is a linear filter that is being used for a nonlinear system. Moreover, Piyabongkarn et al.

(2009) illustrated that developing accurate slip estimation systems using GPS, whether in a standalone mode or integrated with inertial measurements, is relatively expensive.

2.3.4 Visual measurements-based methods

Three main features promote the use of visual sensors for wheel slip estimation. First, the ability to deliver real-time information on the entire surrounding environment (Heewon & Jae-Bok 2013). Second, the possibility of predicting the slip beforehand (Angelova et al. 2006). Third, the fact that measurements' errors at a specific point will not affect the upcoming readings (Song et al. 2008).

A number of visual methods were introduced to address the slip estimation for outdoor navigation especially for rough terrain rovers (Song et al. 2008; Song et al. 2009) and planetary rovers (Helmick et al. 2005; Angelova et al. 2006; Reina et al. 2008). However, the vision techniques can also be used to estimate slip for indoor applications. For instance, Heewon and Jae-Bok (2013) used the slip estimations extracted from camera images to improve the simultaneous localization and mapping (SLAM) algorithm. This algorithm can be used to reduce the localisation errors for robotic vacuum cleaners.

The visual methods for slip estimation were developed using visual data from a single camera (Reina et al. 2008; Song et al. 2008; Song et al. 2009; Heewon & Jae-Bok 2013), or a stereo pair (Helmick et al. 2005; Angelova et al. 2006). The sensor can be oriented in four directions. It can be mounted downward to monitor the terrain surface (Song et al. 2008; Song et al. 2009). Alternatively, it can be placed upward to capture ceiling images in indoor places (Heewon & Jae-Bok 2013). Another solution was to install the camera backwards to observe wheel traces on sandy terrains (Reina et al. 2008). Furthermore, it can be positioned forward to collect data about the regions in front of the rover (Helmick et al. 2005; Angelova et al. 2006).

A number of visual methods were based on visual data only (Angelova et al. 2006; Reina et al. 2008; Song et al. 2009). Other methods combined the visual data with measurements from other sensors such as wheel encoders (Song et al. 2008; Heewon & Jae-Bok 2013), IMU (Helmick et al. 2005), compass, and steer sensors (Reina et al.

2008). To integrate the visual data with other measurements, different techniques were employed such as sliding mode observer (Song et al. 2008), Kalman filter (Helmick et al. 2005), comparison (Heewon & Jae-Bok 2013), and linearised relations (Reina et al. 2008). The visual measurements were obtained using optical flow (Angelova et al. 2006; Song et al. 2008; Song et al. 2009; Heewon & Jae-Bok 2013), Hough transform (Reina et al. 2008), and maximum likelihood estimation (Helmick et al. 2005).

Some researchers had deployed the visual measurements to estimate only lateral slip variables (Reina et al. 2008; Heewon & Jae-Bok 2013). Nevertheless, the vision-based methods can estimate wheel slip in both longitudinal and lateral directions (Helmick et al. 2005; Song et al. 2008; Song et al. 2009). Instead of estimating, Angelova et al. (2006) proposed a regression algorithm for slip prediction. The algorithm predicted slip in unknown areas that a planetary rover was about to traverse. A nonlinear slip model was learnt using training sets extracted from visual measurements in both motion directions.

The major challenge that is encountered with the visual approaches is the necessity of identifying useful traceable features in the scene (Ward & Iagnemma 2008). There is also the known issues of cameras such as illumination problems and image disturbances caused by dynamic obstacles (Reina et al. 2008; Heewon & Jae-Bok 2013). Furthermore, depending on the quality of the visual sensors, these visual methods are considerably expensive (Piyabongkarn et al. 2009).

2.3.5 Other methods

In addition to the major categories mentioned in the previous sections, several contributions can be noted in the area of wheel slip detection. For instance, measurements of the motor current that are related to wheel torques have been used to detect the longitudinal wheel slip. Ojeda et al. (2006) proposed a longitudinal slip detection and odometry correction method for mobile robots travelling over sandy terrain at a constant low speed. The slippage was indirectly estimated by correlating motor current measurements to wheel-terrain interaction through an approximated linear model. Measurements from the motors were also used by Klomp et al. (2014). They exploited the supposedly accurate wheel torque data supplied by electric motors

in hybrid vehicles to detect the longitudinal wheel slip. Employing an if-then-like algorithm, wheel torque and wheel speed were compared against their respective predefined maximum values. The slip was identified when both quantities exceed their allowable limits.

Furthermore, the slippage was determined solely through the available wheel encoder measurements. In the work of Gustafsson (1997), differences in encoders' readings between driven and non-driven wheels were calculated. The longitudinal wheel slip for a two-wheel-drive vehicle was estimated during normal driving utilising these differences. Additionally, Reina et al. (2006) compared the encoders' measurements for wheels on the same side of a six-wheeled planetary rover against each other using fuzzy logic. The result of this comparison was utilised to recognise a case when all wheels slip in the longitudinal direction of motion on soft sandy terrains.

Finally, general observations related to the field of wheel slip estimation can also be noted. Firstly, it was established that wheel slip is related to tyre-road friction (Gustafsson 1997). Therefore, it is relevant to point out that a great body of work exists for tyre-road friction estimation especially in the automotive literature (Muller et al. 2003). Moreover, some researchers have deployed this friction-slip relationship to obtain critical information. For example, Chankyu et al. (2004) used standard vehicle sensors, a fifth wheel, and a set of observers and estimators to calculate the wheel slip ratio and the friction coefficient. They constructed the friction coefficient-slip curve to estimate the maximum friction coefficient for different driving scenarios. Secondly, in spite of being outside the scope of the work presented in this thesis, it should be mentioned that there have been several contributions and advances in the domain of wheel slip control (Changfang Chen et al. 2013).

2.4 Conclusion

The designs of the in-tyre sensing systems were examined. When building a sensing system inside the tyre, the size and material of the wheel and the tyre are determining elements in the design. Therefore, the study of the design of the in-tyre sensing systems was divided in this literature review into two fields: robotic and automotive.

This literature review revealed that the intelligent tyre's technologies and applications have been widely investigated for cars. In contrast, the robotic field has witnessed a limited number of attempts to exploit the intelligent tyre's concepts and benefits. The majority of these attempts targeted the rigid wheels used in the low-speed planetary or rugged terrain's rovers. In addition, only one research presented a sensing system for tyre rubber's deformation in non-pressurised tyres (Lauria et al. 2002). This sensing system measured the deformation of the non-pressurised tyre through indirect sensing using IR sensors. It was designed for a special wheel where the sensors could be fixed on the hub. The sensors were not turning with the rim or the tyre. The measurements of this sensing system were used to estimate only the contact points on the tyre circumference for solely the application of obstacle detection.

Various sensor types, technologies, and configurations were presented to develop in-tyre sensing systems. The following points summarise the main observations about the presented in-tyre sensing systems:

- The contacting strain sensing delivers the most direct tyre deformation measurements. In addition, the strain measurements are robust to changes in the tyre's angular velocity (Moffitt et al. 2009). Moreover, since the strain sensor captures the local deformations near its mounting position, it is more straightforward to extract the relationships between the strain features and the tyre forces, slip variables, and contact patch's dimensions (Matsuzaki & Todoroki 2008a; Yang 2011; Yang et al. 2013).

- Non-contacting deflection sensing tries to estimate the tyre's deformation by interpreting the indirect measurements related to the tyre inner surface's movements (Tuononen 2009). There are two issues here: complex signal processing and higher estimation errors.

- The proposed non-contacting optical sensing systems utilised a position sensitive diode (PSD), CCD camera, or laser sensors mounted on the wheel rim inside the tyre (Matsuzaki et al. 2012; Naranjo et al. 2014; Xiong & Tuononen

2014). Evidently, a large space inside the tyre between the wheel rim and the tyre inner surface is required to build such systems.

- Non-contacting deflection sensing systems based on an ultrasonic sensor has also been used (Magori et al. 1998). Nevertheless, the system was not able to consistently monitor the tyre deformations around the tyre circumference. Within the contact patch, the direction of the main ultrasonic beam might not be perfectly perpendicular to the tyre wall. This produces weak echoes that are vulnerable to interferences from various reflected signals. In addition, this sensing system can be used to measure the vertical tyre's deformations only.

- A special approach of strain sensing was introduced (Matsuzaki & Todoroki 2008b). It utilises a self-sensing technique where the steel wires in the tyre belt serve as electrodes to indicate capacitance variations caused by the tyre's deformations. This approach was designed only for car tyres. It cannot be adopted for small robots' tyres since there are no steel wires integrated into their much simpler structure.

- With acceleration sensing systems, a sophisticated data processing algorithm is crucial to decouple the various measured accelerations and eliminate the unwanted signals. Thus, using such systems to study dynamic problems as complex as tyre-ground interactions further complicates the matter (Ergen et al. 2009). Secondly, it was seen that the accelerometers used to build these systems by other researchers are expensive. It is impractical to embed such high-cost components inside low-cost tyres.

- Only two force sensing systems were proposed (Zhang 2014; Ise et al. 2017). There is an inherent difficulty in the sensor's placement and the installation procedure for the two systems. Furthermore, a highly developed data processing algorithm is required to decompose the measured force into its three-dimensional components.

- It was observed that the design of some sensing systems is very hard due to the difficulty of the associated manufacturing or installation process. For example, some systems depend on instrumenting a tread block and other systems require placing augmented parts like pins that penetrate the tyre tread (Pohl et al. 1999; Breuer et al. 2000).

- Two possible options to place the contacting sensors inside the tyre were identified. Either gluing the sensors to the tyre inner surface or embedding them in the tyre tread. The second option is more difficult to be positioned properly (Zhang et al. 2013). Additionally, the embedded sensors may not provide useful readings because of the relative motion between the sensor and the tyre along the contact patch (Daimler 2005).

- The measurements of the tyre deformations in the longitudinal direction were used to estimate the tyre's mechanical parameters under straight-line steady state and braking/traction rolling. For example, Matsuzaki and Todoroki (2008a) utilised the longitudinal strain profiles to derive the longitudinal wheel slip, the contact patch length, and the driving/braking torque. Lateral deformation measurements were employed to estimate the mechanical variables related to the turning (cornering) condition such as the slip angle and the lateral force (Erdogan 2009). Measuring the tyre deformations in both the longitudinal and lateral directions provides estimations for the tyre's properties related to both straight line and turning conditions (Yang et al. 2013).

Regarding surface identification and obstacle detection utilising measurements of in-tyre sensing systems, only a few contributions have been identified in the literature. None of these systems has used the direct measurements of tyre strain for the intended purpose. For surface identification, most of the proposed in-tyre sensing systems were based on accelerometers. These systems were used to classify the contact surfaces, characterise the roughness of the surface, and examine the surface condition (Braghin et al. 2006; Niskanen & Tuononen 2014; Khaleghian & Taheri 2017). To build a reliable surface identification system based on acceleration measurements, a wide range of the tyre's rotational velocity must be considered. The reason is that the rotational velocity affects the surface signature extracted from the acceleration signal.

For obstacle detection, only one in-tyre sensing system was presented (Lauria et al. 2002). As mentioned earlier in this section, this system was designed for a wheeled robot with non-pressurised tyres. The system monitors the deformation of the tyre's inner surface using a group of IR sensors. The measurements of the system were used to identify the obstacles by detecting the contact points around the circumference of the tyre's outer surface. This detection of the contact points was utilised to adapt the locomotion mechanism so that the robot can climb the detected obstacle. The system was designed for a wheel with a special mechanical design that allows fixing the sensors to the rim. The sensors were not rotating with the rim and tyre. This sensing system can be used to estimate the height of the obstacles, but it might not be efficient in providing information about the texture (rough or smooth) or the condition (dry or wet) of the obstacles.

For wheel slip estimation, the literature showed that most methods were developed based on measurements from sensors mounted on the body of the mobile platform. These methods utilised inertial, absolute, and visual measurements. The inertial methods can provide real-time slip estimations without using additional positioning measurements but they can experience accumulative estimation errors (Zhang 2003). The absolute methods give more consistent estimations for the wheel slip. The main error sources for the absolute methods are the slow update rates and the reflections or blockage of the GPS signal (Daily & Bevly 2004). The visual methods can be used to predict the wheel slip by monitoring the areas that the vehicle is about to traverse (Angelova et al. 2006). The visual methods require identifying distinguishing features in the images to detect the wheel slip. Furthermore, the performance of the visual sensors may be affected by the variation in the lighting or atmospheric conditions. Since the tyre-ground contact area is the region of interest when estimating the wheel slip, all of the aforementioned slip estimation methods required integrating the indirect measurements with accurate vehicle models. However, because of the complexity of wheel-ground interaction, such models that necessarily involve transformations, constraints, and approximations could compromise the slip estimation accuracy. In contrast, the estimation methods that employ direct contact measurements from the in-tyre sensors require less knowledge of vehicle dynamics and provide more accurate estimations (Hong et al. 2013). The in-tyre sensors can collect tactile measurements about the true working condition of the tyre and the

contact surface (Tuononen & Hartikainen 2008). These tactile measurements can significantly improve the estimation of the wheel slip. On the other hand, these methods imply the unavoidable challenges of selecting the appropriate sensor that can operate inside the tyre while being able to deliver meaningful data. In addition, developing a powerful signal processing algorithm is crucial to derive relevant parameters from the sensor measurements and estimate various slip variables.

2.5 Formulation of research work

After reviewing the related studies in the literature, a research gap was identified. No prior research could be identified in the area of examining the possibility of measuring the strain of small non-pressurised tyres through low-cost strain sensors attached directly to the tyre inner surface. Thereby, no previous work has investigated the use of such in-tyre strain measurements to extract information about the tyre and its surroundings. The following points highlight the aspects of this lack of knowledge by suggesting a formulation for the research work.

- This work will focus on building an in-tyre sensing system for small non-pressurised tyres as they are widely used in small to medium-sized mobile robots.

- Taking into account the sensor size, cost, complexity, availability, and compatibility with the tyre's material, the contacting strain sensing utilising a flexible sensor is suggested for this research. A direct strain sensing system for non-pressurised tyres will be constructed utilising standard low-cost strain sensors glued to the tyre inner surface. It was decided to use resistive strain gauges for this research because they are low-cost, general-purpose, and experimentally widely used. In addition, they are extremely thin and flexible. Furthermore, they operate within an adequate temperature range. They also have a high-elongation capability. Additionally, they have a self-temperature compensation (STC) characteristic to reduce thermal effects to the least possible levels. All these features make these sensors an ideal solution for

developing a sensing system inside a small tyre in robotic platforms. Utilising these strain sensors, a new tyre sensing system in terms of sensors' type, number, and configuration will be designed to reach the specific research objectives.

- The sensing system should deliver reasonable measurements under different speed levels, i.e. not only low speed. This ensures that the developed sensing system can be utilised for a wider range of applications. This is an additional reason for deciding to adopt a strain sensing system since the strain measurements are not affected by the tyre's angular velocity.

- Both longitudinal and lateral strain profiles will be captured with this sensing system. This helps in estimating the tyre's mechanical properties and identifying the surface and obstacles during both the straight line and the turning conditions.

- The measurements from the in-tyre strain sensors will be analysed to extract features that correspond to the tyre's mechanical properties as well as to the tyre's surrounding environment. The characteristics of the measured strain waveforms will be employed to detect slip/spin incidents, identify the traversed surface, and detect obstacles. In addition, they will be utilised to estimate the forces in three directions, the contact patch length and centre, the tyre's angular velocity, and the tyre's camber angle.

Chapter 3

Experimental Setup and Tests' Description

This chapter describes the components of the experimental setup and the tests that were conducted to collect the data. Section 3.1 describes the stages of the experimental work that were followed to install the strain gauges inside the small non-pressurised tyre. It also presents the static footprint tests that were conducted to study the contact patch of this tyre. Image processing is utilised to analyse the tyre's footprints and extract the contact patch variables. The results of this analysis are used to suggest the best design for the sensing system for the tyre used in this research. The sensor system design is discussed in terms of selecting a suitable area, sensors' number and positions, and the required specifications. After that, the section presents the series of steps for placing the strain sensing system on the inner surface of the tyre. Section 3.2 presents the static part of the experimental work. It describes the first bench-top rig that was designed to conduct the static tests. The section explains the static tests that were carried out to investigate the readings of the strain sensors. These tests were designed to study the strain profiles of the sensors under different vertical and longitudinal forces. The static tests also examined the measurements of the sensors during slip incidents. Section 3.3 introduces the dynamic part of the experimental work. The section starts by showing the details of the second bench-top rig built to perform the dynamic tests. The section then explains the tests that were utilised to study the effect of various variables on the measurements of the sensors. These variables were the tyre angular velocity, the vertical load, the camber angle, and the contact surface. The data acquired from these dynamic tests will be utilised to investigate the capability of the in-tyre sensors to identify tyre spin, obstacles, and contact surfaces. It will also be used to study the

relationships between the strain measurements and the tyre forces, the contact patch parameters, the angular velocity, and the camber angle.

Three points should be stated about the tests that are presented in this chapter. The measurements of the sensors were collected synchronously by the data acquisition system. In addition, each test was run five times and the average of the data collected from these runs was employed. Thirdly, four identical tyres were used in each of the tests. The sensors' measurements obtained from the four tyres were very close. The readings collected using these tyres were averaged and utilised to draw the observations illustrated in the next chapters.

3.1 Designing an in-tyre strain sensor system

3.1.1 Testing the possibility of building a strain sensing system inside a small non-pressurised tyre

The strain gauges utilised for this research were from Micro-Measurements division (Measurements group, INC.). The gauges' type is CEA - 06 - 240UZ - 120 Student Gauges. The resistance of the gauge is $120.0\,\Omega \pm 0.3\,\%$ and the gauge factor is $2.070 \pm 0.5\,\%$ at $24°$ C. These low-cost, general-purpose, experimentally widely used gauges are extremely thin, 0.056 mm, and flexible. For static strain readings, they operate in a temperature range from -75° C to +175° C. For single cycle use, these high-elongation gauges can measure up to 5 % elongation. To reduce thermal effects to the least possible levels, self-temperature compensation (STC) feature has been added to the gauges during the production process. All these merits make these sensors an ideal solution for developing a sensing system inside a small non-pressurised tyre. It was indispensable to design a new tyre sensing system in terms of sensors' type, number, and configuration to reach the specific research objectives. In the following, the successive stages to bond these sensors on the inner surface of a robotic tyre are described.

Stage 1: Developing a method to bond sensors to tyres using a piece of rubber and plastic samples. Many plastic samples were cut to the same size as the strain gauges.

The three main steps were surface preparation by cleaning, abrading, and marking; plastic samples' preparation; and bonding operation. The benefit of this stage was choosing appropriate cleaning substances, deciding a suitable grit degree for the abrasive paper, learning how to deal with the samples, selecting a proper marker, determining type and amount of adhesive, and mastering the bonding process.

Stage 2: Gluing a real strain gauge on a rubber strip utilising results of the tests in Stage 1. After that, wires were soldered to the gauge. A data acquisition (DAQ) system based on National Instruments' hardware and LabVIEW software was built to collect the sensor reading. It consisted of a NI cDAQ - 9172 and NI 9219 type interface and LabVIEW 2014. The built-in quarter-bridge configuration of NI 9219 was used. During this simple test, the strip was manually pulled to apply a small amount of force and corresponding strain changes were indicated by the sensor output.

Stage 3: Gluing strain gauges on different locations on the inner surface of a small non-pressurised tyre. The previously mentioned surface preparation, gauge bonding, and soldering operations were performed to install the sensors inside the tyre. The only new factor introduced to these operations was the curved surface of the tyre inner liner. It significantly increased the complexity of these tasks especially when taking into account that more than one sensor was placed across the limited space of the tyre width. After installing the sensors inside the tyre, initial tests were conducted on a simple version of a bench-top rig that will be presented in Section 3.2.1. In these tests, the tyre was fixed in place such that the in-tyre sensors are at the centre of the contact patch. Different values of vertical and longitudinal forces were tested and the corresponding sensors' responses were collected using the DAQ system.

3.1.2 Tyre's specifications and footprint tests to examine tyre contact patch

The tyre utilised for this study can be used for a robotic platform called CoroBot Explorer (CoroWare, Inc.). This platform has an articulated, rugged, four-wheel-drive, skid-steered base with a size of (762 mm × 508 mm × 610 mm) and a weight of approximately 157 N. Figure 3.1 presents this platform.

Figure 3.1: The robotic platform (CoroBot Explorer) for which the in-tyre sensing system is designed in this work.

Traditionally, the tyres that are used with this platform are fused to the wheel with a very strong adhesive. Since the application of in-tyre sensors requires the ability to easily get the tyres off the wheels, the standard tyres were not helpful and the best solution was to use the so-called bead-lock rims. In these wheels, the tyre is fixed to the wheel with a bead-lock ring that is secured using screws to fix the tyre edge to the rim. Thus, these wheels are typical for the application. In addition, throughout the course of this work, these bead-lock rims were very useful. They were used to hold a custom-designed bracket in compression tests and, later on, a custom-designed clamp to lock the tyre at different angular positions in static tests. The wheel is approximately 89 mm in inner diameter, 113 mm in outer diameter, and 83 mm in width. The tyres are non-pressurised, i.e., they do not use compressed air. This type of tyres is commonly used for robotic platforms. The tyre is approximately 95 mm in inner diameter, 139 mm in outer diameter, 87 mm in width, and 10 mm in sidewall height.

Compression tests were conducted using a compression machine (HOUNSFIELD H5KS universal testing machine) to study the tyre's contact patch in terms of its shape as well as the effect of changing the vertical force on varying its shape and size. Knowing these features will lead to suggesting a suitable design of the sensory system for the particular tyre used herein. Figure 3.2 shows the experimental setup of these

tests. A u-shaped aluminium bracket was manufactured to hold the tyre in these tests. The small screws in the bead-lock rim were utilised to fix the bracket to the wheel. A 3D printed part was designed and screwed to the upper side of the bracket to attach the tyre to the compression machine. To obtain the footprints of the tyre in the tests, a stamp pad was used to coat the lower half of the tyre outer surface with ink. After that, the tyre was pressed vertically against a flat wooden board on which a white paper was taped. Different values of vertical loads were applied. These values started from the lowest value where the tyre just began to make contact with the board to the maximum value where it was thought that applying a higher force would damage the tyre or the rim. The range of the vertical loads was between 5 N to 100 N in an increment of 5 N.

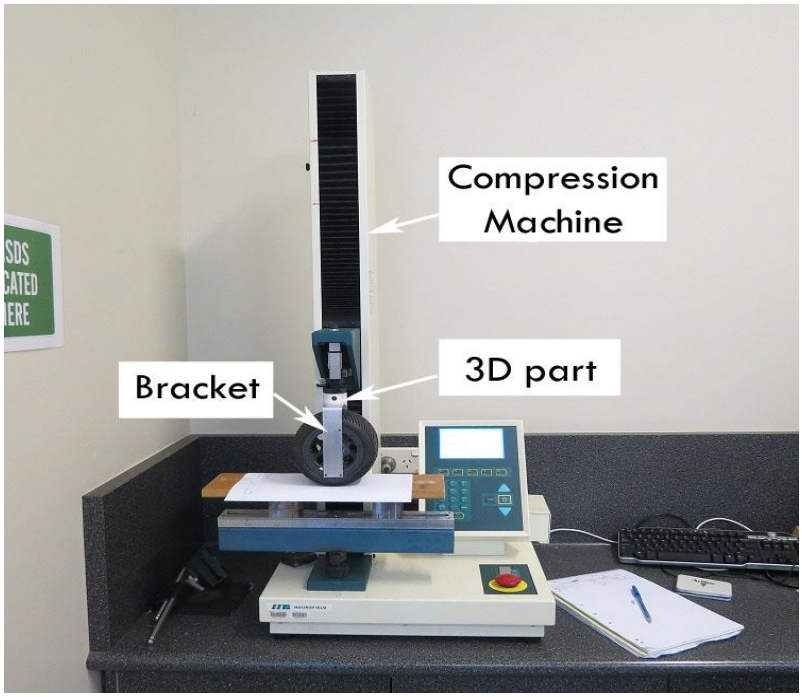

Figure 3.2: Setup of the footprint tests.

After completing the footprint tests, the 20 contact patch prints were scanned into the computer. The images were processed in Matlab to measure, in pixels, the footprint area, the maximum longitudinal length, and the maximum lateral length. Figure 3.3 illustrates the steps of the image processing algorithm used to find the required quantities. A spatial calibration factor was then calculated and used to convert these measurements from pixels to millimetres.

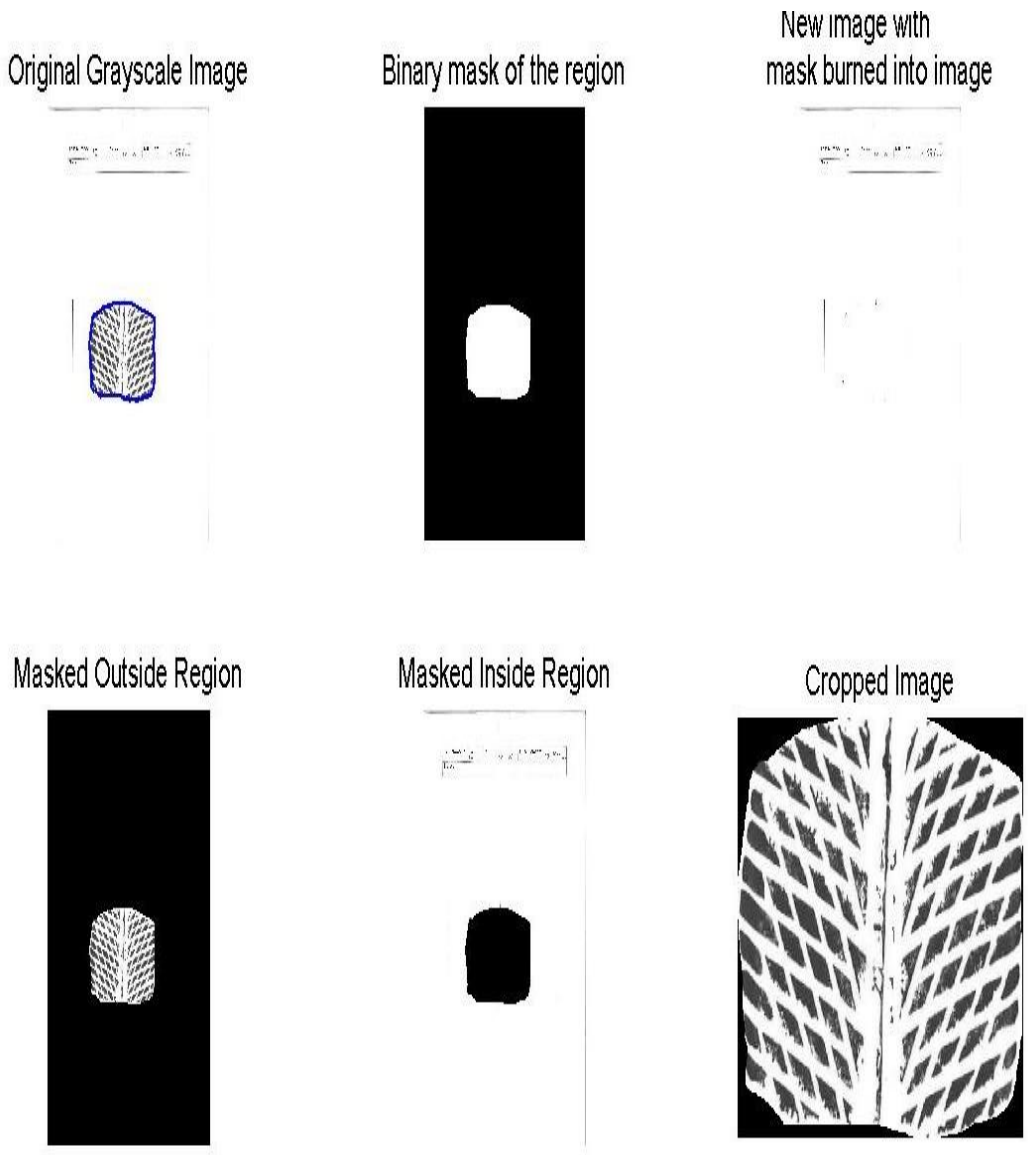

Figure 3.3: Image processing for the tyre footprint.

It can be seen in Figure 3.4- Figure 3.6 below that as the vertical force increases, the vertical tyre displacement (vertical tyre deformation) and the footprint geometry increase. However, it can be noticed that starting from a vertical force of 60 N, the curves almost saturate. It is also observed that the increase in the longitudinal length is more notable than the increase in the lateral length (Figure 3.6).

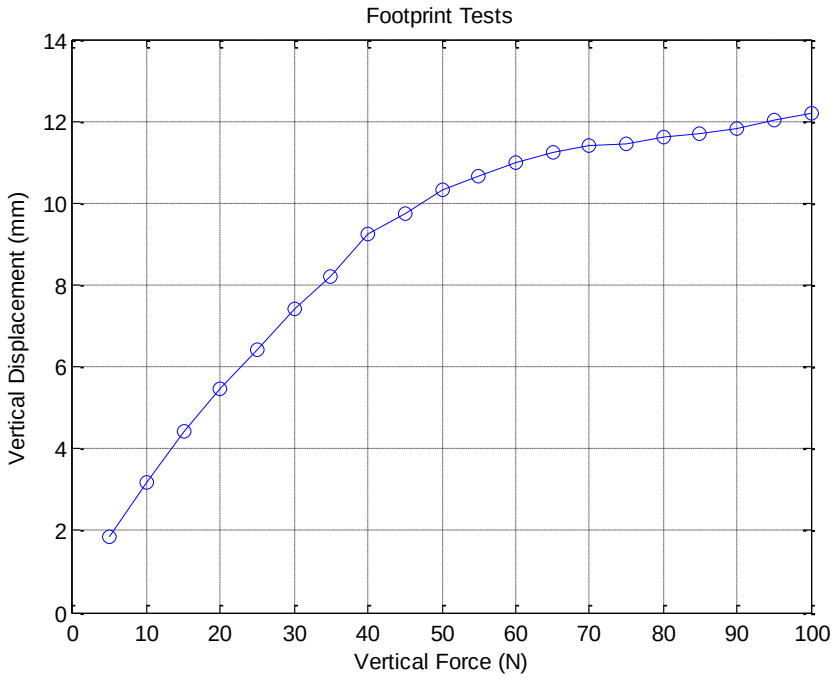

Figure 3.4: Footprint tests: Vertical displacement vs. vertical force.

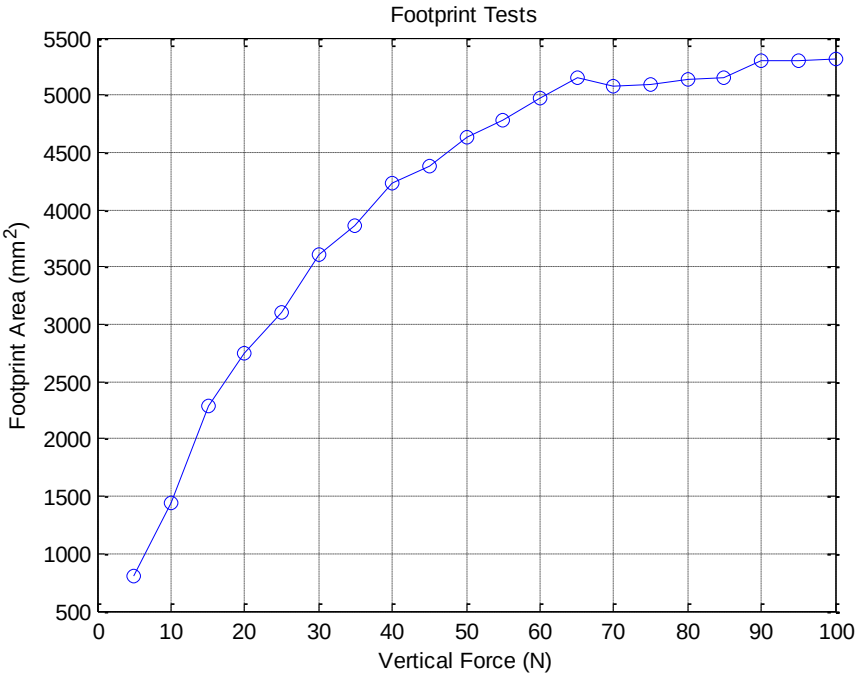

Figure 3.5: Footprint tests: Footprint area vs. vertical force.

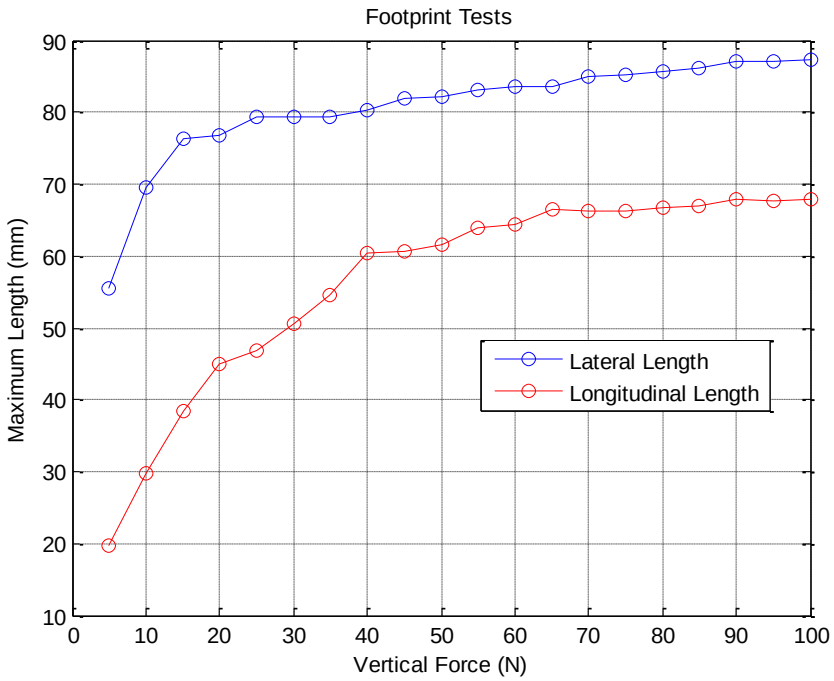

Figure 3.6: Footprint tests: Maximum length vs. vertical force. The lateral length is the footprint length in the lateral direction and the longitudinal length is the footprint length in the longitudinal direction.

3.1.3 Sensor system's design

As stated in Section 3.1.2, the benefit of the static footprint tests was to know the shape and geometry of the contact patch for the specific tyre used herein and thereby to decide the best sensor system's design and sensors' positions. When designing an in-tyre sensing system, it has to be ensured that the position of the sensor is decided such that it is always located inside the contact patch regardless of the tyre working condition (Daimler 2005). Applying this note and utilising the results of the footprint tests, it was decided to place the sensor system in an area that corresponds to the smallest possible footprint, resulting from a vertical load of 10 N. This engineering decision was driven by the fact that this is a reasonable loading for small to medium-sized robots and by the available space inside the tyre. With this placement, it is ensured that all the sensors are located inside the area of the contact patch under all possible loading conditions. Choosing a smaller area, such as the footprint of 5 N, was not possible due to physical limitations where the sensors would have to be placed

close to each other in such a small area. With the strain gauges used in this research, this was not possible since these standard low-cost sensors required delicate operation of gluing and soldering. In addition, this would have resulted in no significant differences in the readings of the sensors since they would be located in the same limited space. Finally, since the sensors are inside the contact patch when 10 N vertical load is applied, they will certainly be within the contact patch when bigger loads are exerted.

To decide the most appropriate sensor system design, some factors were considered. Most importantly, the system must be able to capture measurements reflecting the strain distribution in both longitudinal and lateral directions. The reason for that was to cover the possible cases of tyres' straight-line steady state and braking/traction rolling as well as turning (cornering). Other factors that affected the decision were the tyre dimensions, the minimum number of required sensors, and the best locations to position the sensors. The design explained in this section was judged to be the most promising configuration.

Regardless of the shape of the contact patch, the circumferential (longitudinal) strain can be measured with one sensor placed longitudinally on the centreline, i.e., at the middle of the contact patch. Even under braking or traction, one circumferential sensor placed at the centreline is sufficient to measure the corresponding change in the circumferential strain distribution (Matsuzaki & Todoroki 2008a). In contrast, two sensors placed laterally and symmetrically about the centreline are required to measure the change in the axial (lateral) strain distribution. These two lateral sensors give different measurements during steering (cornering) because they capture the asymmetric lateral strain distribution (Yang 2011). The presented research focuses on the tyre's movement in the longitudinal direction of motion rather than on steering. However, monitoring the change in the lateral strain across the width of the contact patch was important for two reasons: studying the effect of camber angles and getting a rough estimation of the applied/generated lateral forces during the tests. Therefore, two axial strain sensors placed symmetrically about the centreline were included in the design.

In the selected design, six strain gauges were glued on the tyre inner surface as illustrated in Figure 3.7. The implemented design consists of three pairs of strain

gauges. In each pair, one strain gauge is placed longitudinally while the other is placed laterally with respect to tyre direction of rotation. One pair is mounted on the tyre centreline while the other two pairs are placed symmetrically about the centreline. If a higher data update rate is required, this design can be repeated circumferentially, for example, it could be located at 120°, 0°, and -120°. Considering the previous points related to placing longitudinal and lateral sensors, it can be concluded that the proposed design contains three redundant sensors. These are the two side longitudinal sensors and the middle lateral sensor. The reason for that was to account for possible misalignments in sensors' mounting as well as different degrees of thickness across the tyre due to tread pattern. In addition, distributing the sensors across the tyre width is useful in estimating the shape of the contact patch. Furthermore, it is helpful to place sensors on different positions to compare their readings and to validate the derived conclusions.

Lastly, it can be mentioned that some previous works suggested that placing sensors on the tyre sidewall might give useful information that could complement the readings collected from the tyre tread. However, with the robotic tyre used in this work, where the sidewall is very small (less than 10 mm), it is physically very difficult to put a sensor that would operate properly. The main issue would be the small space where the sensor is supposed to be glued. There is also the high probability of sensor de-bonding when the sidewall is stretched or compressed due to applied forces. Another issue is the technical challenge of the soldering and wiring.

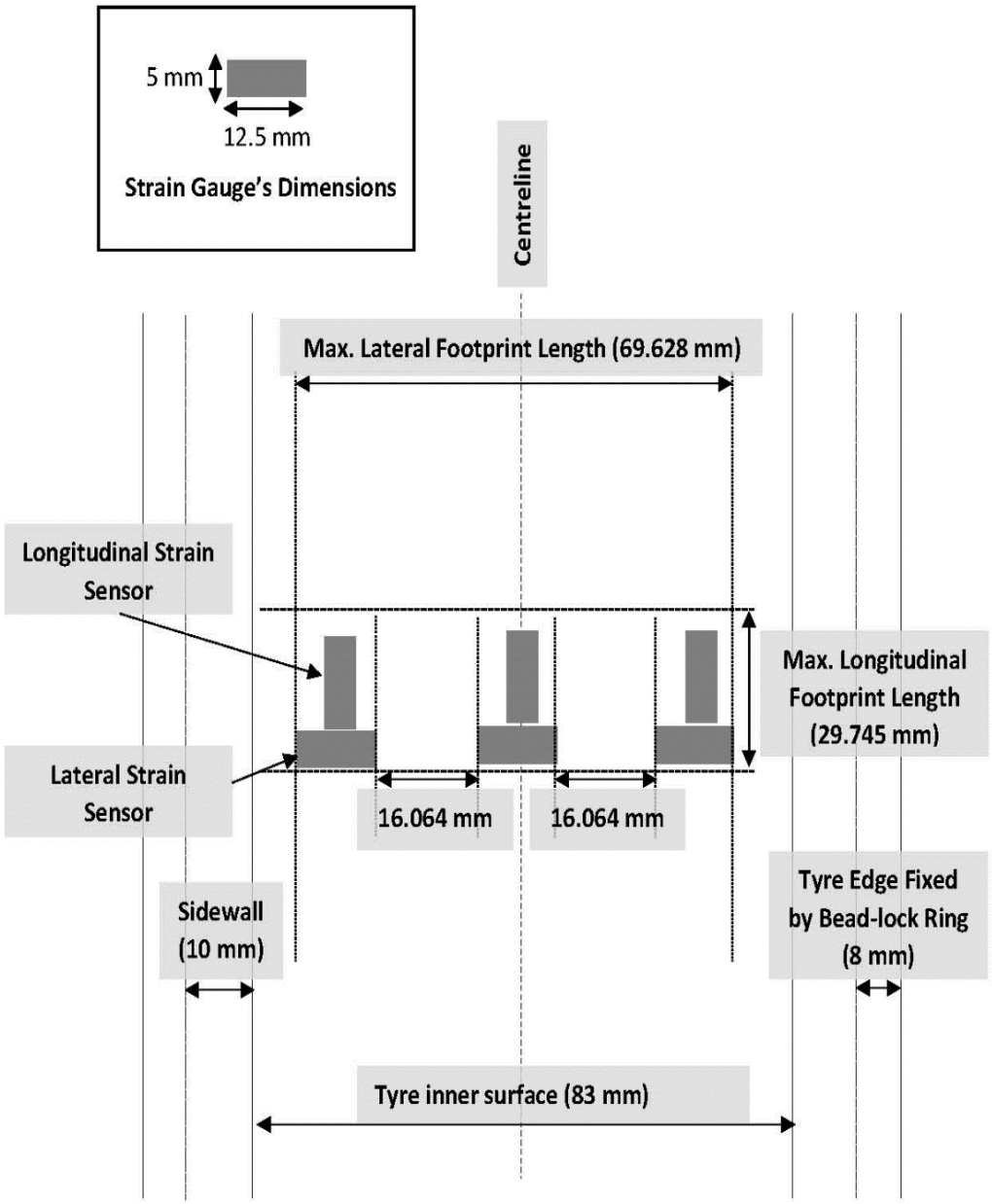

Figure 3.7: Diagram of the tyre inner surface with the sensor system design.

To summarise, this section aimed at proposing a design for the in-tyre strain sensing system for the tyre used in this work. For this purpose, the images of the tyre's footprints acquired from the static compression tests were processed in Section 3.1.2. This image processing helped in studying the shape of the contact patch. It also provided the dimensions of the contact patch under different vertical loads. To account for the various loading conditions, the smallest footprint was selected to place the design. The idea was to position all the sensors inside the contact patch under all

expected loading conditions for the tyre. The dimensions and shape of the selected footprint were utilised to decide the number, orientation, and positions of the sensors. The maximum allowable number of longitudinal and lateral sensors were placed inside the selected area. This design ensures the collection of the strain data that could be used to estimate the tyre's mechanical properties in the straight-line steady state rolling, braking/traction, and turning cases. It also accounts for possible installation imperfections and allows comparing the strain measurements collected at different points. The design consists of three longitudinal-lateral pairs of sensors distributed across the width of the contact patch. One pair is placed on the tyre's centreline and the other two pairs are mounted symmetrically about the centreline.

3.1.4 Sensor system's placement

Based on the results of the footprint tests, a sensor system design was suggested to meet the research objectives (more details were presented in Sections 3.1.2 and 3.1.3). This section describes the process of placing this design inside the tyre. This process involved three stages: bonding the design to the tyre inner surface, soldering wires to the gauges, and assembling the wheel. The following operations were performed to prepare the tyre inner surface for the bonding stage. First, degreasing an area that is bigger than that needed for the sensor system placement using isopropyl alcohol and gauze swabs. Then, abrading the same area using 320-grit abrasive paper. After that, removing residuals from the abrasion operation using alcohol and gauze. Finally, marking the tyre centreline near the area.

To build the sensor system, six strain gauges were prepared. The following steps were followed. A paper with a diagram of the desired sensor design, as in Figure 3.7, was attached to the bottom side of a glass board that was used as the work surface. The diagram in this paper showed the exact positions of the sensors based on the results of the footprint tests. Afterwards, the resistance of each of the six strain gauges was measured using a digital multimeter to ensure that they were in a good working condition. The resistance value was around 120 Ω for each of the gauges. Then, the bonding side of the gauges was wiped with alcohol then they were left for two minutes to dry on a piece of gauze. After that, the gauges were transferred to the glass board

and positioned to their suggested locations in the design. Lastly, a piece of wide sticky tape was used to transfer all the gauges at once to the tyre inner surface.

To bond the sensors, the sticky tape was attached to the tyre inner surface such as the sensors are positioned to their correct locations. To do so, the marks drawn on the tyre inner centreline were used as a reference. Next, the design was mounted on the tyre inner surface with three consecutive steps. In each step, a part of the sticky tape that holds two adjacent sensors, one longitudinal and one lateral, was lifted. Then, enough amount of adhesive (alkyl glue) was placed on the tyre and then the sensors were returned to their positions on the tyre. A piece of gauze was used to wipe on the tape to spread the glue and then a firm thumb pressure was applied for two minutes. Additional two minutes were waited before lifting the tape from the gauges. Figure 3.8 shows the sensor system design glued to the tyre inner surface. Before moving to the next process, the positions of the six sensors were marked on the tyre outer surface.

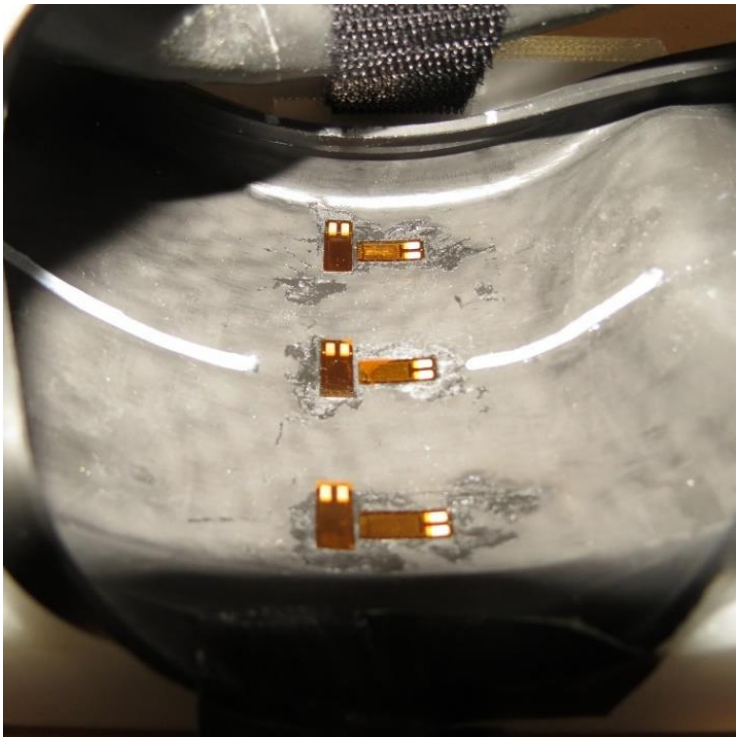

Figure 3.8: The sensor system glued to the tyre inner surface.

The second stage was soldering wires to the gauges. For each of the gauges, two lead wires were soldered to the two gauge's tabs and then a strain relief loop was made. Figure 3.9 shows the sensor system after the soldering process.

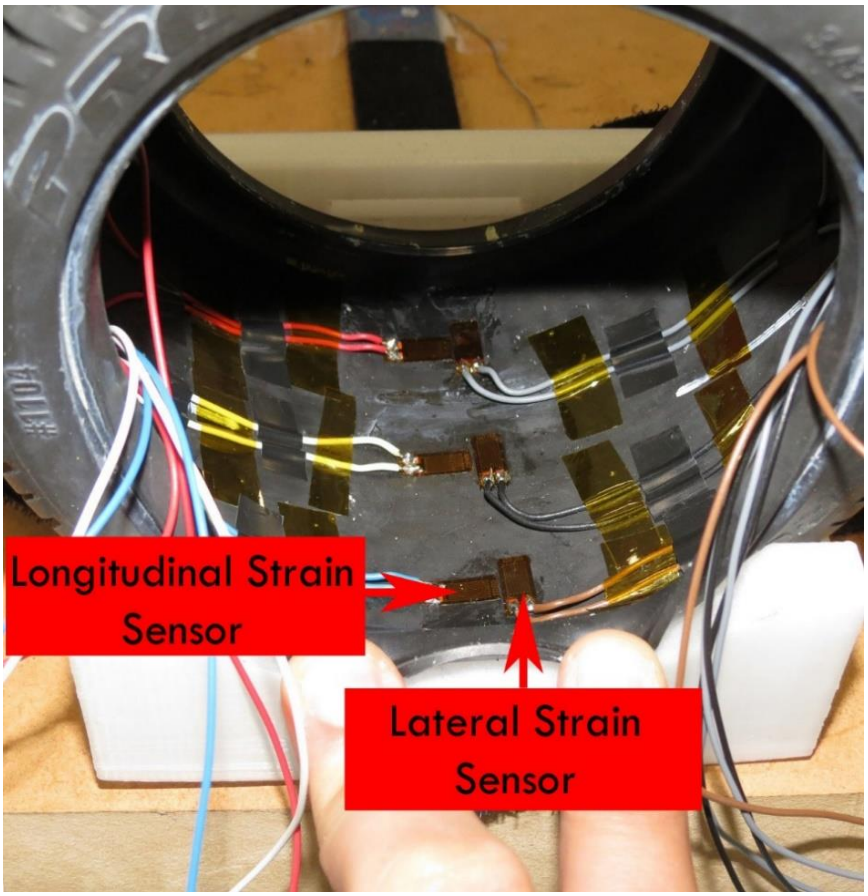

Figure 3.9: The sensor system after the soldering process.

The Final step was assembling the tyre, foam, and wheel together. To do this, two holes were created in the foam to pass the wires from inside the tyre to outside the foam. Then, two existing holes in the wheel were used to pass the twelve wires (six through each hole) to outside the tyre as shown in Figure 3.10a. Then, the two wires coming from each of the six sensors were labelled, for example, longitudinal 1. These wires will be connected directly to the National Instruments system to collect the strain readings from the in-tyre sensors. After that, the foam was carefully inserted inside the tyre as shown in Figure 3.10b. Finally, the wheel was placed inside the tyre and foam assembly as shown in Figure 3.10c. The tyre was then fixed to the rim using the two bead-lock rings.

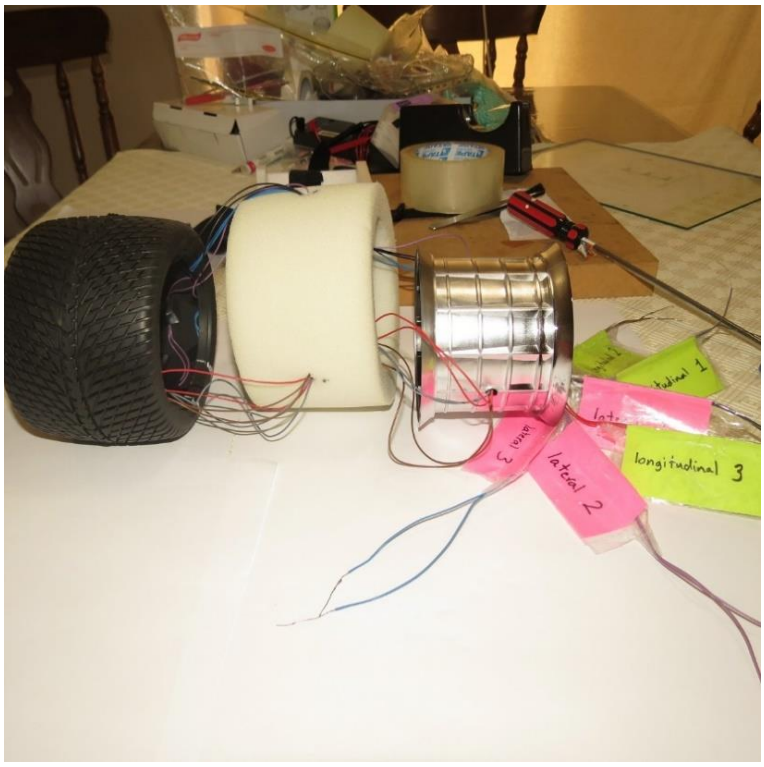

(a) Step 1: The wires are passed from inside the tyre to outside the wheel.

(b) Step 2: The foam is inserted inside the tyre.

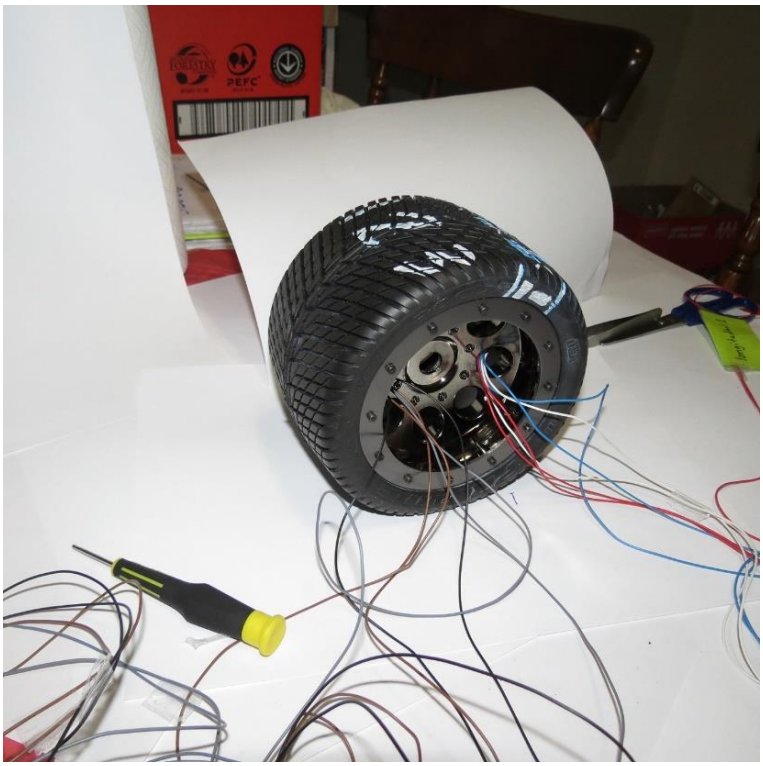

(c) Step 3: The wheel is placed inside the tyre and foam assembly.

Figure 3.10: Assembling the wheel.

3.2 Setup and description of the static tests

3.2.1 Bench-top rig used for the static tests

A single-wheel bench-top test rig, shown in Figure 3.11, was built to examine the performance of the in-tyre strain sensors using static tests. Different vertical forces (F_z), longitudinal forces (F_x), and angular positions can be tested with this rig.

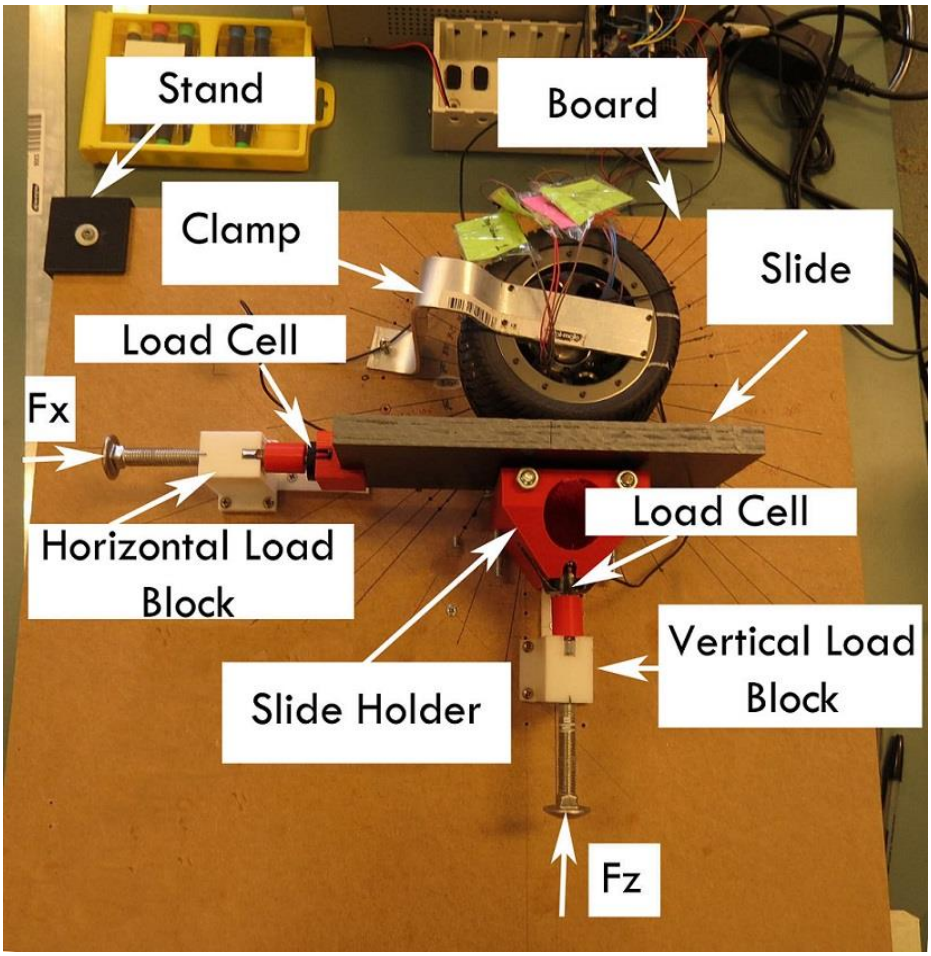

Figure 3.11: Tyre bench-top rig used for the static tests.

The rig consists of a wooden board (600 mm × 600 mm × 17 mm), 3D parts printed using both ABS (Acrylonitrile Butadiene Styrene) and PLA (Polylactic Acid), aluminium clamp, bolts, screws, and bearings. Four corner stands and one central stand hold the board on a bench. A vertical load block is used to apply vertical forces to the tyre. The vertical load block is a 3D printed bracket with a track attached to its base and a bolt that passes through a hole in its upper part. By turning the bolt, a slide is

pushed towards the tyre in the radial direction. A horizontal load block is used to apply longitudinal forces on the tyre by directly pushing the slide in the longitudinal direction with respect to the tyre contact patch. The horizontal load block has the same design as the vertical load block. A slide holder is designed to enable the slide to move both vertically and horizontally with respect to the tyre contact patch. The slide holder is a 3D printed part that moves along the track of the vertical load block. To build the sliding mechanism, a group of bearings, bolts, and threaded rods were placed inside the slide holder. The slide is a wooden board (250 mm × 120 mm × 17 mm) that is placed on the bearings of the slide holder. It is used to apply vertical and longitudinal forces to the tyre. A cylindrical 3D printed part is used to hold the tyre. This tyre holder is screwed to the board with four screws and contains a central bolt hole. An M12 × 120 mm type bolt was used to secure the wheel through its centre axis. This bolt passes through the centre of the wheel to the central hole in the tyre holder and to the board. A custom-designed aluminium clamp is built to hold the tyre at different angular positions. As seen in Figure 3.11, this clamp was fixed at one end to the wheel through four screws in the bead-lock rim and at the other end to the board. To fix the tyre at different angles, the clamp was moved and screwed to the board at specified positions. Two compression load cells (Type FC2231 - 0000 - 0025 - L) from TE Connectivity are used to measure the applied vertical and longitudinal loads. The first load cell was placed on the slide holder to measure the applied vertical force while the second cell was placed at the edge of the slide to measure the longitudinal forces. As the bolts that are used to push the slide vertically and horizontally contact the load cells, the cells read the corresponding vertical and longitudinal forces.

3.2.2 Vertical load tests

First, an unloaded test was conducted to record the bias readings of the sensors. The slide used in the bench-top rig was lifted so that no vertical or longitudinal forces are exerted on the tyre.

The first set of tests was to examine the response of the sensors to the change in vertical load (F_z) only. Studying the effect of F_z is important for two reasons. First, a vertical load is always applied on the tyre as it represents the weight of the vehicle. Second, it

is a dominant factor in tyre dynamics since it affects all forces and moments experienced by the tyre (Pacejka 2005).

The tyre was fixed at 0° angle so that all the sensors are in the centre of the contact patch. After that, a vertical force was applied as one rotation of the bolt at a time step of one minute then increased by one rotation and so on. Six values of F_z were applied.

The sensors' measurements collected with these tests will be analysed in Section 4.1.1.

3.2.3 Static tests to detect slip and construct strain profiles

A second set of tests was conducted to examine the sensors' response during slip incidents. These tests aimed at investigating imitated real-life situations of a running tyre. In these situations, the tyre rotates, experiences possible changes in vertical load (wheel load) due to variation in the road surface, and encounters potential sudden forces in its circumferential direction of motion as a result of braking or traction. Hence, the performance of the sensors in response to changes in angular position, vertical force, and longitudinal force was examined.

To induce slip during the static tests, the slide was progressively pushed in the longitudinal direction over the surface of the fixed tyre. In each of these tests, the tyre was fixed at a certain angle, a constant vertical force was applied, and the value of the longitudinal force (F_x) was changed by increasing the number of rotations of the bolt from 0 to 15 rotations in steps of 1 rotation. A fixed time was left before applying each rotation. The direction of applying F_x was from left to right.

To obtain the strain profiles at different values of vertical and longitudinal forces, these tests were repeated for 13 angular positions (from 120° to -120° in steps of 20°) with three values of vertical force (F_z = 33 N, 44 N, or 60 N) in each angle. With respect to the centre of the contact patch, the positive angles are to the right-hand side while the negative angles are to the left-hand side. The most important angles are between 60° and -60°. This region is in the vicinity of the contact patch, i.e., before entering the contact patch, in the contact patch, and after leaving the contact patch. It is expected that the strain variation will be more significant in this region compared to other angular positions where the sensors are far from the contact patch. It was not possible

to examine angles that lie outside the previously mentioned range as the clamp used to fix the tyre at these angles would be blocked by other parts of the rig. Considering another limitation, choosing a smaller angular increment would have led to drilling more holes in the board to fix the tyre. Consequently, this would have resulted in a weak structure that is unable to bear the applied forces and the subsequent motions of the rig's components.

The sensors' measurements collected with these tests will be analysed in Sections 4.1.1, 4.1.2, 4.3, 5.1, and 7.1.

3.3 Setup and description of the dynamic tests

3.3.1 Bench-top rig used for the dynamic tests

A single-wheel bench-top rig, shown in Figure 3.12, was designed and built to conduct the dynamic tests. It consists of a wooden board (1200 mm × 500 mm × 17 mm), a rail (12 mm Diameter Chrome Shaft × 1000 mm), two brackets (rail support blocks), shims, two linear bearings, an aluminium sliding piece (cart), a motor, a motor's shaft extension piece, and weights (slotted rings, 100 g each).

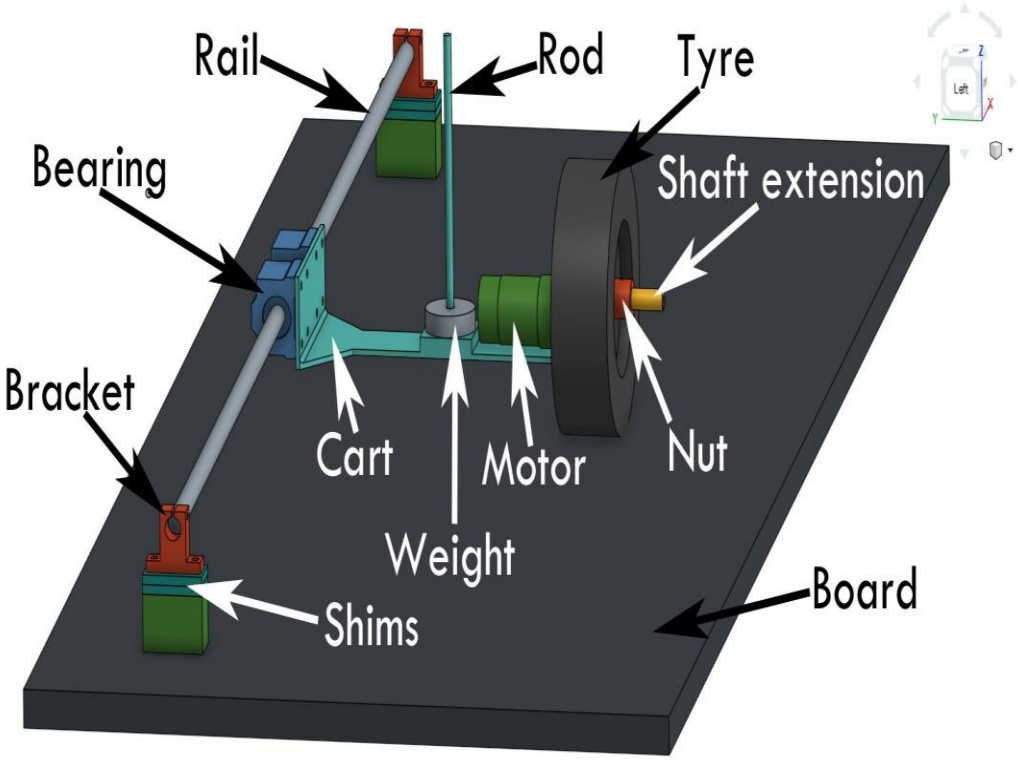

Figure 3.12: A single-wheel bench-top rig used for the dynamic tests.

The board is fixed to a table by two bar clamps. The rail is held by means of two brackets. A group of shims, which are screwed to the board, supports the brackets. The cart holds the motor at one end and is attached to two linear bearings on the other end. The linear bearings slide on the rail. The gear motor (37 D × 68 L mm) is a 12 V brushed DC motor with a 30:1 metal gearbox and an integrated quadrature encoder. Near the middle of the cart and just behind the motor, a rod is welded to a rectangular base to hold the slotted weights. The motor's shaft extension piece, shown in Figure 3.13, consists of three sections: a cylindrical base that is fixed to the motor shaft by a grub screw, a hexagon part on which the wheel hub sits, and a cylindrical rod that goes through the wheel hub. The cylindrical rod contains a threaded part on which a nut is tightened up to secure the wheel to the shaft extension piece. The cylindrical rod also contains a slot inside which the sensors' wires will be placed.

To replicate a four-wheeled robot on a flat surface, the level of the cart is checked using a spirit level to ensure that it is not tilted before conducting each run in the dynamic tests. Changes such as loading the cart or placing a surface on the board may

cause the cart to incline; therefore, a group of shims can be used below the brackets to adjust the height of the rail in order to make the system level.

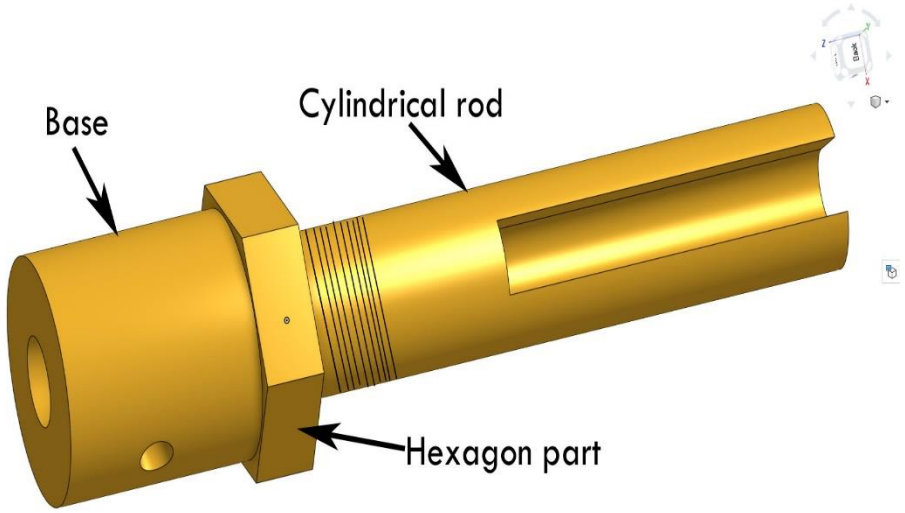

Figure 3.13: Motor's shaft extension piece.

The sensor wires are inserted in the slot that is present at the end of the shaft extension piece, shown in Figure 3.13, and secured by cable ties. Then, long flexible plastic spiral wire wrapping is used to hold the wires. The wires connect to a National Instruments system located right of the system rig. Two NI 9237 modules were used to collect the readings of the strain sensors. The quarter bridge II configuration was used for the NI 9237 modules. One NI 9222 module was used to collect the encoder's two pulses, the supply voltage, and the current sensor's readings. The current sensor (ACS714) was used to measure the motor's current during the movement of the tyre. ACS714 is a Hall effect-based linear current sensor integrated circuit (IC) with an optimised range of ± 5 A and a sensitivity of 185 mV/A. One NI 9481 was used to switch the motor on and off. A LabVIEW interface was built to acquire the sensors' data. A sampling frequency of 10 kHz was used to capture the encoder data correctly.

3.3.2 Angular velocity tests

A number of tests were conducted to investigate the effect of the tyre's rotational speed on the strain measurements. In these tests, the tyre was made to run on the bench-top rig at different speeds by changing the supply voltage to the motor. The other parameters, i.e., wheel load, surface texture, and camber angle were kept constant during these tests. Ten values of speed, ranging from 3.50 rad./sec. to 12.20 rad./sec., were examined by incrementally increasing the supply voltage to the motor from 2 V to 11 V with a step of 1 V. Section 4.2.2 presents the results of these ten angular velocity tests and states the reasons for selecting the strain profiles resulted from three representatives of these rotational speeds to be mostly presented in this thesis. These three representatives are the low rotational speed (LS), medium rotational speed (MS), and high rotational speed (HS). The angular velocities were tested under different vertical loads, contact surfaces, and camber angles.

The sensors' measurements collected with these tests will be analysed in Sections 4.2.1, 4.2.2, 4.2.3, 4.2.4, 5.2.1, 7.1, 7.2, and 7.3.

3.3.3 Vertical load tests

The tyre cart was loaded with ten different values of vertical load (F_z), from 0 N to 9 N with a 1 N increment. Section 4.2.2 presents the results of these ten vertical load tests and states the reasons for selecting four of the strain profiles to be mostly presented in this thesis. These four profiles represent the strain measurements for the no-load (F_z = 0 N), low-load (F_z = 3 N), medium-load (F_z = 6 N), and high-load (F_z = 9 N) cases.

Using a relatively small bench-top rig did not allow testing high load values. Hence, it was decided to use the tyre without placing a foam around its inner surface. This is because inserting a foam would increase the inner tyre pressure and thereby enables the tyre to resist high wheel loads without noticeable deformations. This conclusion was drawn from the results of the static tests where the foam planted inside the tyre enabled the tyre to hold a vertical force in the range of 30 N to 60 N. This means that

a vertical force of at least 30 N was barely enough to produce deformations and strains high enough to be captured by the in-tyre strain gauges. This point is discussed extensively in Sections 7.1 and 7.2 where the relationships between the applied force and the resulting tyre strain and deformation are thoroughly examined.

With each of the vertical loads, several speeds, contact surfaces, and camber angles were tested.

The sensors' measurements collected with these tests will be analysed in Sections 4.2.1, 4.2.2, 4.2.3, 4.2.4, 4.3, 5.2.2, 7.1, 7.2, and 7.3.

3.3.4 Slip/Spin tests

A number of tests were conducted to examine the in-tyre sensors' readings during slip/spin incidents. To achieve a higher possibility for tyre slip/spin, different surfaces, speeds, and vertical loads were used. In terms of the contact surface, the second half of the track on the bench-top rig was modified. This was done by either spraying a liquid (screen and computer cleaning spray) on the rig's board or by placing another surface on the board. Four surfaces were examined, wood, glass, vinyl, and plastic. As can be observed, the goal was using a low-friction surface regardless if it is a common ground surface or not. When it was possible, liquid or dirt (soil) was used to reduce the friction between the tyre and these surfaces. Therefore, seven combinations of surfaces were tested: wood (control surface), wood + liquid, wood + dirt, glass + liquid, vinyl + liquid, vinyl + dirt, and plastic + liquid. Figure 3.14 shows one of these surfaces placed on the rig. Regarding the tyre's speed, ten values were tested; however, it was noticed that the tyre is more likely to slip/spin when it runs at high speeds. With respect to the vertical load (F_z), ten loads were employed. Among these, a relatively low wheel load of 3 N was found to be suitable for inducing spin and providing meaningful results. A higher load would increase the resistance of the tyre to overcome slip/spin situations. At the same time, 3 N produces a sufficient loading to ensure that the tyre is pressed against the board so that more-stable readings are collected from the in-tyre sensors during these situations.

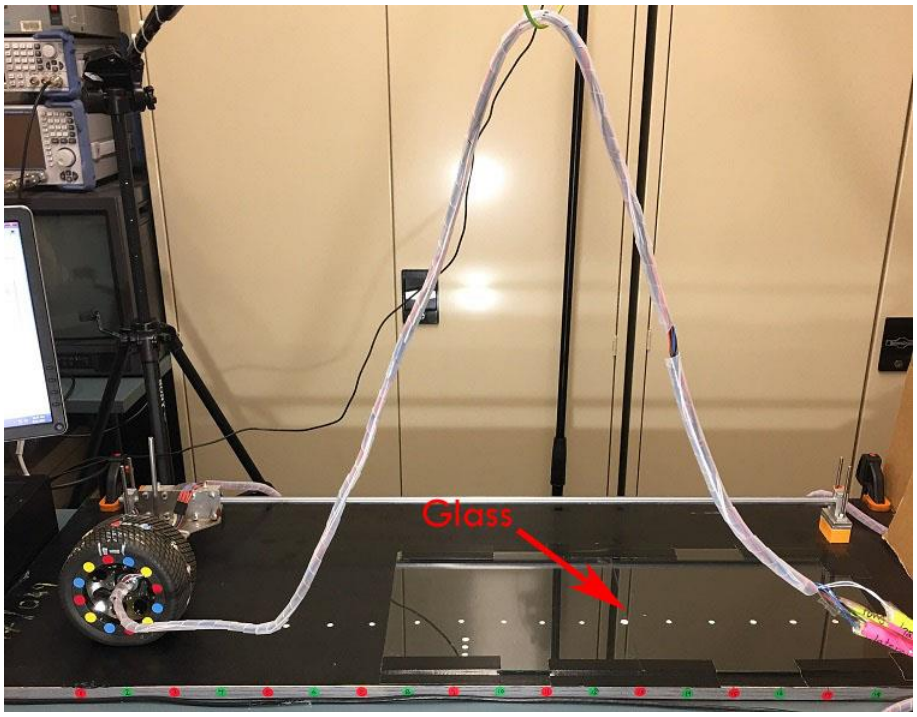

Figure 3.14: The rig in one of the slip/spin tests.

Another type of tests was conducted to induce slip/spin incidents. In these tests, the tyre speed was changed during its run. The speed was increased from a low to a medium level, a medium to a high level, and a low to a high level. It is hypothesized that an immediate increase in the acceleration of the tyre acts as applying a higher longitudinal force instantaneously at the point where the speed is changed. Consequently, this would cause the tyre to slip momentarily. It will be shown that the increase in speed was gradual (more details on these tests are presented in Section 5.2.3).

The sensors' measurements collected with these tests will be analysed in Sections 5.2.3 and 6.2.

3.3.5 Camber angle tests

A group of tests was conducted to examine the effect of camber angles on the tyre strain. Different camber angles were generated by changing the level of the tyre cart as shown in Figure 3.15. This was achieved by changing the height of the shims that

carry the rail. Four negative camber angles were obtained by sequentially reducing the shims' height. As previously mentioned, a vertical load of 3 N was found to be a proper loading for the tyre.

The sensors' measurements collected with these tests will be analysed in Section 7.4.

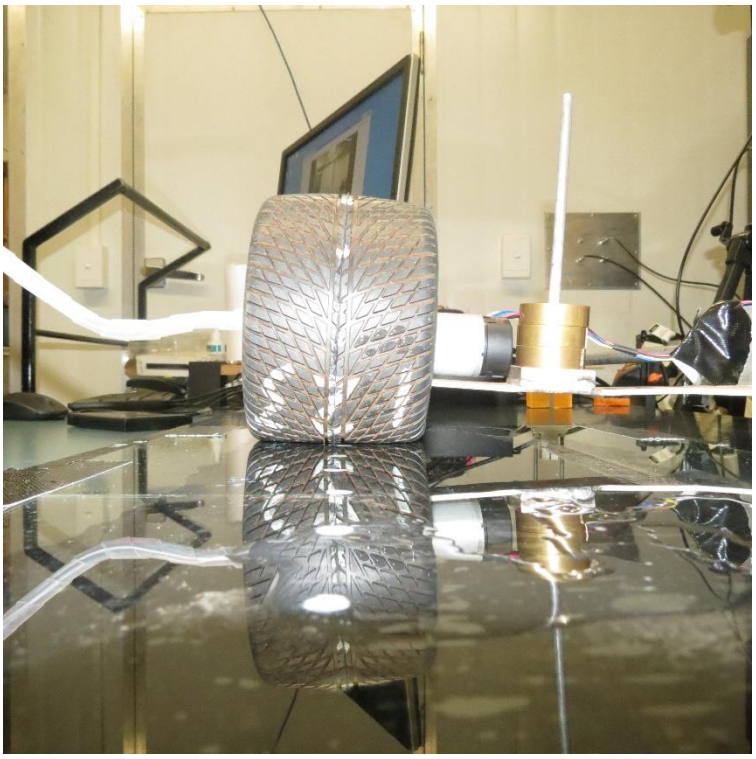

Figure 3.15: The tyre in the camber angle tests.

3.3.6 Contact surface tests

The ability of the in-tyre sensing system to identify travelling on different surfaces was also investigated. A surface was placed on the second half of the track so that the tyre completes its first revolution on the first surface (the control surface (wood)) and the next revolutions on the second surface. With such a placement, the first cycle in the resultant strain waveform shows the sensors' readings when the tyre is on the first surface. The other cycles correspond to travelling on the second surface. Thus, by comparing the first cycle to the rest of the strain waveform, the change in strain caused by passing over different surfaces is analysed.

The tested surfaces are classified into two groups: rough surfaces and smooth surfaces. The rough surfaces are loop pile carpet, fake grass, and dirt (soil containing gravel and a few stones of various sizes). The smooth surfaces are vinyl, glass, and plastic (Ultra-high molecular weight polyethylene (UHMWPE)). Figure 3.16 presents an example of these tests.

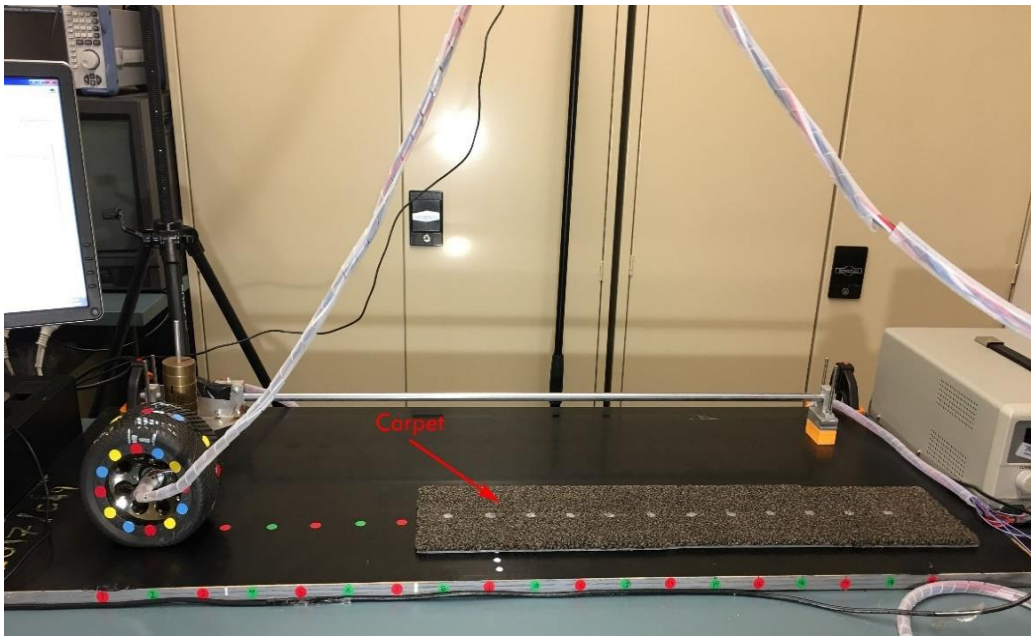

Figure 3.16: Example of the contact surface tests (carpet).

Unlike the other surfaces, the plastic surface was used for the entire tyre track on the rig (Figure 3.17). To clarify, it was not possible to put the plastic on only the second half of the track since the height of the available sample was large; therefore, the tyre would not be able to climb the sample. To determine the strain changes caused by going over the plastic, the acquired sensors' readings are compared to the case of the full-wood track.

The sensors' measurements collected with these tests will be analysed in Sections 6.1, 6.2, and 6.3.

Figure 3.17: Example of the contact surface tests (plastic (UHMWPE)).

Chapter 4

Data Analysis

This chapter discusses the initial analysis of the results of the experimental work presented in Chapter 3. Section 4.1 presents the basic analysis of the results of the static tests conducted on the first rig. It shows and compares the default readings of the sensors. It also presents the results of filtering the sensors' readings. Then, the section describes the process of collecting the strain readings in these static tests to construct the strain profiles. These strain profiles for both the longitudinal and the lateral sensors are examined in detail here. Section 4.2 presents the first steps in processing the results of the dynamic tests. It describes the raw strain profiles for the longitudinal and lateral sensors. A moving average filter was utilised to smooth these profiles. The section then presents the results of differentiating these profiles. Following this, the results of ten angular velocity and vertical load tests are shown. Next, the measurements of the encoder are shown and employed to illustrate the operation of the motor. The process of utilising the encoder's readings to obtain the strain measurements with respect to the tyre's rotational angles is explained. After that, the measurement of the motor's current sensor is shown. A method of extracting the longitudinal force from these current measurements is demonstrated. Lastly, Section 4.3 compares the results obtained from the static and dynamic tests.

The sensors' measurements that are presented in this chapter were collected from the tests described in Chapter 3. The following table shows the sections of Chapter 4 and refers to the sections in Chapter 3 where the related experimental work was reported.

Table 4.1: Linking the sections in Chapter 4 to the corresponding sections that described the experimental setup and tests in Chapter 3.

Sections in Chapter 4	**Associated sections that explained the experimental setup and tests' description in Chapter 3**
4.1.1 Results of the static tests on the bench-top rig	3.2.2 Vertical load tests + 3.2.3 Static tests to detect slip and construct strain profiles
4.1.2 Description of the strain profiles extracted from the static tests	3.2.3 Static tests to detect slip and construct strain profiles
4.2.1 Measurements of the in-tyre strain sensors	3.3.2 Angular velocity tests + 3.3.3 Vertical load tests
4.2.2 Results of the angular velocity and vertical load tests	3.3.2 Angular velocity tests + 3.3.3 Vertical load tests
4.2.3 Comparing the results of two tyres in the dynamic tests	3.3.2 Angular velocity tests + 3.3.3 Vertical load tests
4.2.4 Measurements of the encoder and the current sensor	3.3.2 Angular velocity tests + 3.3.3 Vertical load tests
4.3 Comparing the results of static and dynamic tests	3.2.3 Static tests to detect slip and construct strain profiles + 3.3.3 Vertical load tests

4.1 Analysing data of the static tests

4.1.1 Results of the static tests on the bench-top rig

Knowing the bias values of the sensors is useful in analysing results of the next static tests, where a vertical force and/or a longitudinal force will be introduced. These default values will be subtracted from the strain readings to get the true (normalised) strain values.

As shown in Figure 4.1 the readings were filtered using a moving average filter where the polynomial order was three and the frame size was fifteen. The purpose of filtering was to slightly smooth the data without losing existing features.

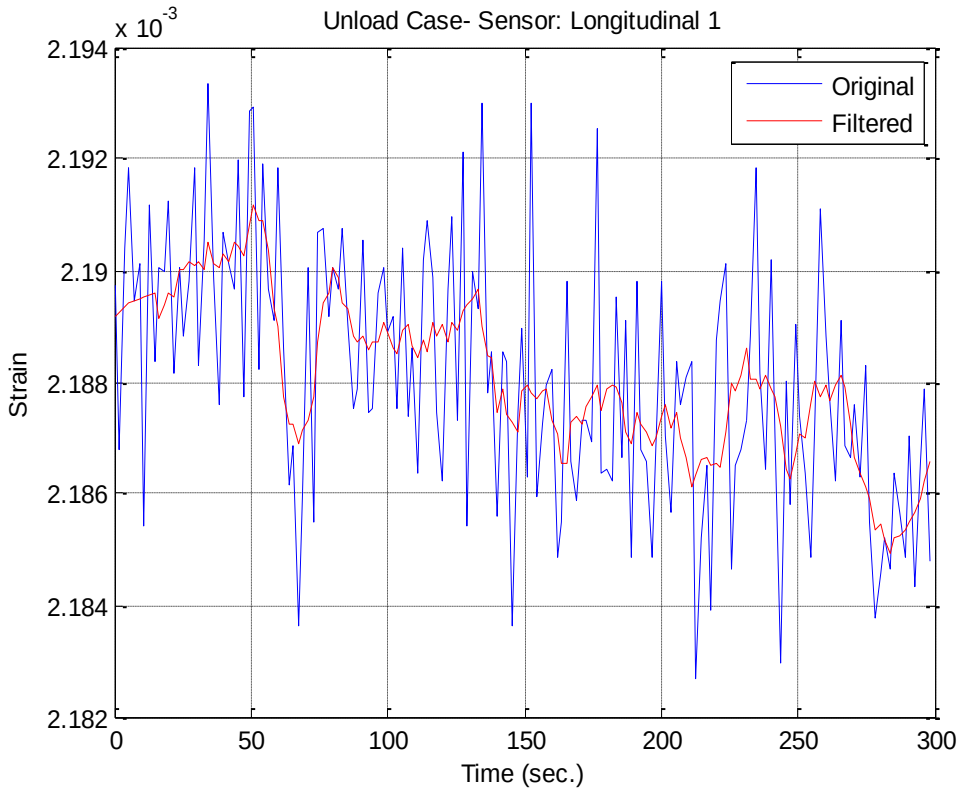

Figure 4.1: Filtering the bias readings of the sensors
(Example: Sensor- Longitudinal 1).

The value of the default strain measured by one sensor is slightly different from the readings of the other sensors, as can be seen in Figure 4.2. This is the result of different

mounting positions for the six sensors on the curvature of the tyre inner surface. In addition, the difference in measurement between the longitudinal and lateral sensors is because they are positioned with a different orientation, i.e. longitudinal and lateral directions with respect to the tyre centreline. Another reason is the different strain caused by gluing, soldering, and wiring of each sensor. For example, due to limited available space, a strain relief loop was created in a way that is not exactly the same for all the sensors. Therefore, each sensor has an individual specific bias reading that will be estimated and removed.

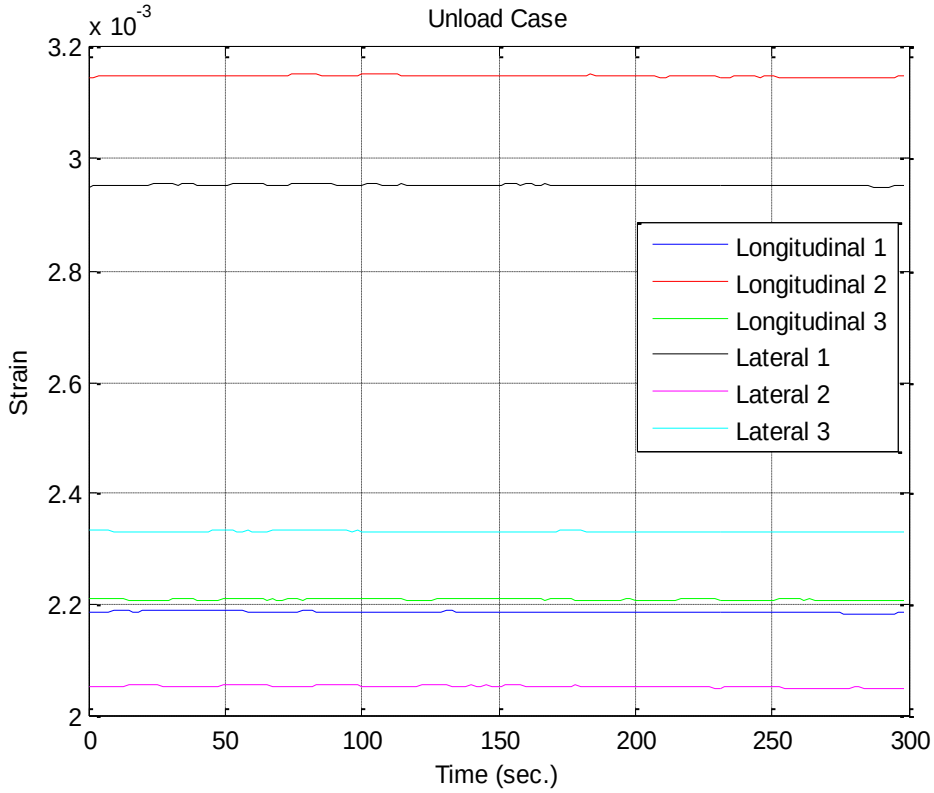

Figure 4.2: Bias readings of the sensors in the static tests.

Figure 4.3 below shows the sensors' readings in the vertical load (F_z) tests. The readings of the strain gauges, except for the sensor called longitudinal 1, indicate an increase in the strain value in correspondence with the increase in the value of the vertical load. Therefore, a staircase-like response can be seen in the outputs of the sensors. To explain, each increase in the vertical force leads to pushing the tyre inwards. As a result, the strain gauges mounted on the tyre inner surface will stretch and thereby give a higher strain measurement.

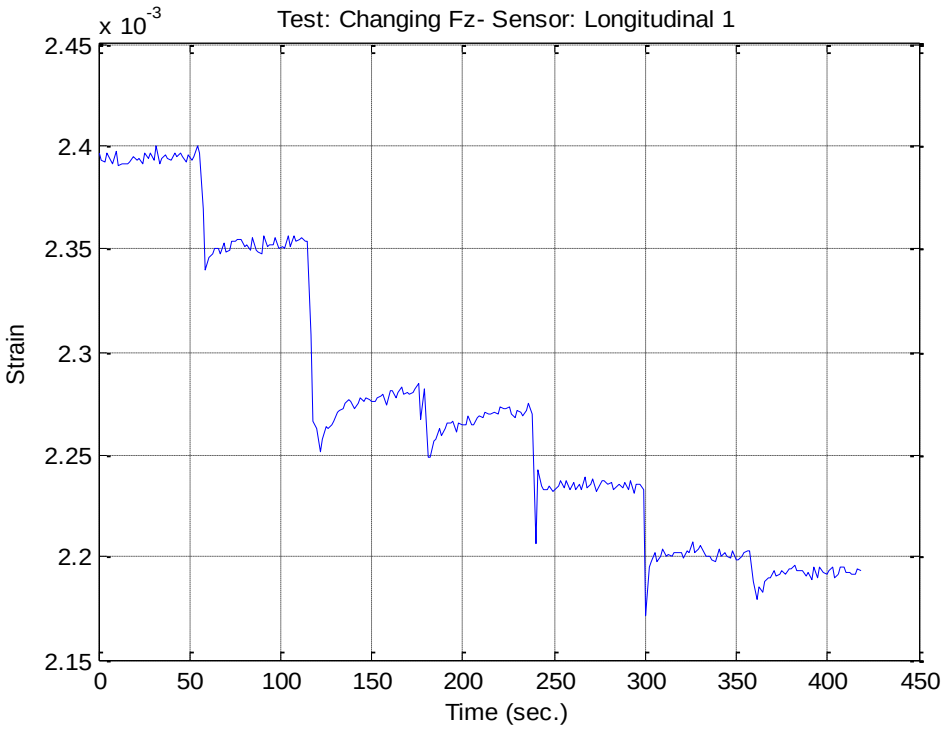

(a) Sensor: Longitudinal 1.

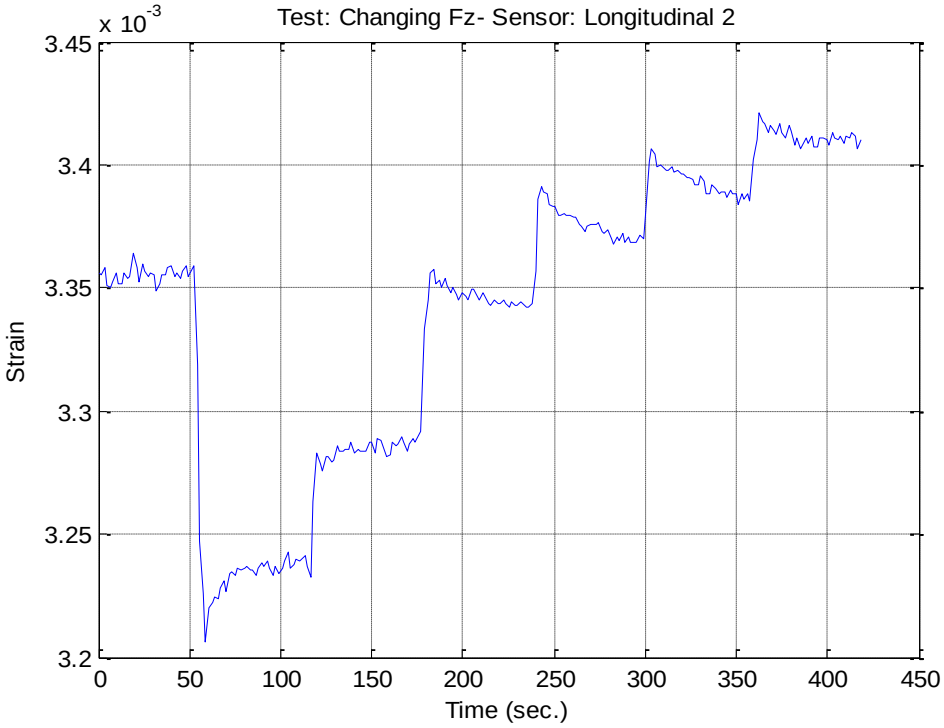

(b) Sensor: Longitudinal 2.

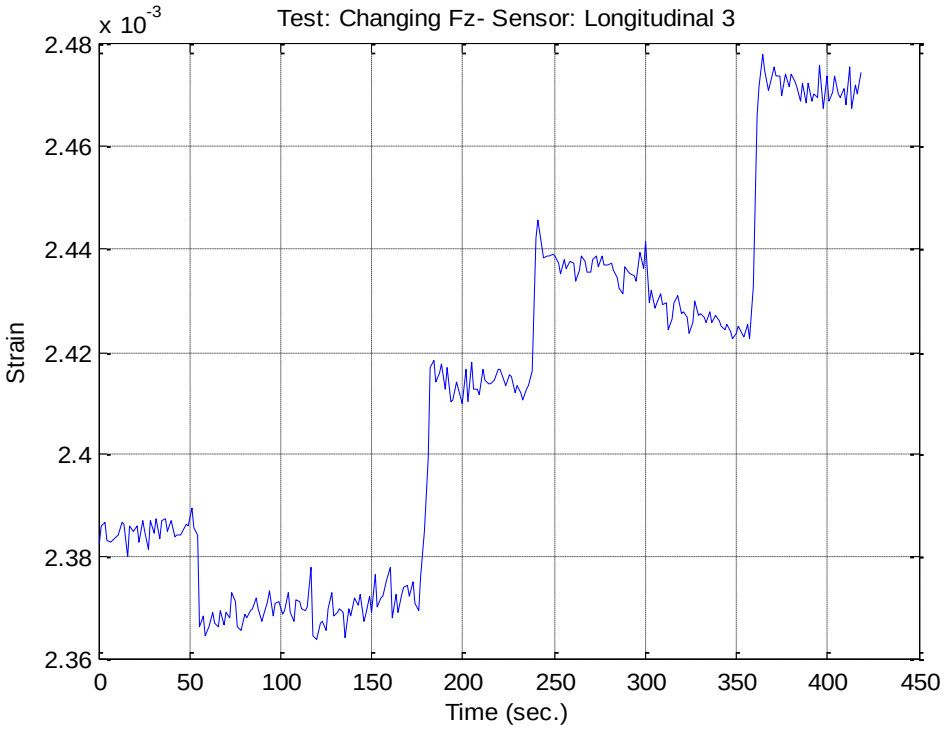

(c) Sensor: Longitudinal 3.

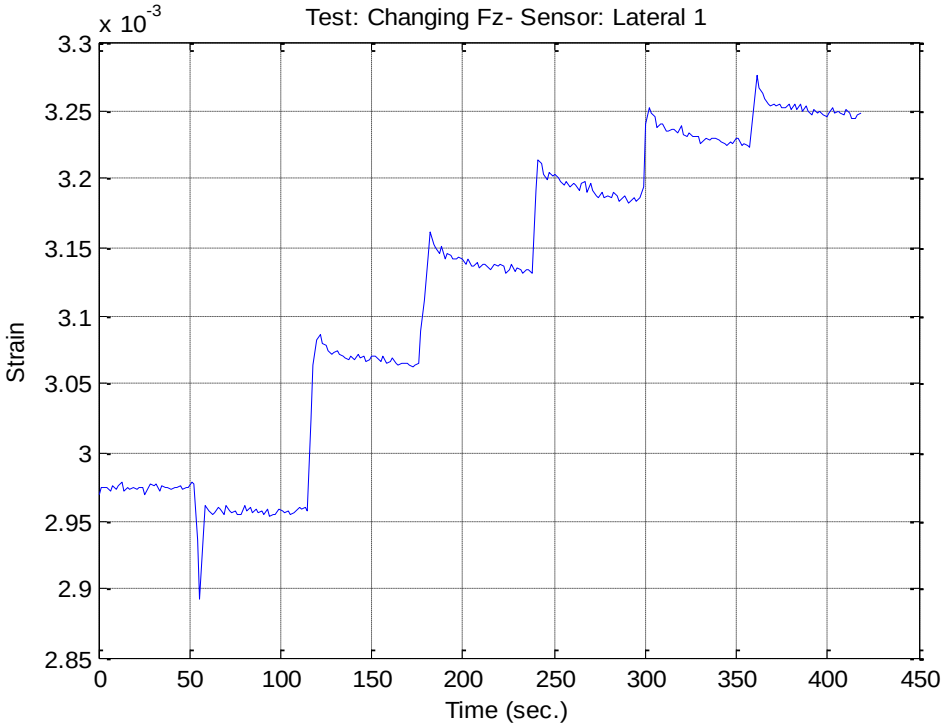

(d) Sensor: Lateral 1.

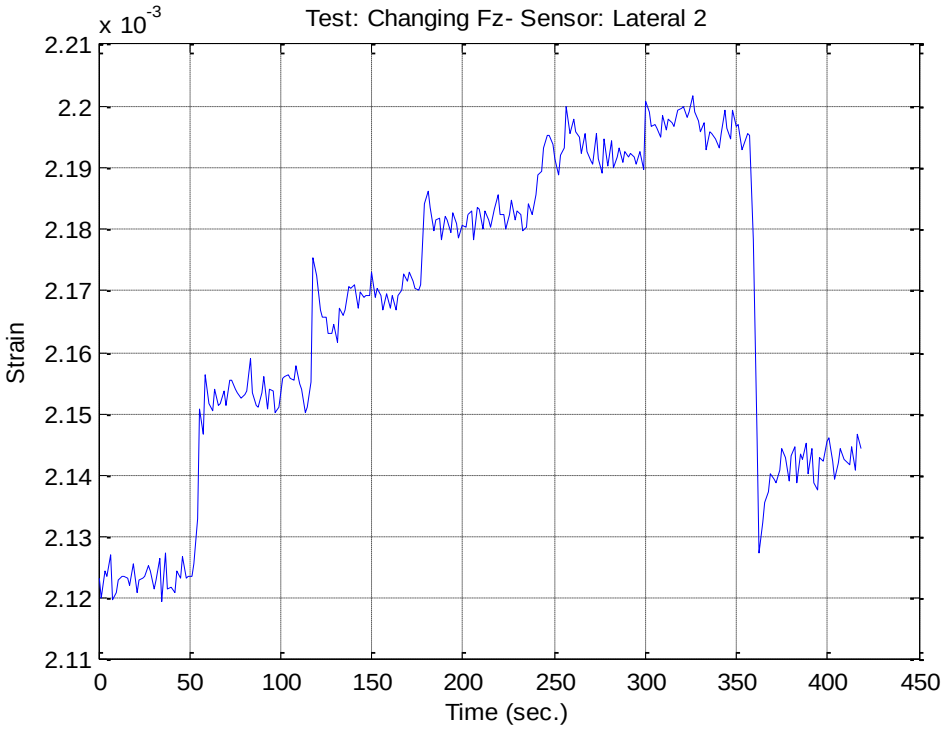

(e) Sensor: Lateral 2.

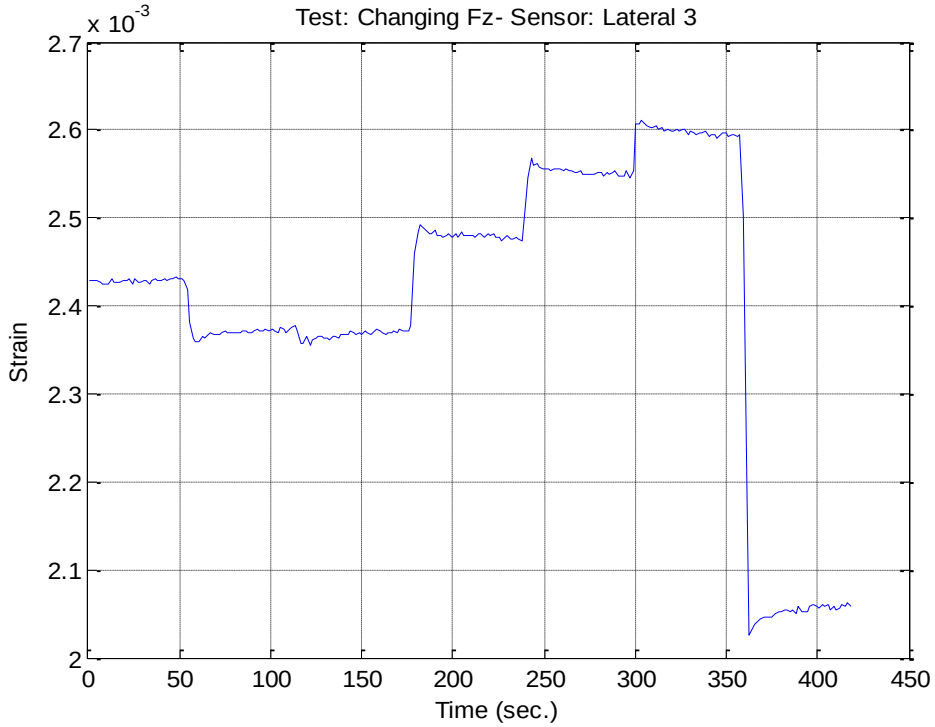

(f) Sensor: Lateral 3.

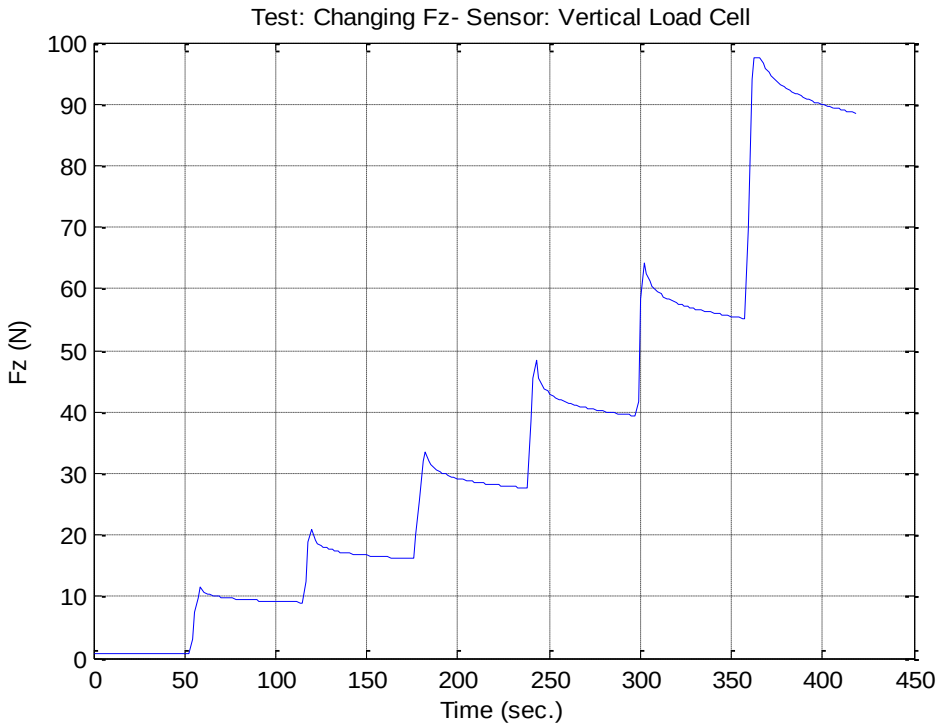

(g) Vertical load cell.

Figure 4.3: Sensors' readings in the vertical load (F_z) tests (F_x = 0 N, Angle = 0°).

The readings of the sensors acquired during the second set of the static tests (static tests to detect slip) are analysed. Figure 4.4 shows the readings of a longitudinal and a lateral sensor respectively for one of the static tests to detect slip. For each sensor, the original (raw) reading as well as the corresponding filtered signal is plotted.

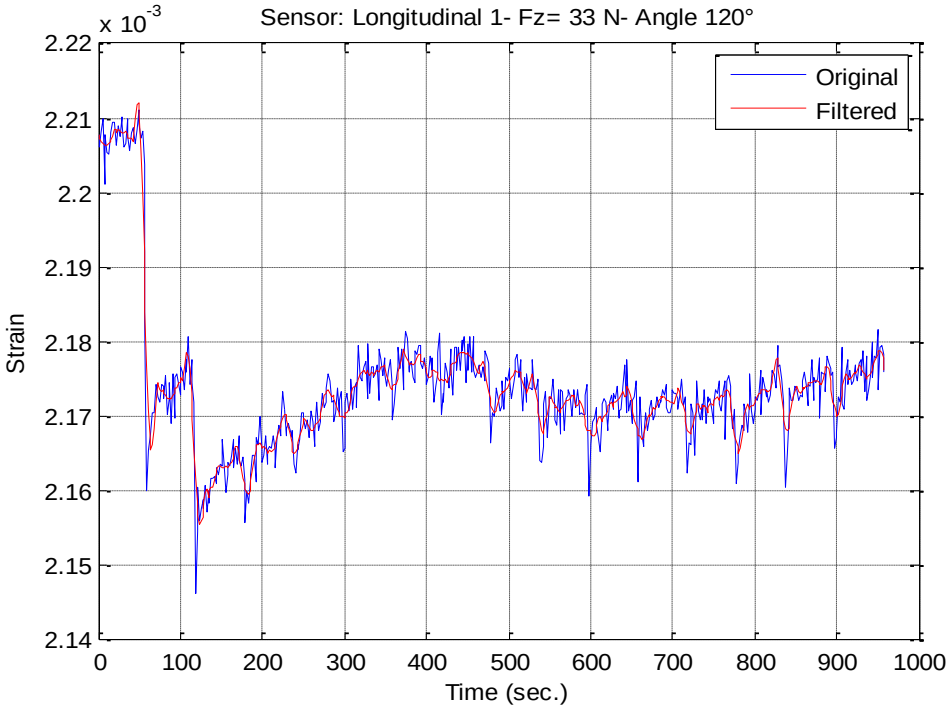

(a) Sensor: Longitudinal 1.

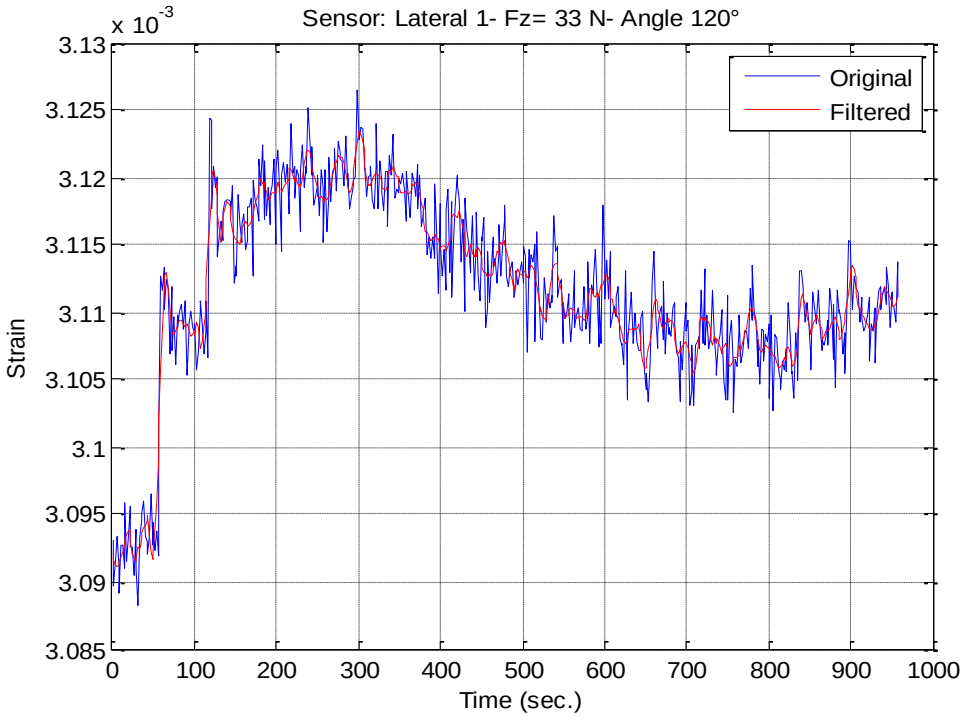

(b) Sensor: Lateral 1.

Figure 4.4: Example of sensors' readings in the static tests to detect slip (F_z = 33 N, Angle = 120°).

Figure 4.5 below shows an example of the relationship between the longitudinal load (F_x) and the strain at a specific vertical load (F_z) and a specific angle for a longitudinal and a lateral sensor respectively.

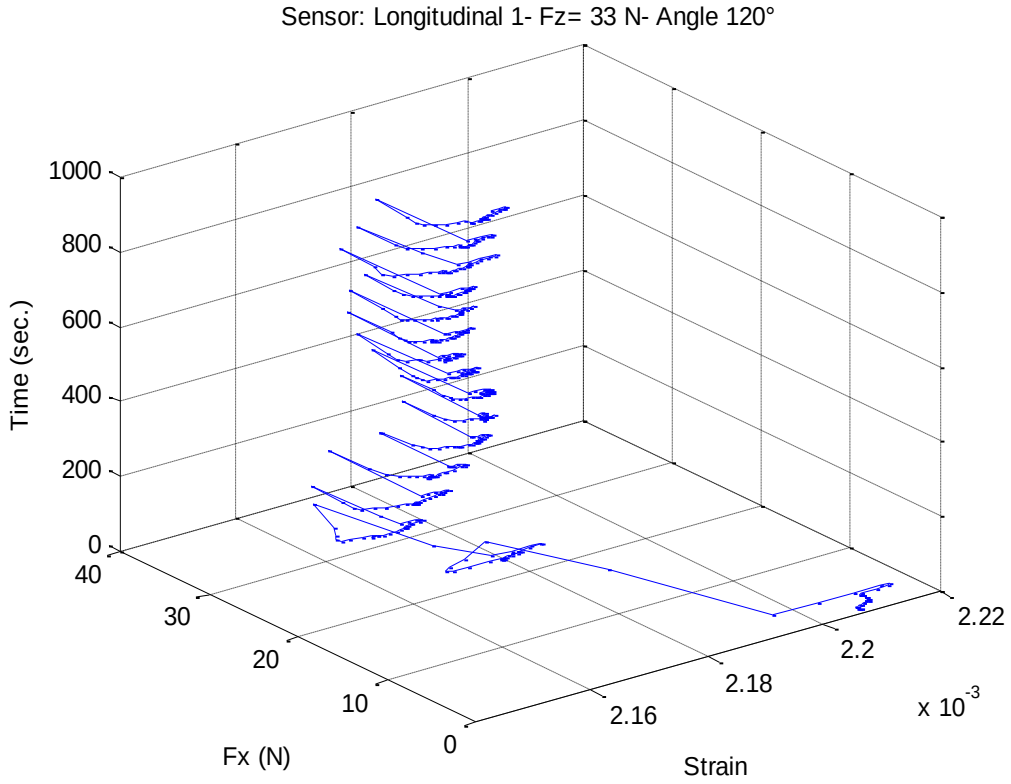

(a) Sensor: Longitudinal 1.

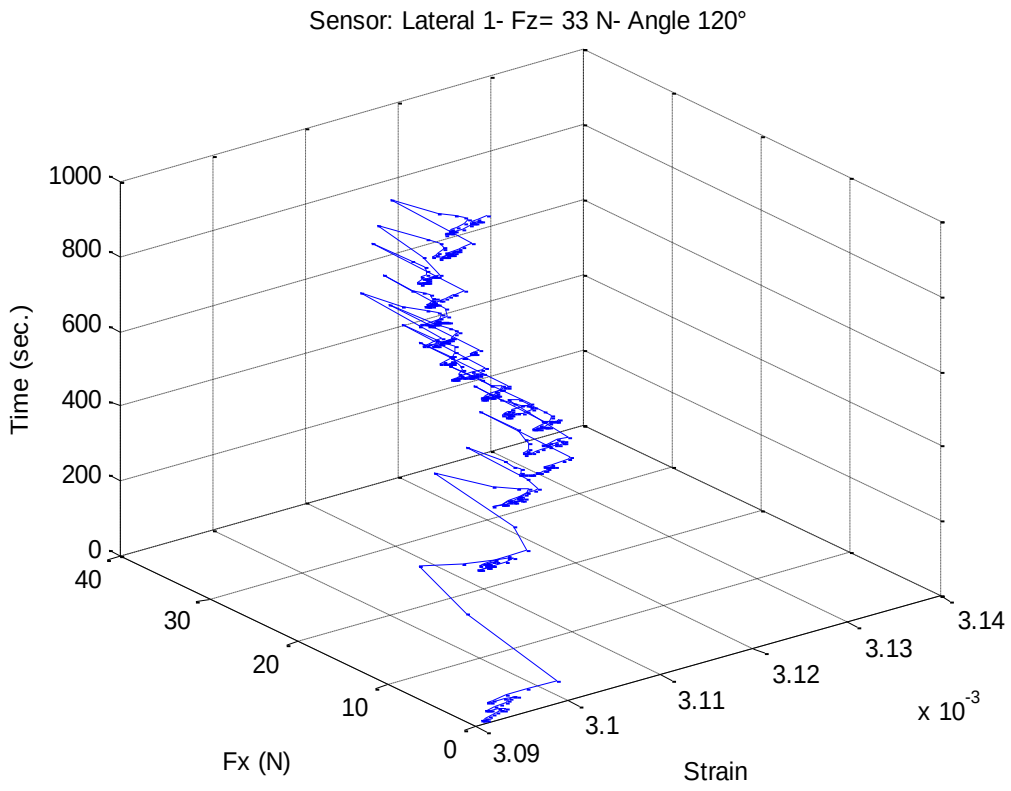

(b) Sensor: Lateral 1.

Figure 4.5: Example of the relationship between strain and longitudinal load (F_z = 33 N, Angle = 120°).

The relationship between the longitudinal load and the strain at a specific vertical load was plotted for each of the 13 angular positions for the six strain gauges. It was deduced that the graphs follow a particular overall direction in the positive angles (angles 120° to 20°) then this direction flips over in the negative angles (angles 0° to -120°). In other words, the centre of the contact patch (angle 0°) is the point that separates between these two groups. It is also noticed that this change in the overall direction of the graphs for the three longitudinal sensors is opposite to the change found in the three lateral sensors' readings. For the longitudinal sensors, the change in direction is from a descending order at the positive angles to an ascending order at the negative angles. For the lateral sensors, the change is from an ascending trend at the positive angles to a descending trend at the negative angles. The reason for this difference between the longitudinal and lateral sensors will be explained in Section 5.1 by comparing the readings of the strain sensors to the measurements of the horizontal

load cell. It will be observed that in the negative angles, the longitudinal sensors are stretching in the same direction of the longitudinal load whereas the lateral sensors are stretching in the opposite direction of this load. The responses of the strain sensors to the longitudinal load are reversed in the positive angles. To conclude this point, these longitudinal load-strain measurement relationships show if the tyre is stretching or compressing at a known angular position in response to applied longitudinal forces.

These relationships between the longitudinal load (F_x) and the strain were used to construct the strain profiles, i.e., the strain values with respect to the angular positions at a specific vertical and longitudinal force. The value of the strain at a particular vertical and longitudinal load was recorded. This operation was repeated for the other angular positions. As a result, the strain profiles were concluded for different values of F_x and F_z.

The strain profiles are utilised in this work to study the application of the in-tyre strain sensing for slip estimation, obstacle detection, and surface identification. The profiles will also be employed to investigate the relationships between the strain measurements and the tyre's forces, contact patch, angular velocity, and camber angle.

4.1.2 Description of the strain profiles extracted from the static tests

Figure 4.6 below shows an example of the strain profiles measured by the sensors. This figure illustrates that the strain profiles produced by the three longitudinal sensors convey similar features in terms of waveform shapes and strain variations at angular positions. This similarity is more perceptible in the readings of the two side sensors, named longitudinal 1 and longitudinal 3. This is related to the fact that these two sensors are mounted in the same spot on the two opposite sides. As a result, they stretch in the same manner in response to the applied forces and thus they give comparable results. This observation is also true for the readings of the lateral sensors. In the same context, it is worth mentioning that there are no clear similarities between the longitudinal sensors' readings and the lateral sensors' readings. This is because the longitudinal sensors indicate the strain caused by stretching of the tyre in a direction parallel to the direction of the application of the longitudinal force. The lateral sensors record the strain caused by stretching in a direction perpendicular to the longitudinal

force. From these comparisons, it can be concluded that the strain gauges are working properly since their readings are related to their position and orientation.

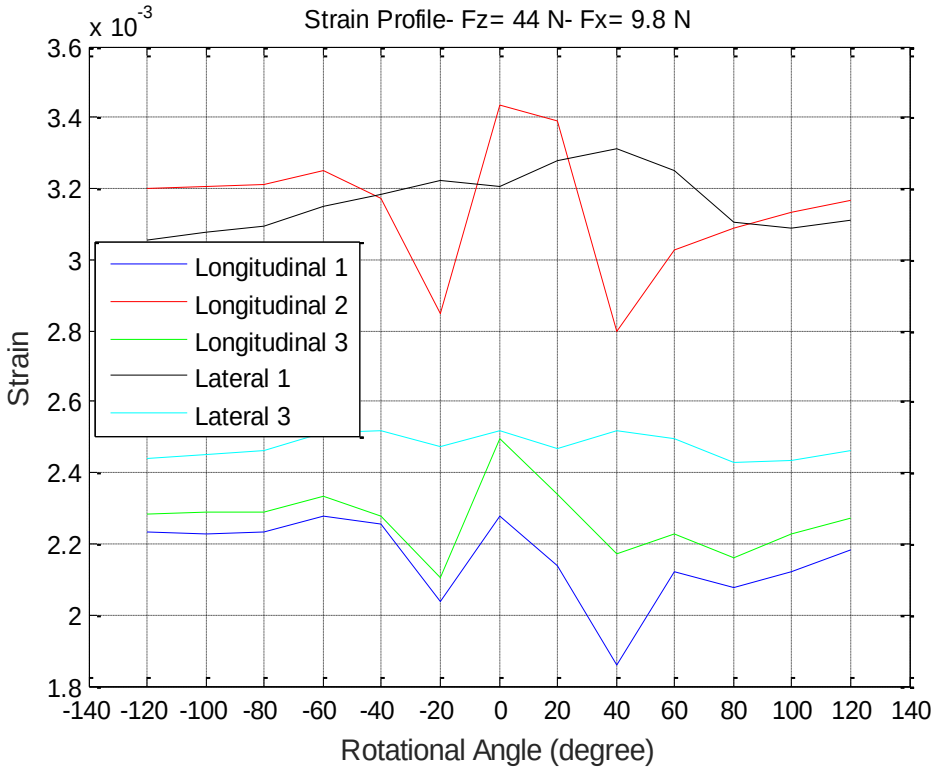

Figure 4.6: Example of the strain profiles collected by the strain gauges. Lateral 2 is not presented because it has malfunctioned (F_z = 44 N, F_x = 9.8 N).

In Figure 4.6, assuming that angle 0° is the centre of the contact patch in the static tests, slight changes in strain values are noticed in the angles far from the contact patch at both sides, i.e., angles -120° to -60° and 60° to 120°. On the contrary, such variations become more significant in the vicinity of the contact patch, namely, at angles -60° to 60°. Same observations about strain changes were reported by (Yang 2011). These strain variations are attributed to corresponding deformations around the tyre's circumference. The part of the tyre that contacts the ground is the most deformed since it endures the effects of applied vertical and horizontal forces. Therefore, the strain changes are higher in this area.

Figure 4.6 also indicates that the tyre is stretching in one direction at some of the angles whereas it stretches in the opposite direction (compresses) at other angles. For the three longitudinal sensors, it can be seen that tensile strain is recorded at the centre of the

contact patch, which is 0°, while compressive strains are noticed in nearby regions at the two sides of the contact centre, i.e., around ± 20°. This agrees with the results presented by (Matsuzaki & Todoroki 2008a). For the lateral sensors, the lateral strain profile shows features that are the opposite of those for the longitudinal strain profiles. This behaviour is especially observable in the readings of the sensor called lateral 1. Therefore, the tyre is under tensile lateral strain both before and after the contact region while it is under compressive lateral strain within this region. The same conclusion regarding lateral strains is reported by (Yang 2011).

As previously mentioned, the only possible increments of angular positions at which the tyre could be fixed in the rig used in the static tests were 20°. However, 20° is a discrete distance on the curves of the strain profiles. Two reasons necessitate finding the strain values at smaller angular steps when constructing the strain profiles. First, identifying the peaks' positions in the strain profiles as accurate as possible since they indicate significant points that will be used to locate the contact patch. Second, it was essential to obtain the derivatives of the strain profiles so that a proper data analysis could be performed. Differentiating such a discrete range of data points would have certainly led to erroneous results.

In order to obtain the strain at the intermediate angles in a step of 1° increment without having to repeat the above tests, the experimental data sets were interpolated. Five different interpolation methods were investigated: linear interpolation, nearest neighbour interpolation, piecewise cubic interpolation, cubic convolution, and spline interpolation. The piecewise cubic interpolation method was more helpful in identifying the change in the angular position of the contact patch centre and edges that corresponds to changes in vertical and longitudinal forces. As seen in Figure 4.7, this method uses a shape-preserving piecewise cubic fit and generates signals with fewer overshoots and oscillations and, thereby, more constrained results. Original and normalised strain profiles were interpolated using the selected method.

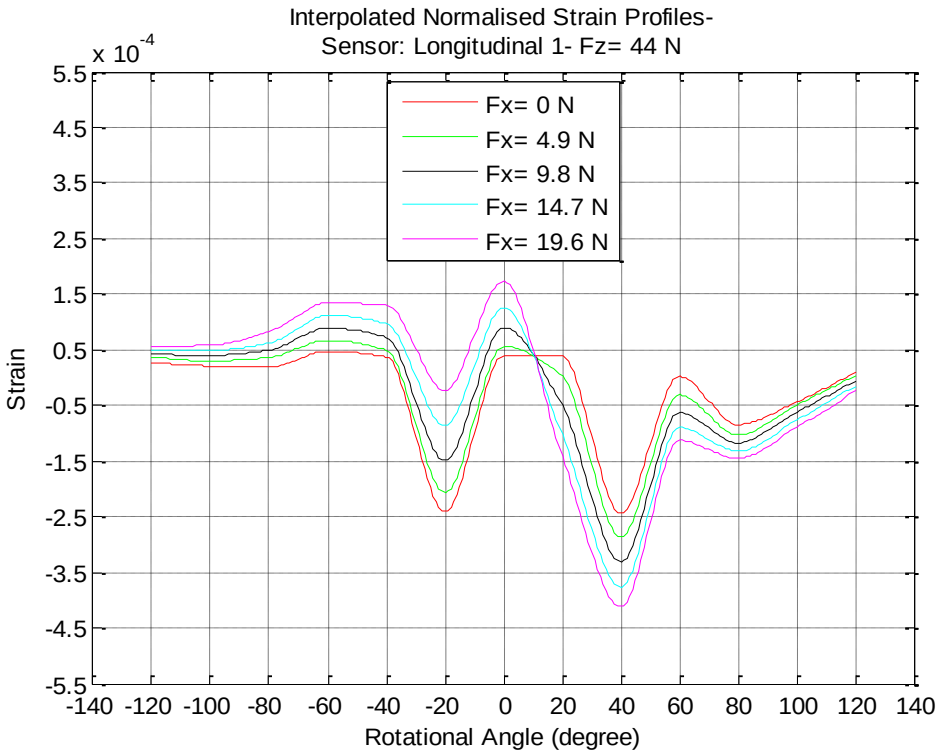

Figure 4.7: Interpolated normalised strain profiles- constant F_z and variable F_x (Sensor: Longitudinal 1, F_z = 44 N).

In order to study the change in the strain readings with respect to changes in the angular positions, the interpolated strain profiles were differentiated twice as shown in Figure 4.8 and Figure 4.9. The strain derivative profiles were used for two reasons. Firstly, according to previous work related to locating tyre contact patches from strain profiles, the strain rate (differential of strain signal) is used to find the contact patch edges and length (Matsuzaki & Todoroki 2008a; Yang 2011). Therefore, the interpolated strain signals were differentiated to extract these patch dimensions. Secondly, the original strain profiles (without differentiation) did not reflect clear variations in correspondence with changing the longitudinal force (F_x).

To compute the strain derivatives, three difference techniques (forward, backward, and central) were examined. It was decided that approximating the derivative with central differences produces a smaller error than when using the forward or backward difference. This is because the central difference at a specific point is calculated using both the past and future points. As a result, it is known theoretically that the central difference gives a derivative approximation that is close to the analytical derivative. Hence, the central difference was utilised when calculating the derivatives in this work.

It is concluded from Figure 4.8 below that the first derivative of the strain profiles agrees with the results of Yang (2011) and Matsuzaki et al. (2010) for pneumatic car tyres. The similar features are the shape of the waveforms and the way in which they change according to changing F_x.

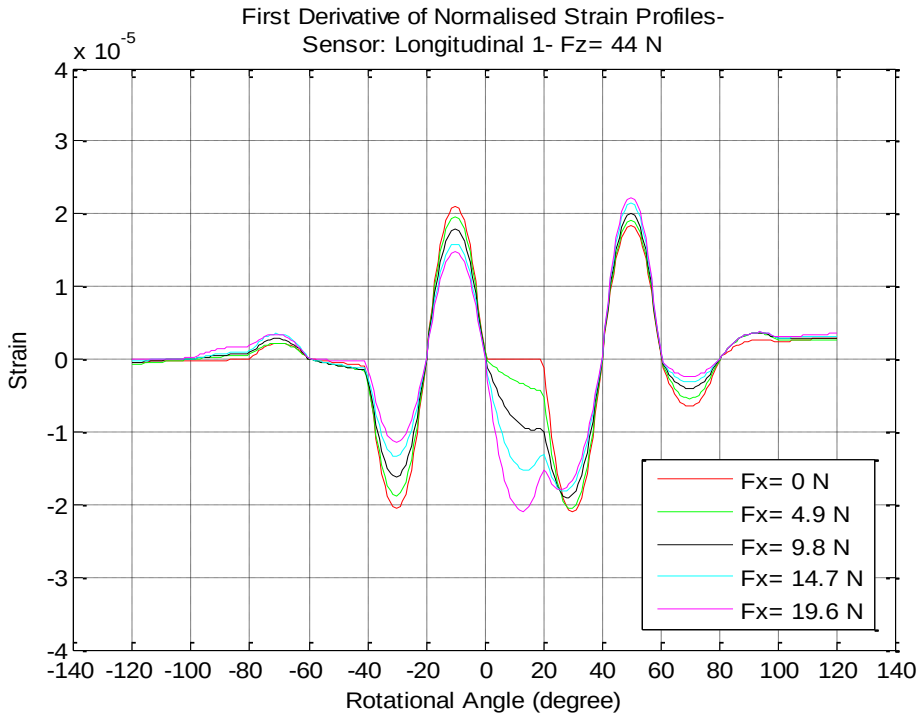

Figure 4.8: First derivative of normalised strain profiles- constant F_z and variable F_x (Sensor: Longitudinal 1, F_z = 44 N).

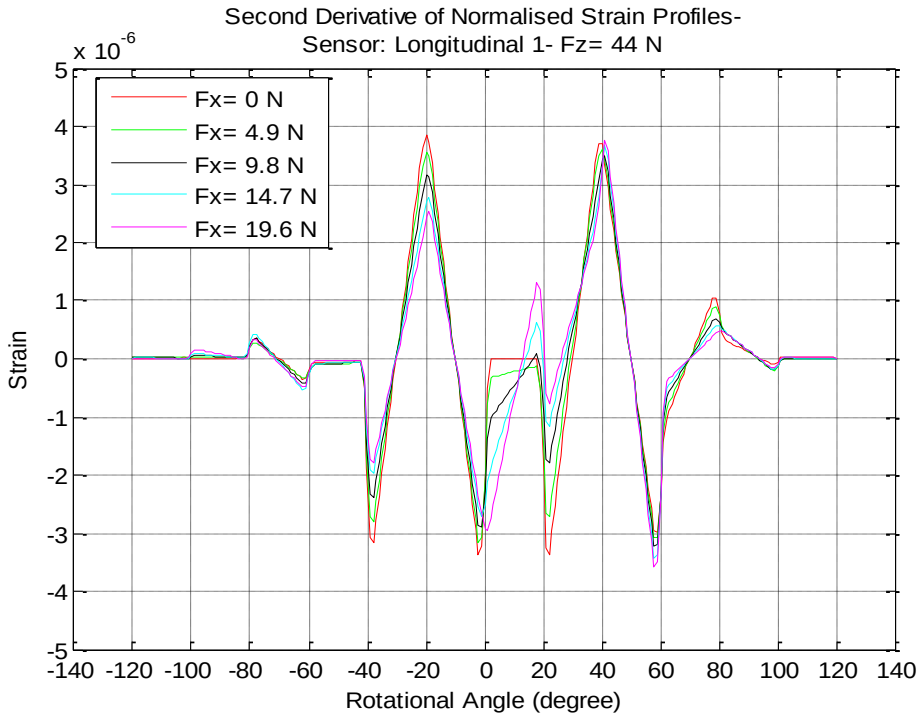

Figure 4.9: Second derivative of normalised strain profiles- constant F_z and variable F_x (Sensor: Longitudinal 1, $F_z = 44$ N).

4.2 Analysing data of the dynamic tests

4.2.1 Measurements of the in-tyre strain sensors

Unloaded tests conducted at different times showed that the sensors can give slightly different bias readings. This is caused by the effect of temperature change on the performance of the sensors, although the tests were conducted in a controlled environment. Figure 4.10 shows the bias measurements taken at different days for one of the sensors. It illustrates the difference in strain values for some of the tests.

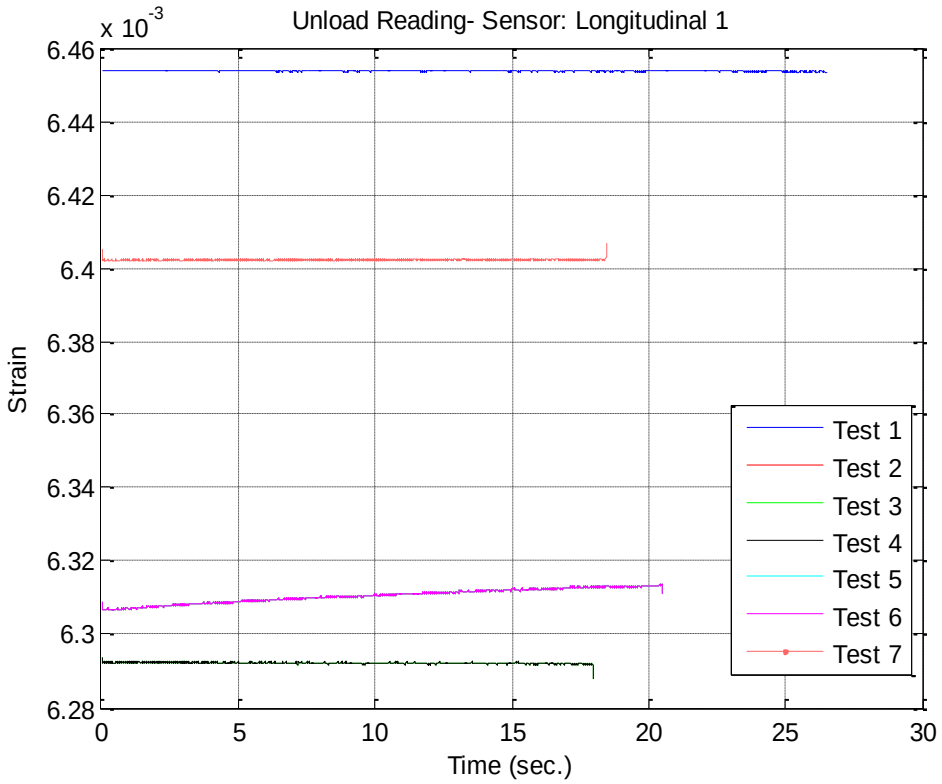

Figure 4.10: Bias readings of a strain sensor at different days during the dynamic testing (Only four lines can be seen in the graph because the bias lines in three tests were close to other lines. These lines overlapped each other).

The lateral strain profiles produced by the three lateral sensors present stable low readings in the points far from the contact patch, tensile peaks at the edges of the patch, and a compressive peak at the centre (Figure 4.11a). Opposite strain patterns are captured by the three longitudinal sensors. The longitudinal strain profiles produced by the three longitudinal sensors show constant near-zero strain readings in the region far from the contact patch, compressive strain peaks at the edges of the patch, and a tensile strain peak at the centre of the contact patch (Figure 4.11b).

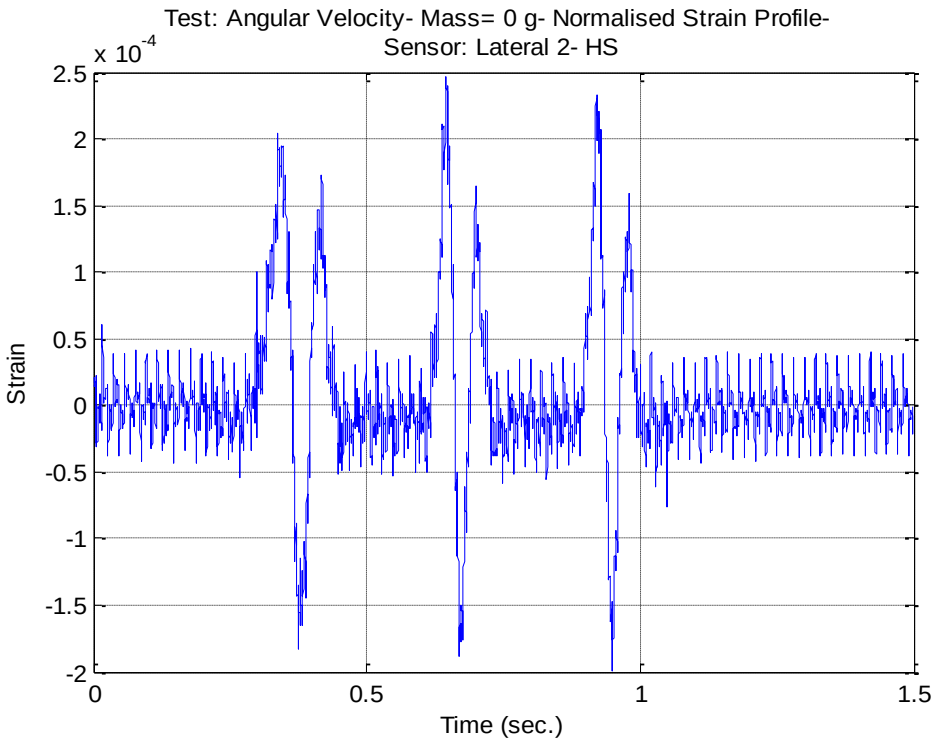

(a) Sensor: Lateral 2.

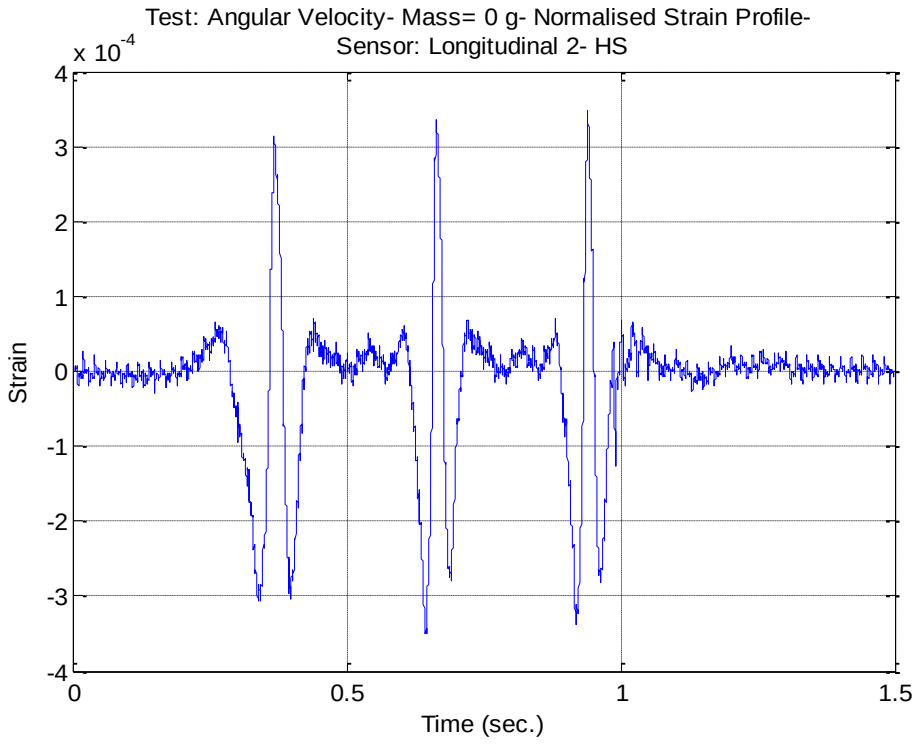

(b) Sensor: Longitudinal 2.

Figure 4.11: Sensors' readings in a speed test

(HS = High Speed (12.20 rad./sec. = 116.50 RPM), F_z = 0 N).

With the bench-top rig used in the dynamic tests, it was only possible to apply a traction torque. Thus, the lateral sensors' readings (Figure 4.11a) show that the front lateral tensile strain peak is greater than the rear lateral tensile strain peak. Similarly, the longitudinal sensor's measurements (Figure 4.11b) show that the front compressive strain peak is greater than the rear compressive strain peak.

It can be seen in Figure 4.11 that the sensors' readings contain a large amount of noise; therefore, it was essential to smooth these readings before any proper analysis can take place. After trying different filters, it was concluded that the Savitzky-Golay smoothing filter could smooth the sensors' readings effectively as it was able to track the signals more closely. The Savitzky-Golay smoothing filter is a weighted moving average filter. It fits a polynomial of a specified order over a specified number of samples in a least-squares sense. For maximal filtering, the frame for the filter is calculated using the following:

$$Frame = \frac{Sampling\ Rate\ (Hz)}{Frequency\ of\ Noise\ (Hz)} \tag{4.1}$$

Figure 4.12 below shows the results of this smoothing process.

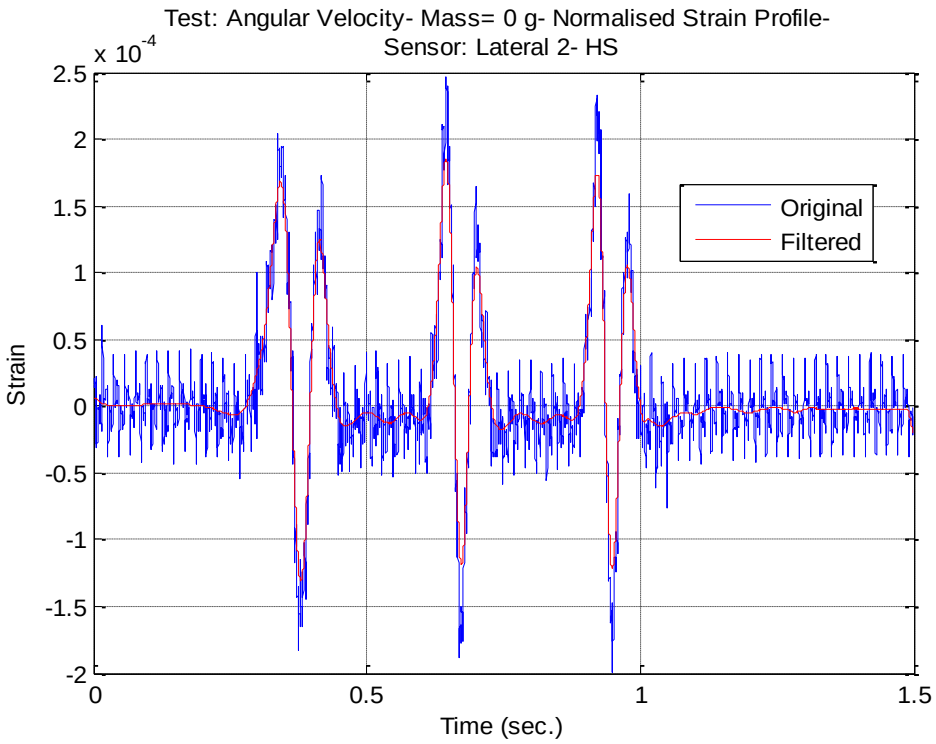

(a) Sensor: Lateral 2.

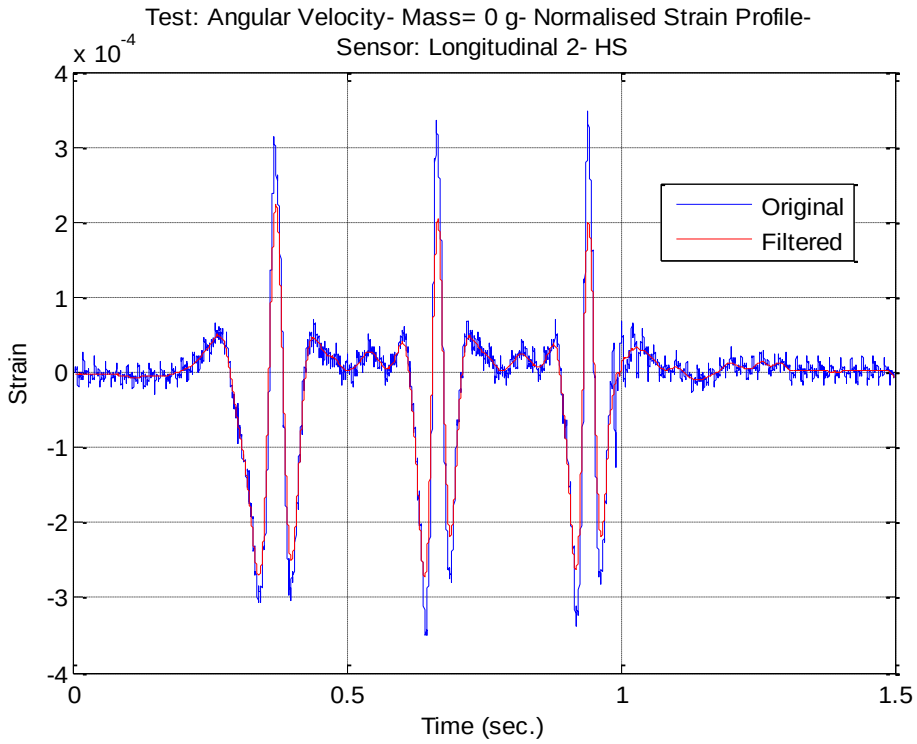

(b) Sensor: Longitudinal 2.

Figure 4.12: Filtering the sensors' readings

(HS = High Speed (12.20 rad./sec. = 116.50 RPM), F_z = 0 N).

Since it is difficult to follow the strain changes by examining the strain profiles with respect to time, the sensor readings were plotted against the rotational angles (more details are provided in Section 4.2.4). These (Strain vs Rotational Angle) figures make it easier to examine the change in strain at a specific angle as a result of changing a tested variable, being speed in the following figure (Figure 4.13). Additionally, it will be seen in the next chapters that overlapping different strain profiles with respect to the tyre's rotational angles reveal important information about tyre's spin, obstacles, contact surfaces, and tyre's mechanical properties. In Figure 4.13, each revolution in the strain profiles illustrates that the position of the rotational angle around 180° corresponds to the centre of the tyre contact patch. The angles 0° and 360° in each revolution in the strain waveforms correspond to the position on the tyre that is opposite to the centre of the contact patch.

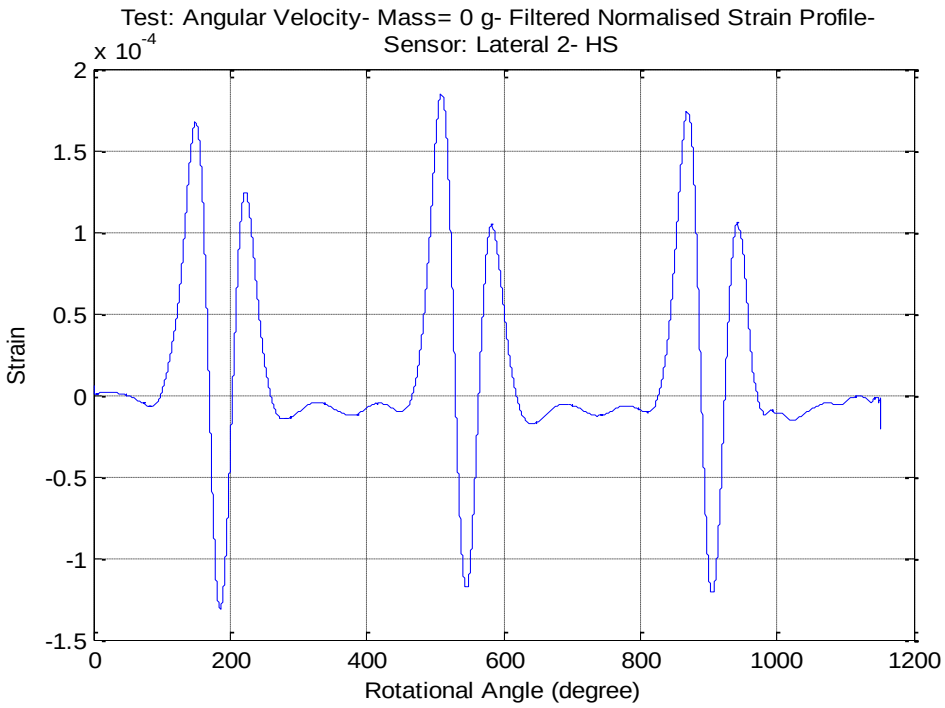

(a) Sensor: Lateral 2.

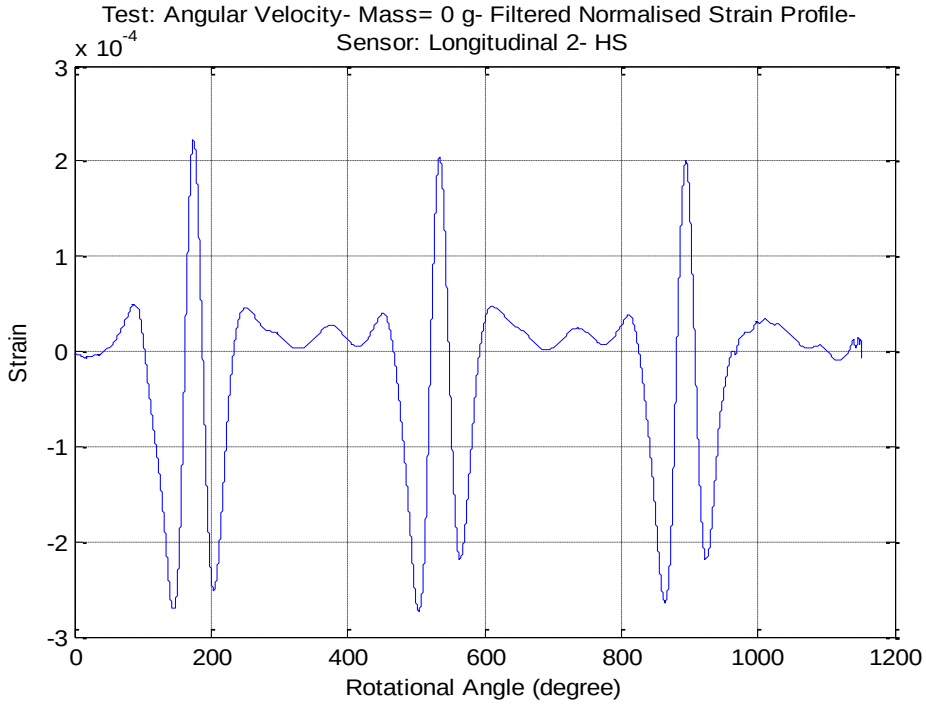

(b) Sensor: Longitudinal 2.

Figure 4.13: Filtered sensors' readings with respect to tyre's rotational angles (HS = High Speed (12.20 rad./sec. = 116.50 RPM), F_z = 0 N).

The normalised strain profiles were differentiated twice with respect to time in order to examine the changes in strain more closely. Since differentiation increases the existing noise in a signal, the original profiles were smoothed first before calculating their first derivatives. Similarly, the first derivatives were smoothed before differentiation. Finally, the second derivatives were smoothed to attenuate the noise so that the main features in the data can be better observed.

Recalling basic properties of differentiation to describe these derivative profiles, the following can be stated. Where the original signal has a positive slope, it will have a positive derivative. Where it has a negative slope, its derivative will be negative. Where it has a zero slope, it would have a zero derivative. In addition, mathematically, the derivative is obtained by dividing the differences between adjacent y-axis values by the x-axis increment. Therefore, for the strain derivative profiles shown in Figure 4.14 and Figure 4.15, the y-axis values are higher compared to the original profiles. This is the result of dividing small fractional numbers by an x-axis increment of 0.0001 (because a sampling frequency of 10000 Hz was used to collect the readings).

For the lateral sensor (Figure 4.14), the first derivative profiles show two zero-crossing points, where the derivative passes from positive to negative strain values. These points appear at the same positions of the tensile peaks located at the edges of the contact region in the original profiles. A third zero-crossing point, where the derivative passes from negative to positive strain values, occurs at the same location of the compressive peak in the original profile.

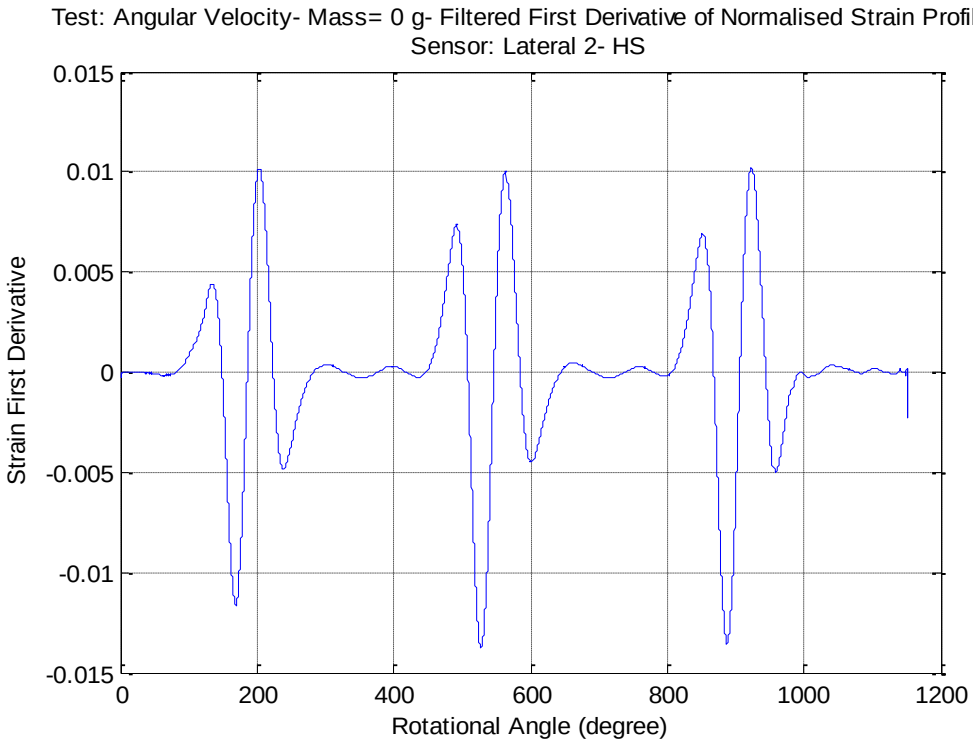

Figure 4.14: First derivative of strain profiles for the lateral sensors (HS = High Speed (12.20 rad./sec. = 116.50 RPM), F_z = 0 N).

The first derivative of the longitudinal strain profile presented in Figure 4.15 includes two zero-crossing points, where the derivative passes from negative to positive strain values. These points reflect the position of the compressive peaks at the contact patch edges in the original profile. Another zero-crossing point, where the derivative passes from positive to negative strain values, appears in the derivative. This point indicates the location of the tensile peak existed at the centre of the patch in the original profile.

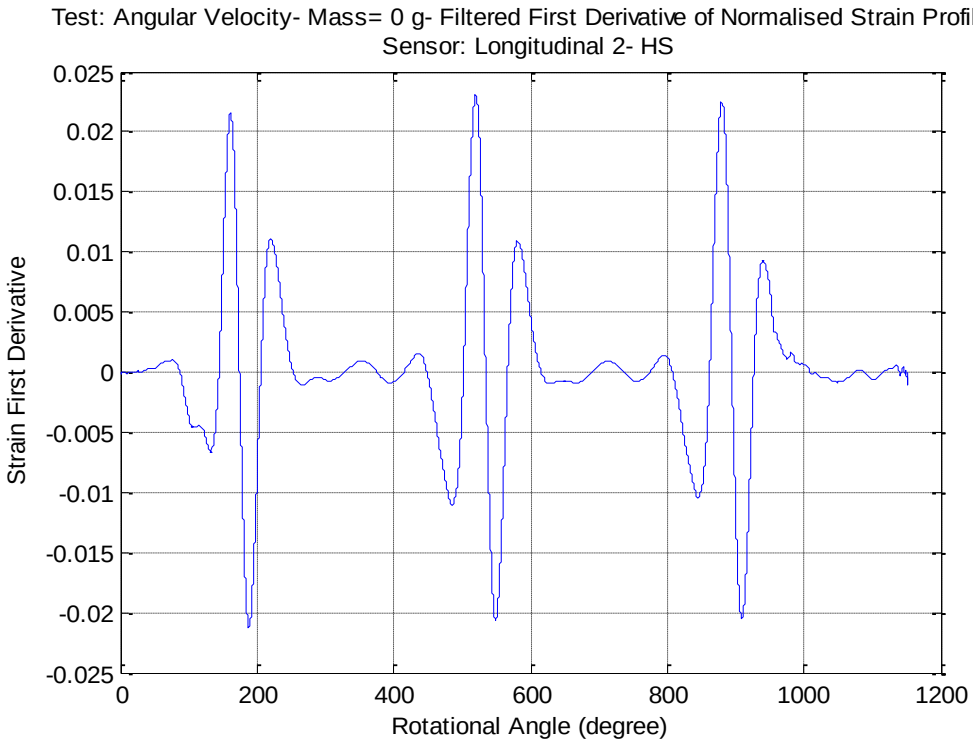

Figure 4.15: First derivative of strain profiles for the longitudinal sensors (HS = High Speed (12.20 rad./sec. = 116.50 RPM), F_z = 0 N).

Figure 4.16 shows an original (non-smoothed) derivative with its corresponding smoothed signal. It is evident that the Savitzky-Golay filter was capable of closely following the main features in the signals. However, the smoothing process has led to a slight reduction for the values of the strain first derivative. This reduction becomes more pronounced at the peaks' locations.

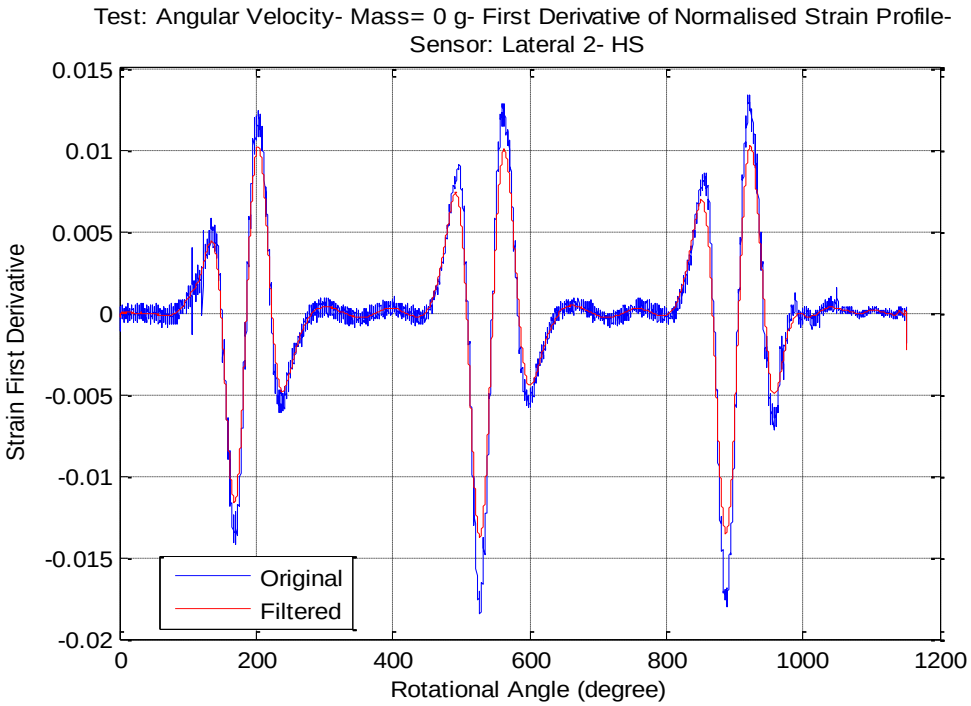

(a) Sensor: Lateral 2.

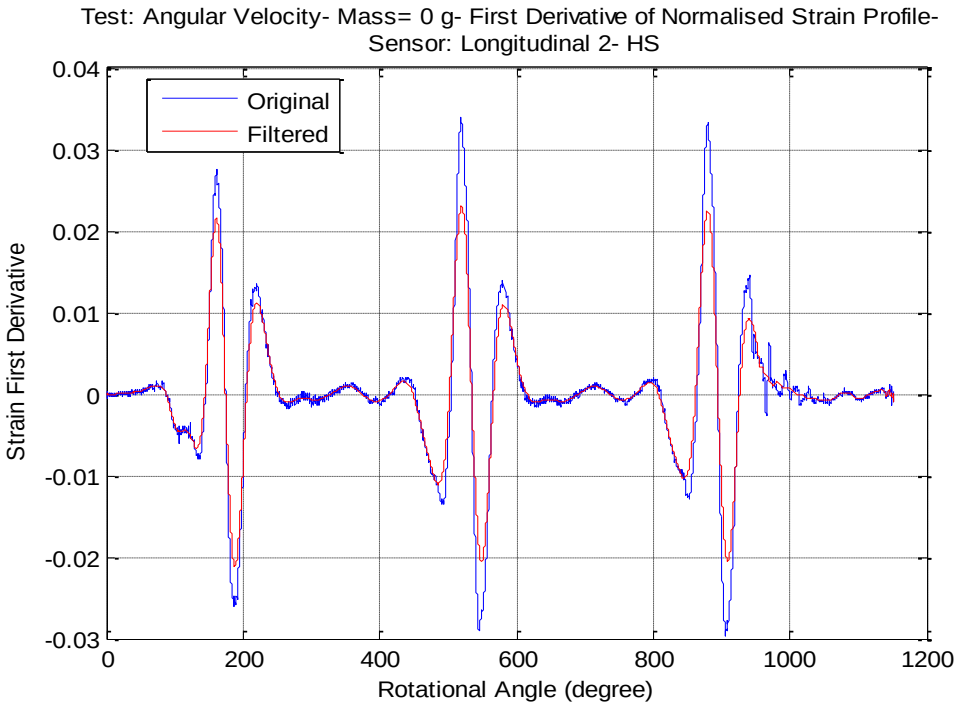

(b) Sensor: Longitudinal 2.

Figure 4.16: Comparing original (non-filtered) and filtered first derivative of strain profiles (HS = High Speed (12.20 rad./sec. = 116.50 RPM), F_z = 0 N).

As previously mentioned, differentiating strain profiles gives derivatives with higher amplitudes than the original signals. Therefore, the y-axis values in the second derivative waveforms (Figure 4.17 and Figure 4.18) are higher than the values in their corresponding first derivatives.

For the second derivative of the lateral strain profile (Figure 4.17), two valleys identify the front and rear regions of the contact patch. These valleys correspond to the tensile peaks in the original profiles. Also, a peak appears at the centre of the patch as a result of the compressive peak in the original profile.

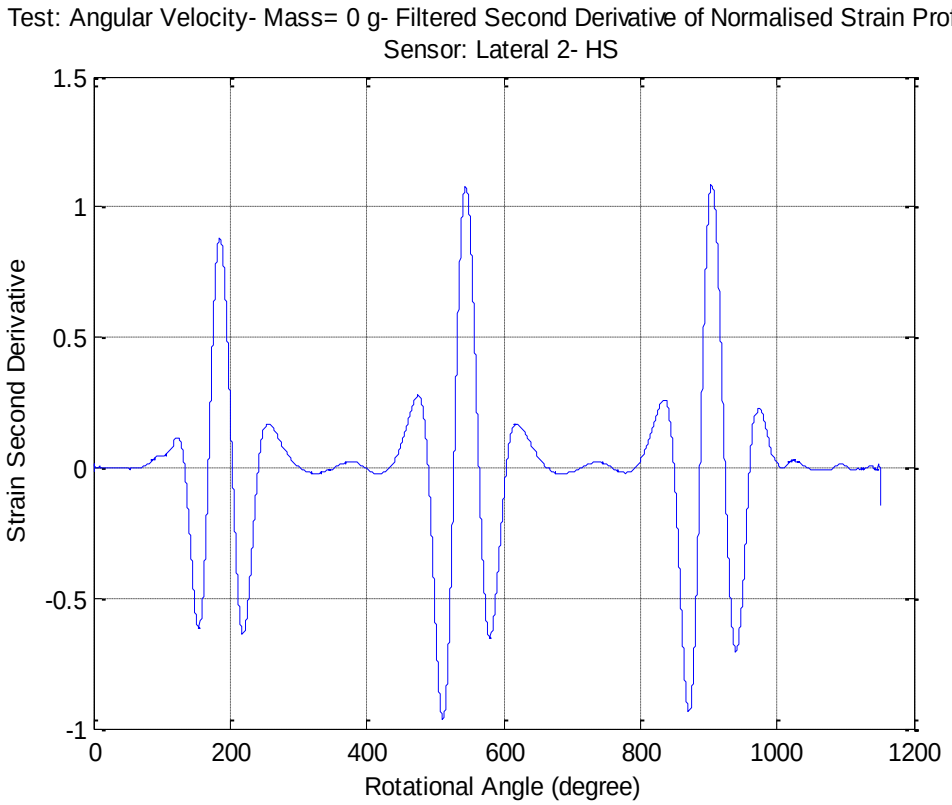

Figure 4.17: Second derivative of strain profiles for the lateral sensors (HS = High Speed (12.20 rad./sec. = 116.50 RPM), F_z = 0 N).

In the second derivative profile of the longitudinal sensor's readings (Figure 4.18), two peaks appear at the location of the compressive peaks existed in the original profile. By contrast, a valley corresponds to the tensile peak in the original profile.

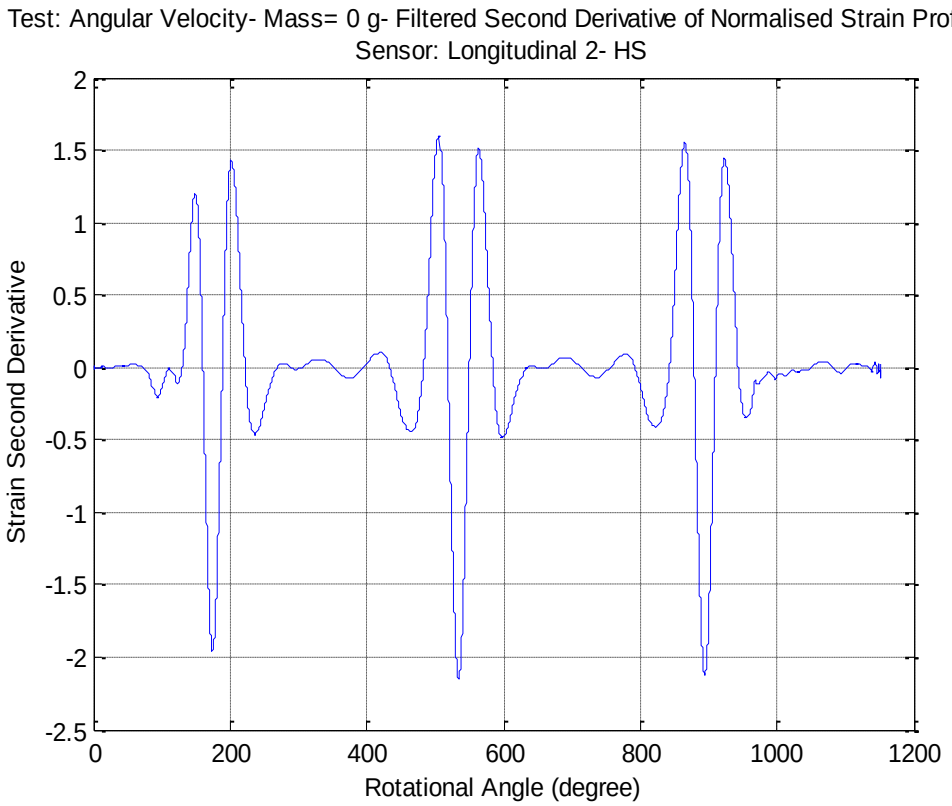

Figure 4.18: Second derivative of strain profiles for the longitudinal sensors (HS = High Speed (12.20 rad./sec. = 116.50 RPM), F_z = 0 N).

Figure 4.19 shows the effect of the smoothing process using the Savitzky-Golay filter on the second derivative profiles. A small amplitude difference between the original and the smoothed signals can be seen, especially in the peaks' points.

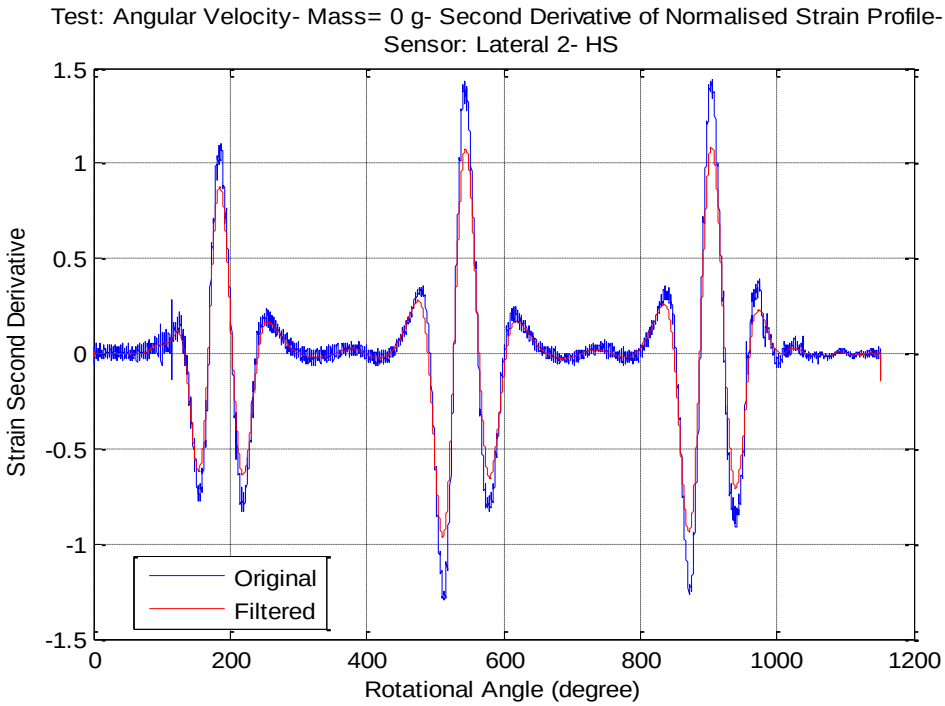

(a) Sensor: Lateral 2.

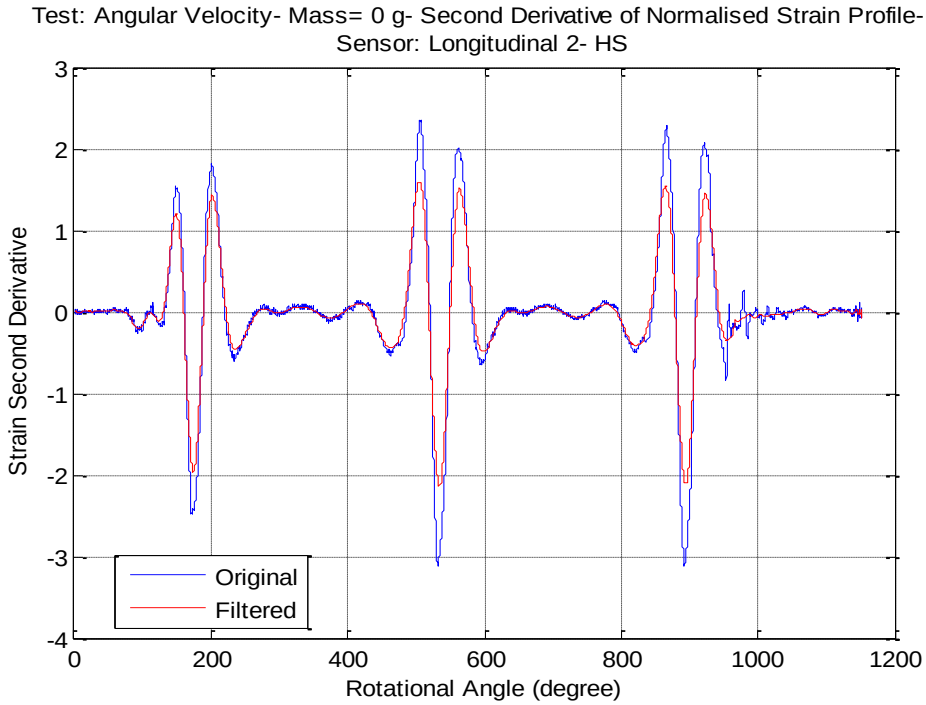

(b) Sensor: Longitudinal 2.

Figure 4.19: Effect of the smoothing process on the second derivative profiles (HS = High Speed (12.20 rad./sec. = 116.50 RPM), F_z = 0 N).

4.2.2 Results of the angular velocity and vertical load tests

As reported in Section 3.3.2, ten values of the tyre's angular velocity were examined by progressively increasing the voltage to the motor. This section presents the sensors' readings resulting from these ten angular velocity tests. The range of the tested angular velocity was from 3.50 rad./sec. to 12.20 rad./sec. Figure 4.20 shows the raw strain measurements for a lateral and a longitudinal sensor in these tests.

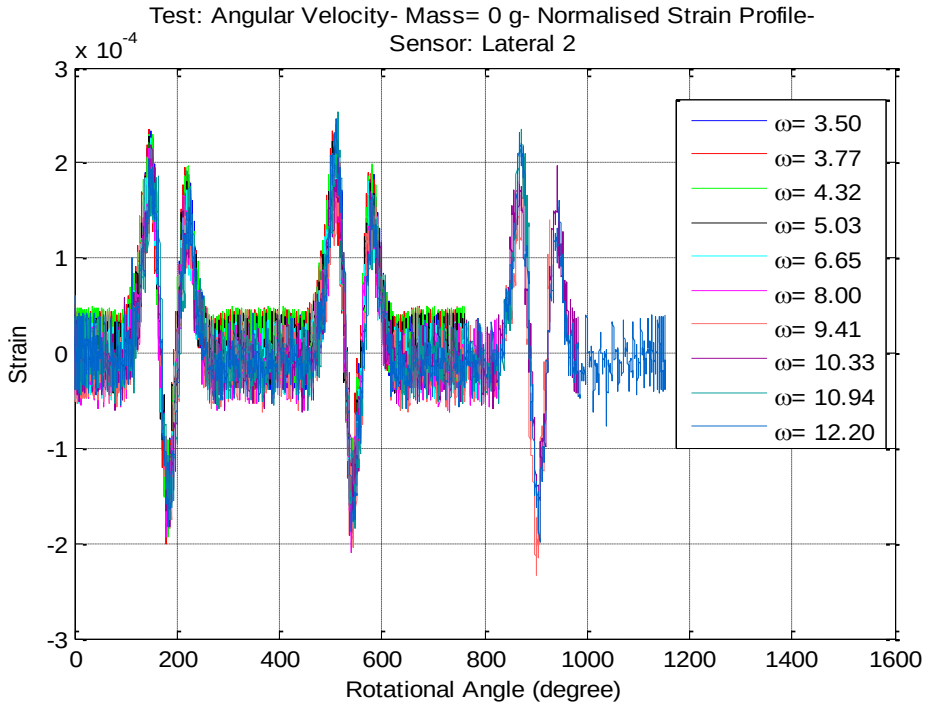

(a) Sensor: Lateral 2.

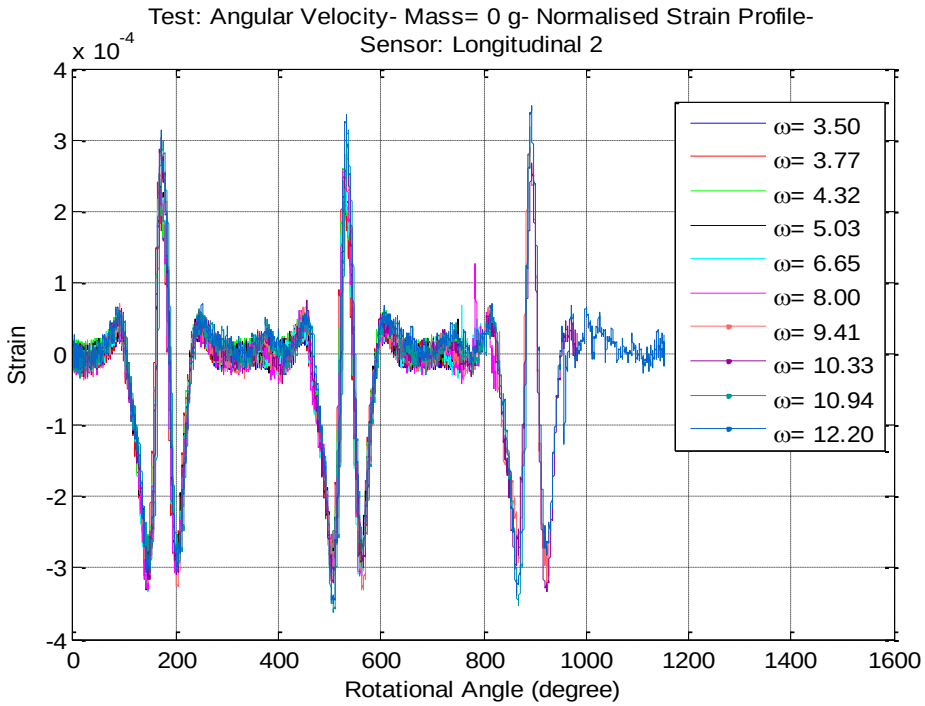

(b) Sensor: Longitudinal 2.

Figure 4.20: Readings of the sensors for the angular velocity tests
(ω = Tyre's angular velocity (rad./sec.), F_z = 0 N).

The characteristics of the individual strain waveforms were described in Section 4.2.1. It can be seen in Figure 4.20 that these characteristics are consistent in the strain readings that result from applying the ten different angular velocities. These readings are smoothed using the weighted moving average filter described in the previous section. Figure 4.21 below shows the smoothed strain waveforms for the ten values of angular velocity. The effect of the smoothing process on the sensors' readings was covered in the previous section.

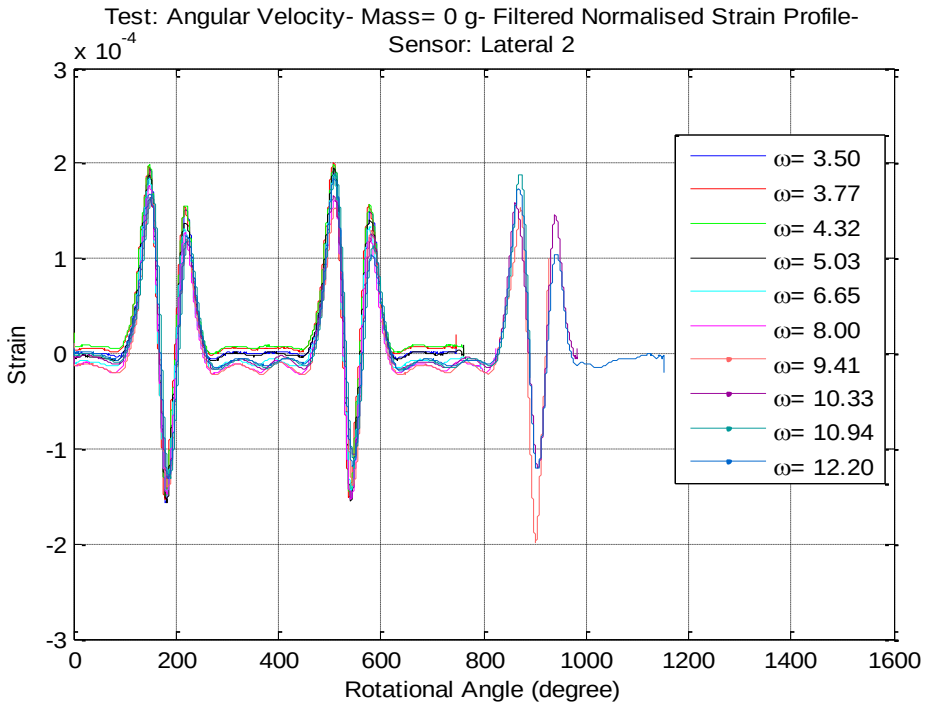

(a) Sensor: Lateral 2.

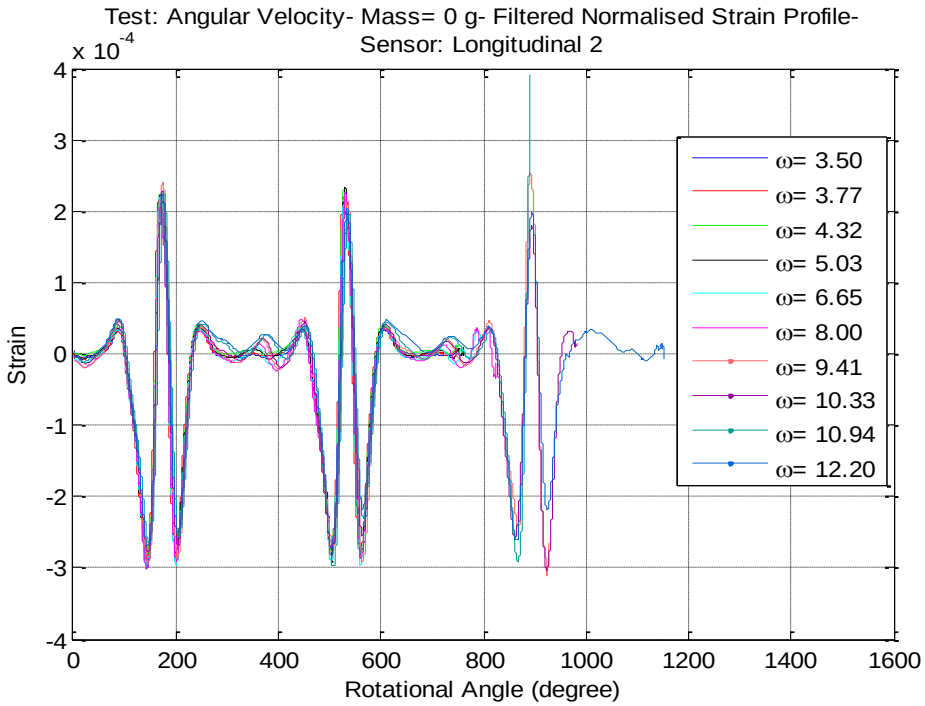

(b) Sensor: Longitudinal 2.

Figure 4.21: Filtered readings of the sensors for the angular velocity tests (ω = Tyre's angular velocity (rad./sec.), F_z = 0 N).

It can be observed in Figure 4.20 and Figure 4.21 that the ten strain waveforms corresponding to the incremental angular velocity are very similar in nature. Very small differences are noticed between these waveforms in terms of the shapes and the strain values. Therefore, three of these strain waveforms will be used in this thesis whenever it is required to compare the strain waveforms resulting from different angular velocities, for example, in Sections 5.2.1 and 7.3. The three strain waveforms are chosen to represent the tyre's low rotational speed (LS = 3.50 rad./sec. = 33.42 RPM), medium rotational speed (MS = 6.65 rad./sec. = 63.50 RPM), and high rotational speed (HS = 12.20 rad./sec. = 116.50 RPM).

As explained in Section 3.3.3, ten values of vertical load were examined in the dynamic tests. This was done by loading the cart used in the second bench-top rig with slotted rings. The raw sensors' readings resulting from these ten tests are shown in Figure 4.22. As can be seen in the figure, the range of the vertical load was from 0 N to 9 N with a 1 N increment.

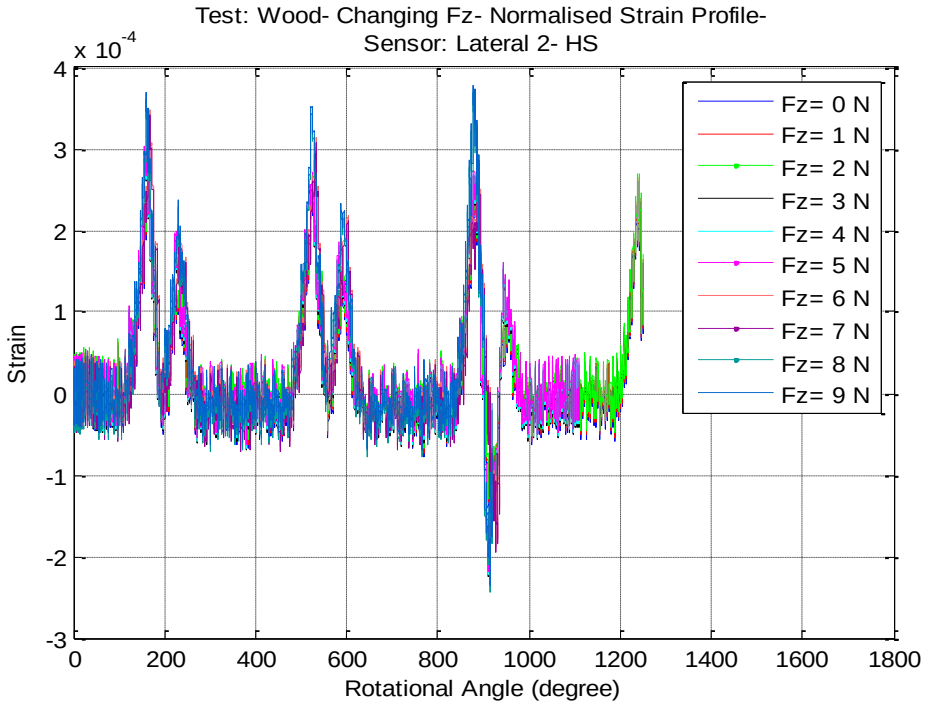

(a) Sensor: Lateral 2.

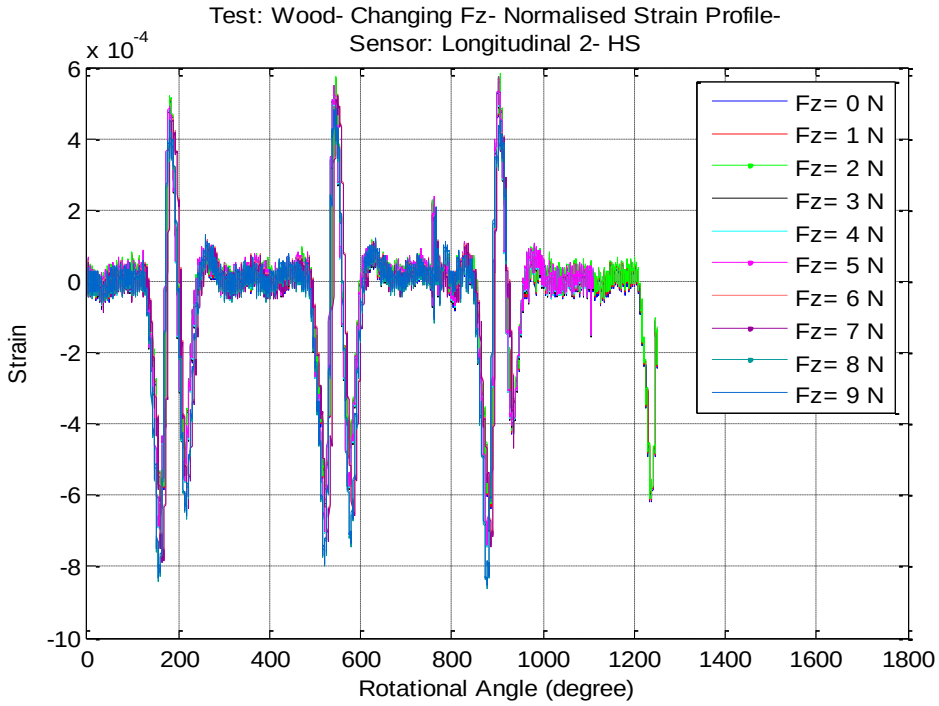

(b) Sensor: Longitudinal 2.

Figure 4.22: Readings of the sensors for the vertical load tests
(HS = High Speed (12.20 rad./sec. = 116.50 RPM)).

These raw measurements are smoothed using the filter described in the previous section. Figure 4.23 presents the filtered strain waveforms for the ten values of the vertical load.

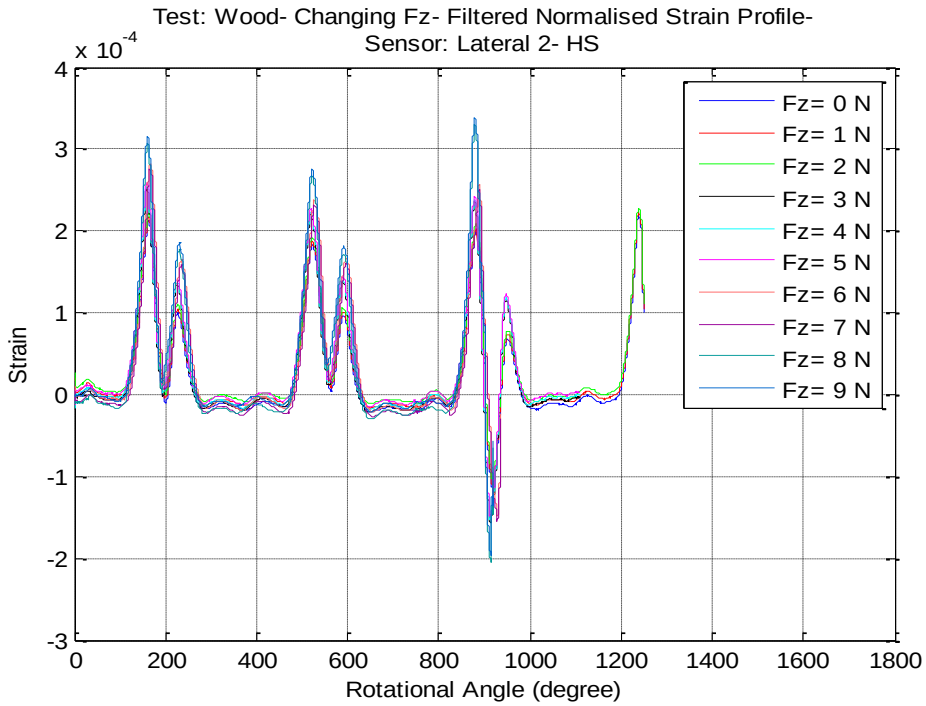

(a) Sensor: Lateral 2.

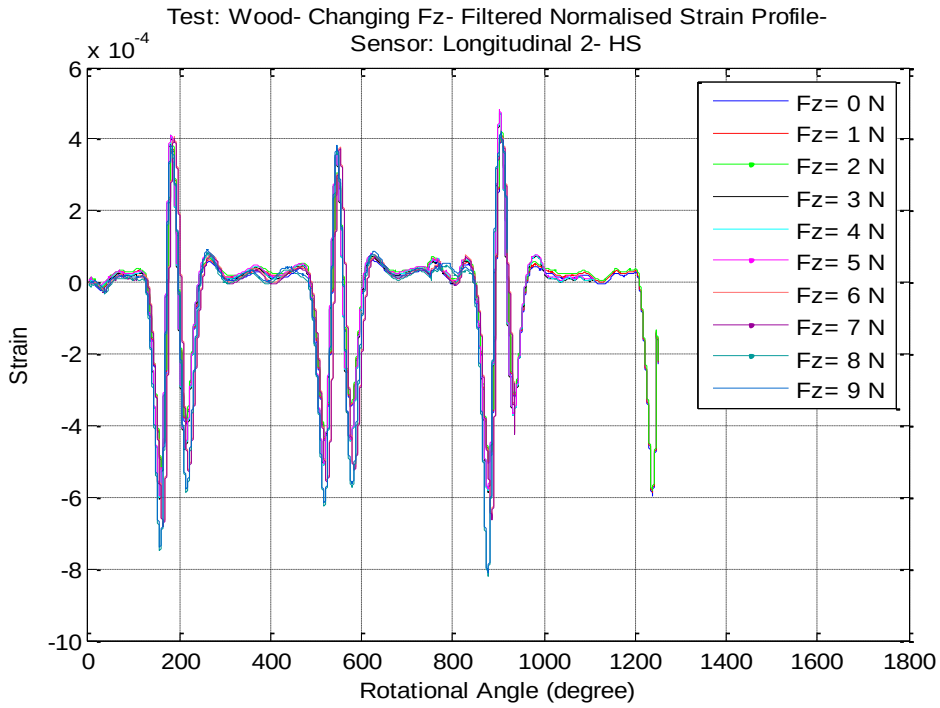

(b) Sensor: Longitudinal 2.

Figure 4.23: Filtered readings of the sensors for the vertical load tests (HS = High Speed (12.20 rad./sec. = 116.50 RPM)).

From the results presented in Figure 4.22 and Figure 4.23, it is evident that the strain profiles are very similar. Only small changes are observed when examining the successive strain waveforms. It is therefore decided to use four of these strain waveforms in the rest of this thesis when discussing the effect of increasing the vertical load on the strain measurements, for example, in Sections 5.2.2, 7.1, 7.2, and 7.3. These four waveforms represent the strain readings that correspond to the no-load (F_z = 0 N), low-load (F_z = 3 N), medium-load (F_z = 6 N), and high-load (F_z = 9 N) cases.

In summary, due to the similarities in the strain waveforms resulting from applying the ten values of the angular velocity and vertical load, three values of angular velocity and four values of vertical load will be used in this thesis. These values are chosen to highlight the distinct differences between the waveforms. The three values of the angular velocity represent the tyre's low, medium, and high rotational speeds. The four values of the vertical load represent the no-load, low-load, medium-load, and high-load for the tyre. These values are found to be suitable representations of the results and sufficient to capture the tyre's behaviour under different levels of angular velocity and vertical load.

4.2.3 Comparing the results of two tyres in the dynamic tests

As mentioned earlier, four identical tyres were used in the tests. The sensors' readings obtained from the four tyres were very close. This section compares the results of two of the tyres where the differences were more noticeable as compared to the other tyres.

Figure 4.24 presents a comparison of a lateral and a longitudinal sensor's readings for the two tyres. A high degree of similarity exists in the strain waveforms in terms of the presence of the compression and tension strain regions. Additionally, the front tensile peak is higher than the rear tensile peak in the lateral strain waveforms of both tyres. Similarly, the front compressive peak is less than the rear compressive peak in the longitudinal strain profiles for the two tyres. Moreover, the contact patch length calculated from the strain derivatives is very close for the two tyres. For example, for a vertical load of 3 N, the contact patch length is 23.06° (25.42 mm) for the first tyre and 24.38° (26.86 mm) for the second tyre.

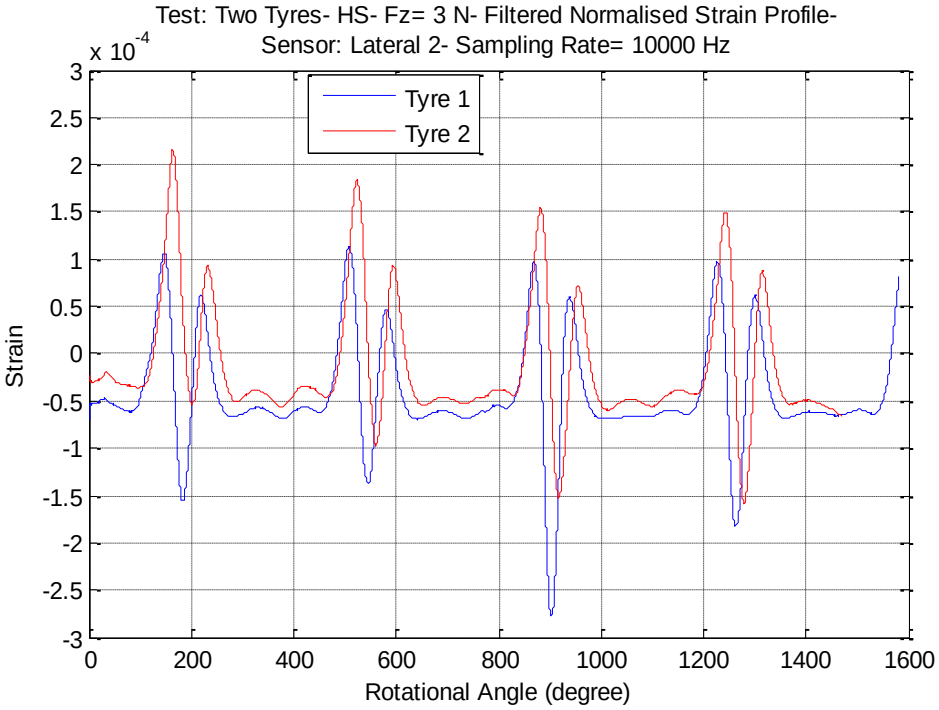

(a) Sensor: Lateral 2.

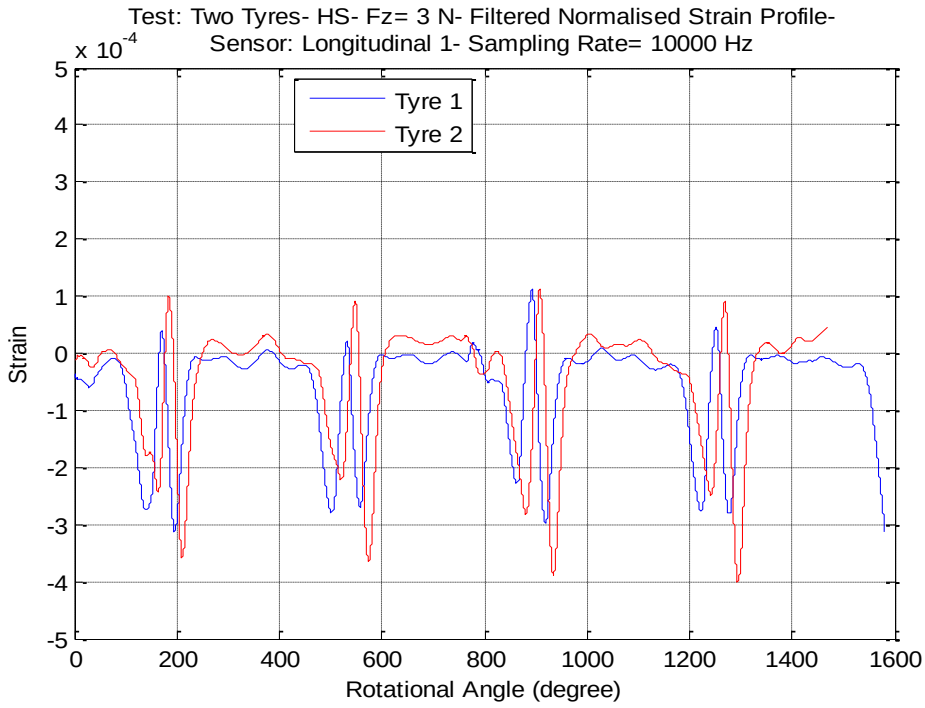

(b) Sensor: Longitudinal 1.

Figure 4.24: Comparing readings obtained from two tyres in the dynamic tests (HS = High Speed (12.20 rad./sec. = 116.50 RPM), F_z = 3 N).

Despite these similarities between the measurements collected using the two tyres, minor differences are observed. Firstly, a slight vertical shift is seen between the strain values of the two cases. This shift is caused by the mechanical wear and tear for some parts of the rig, which leads to producing a slightly different response for the same load in the tests with the two tyres. A second reason for this vertical shift is that the sensors in the two tyres are stretched to different degrees. This is caused by small unavoidable differences in the installation processes of the sensor systems, namely, gluing, soldering, and creating strain relief loops. Secondly, a horizontal shift is noticed in the rotational angles' measurements. This shift results from a small difference in the initial angular position of the tyres or in the initial reading of the motor's encoder. Another reason for this horizontal shift is a variation in the tyre angular velocity during the test because of the motor's performance. To explain, the tyres ran at relatively different speeds during the two tests although the supply voltage was set to the same value.

4.2.4 Measurements of the encoder and the current sensor

It takes the motor a few tenths of a second to reach the full speed allowed by the applied value of the supply voltage. Figure 4.25 presents the encoder readings in one of the tests. It shows that the tyre accelerates between points A (0 sec.) and B (0.3736 sec.). After that, it moves at a constant speed, between points B and C (1.018 sec.). It then decelerates, between points C and D (1.272 sec.), until it stops at point D.

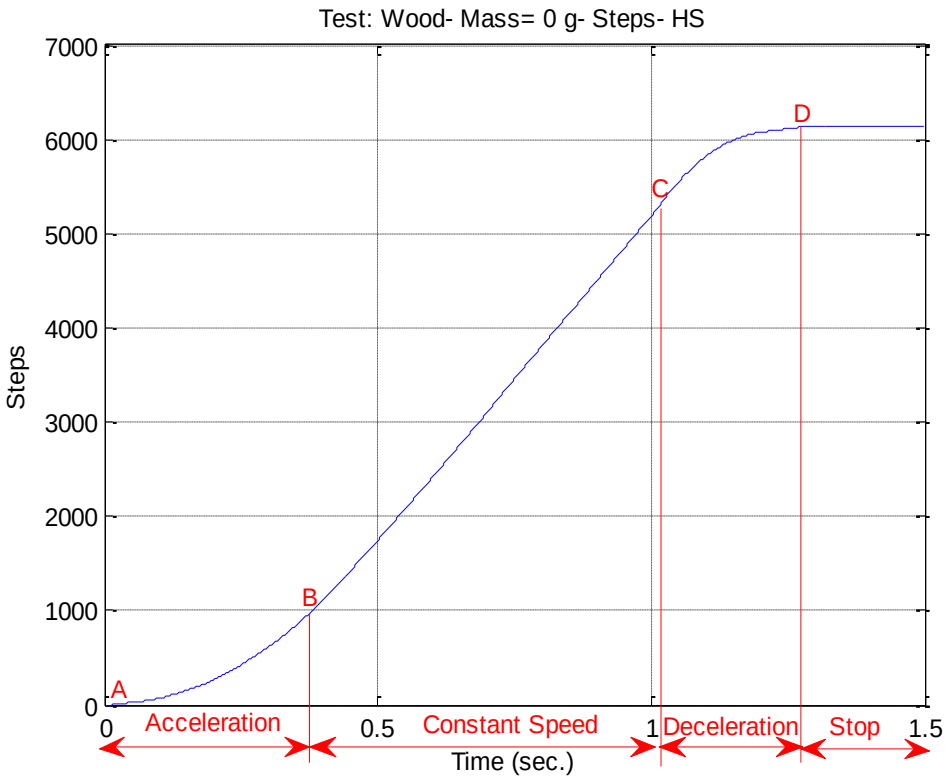

Figure 4.25: Encoder's readings for a speed test

(HS = High Speed (12.20 rad./sec. = 116.50 RPM), F_z = 0 N).

Therefore, the time required to complete the first tyre revolution is usually longer than the time for the next revolutions. This became more evident in tests where high speeds were used. Table 4.2 shows the time required to complete the first two tyre revolutions, i.e. to travel the track, and a third revolution (an extra rotation) during the tests.

Table 4.2: Time for individual tyre revolutions during the speed tests (LS = Low Speed (3.50 rad./sec. = 33.42 RPM), MS = Medium Speed (6.65 rad./sec. = 63.50 RPM), HS = High Speed (12.20 rad./sec. = 116.50 RPM)).

Speed / **Time of revolution**	**LS**	**MS**	**HS**
First Revolution	2.3973 sec.	0.7543 sec.	0.5275 sec.
Second Revolution	2.4058 sec.	0.5905 sec.	0.2785 sec.
Third Revolution			0.2829 sec.

The encoder's reading was deployed to plot the strain sensors' measurements against the tyre's rotational angles. To do so, first, the steps' readings (Figure 4.25), were converted to angles using the following formula:

$$\begin{aligned} \text{Rotational Angles (degree)} &= \text{Revolutions} \times 360 \\ &= \frac{Steps}{1920} \times 360 \end{aligned} \tag{4.2}$$

Where the integrated quadrature encoder provides a resolution of 64 counts per revolution of the motor shaft. This is equivalent to 1920 counts per revolution of the gearbox's output shaft for the 30:1 gear motor used in the dynamic tests.

The next step was obtaining the time when each rotational angle is reached as illustrated in Figure 4.26.

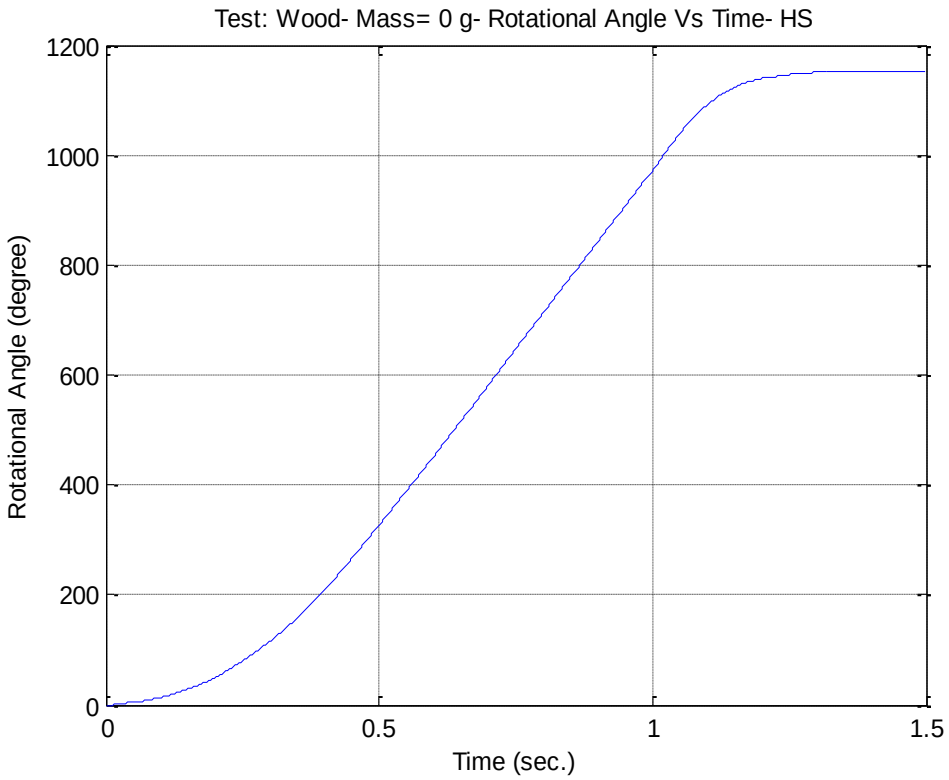

Figure 4.26: Tyre's rotational angles vs. time
(HS = High Speed (12.20 rad./sec. = 116.50 RPM), F_z = 0 N).

The final step was using the time where a particular angle is reached to change the (Strain vs Time) figures to (Strain vs Rotational Angle) figures, as was presented in Figure 4.13.

A current sensor was used to monitor the current of the motor during tyre rotations. Readings of this current sensor were utilised as an indication for the longitudinal force (F_x) experienced by the tyre. To convert the current sensor's readings to force measurements, the motor current vs. motor torque graph is plotted using the motor specifications. Next, the slope of the line representing the relationship between current and torque is calculated. After that, the current sensor readings are smoothed using a moving-average filter as shown in Figure 4.27.

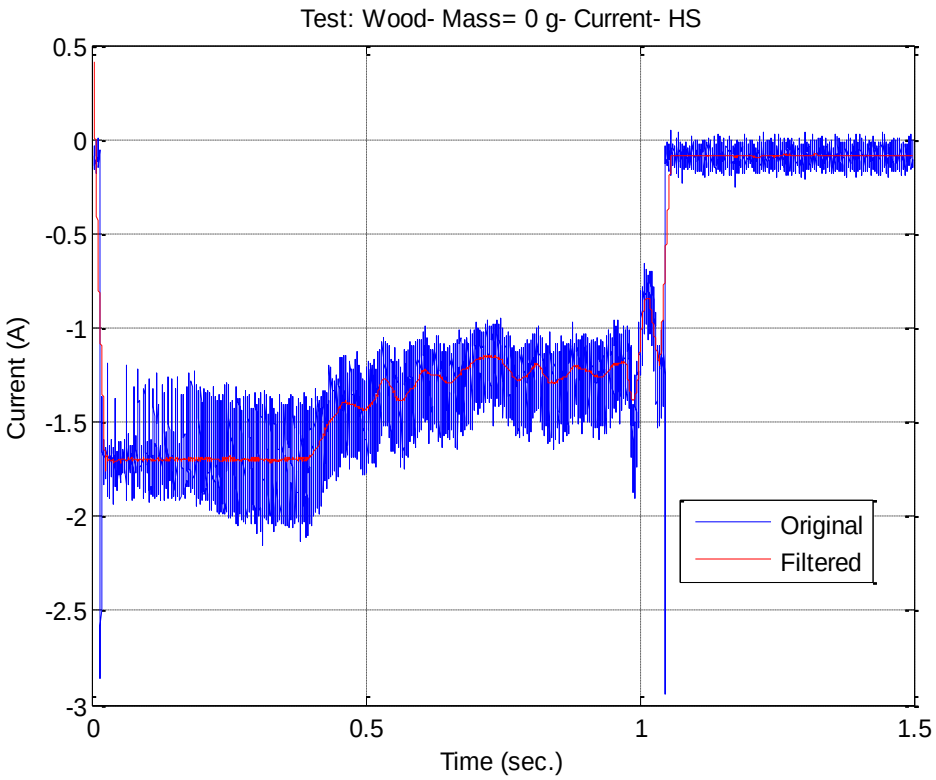

Figure 4.27: Current sensor readings

(HS = High Speed (12.20 rad./sec. = 116.50 RPM), F_z = 0 N).

The following formula is then used to convert current to torque:

$$T(oz-in) = I(A) \times K_m \tag{4.3}$$

where:

T is the torque (oz-in)

I is the current (A)

K_m is the motor torque constant = reciprocal of the slope for current vs. torque graph = 0.023404.

The next step is converting torque calculations to force readings using the formula:

$$T\ (N.m) = F_x\ (N) \times motor\ radius\ (m) \tag{4.4}$$

where F_x is the longitudinal force (N).

The final step is filtering the resulting force measurements using the Savitzky-Golay filter. Figure 4.28 shows both the original and smoothed longitudinal force readings for one of the tests.

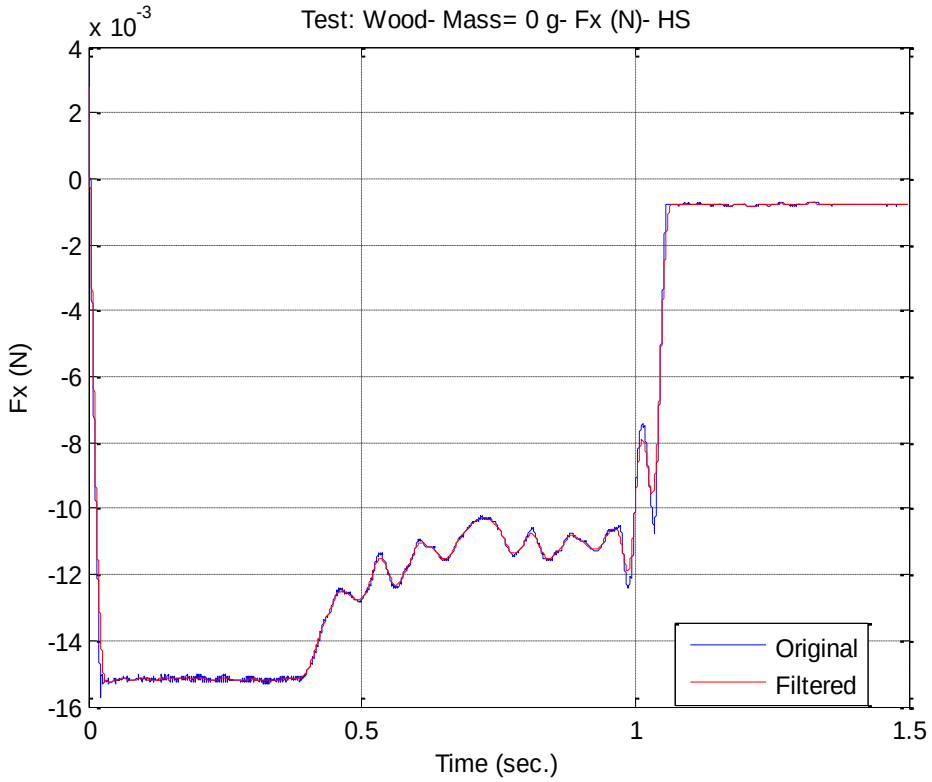

Figure 4.28: Longitudinal force extracted from the current sensor's readings (HS = High Speed (12.20 rad./sec. = 116.50 RPM), F_z = 0 N).

4.3 Comparing the results of static and dynamic tests

This section compares the results of the static and dynamic tests. The working conditions inside the laboratory, in terms of the external factors such as temperature and humidity, were the same in the tests. Another similarity is the use of a wooden board as the contacting surface for the tyre. Figure 4.29 presents a comparison between the results of these tests using the readings of a lateral and a longitudinal sensor respectively. A high degree of similarity is seen in the readings. For the two types of tests, the strain waveforms contain the same regions of compression and tension.

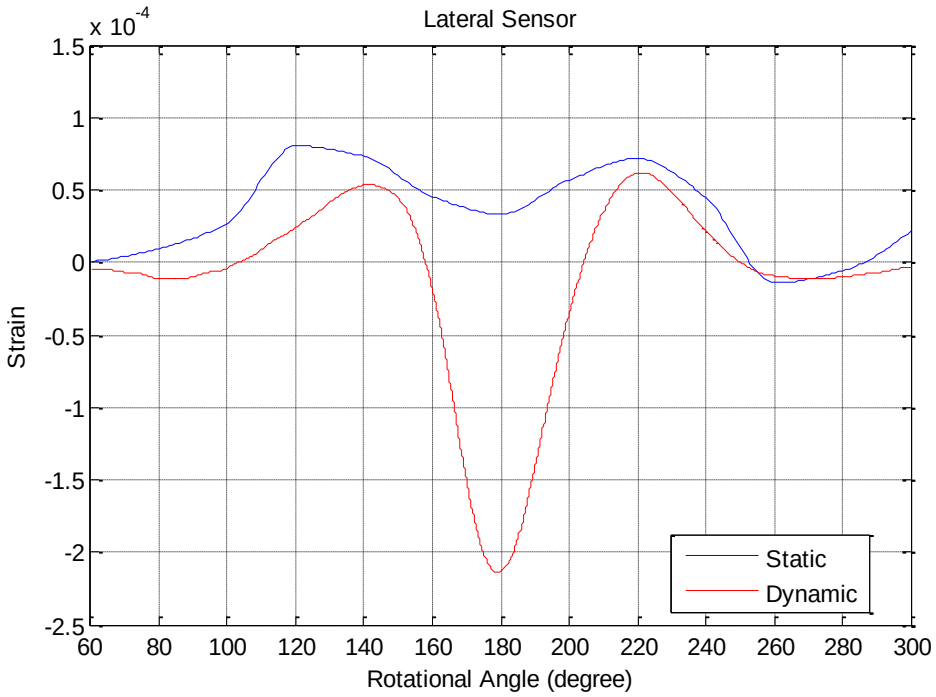

(a) Lateral Sensor.

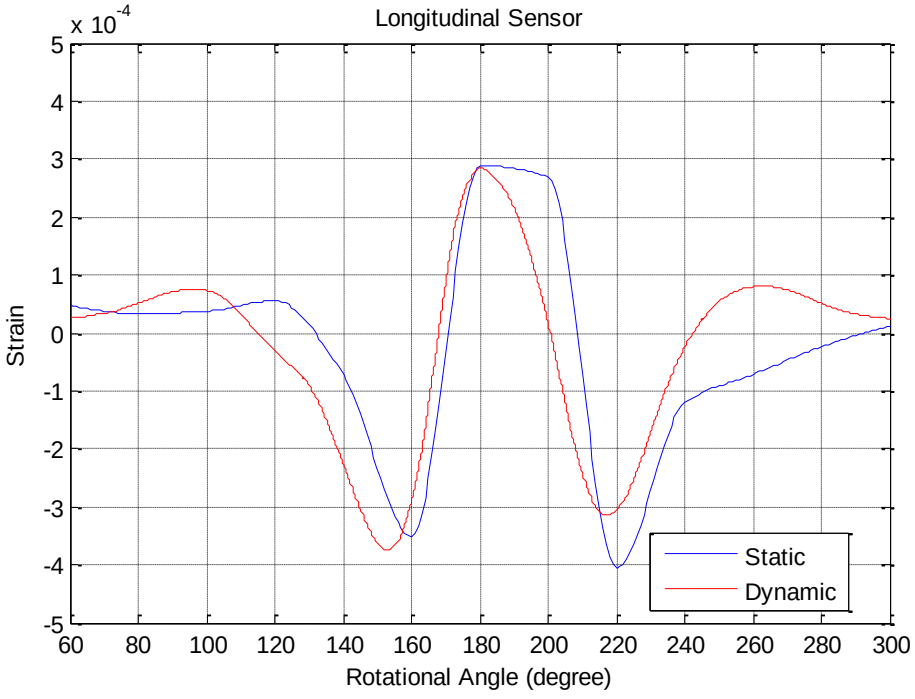

(b) Longitudinal Sensor.

Figure 4.29: Comparing the results of the static tests and dynamic tests.

On the other hand, there are two main differences between the static and the dynamic tests. First, two different testing beds were used in these tests where a specially designed bench-top rig was dedicated for each type. For these two rigs, the level of sensors' noise caused by the mechanical vibrations of the individual parts was not the same. For the rig of the static tests, these vibrations were caused by the manual application of the forces and the subsequent movements of the parts. For the rig of the dynamic tests, the mechanical noise resulted from the movement of the tyre and the resultant vibrations of the cart and the rail. Second, two different tyres were utilised in these tests. Unlike the tyre of the dynamic tests, a foam ring was used inside the tyre of the static tests. As a result, higher force values were possible to be tested in the static tests. Also, the addition of the foam inside one of the tyres makes the response to the applied forces different in the two tyres. Because of these two differences, Figure 4.29 demonstrates slight differences in the measurements of the sensors in the tests.

To conclude, a sufficient level of agreement is noted when comparing the results of the static and dynamic tests. This similarity is an indication of the applicability of the tools that were utilised such as the sensors, the test rigs, and the DAQ system for this research. It also shows the success in developing a method for mounting a strain sensor system on the inner surface of small non-pressurised tyres. The results imply a high degree of consistency in terms of sensors' positions as well as other installation-related operations like gluing, soldering, and wiring. Therefore, the outcomes of the tests presented in this work can be deployed to show the usefulness of placing sensors inside tyres to measure the strain. In the next chapters, these in-tyre strain measurements will be analysed in more details. They will be employed to extract useful information about the nature and texture of the contacting surfaces, the obstacles, as well as the various variables related to the tyre's working conditions.

4.4 Summary

The data analysis presented in this chapter is divided into three main parts. The first part (Section 4.1) presented the initial steps for the analysis of the experimental data resulted from the static tests conducted on the first rig. The following points highlight some of these steps:

- There was a small difference in the bias readings of the sensors. This difference was caused by the different mounting positions and orientations for the sensors. The strain resulted from the installation processes of each sensor also contributed to this difference in the default measurements.

- A moving average filter was utilised to attenuate the existing noise in the strain measurements.

- The relationships between the longitudinal load and the strain at a particular vertical load were plotted for the tested angular positions. These relationships were used to build the strain profiles for different values of F_x and F_z. These strain profiles were described in detail in Section 4.1.2. The interpolation and differentiation of the profiles were also presented.

The second part (Section 4.2) showed the first stages of analysing the results of the dynamic tests that were conducted on the second rig. The following presents some of these stages:

- The bias readings of the sensors were examined. It was observed that the effect of temperature led to a slight difference in the readings collected at different days.

- An appropriate weighted moving average filter (Savitzky-Golay) was used to smooth the readings.

- The strain profiles were differentiated twice to investigate the changes in strain.

- The strain profiles, the strain derivatives, and the effect of the filtering process on the readings were described in detail in Section 4.2.1.

- The results of ten angular velocity and vertical load tests showed strain profiles with small differences. Therefore, the strain waveforms resulted from three values of angular velocity and four values of vertical load will be used in the next chapters for clarity in comparisons. These strain waveforms were chosen because they could describe the behaviour of the tyre at different levels of angular velocity and vertical load.

- The measurements of the encoder were presented to illustrate the operation of the motor. The encoder measurements were used to plot the readings of the strain sensors with respect to the tyre's rotational angles.

- A method of converting the measurements of the motor's current sensor to longitudinal force was explained.

The third part (Section 4.3) compared the strain profiles acquired from the static and dynamic tests. A sufficient degree of agreement between the readings was reported. It was stated that this is an indication for the applicability of the employed tools and experimental procedure.

To sum up, the chapter has presented the basic data processing for the readings collected in the static and dynamic tests. A further analysis will be presented in Chapter 5 and Chapter 6 where the strain measurements will be utilised to extract features that indicate slip and spin incidents, the presence of obstacles, and traversing different surfaces. Most importantly, this chapter showed that the strain profiles of the non-pressurised tyre used in this work are similar to that of pneumatic car tyres (Matsuzaki & Todoroki 2008a; Yang 2011). This suggests that the models that are used to relate the measurements of the tyre strain to the mechanical properties in the pneumatic tyres can be utilised for the non-pressurised tyres used herein. This will

be investigated in Chapter 7 to derive the forces, the contact patch length and centre, the angular velocity, and the camber angles from the strain measurements.

Chapter 5

Slip/Spin and Obstacle Detection

This chapter investigates the in-tyre sensors' potential in detecting tyre slip/spin incidents. It also examines the sensors' readings to determine their capability of identifying the presence of obstacles in the traversed path. The sensors' ability to detect the occurrence of the slip is examined using the results of the static experiments performed on the first rig. With regard to the spin and obstacle detection, dynamic experiments were conducted on the second rig. In these dynamic tests, different tyre's angular velocities, vertical loads, surfaces, and speed settings were examined. The effect of these variables on the performance of the in-tyre sensors in detecting the spin and the obstacles will be analysed.

The data used in this chapter were acquired utilising the tests explained in Chapter 3. Table 5.1 below lists the sections of Chapter 5 and the relevant sections in which the tests were introduced in Chapter 3.

Table 5.1: Linking the sections in Chapter 5 to the corresponding sections that described the experimental setup and tests in Chapter 3.

Sections in Chapter 5	**Associated sections that explained the experimental setup and tests' description in Chapter 3**
5.1 Slip detection using results of the static tests	3.2.3 Static tests to detect slip and construct strain profiles
5.2.1 Effect of angular velocity	3.3.2 Angular velocity tests
5.2.2 Effect of vertical load	3.3.3 Vertical load tests
5.2.3 Effect of the contact surface	3.3.4 Slip/Spin tests

5.1 Slip detection using results of the static tests

A relative motion was generated between the slide and the tyre to induce the slip using the first rig, as presented in Section 3.2.3. This was achieved by pushing the slide over the surface of the fixed tyre at constant time increments. The horizontal movement of the slide on the tyre was created by turning the bolt in the horizontal block. Figure 5.1 shows the readings of a longitudinal and a lateral sensor, respectively, for one of the static tests. A weighted moving average filter was applied to smooth the data without manipulating its real features so that the instantaneous variations caused by applying the longitudinal force (F_x) remain easily traceable in the measurements. Thus, a Savitzky-Golay filter, where the polynomial order is four and the frame size is nineteen, was utilised. Inconsistencies in the results are caused by the amount of vibrations resulted from manual applications of F_x as well as from the sliding mechanism of the rig.

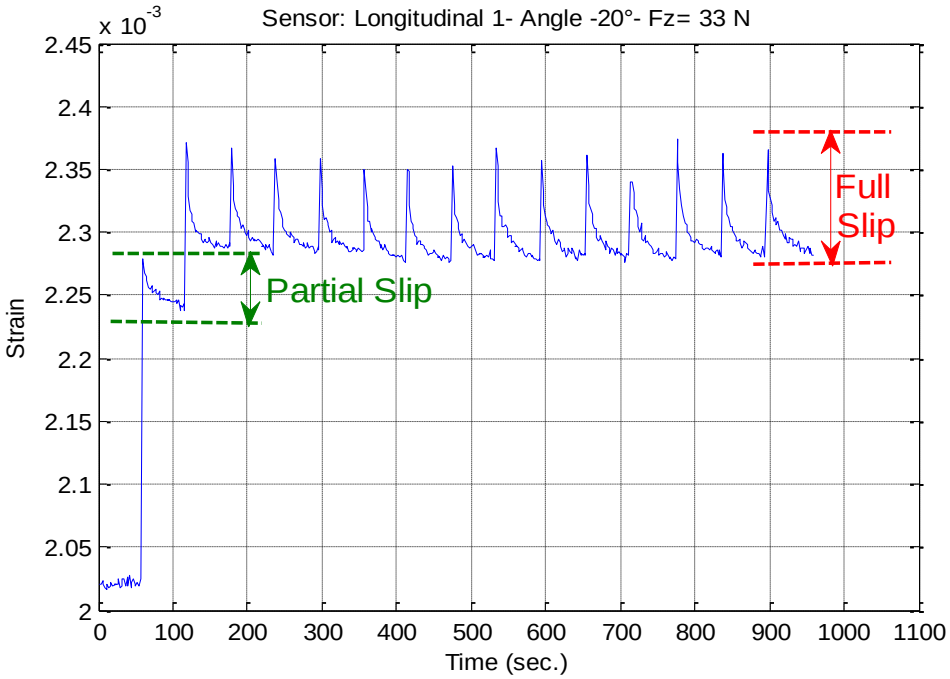

(a) Sensor: Longitudinal 1.

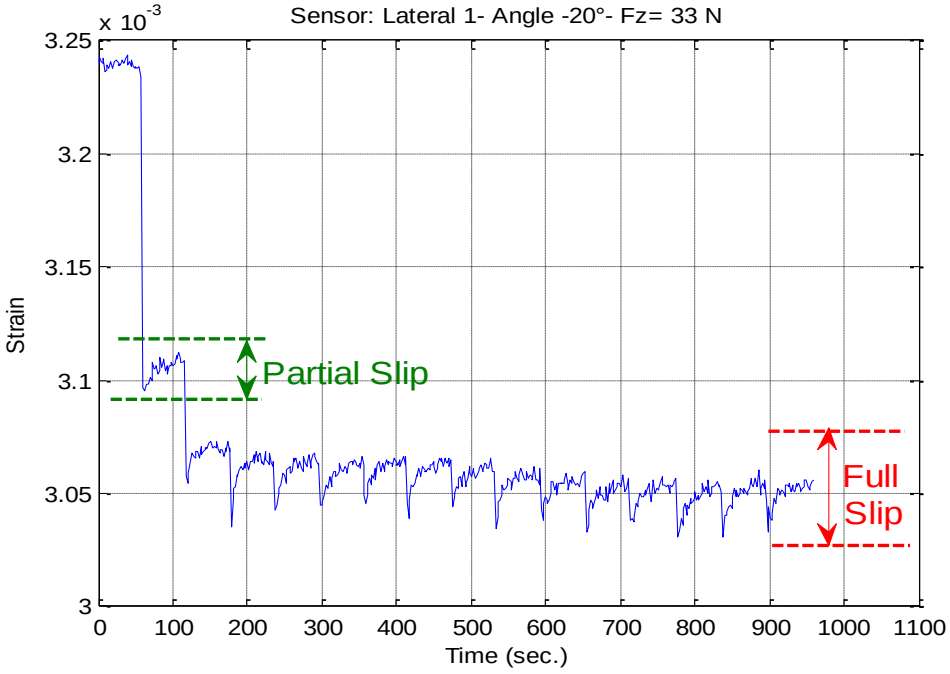

(b) Sensor: Lateral 1.

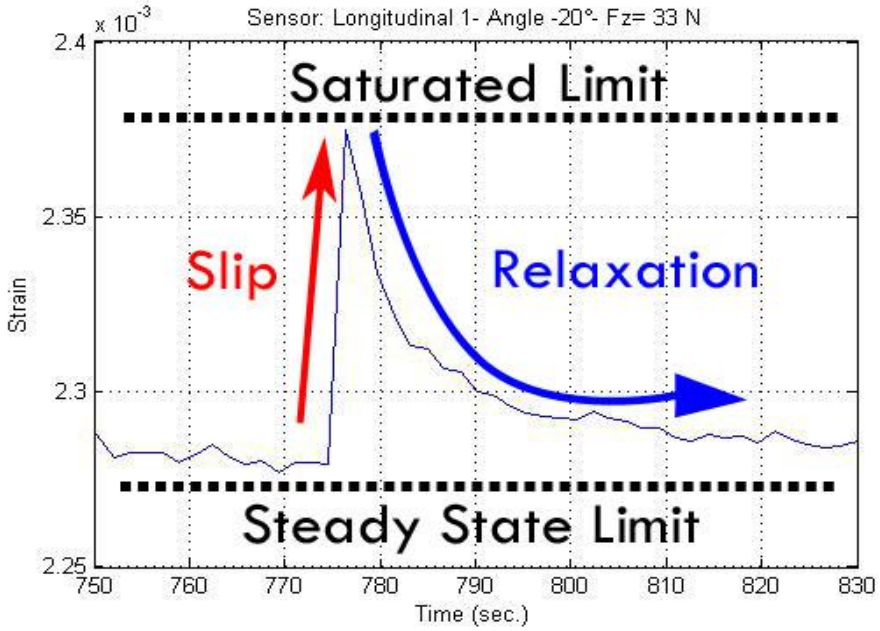

(c) One full slip oscillation (zoomed in from (a) above).

Figure 5.1: Slip region detected in the sensors' readings in a static test (F_z = 33 N, Angle = -20°).

It is noticed in Figure 5.1 that each application of rotation for the horizontal bolt in the rig introduces a change (a spike) in the readings of the strain sensors. To explain, the tyre endures significant changes in the strain each time F_x is being applied then, after F_x is no longer exerted, the tyre relaxes and tries to return to its natural shape. As a result, a zigzag pattern appears in the readings. These sensors' readings are attributed to the elastic behaviour of the non-pressurised tyre in responding to the external loads. The tyre embedded with foam is compressed during the application of F_x. The tyre then tries to regain its original position after this external force is no longer applied. However, the strain does not return to its starting value because the tyre is still compressed.

Another observation about the readings in Figure 5.1 is that the change in the longitudinal strain is opposite to that of the lateral strain. In other words, the longitudinal sensor's readings provide an ascending shape whereas the lateral sensor's readings reflect a descending trend. This observation can be better understood by comparing the readings of the strain sensors to the measurements of the horizontal load cell shown in Figure 5.2. It can be seen that the longitudinal strain sensor stretches in

the same direction as the applied longitudinal load (F_x). In contrast, the lateral strain sensor stretches in the opposite direction with respect to the longitudinal load. A detailed discussion about the strain sensors' measurements and responses to the applied longitudinal load was presented in Section 4.1.1.

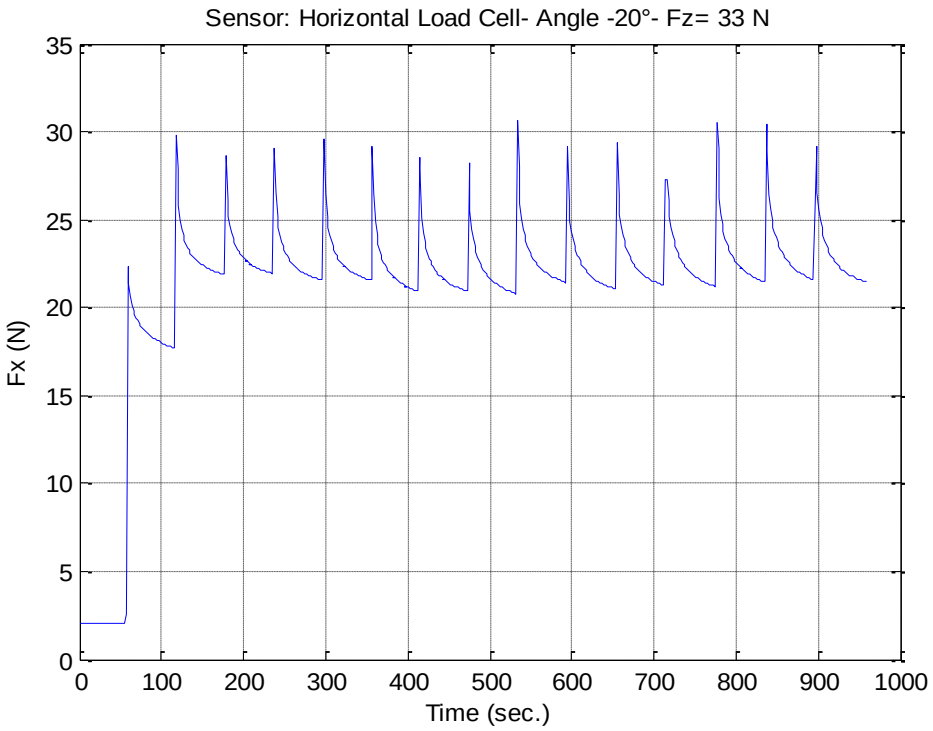

Figure 5.2: Measurement of the horizontal load cell in a static test (F_z = 33 N, Angle = -20°).

To further examine the readings of the strain sensors during the slip incidents, Figure 5.3 presents the relationship between the longitudinal load (F_x) and the strain at a specific angle and vertical load. The first part of the graphs demonstrates a linear relationship. This indicates that the tyre is trying to adapt its structure according to the applied longitudinal load. As a result, there is no slipping. This part is followed by a small region of nonlinearity where for one value of the longitudinal load there are at least two values of strain. This area represents a region of partial slip. The partial slip is identified by a small region where a small number of oscillations appear between two close values of the strain. As the value of the longitudinal load increases, the tyre is able to get out of this region, i.e., to recover from this partial slip situation. However, when the longitudinal load exceeds a certain limit, 21.19 N in Figure 5.3, the tyre completely slips. This fact combined with the effect of the deformation of the tyre

rubber material and foam causes the strain readings to oscillate between a saturated limit and a steady state limit in this full-slip region, as shown in Figure 5.3c. The saturated strain limit is 0.002375 in Figure 5.3a and 0.003031 in Figure 5.3b. This saturated limit is reached when the maximum longitudinal load is applied, i.e., at the end of applying a full rotation of the horizontal bolt. The steady state strain limit is 0.002282 in Figure 5.3a and 0.003068 in Figure 5.3b. This steady state limit is reached after a set relaxing time for the tyre in the test. Compared to the partial slip region, the full slip region is larger and contains higher strain values and a higher number of oscillations.

After concluding these indications about the partial and full slip regions from the graphs in Figure 5.3, the raw measurements of the strain sensors (Figure 5.1) are analysed to identify the corresponding indications. The partial slip region is identified in the graphs of Figure 5.1 by a single isolated spike in the measurements. The full slip region is identified by a repeated pattern where the output starts to repeat itself when applying F_x. After entering this full slip region, each time a longitudinal load is applied, the strain reaches a saturated level. After that, the strain returns to a steady state value when the effect of the longitudinal load expires. Thus, the full slip situation can be detected using the raw sensors' readings or the relationship between the longitudinal load and the strain values measured by the sensors.

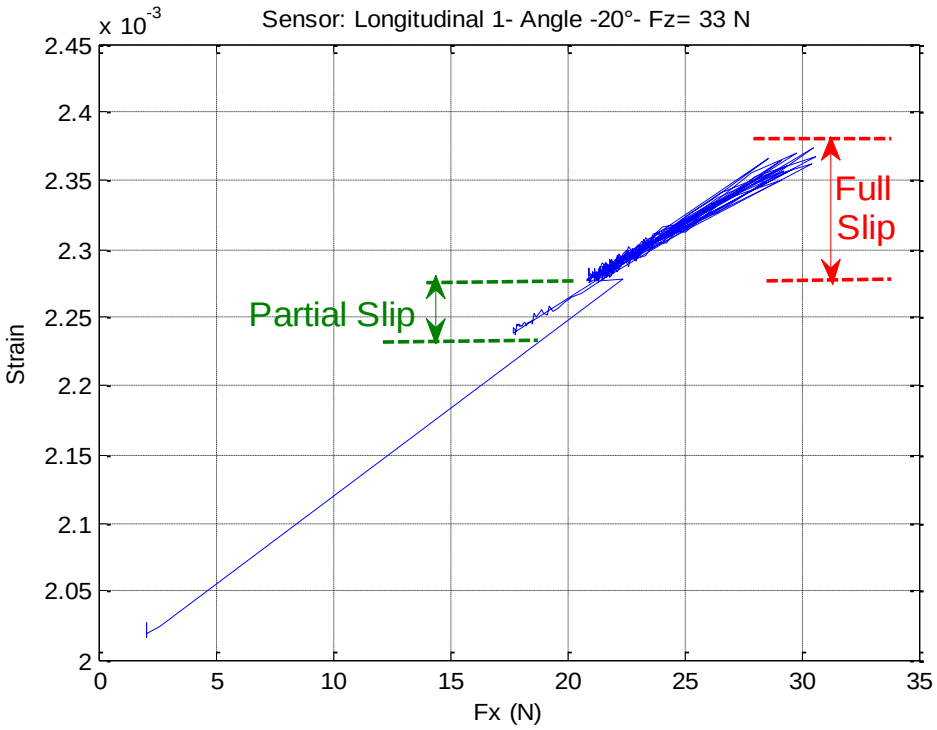

(a) Sensor: Longitudinal 1.

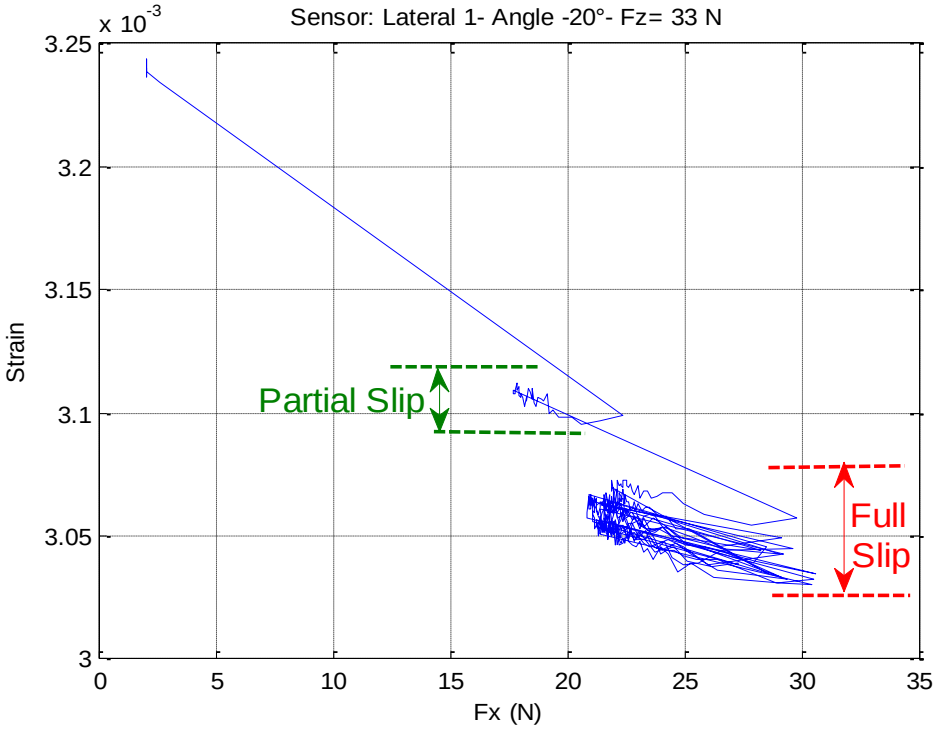

(b) Sensor: Lateral 1.

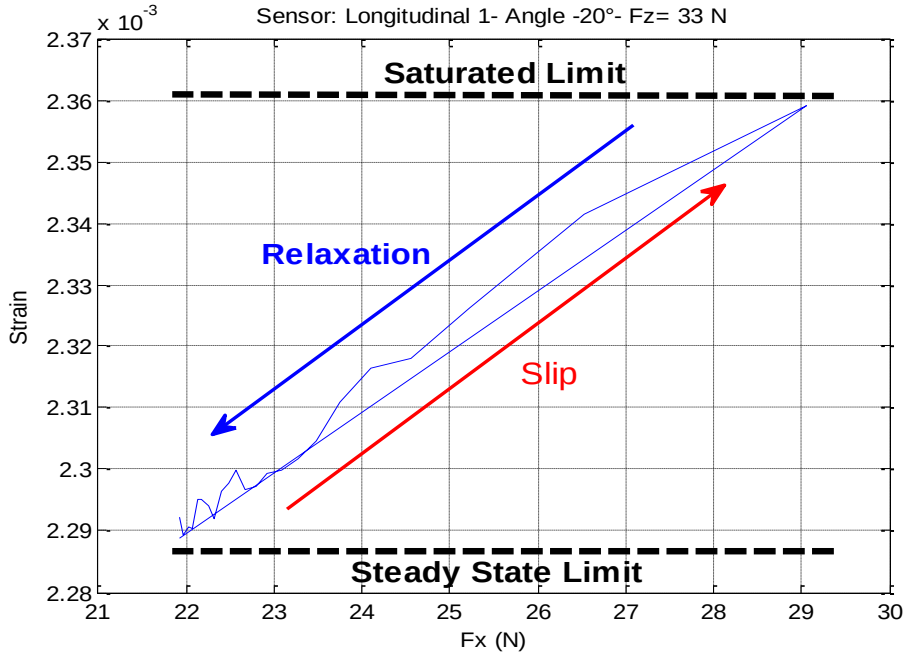

(c) One full slip oscillation (zoomed in from (a) above).

Figure 5.3: Slip region detected in the longitudinal load-strain relationship for the strain sensors (F_z = 33 N, Angle = -20°).

The previous observations were confirmed by carefully examining successive screenshots from a video recorded for one of these tests. First, when applying small values of the longitudinal load (F_x), i.e., at the beginning of the test, the tyre tread blocks try to grip contact with the slide by moving in the same direction of applying F_x. Therefore, there is no slipping. Then, when the value of F_x increases, the tread blocks become partially bent and partial slip takes place. After that, when the value of F_x further increases, the tread blocks become straight with respect to the slide and this is when the slide starts to fully slip on the tyre. From this moment onwards, the slide slips on the contacting blocks each time F_x is applied.

Two additional points can be mentioned about the relationships in Figure 5.3. First, only the first portion of these relationships, i.e., from the beginning of the graph to the full slip region contains the important information to build the strain profiles since the rest of the graph is a repetition. Second, it is perceived that the magnitude of the longitudinal load that initiates the slippage phase is higher than the magnitude that maintains the slippage afterwards. To clarify, after the tyre slips starting from a

longitudinal load of 21.19 N, any additional load is sufficient to force the tyre to continue to slip.

To evaluate the performance of the sensing system, Figure 5.4 compares the sensors' readings in terms of the values of F_x which initiate the full slip at different vertical forces (F_z). This figure illustrates that the sensors deliver very similar results; therefore, it is concluded that the strain sensors can detect the start of the full slip region with a high degree of consistency. The readings of the sensor called Lateral 2 is not presented in this figure as it stopped working after a number of tests.

Another interesting observation in Figure 5.4 is that as the magnitude of the applied vertical force (F_z) increases, the value of the longitudinal force (F_x) which is required to make the tyre starts slipping increases. As expected, the heavier the load on the tyre is, the larger the contact patch will be with the road and thereby a higher longitudinal force is required to force it to slip.

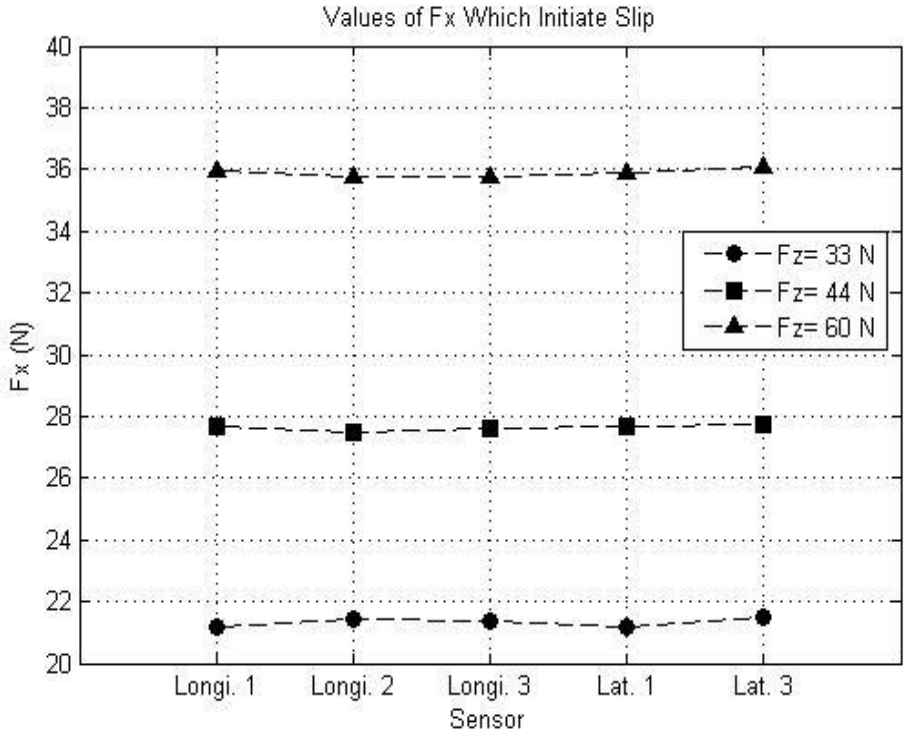

Figure 5.4: Comparing the sensors' readings in terms of F_x values that initiate slip at different F_z values (Longi. = Longitudinal, Lat. = Lateral, Lateral 2 is not presented because it has malfunctioned).

5.2 Spin and obstacle detection using results of the dynamic tests

5.2.1 Effect of angular velocity

Several tests were conducted on the second rig where the angular velocity of the tyre was changed by increasing the voltage to the motor. The results of these tests were analysed to investigate the readings of the sensors during the spin incidents and the presence of obstacles under different rotational speeds. Figure 5.5a shows the strain readings for three levels of speed with respect to time. For clearer comparisons of the profiles, Figure 5.5b overlaps the same readings with respect to the tyre's rotational angles.

The length of the rail allowed the tyre to make two revolutions on the track and this is seen in the sensor readings for low-speed tests (LS in Figure 5.5). However, in high-speed tests (HS in Figure 5.5), three wave cycles are noticed in the strain profiles. This indicates that the tyre has made one extra revolution. This is because the cart hit the shims at the end of the track in the dynamic tests. In the high-speed tests, the tyre continued to rotate after hitting the shims because of its high momentum. Hitting the shims made the cart reverse for a short distance within which the tyre continued to spin until it completely stopped. It will be shown later that, depending on the tyre's speed and how slippery the contact surface is, the tyre may continue to make extra revolutions. Therefore, the readings of the in-tyre strain sensors can be used to decide that a tyre with a known radius has travelled a known distance with or without spinning. This information can be compared against the exact number of revolutions that the tyre should make while travelling this distance. The controller can use this extra input to take appropriate actions. While similar information about the extra tyre spins can be extracted from the wheel encoder, the in-tyre strain sensors provide more details. It was shown in Section 5.1 that the strain sensors can detect the occurrence of the slip. This is a significant advantage over the encoders that provide false estimations during the slip incidents. Therefore, the readings of the strain sensors can complement or correct the encoder's estimations during the slip. It will also be shown in the next sections and chapters that the strain sensors can indicate passing over obstacles and traversing rough surfaces. Furthermore, the readings of the strain sensors will be utilised to estimate the tyre's forces in three directions, the contact patch, and the camber angle.

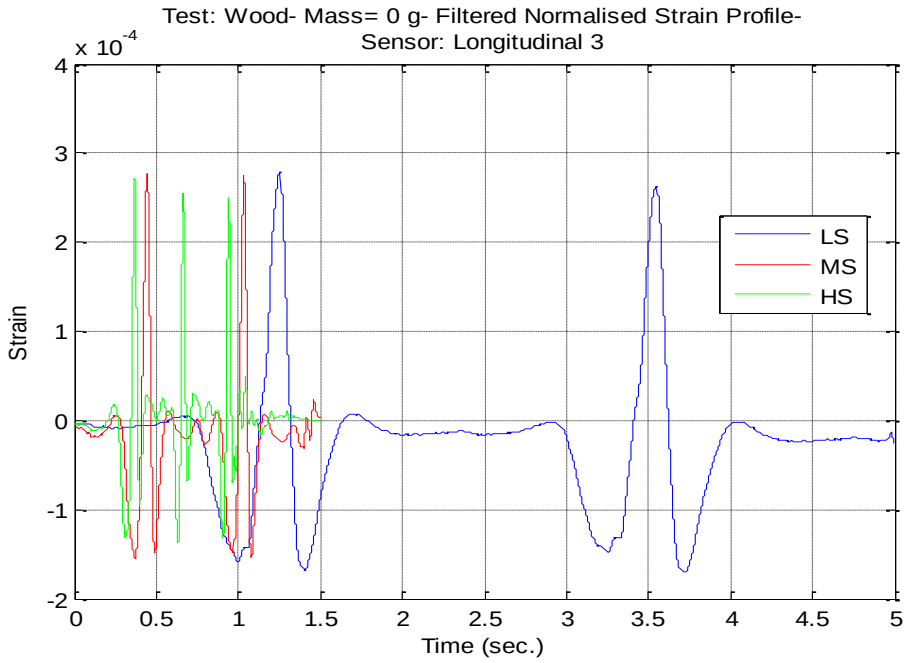

(a) Strain readings with respect to time.

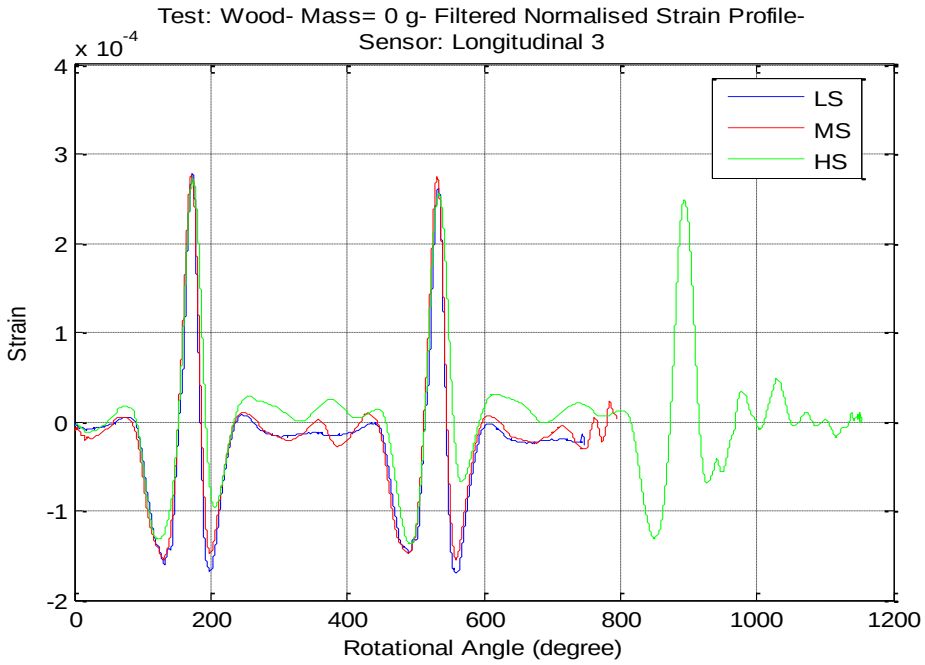

(b) Strain readings with respect to rotational angles.

Figure 5.5: Sensor readings in tests with different angular velocities

(Sensor: Longitudinal 3, LS = Low Speed (3.50 rad./sec. = 33.42 RPM),

MS = Medium Speed (6.65 rad./sec. = 63.50 RPM),

HS = High Speed (12.20 rad./sec. = 116.50 RPM), F_z = 0 N).

The point where the tyre's cart hit the shims at the end of the rail can be located in the strain waveform by identifying the beginning of a region that has a different shape compared to the previous wave cycles. Figure 5.6 illustrates this using the readings of a sensor during the high-speed test. The different region is enclosed by two red lines. It starts from a rotational angle of around 952° (232° in the third cycle). This distinctive area is recognised by several, adjacent, high-value spikes because the impact of hitting the shims made the tyre bounce up and down on the board.

As it was explained, two wave cycles are generated when the tyre travels the full track. In addition, the part where the cart hit the shims at the track's end is identified in Figure 5.6. Based on these two observations, it can be concluded that the tyre has span before reaching the end of the track. In other words, the part from the end of the second cycle to the point where the cart hit the shims represents spinning before the track's end. This part is similar in shape and strain values to the previous cycles. Thus, it is concluded that the same strain measurements are produced whether the tyre is rolling on the board or spinning on a spot.

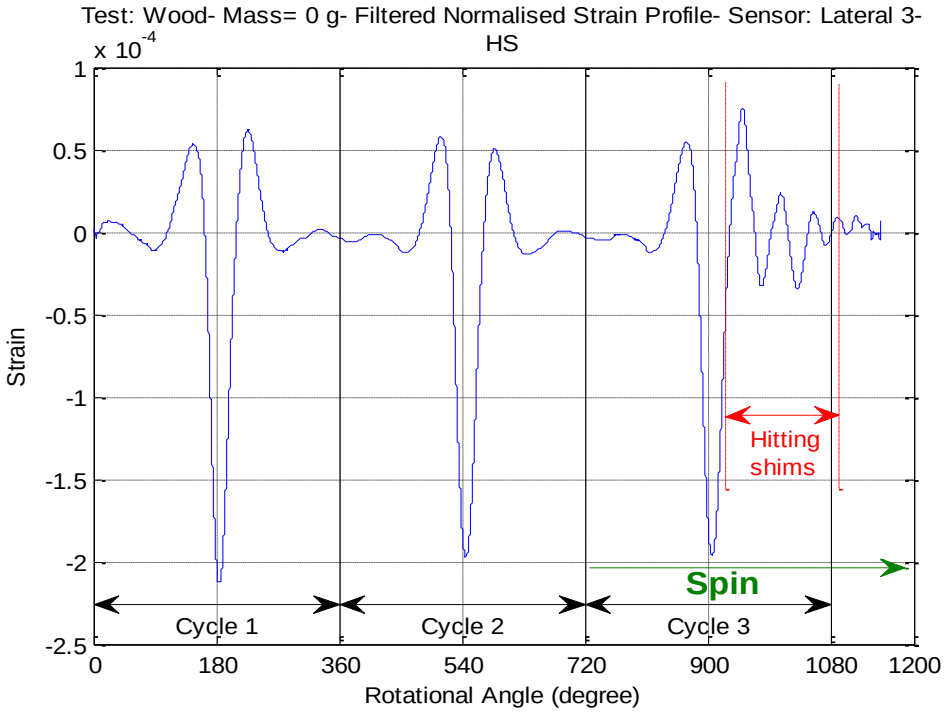

Figure 5.6: Spin region in the sensor's readings in a high-speed test (Sensor: Lateral 3, HS = High Speed (12.20 rad./sec. = 116.50 RPM), F_z = 0 N).

The strain rate is examined to study the difference between the normal strain cycles (cycles 1 and 2) and the spin cycle (cycle 3). Figure 5.7 presents the first derivative waveform for the strain profile in the high-speed test. It shows that the rate of change during spinning is similar to the other cycles except for the part enclosed by two red lines. This part represents the derivative during the vertical movement of the cart, i.e. when the tyre bounced up and down after hitting the shims. Within this part, the first derivative changes sign frequently because the strain values in the original profile are repeatedly increasing and decreasing.

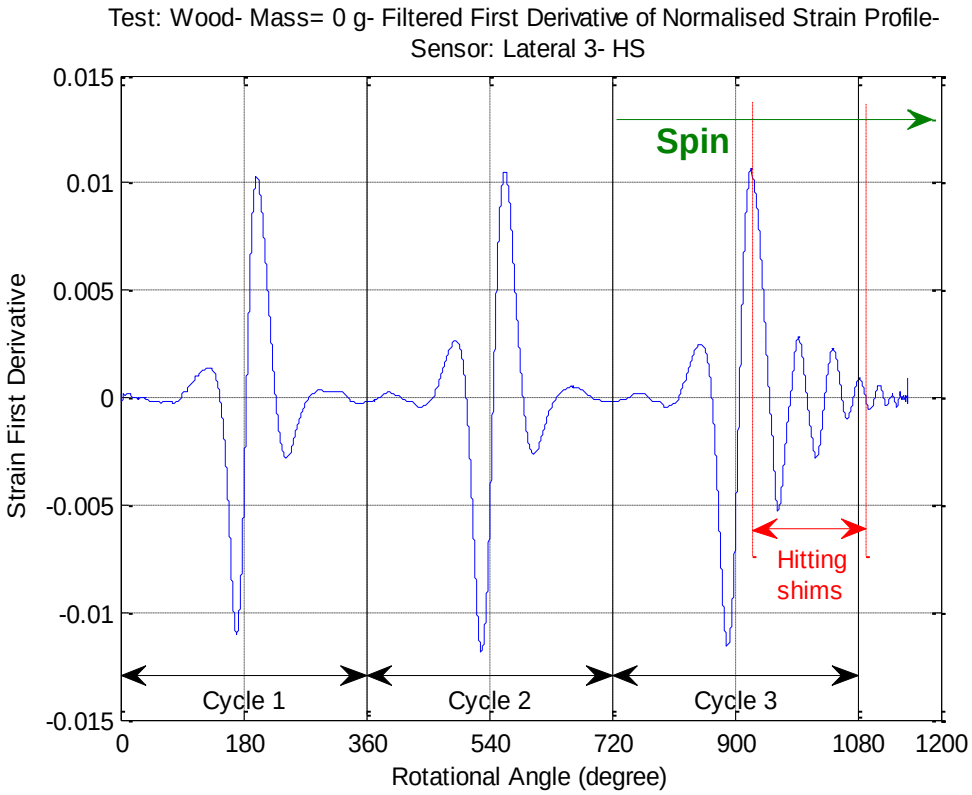

Figure 5.7: First derivative of strain profile in a high-speed test
(Sensor: Lateral 3, HS = High Speed (12.20 rad./sec. = 116.50 RPM), F_z = 0 N).

5.2.2 Effect of vertical load

The effect of increasing the vertical load (F_z) on the operation of detecting spin and obstacles by the strain sensors is examined. Figure 5.8 shows the strain profiles acquired by a sensor for four values of the vertical load. The distinctive part that indicates hitting the shims at the rail's end is seen in the four profiles (the part between

two red lines). It is also noticed that increasing the vertical load led to decreasing the tyre spins at the end of the track. This can be seen in the last part of the waveforms where the strain profiles became shorter as the wheel load increased.

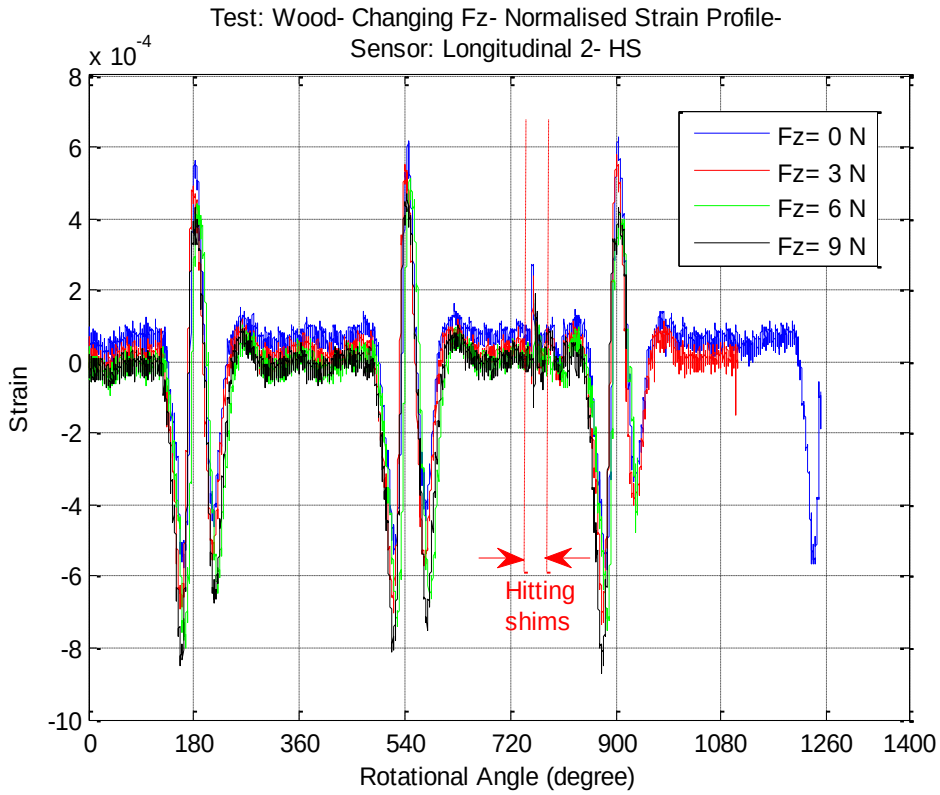

Figure 5.8: Strain waveforms at different wheel loads
(Sensor: Longitudinal 2, HS = High Speed (12.20 rad./sec. = 116.50 RPM)).

To decide the start of the spinning phase at the end of the track, the strain readings that correspond to hitting the shims are closely analysed. Figure 5.9 zooms in on these readings for the four values of the load. It is observed that the tyre started spinning at a higher rotational angle with higher wheel loads. This means that increasing the vertical load on the tyre resulted in delaying the spin phase at the end of the track.

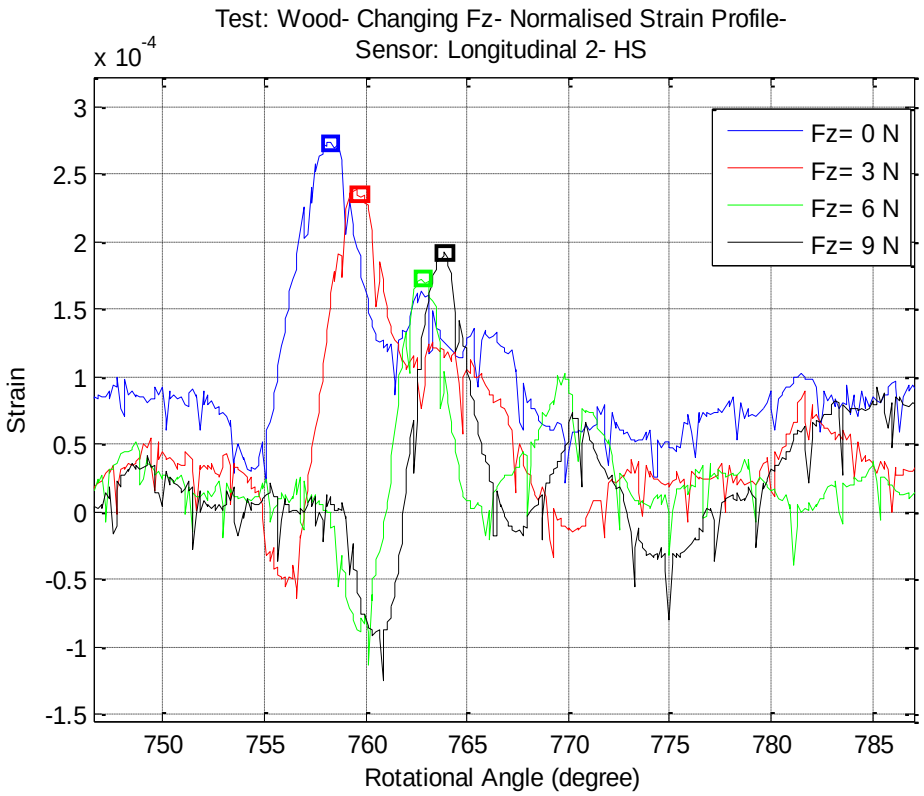

Figure 5.9: Strain waveforms at different wheel loads (zoomed in)
(The boxes represent the start of tyre spinning after hitting the shims).
(Sensor: Longitudinal 2, HS = High Speed (12.20 rad./sec. = 116.50 RPM)).

The observations that increasing the vertical load causes a reduction in the number of the spins and a delay for the start of the spinning phase indicate that loading the tyre increases its grip. Table 5.2 summarises these two points by comparing the rotational angles for the start of the spinning and the angles for the entire waveform for the strain profiles resulted when applying the four values of the wheel loads.

Table 5.2: Effect of F_z on tyre spinning.

F_z (N)	Angle for the start of spinning (degree)	Angle at the end of the test (degree)
0	758.3	1249.5
3	759.8	1108.1
6	762.8	935.8
9	763.9	918.7

The conclusions extracted from the strain measurements showed that the in-tyre sensors could identify the presence of the obstacles (the shims) regardless of the amount of the applied vertical load. In addition, it suggested that loading the tyre enhances its ability to grip the road. This information can be utilised to build a better comprehension of the correlation between the wheel load and the rotation of the tyre. One possible aspect of exploiting this comprehension is the design of speed controllers that accurately account for this correlation.

5.2.3 Effect of the contact surface

The detection of the spin and obstacles utilising the readings of the strain sensors was assessed for different contact surfaces. Figure 5.10 shows the readings of one of the sensors for the tests with these surfaces. It is seen that all these readings contain the distinctive region that represents the measurements when the cart hit the shims at the end of the rail. This region is enclosed by two red lines in the graphs. This indicates that the texture of the contact surface did not impair the capability of the strain sensors in identifying the obstacles.

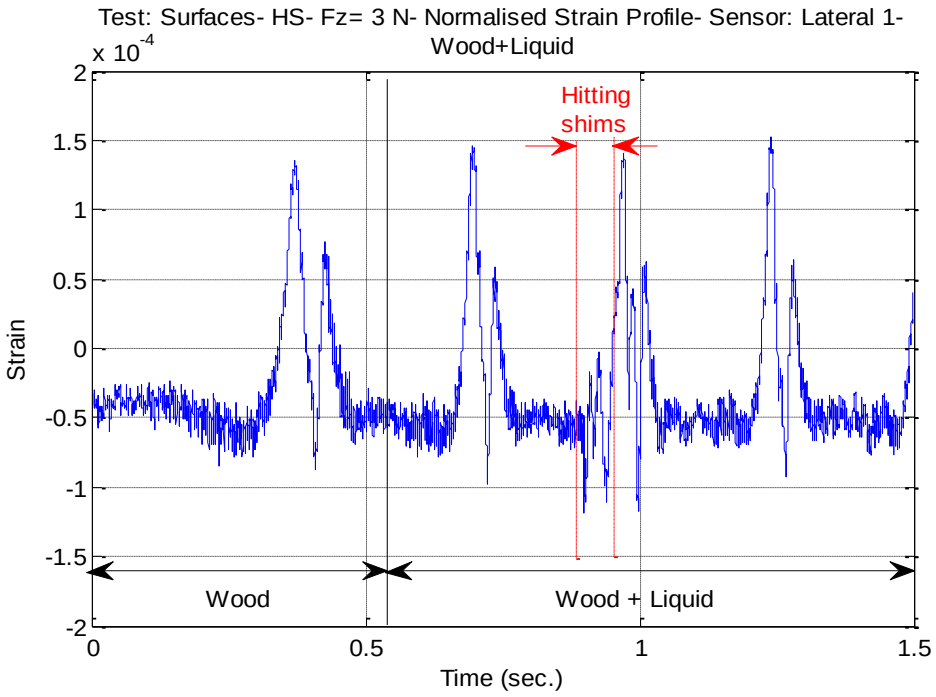

(a) Wood+ Liquid.

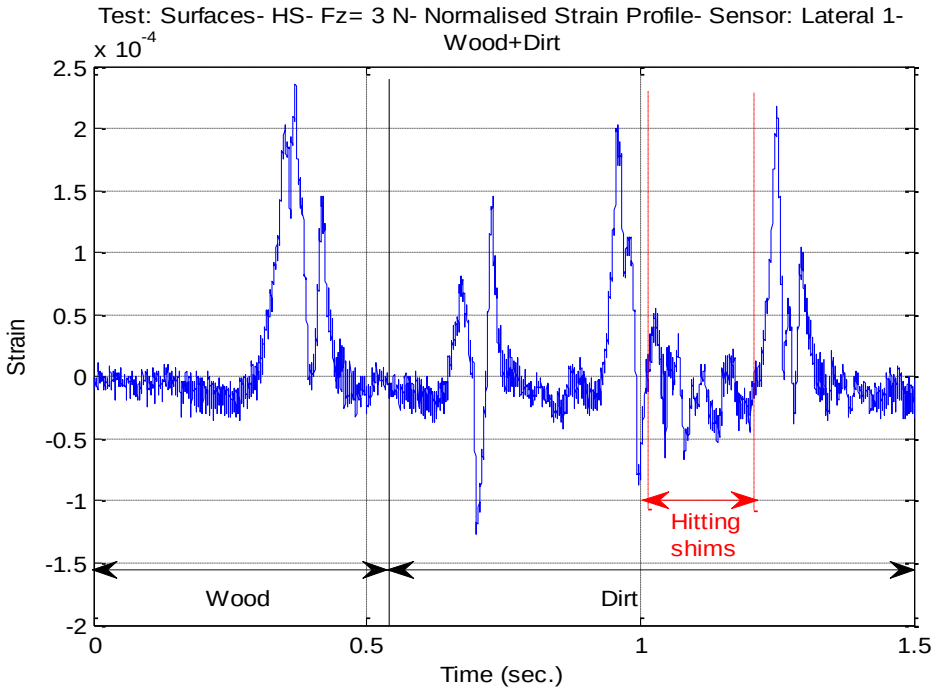

(b) Wood+ Dirt.

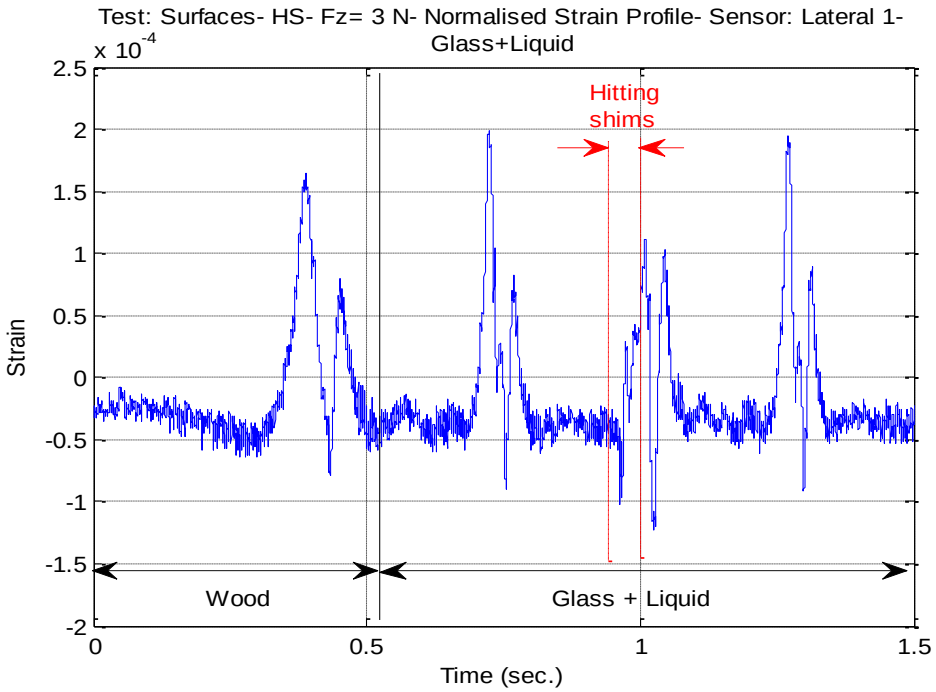

(c) Glass+ Liquid.

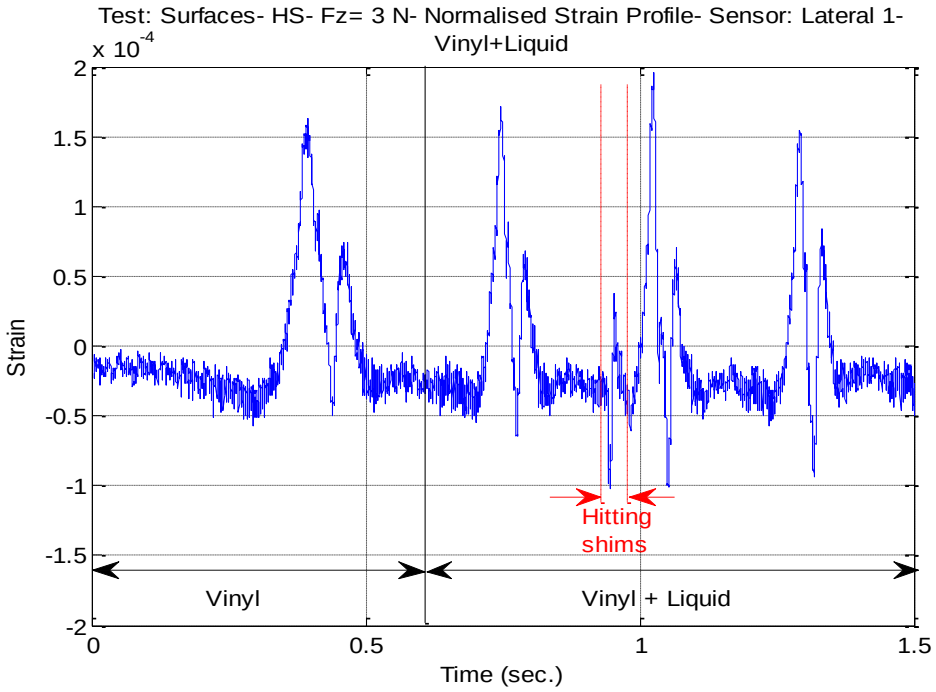

(d) Vinyl+ Liquid.

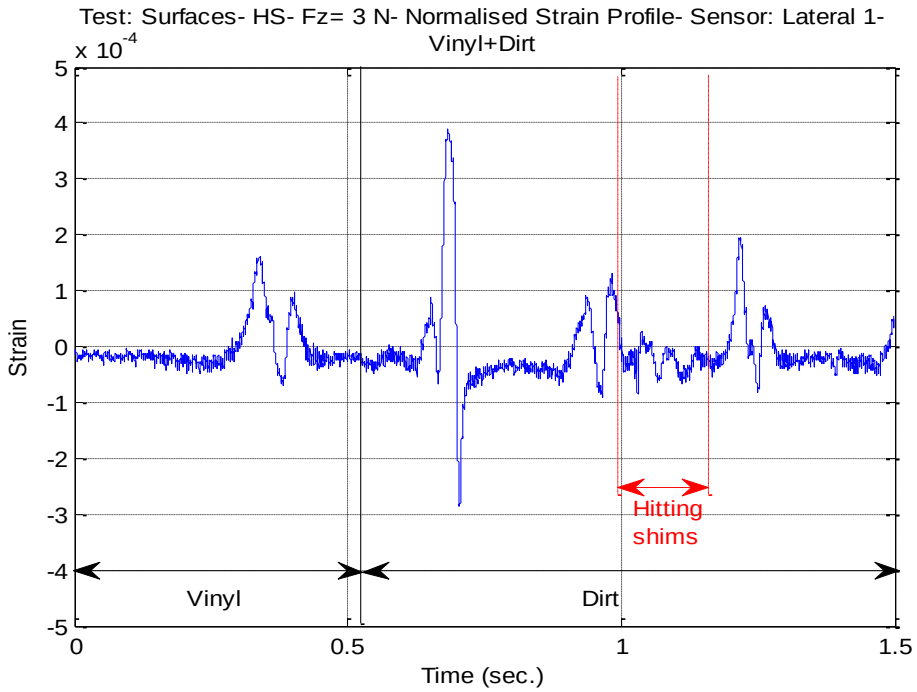

(e) Vinyl+ Dirt.

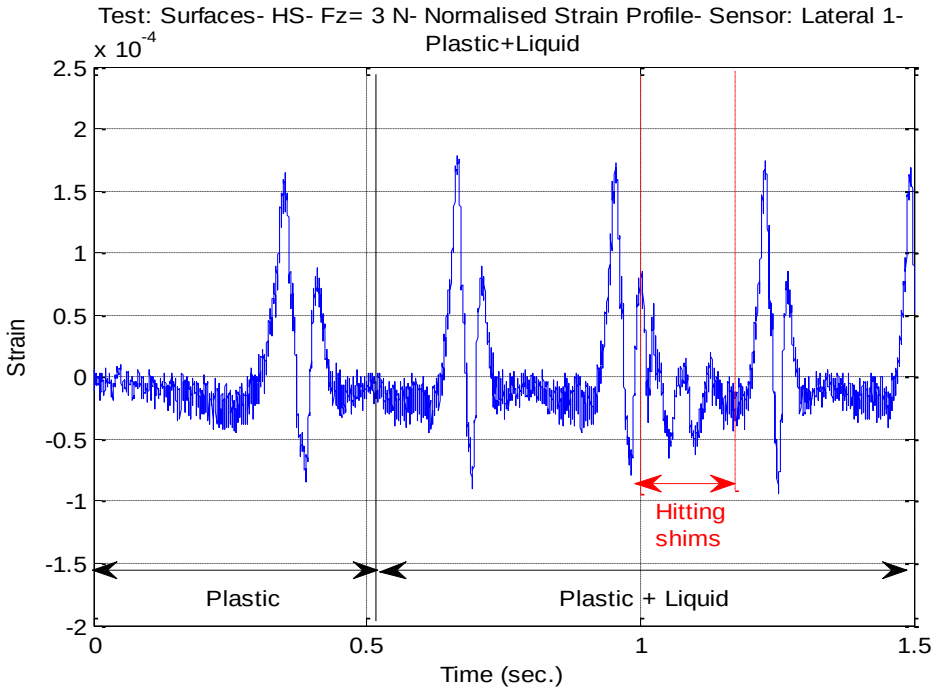

(f) Plastic+ Liquid.

Figure 5.10: Sensor readings in different test cases (different surfaces)

(Sensor: Lateral 1, HS = High Speed (12.20 rad./sec. = 116.50 RPM), F_z = 3 N).

The readings obtained when using (wood + liquid) are considered the default case. The other surfaces are compared to this default case to identify any variation in the strain profiles. Figure 5.11 presents an example of these comparisons. It overlaps the (wood + dirt) case and the default case and zooms in on the segment when the cart hit the shims. The lines represent the point when the cart hit the shims in the two cases. It is seen that the tyre hit the shims earlier in the (wood + liquid) case. This means that the tyre rotated more before hitting the shims in the (wood + dirt) case.

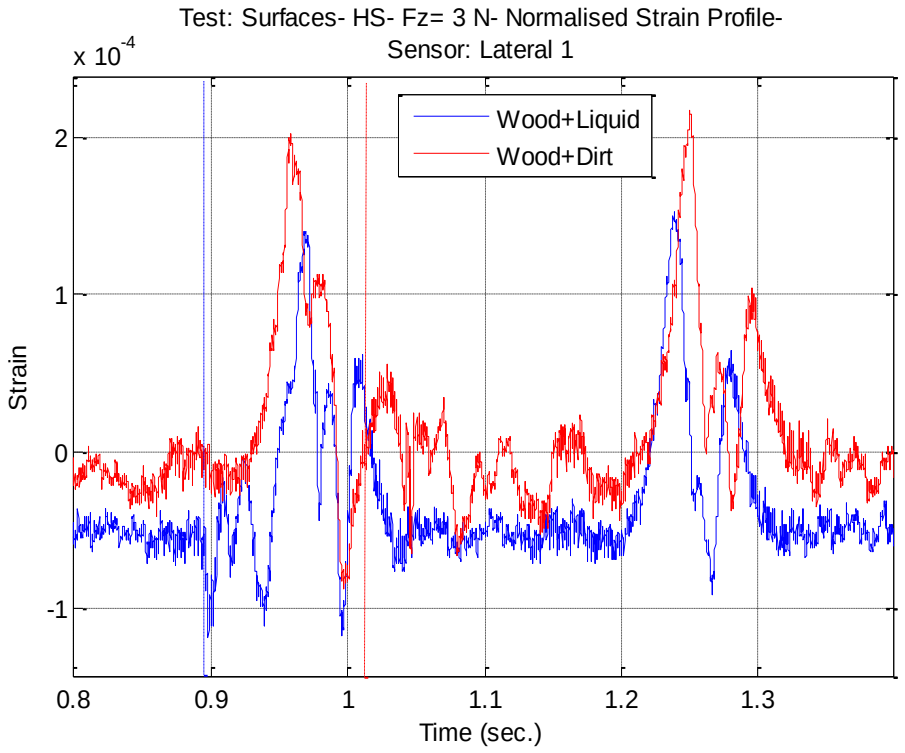

Figure 5.11: Comparing a segment of the strain profiles produced with two cases (wood + liquid vs. wood + dirt) for a sensor. The lines represent the point where the cart hit the shims (a blue line for the (wood + liquid) case and a red line for the (wood + dirt) case.

A further discussion on the effect of the contact surfaces on the readings of the in-tyre sensors is presented herein using the data of the (plastic + liquid) case. Figure 5.12 shows the readings of the sensors for this case. The surface was very smooth; hence, the tyre made many revolutions, i.e. it spun, during its movement. The part between the two red lines in the graphs (between 1.017 sec. and 1.167 sec.) represents the strain readings when the tyre's cart hit the shims at the end of the path. Hitting the shims caused the cart to reverse while the tyre bounced vertically and continued to rotate.

Identifying this part in the readings of the sensors is useful for three reasons. First, it indicates the beginning of tyre spinning at the end of the path. Second, it reveals whether the tyre has made extra revolutions before reaching the end of the path. It is known that only two tyre revolutions are required to travel the path. In the presented graphs, there are three revolutions before this part. This means that the tyre made one extra revolution before the cart hit the shims. Third, it shows which sensors gave more accurate measurements. To explain, this part can be clearly noticed in the readings of all the sensors except the middle sensor, called Lateral 2. This sensor is placed laterally on a position where the tread design on the outer surface consists of a thin rubber strip surrounded by grooves. This tread arrangement prevents this sensor from stretching or compressing in a manner that correctly corresponds to the strain resulted after hitting the shims. Therefore, the middle sensor could not provide clear signs that the tyre has hit an obstacle.

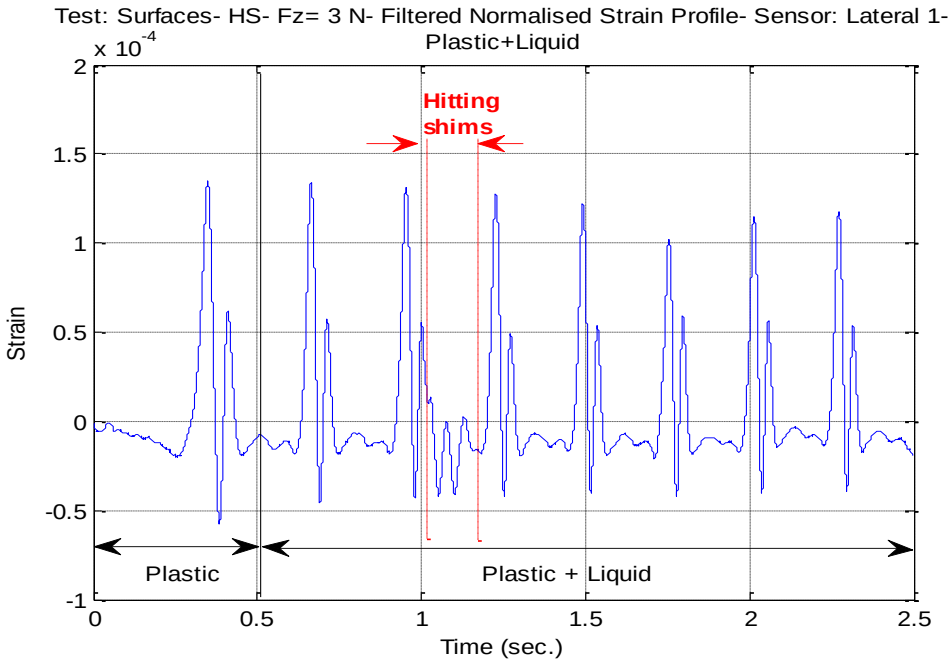

(a) Sensor: Lateral 1.

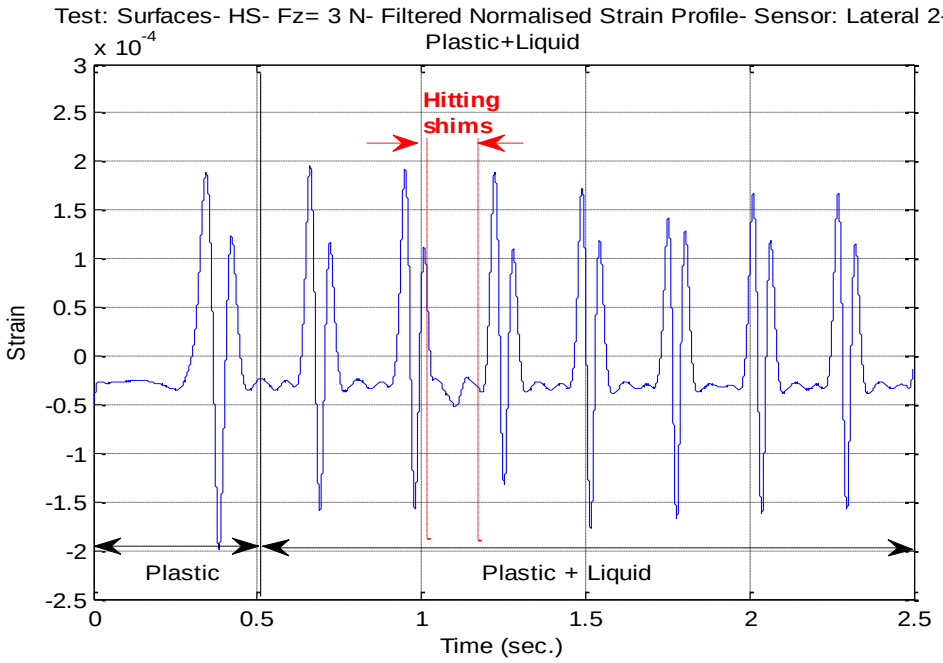

(b) Sensor: Lateral 2.

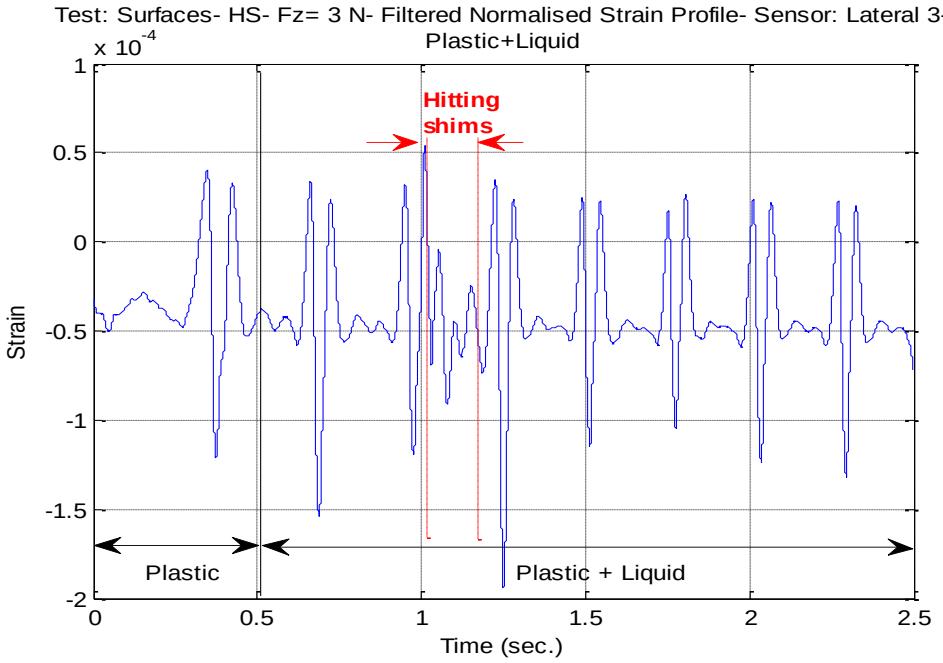

(c) Sensor: Lateral 3.

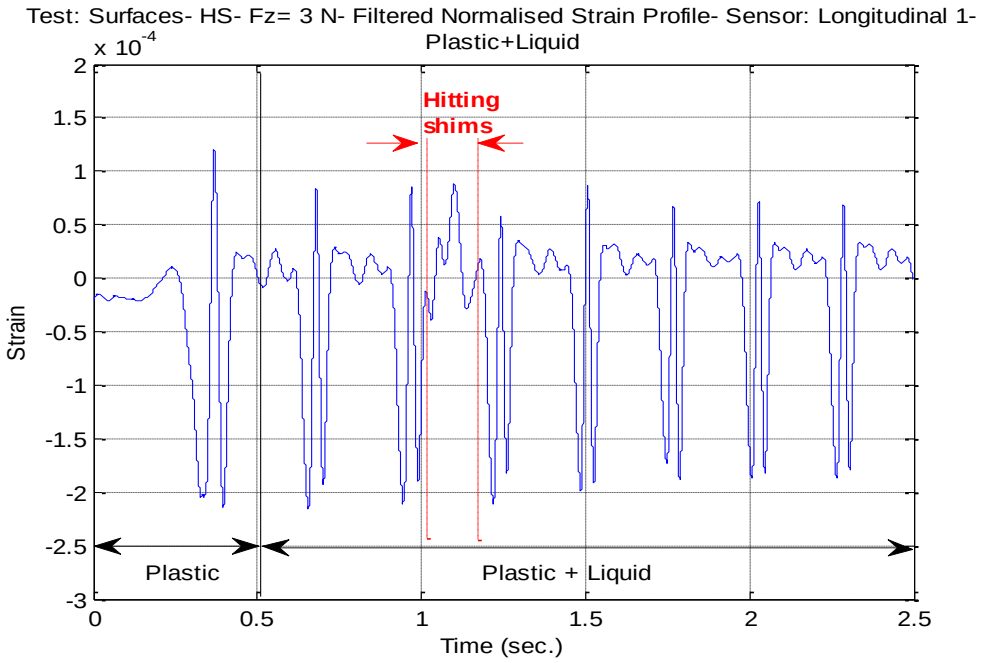

(d) Sensor: Longitudinal 1.

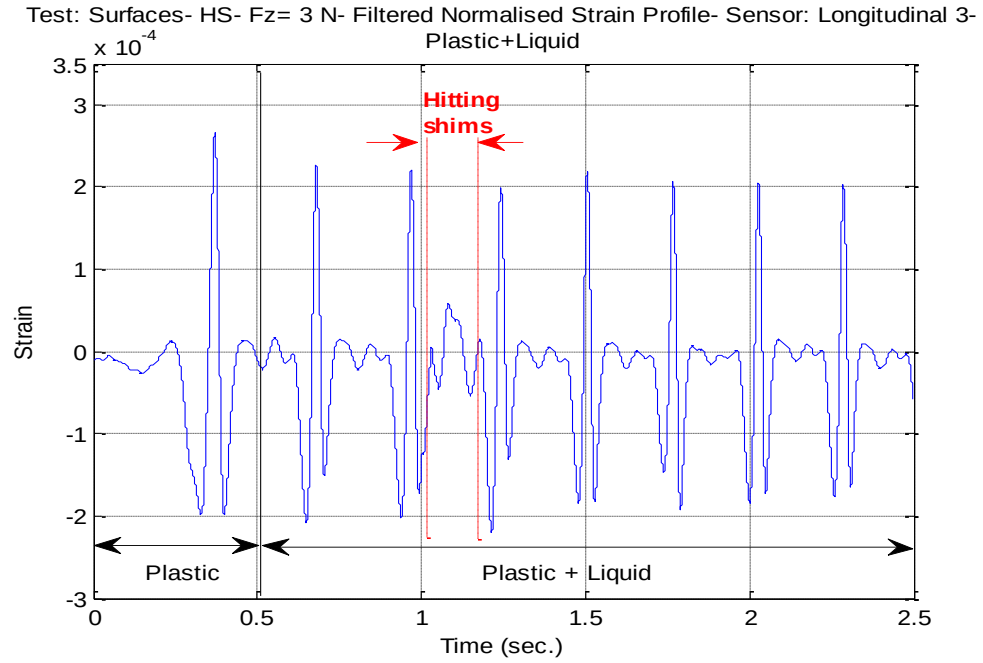

(e) Sensor: Longitudinal 3.

Figure 5.12: Sensors' readings with Plastic+ Liquid

(Longitudinal 2 is not presented because it has malfunctioned).

(HS = High Speed (12.20 rad./sec. = 116.50 RPM), F_z = 3 N).

To investigate how changes in speed affect the sensors' readings during spin incidents, the tyre speed was changed during its run. This type of tests is presented here with results obtained by using the (plastic+ liquid) surface and considering the cases where the speed was changed from a low to a high level. The spin possibility was the highest with this surface and with this change in speed levels.

To locate the point where the change in speed started, readings of the motor's encoder (steps' readings), and/or current sensor can be used. It should be mentioned here that the National Instruments system used for data acquisition did not allow the collection of all voltage readings (the maximum voltage value that could be collected was 10.6 V); therefore, the voltage measurements could not be used for identifying the change in speed. Figure 5.13 shows that the voltage curve saturates at around 1.753 sec. whereas the readings of the current sensor (Figure 5.14) and the encoder (Figure 5.15) illustrate a variation in the measurements beyond this point.

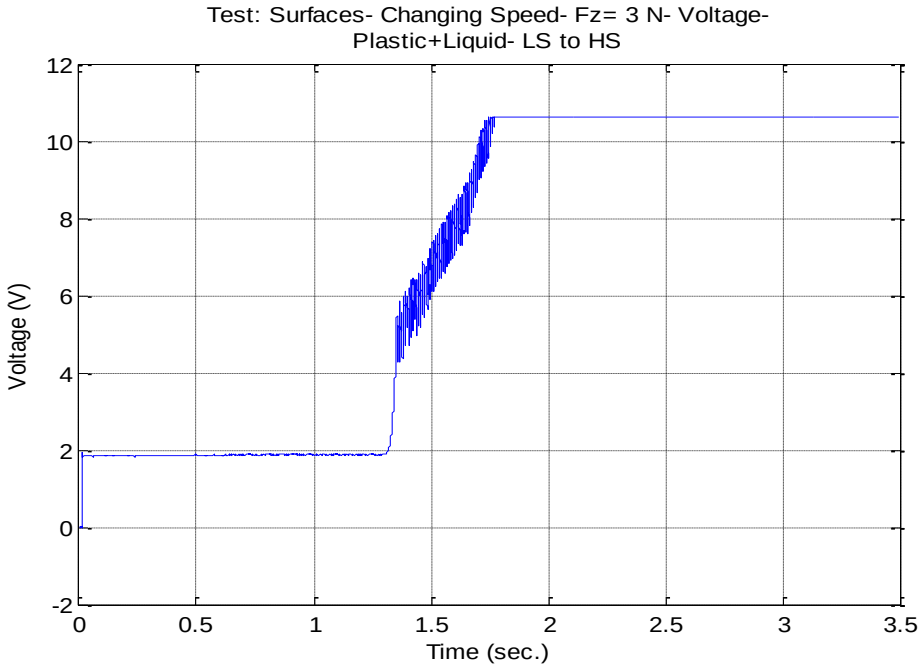

Figure 5.13: Voltage readings with respect to time in a variable-speed test
(LS = Low Speed (3.50 rad./sec. = 33.42 RPM),
HS = High Speed (12.20 rad./sec. = 116.50 RPM), F_z = 3 N).

The readings of the current sensor during the variable-speed test are shown in Figure 5.14. Three regions can be identified in this figure. The first region reflects the

measurements during the low-speed phase. The second region represents the transit phase between the low and high-speed regions. As mentioned earlier, the change in speed was gradual and this is seen in the current measurements within the transit phase. Finally, the third region indicates that the speed levelled out at the high-speed phase. Similarly, the steps' readings (Figure 5.15) consists of these three regions, which can be recognised by locating two acceleration points in the graph.

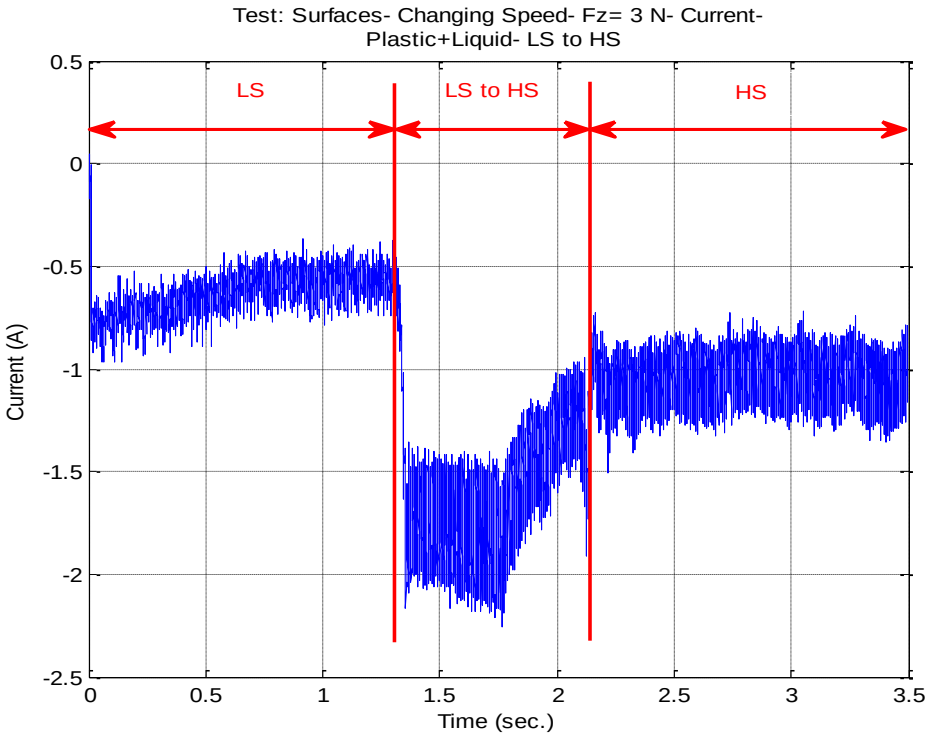

Figure 5.14: Current readings with respect to time in a variable-speed test
(LS = Low Speed (3.50 rad./sec. = 33.42 RPM),
HS = High Speed (12.20 rad./sec. = 116.50 RPM), F_z = 3 N).

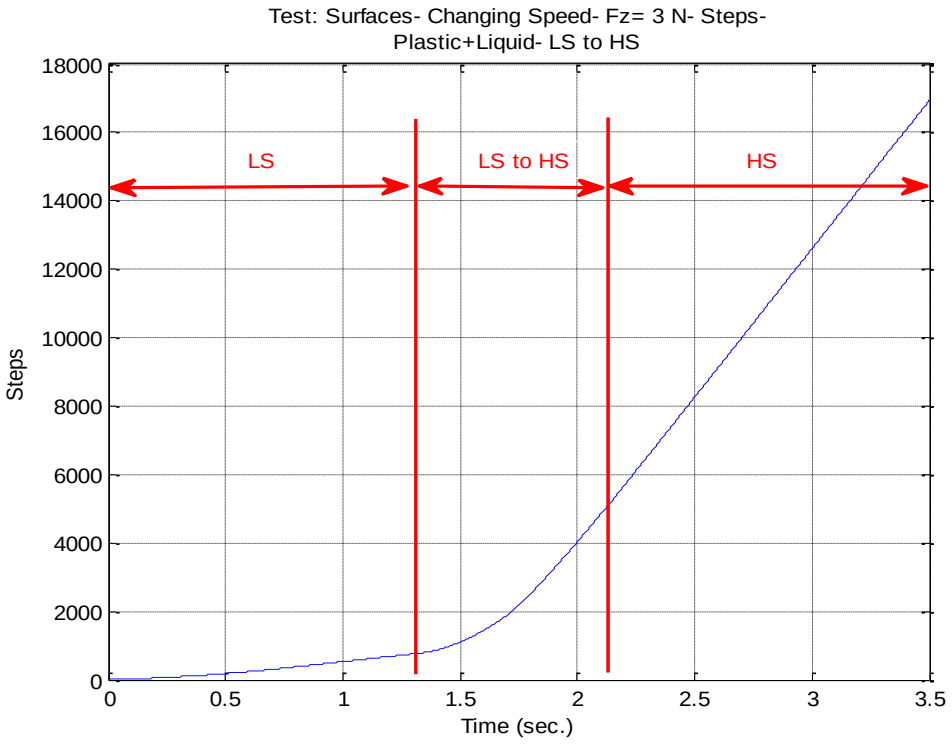

Figure 5.15: Steps' readings with respect to time in a variable-speed test
(LS = Low Speed (3.50 rad./sec. = 33.42 RPM),
HS = High Speed (12.20 rad./sec. = 116.50 RPM), F_z = 3 N).

The reading of one of the sensors during one of these variable-speed tests is presented in Figure 5.16. The speed was changed at a point where the sensors became close to the centre of the contact patch. This was done to maximise the chances that the readings would reflect the effect of this speed variation.

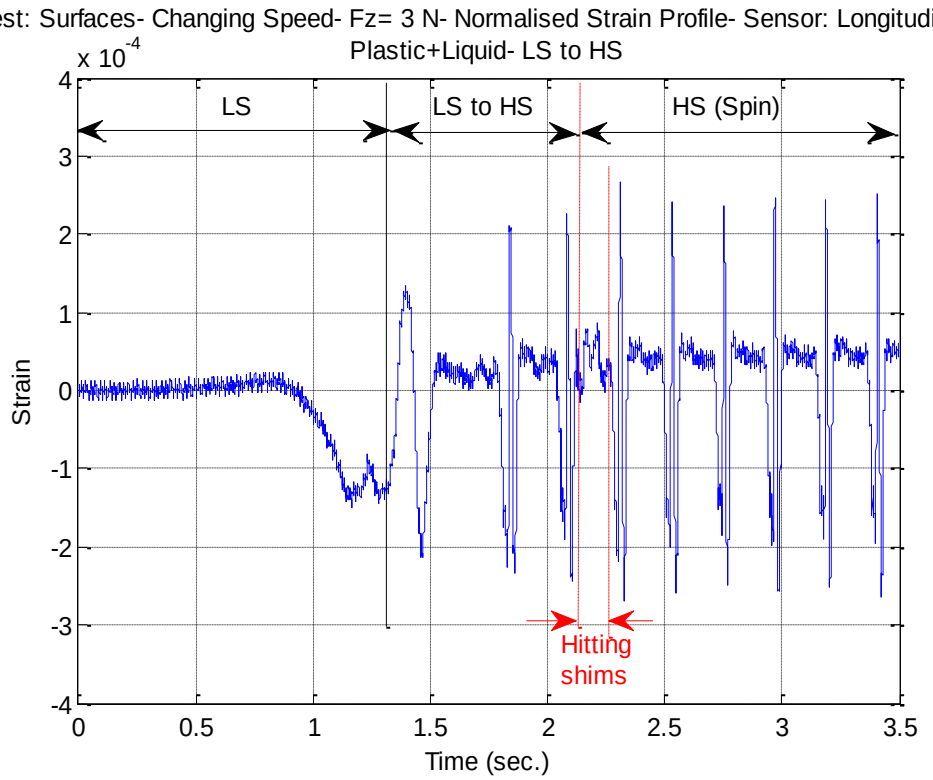

Figure 5.16: Strain profile for a sensor with respect to time in a variable-speed test (Sensor: Longitudinal 1, LS = Low Speed (3.50 rad./sec. = 33.42 RPM), HS = High Speed (12.20 rad./sec. = 116.50 RPM), F_z = 3 N).

Since it is hard to follow the strain changes when the readings are plotted with respect to time, the x-axis in Figure 5.16 was changed to rotational angles in degrees in Figure 5.17.

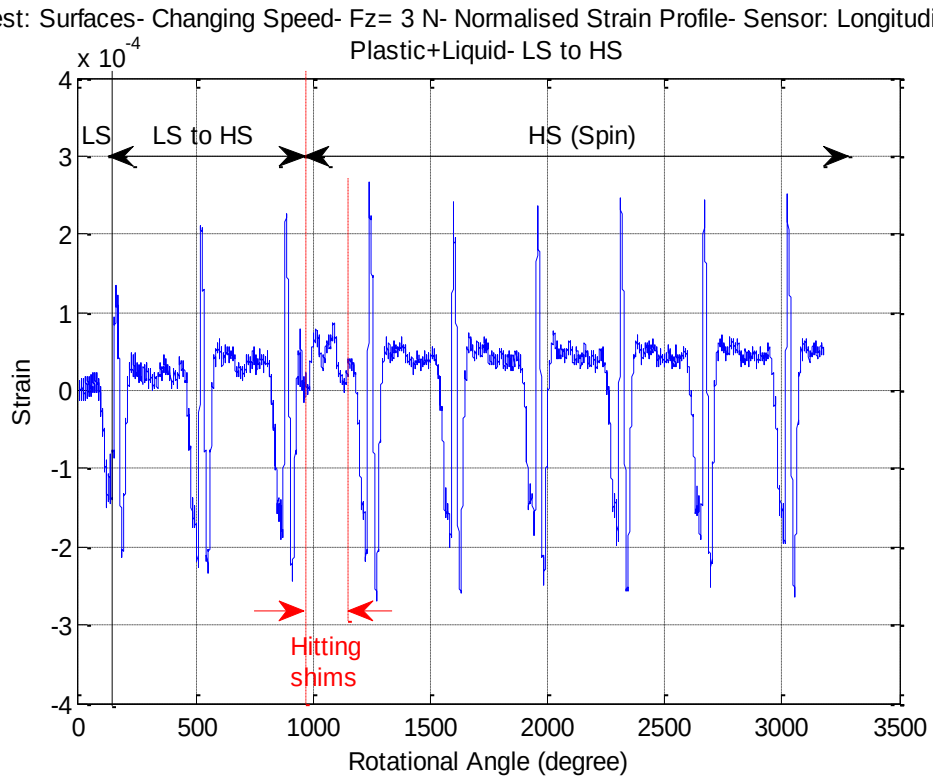

Figure 5.17: Strain profile for a sensor with respect to tyre rotational angle in a variable-speed test

(Sensor: Longitudinal 1, LS = Low Speed (3.50 rad./sec. = 33.42 RPM), HS = High Speed (12.20 rad./sec. = 116.50 RPM), F_z = 3 N).

Three points can describe the spin-related information in Figure 5.17. First, it can be noticed in the second region, which is the transit phase between low and high speed, that increasing the speed resulted in a gradual increase for the strain values. This is because the tyre was working harder to maintain a sufficient grip with the surface. Second, the readings indicate that the tyre made one extra revolution before reaching the end of its track. The last conclusion was drawn by locating the part that represents the measurements when the cart hit the shims at the track's end. This part is enclosed by two red lines in the graph. Third, the tyre made six revolutions (spins) after hitting the obstacle.

The effect of the speed change on the strain measurements was investigated more by comparing the readings obtained from the variable-speed tests and from the constant-speed tests, as shown in Figure 5.18. The surface is the same for the two tests presented

in the figure. The main difference is the gradual increase of the values at the tensile strain peaks within the second region in the variable-speed test. Other than this difference, the two readings are similar except for a slight difference in the strain values and in the measured angles. The difference in the strain can be attributed to a slight difference in the temperatures while conducting the two tests. The small shift in the angles can be caused by a slightly different starting position of the tyre in the tests. Thus, it is concluded that changing the speed of the tyre during its run has resulted in a gradual increase of the strain during the corresponding spin incidents.

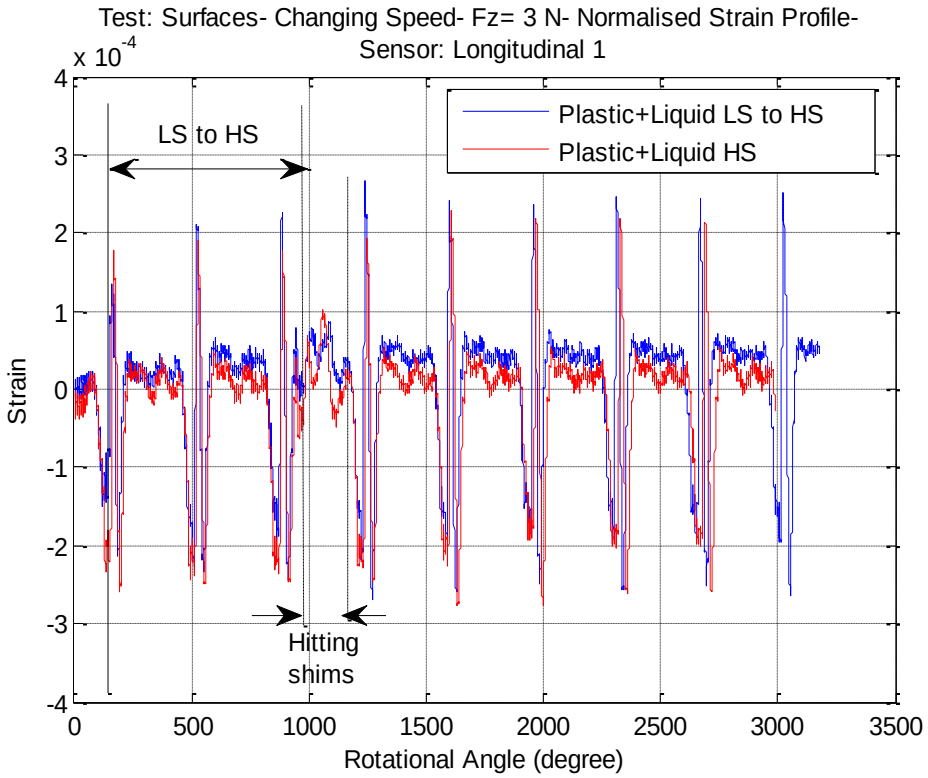

Figure 5.18: Comparing strain profiles produced with two speeds' setting (constant speed and changing speed) for a sensor in the (Plastic+ Liquid) case (Sensor: Longitudinal 1, LS = Low Speed (3.50 rad./sec. = 33.42 RPM), HS = High Speed (12.20 rad./sec. = 116.50 RPM), F_z = 3 N).

5.3 Summary

This chapter has examined the measurements of the in-tyre strain sensors for slip, spin, and obstacle detection. The slip detection was investigated using the readings collected from the static tests on the first rig. It was shown that the strain measurements contain indications for two states of slip: partial and full slip. The partial slip was identified in the relationship between the longitudinal load and the strain readings as a small region of minor oscillations. The full slip region is larger and contains oscillations with higher strain values. In the full slip region, the strain values oscillate between a steady state limit and a saturated limited due to the effect of the deformation of the rubber material and foam in the non-pressurised tyre. It was illustrated that all the sensors could estimate the value of the longitudinal force that initiates the full slip state. The sensors provided close estimations under different values of vertical force.

The spin and obstacle detection were explored utilising the strain measurements acquired in the dynamic tests conducted on the second rig. The key for the spin detection was locating a segment with different features within the strain measurements. This segment represents the readings resulted from the impact of hitting the shims (the obstacle) at the end of the rig. This impact caused the tyre to bounce; therefore, corresponding spikes appeared in the strain profile. Since it is known that the tyre used in the tests travels the full track on the rig by completing two revolutions, the spin can be determined by counting the number of wave cycles with respect to the mentioned segment. It was concluded that the in-tyre strain sensors produced similar waveforms whether the tyre is running on the board or spinning on a spot.

The ability of the sensors to identify the spin and the obstacles was examined for different angular velocities, vertical loads, and contact surfaces. The following points summarise the main effects of these variables on the strain measurements:

- With higher angular velocities, extra revolutions were generated because the high momentum of the tyre caused it to continue rotating after the cart hit the shims at the track’s end.

- Higher vertical loads resulted in lagging the start of the spin and decreasing the number of tyre spins after hitting the shims.

- The strain measurements contained an indication of hitting the shims regardless of the contact surface. This means that the contact surface did not affect the obstacle detection using the in-tyre strain measurements.

- Increasing the speed of the tyre during its run resulted in a gradual increase in the strain values for the spin cycles.

The information extracted from the in-tyre strain sensors can be utilised for more accurate positioning and control for robots. The estimation of slip using the strain measurements can be used to correct the encoder readings. Therefore, the in-tyre strain sensors can complement the wheel encoder to build reliable positioning systems. In addition, the in-tyre strain data can be employed to design optimum controllers for the robot. These controllers can exploit the strain information to accurately address the effects of the obstacles, rotational speed, wheel load, and contact surface on the robot's motion.

Chapter 6

Surface Identification

The ability of the in-tyre sensors to identify traversed surfaces is examined in this chapter. Since the tyre reacts differently to different surface materials, the deformations of the tyre rubber are different on each surface. Accordingly, the resulting strain waveforms are examined for any indications of traversing different surfaces. The sensors' data are used to profile the surfaces more accurately or to indicate that the traversed surfaces are changing. These sensors can provide more reliable predictions about the surfaces when compared to visual sensors. To clarify, some surfaces have textures that may not be accurately described with visual data. For example, there is vinyl that looks like wood, carpet that looks like wood, carpet or rug that looks like gravel, etc. In such cases, the robots' cameras may not provide correct information about the surface. Therefore, identifying the surfaces with the tactile data from the in-tyre sensors is much better. In addition, these sensors can supply more details about the true nature of the surface. For instance, they can detect how slippery the surface is. The robot can utilise this additional detail about the surface to adjust its movement accordingly.

Several surfaces were utilised to study this property in the dynamic tests as presented in Section 3.3.6. The second half of the track was covered with a surface. Therefore, the first cycle in the strain profiles presented in this chapter represents the sensors' readings when the tyre was travelling the control surface (wood). The other wave cycles reflect the strain measurements while traversing the second surface. The tested surfaces are classified into two groups: rough surfaces (loop pile carpet, fake grass, and dirt (soil)), and smooth surfaces (vinyl, glass, and plastic (Ultra-high molecular

weight polyethylene (UHMWPE))). The chapter also presents the results of using the in-tyre measurements to identify the liquid surfaces. Finally, Section 6.3 discusses the identification of the contact surfaces by analysing the frequency content of the in-tyre strain profiles.

The sensors' readings that are analysed in this chapter were obtained from the experiments presented in Chapter 3. The following table links the sections of Chapter 6 to the sections that explained the required tests in Chapter 3.

Table 6.1: Linking the sections in Chapter 6 to the corresponding sections that described the experimental setup and tests in Chapter 3.

Sections in Chapter 6	**Associated sections that explained the experimental setup and tests' description in Chapter 3**
6.1 Identifying rough surfaces	3.3.6 Contact surface tests
6.2 Identifying smooth surfaces	3.3.6 Contact surface tests + 3.3.4 Slip/Spin tests
6.3 Using the frequency content of the strain waveforms to identify surfaces	3.3.6 Contact surface tests

6.1 Identifying rough surfaces

The tested rough surfaces were carpet, grass, and dirt. As mentioned, the tyre completed one revolution on the control surface of the rig (wood) then it rotated on the rough surface. Figure 6.1 shows the response of a lateral and a longitudinal sensor respectively when the tyre travelled over wood then carpet. It shows that the strain increased when the tyre moved on the rough surface. This increase suggests that the tyre was working harder on this gripping surface to avoid being stuck and to continue its movement. Similar results were seen for the other rough surfaces.

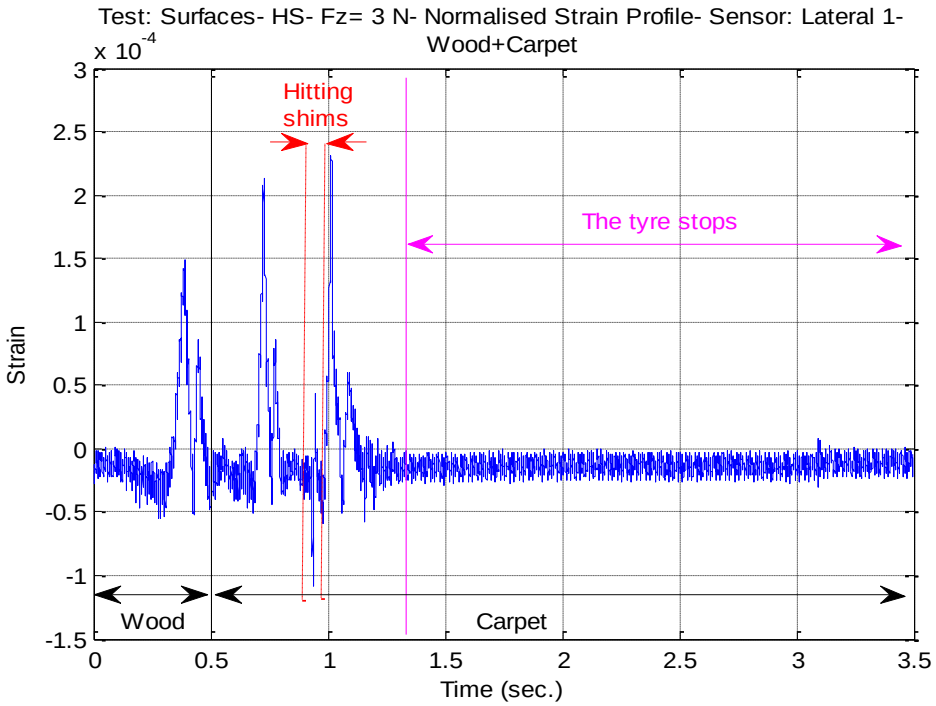

(a) Sensor: Lateral 1.

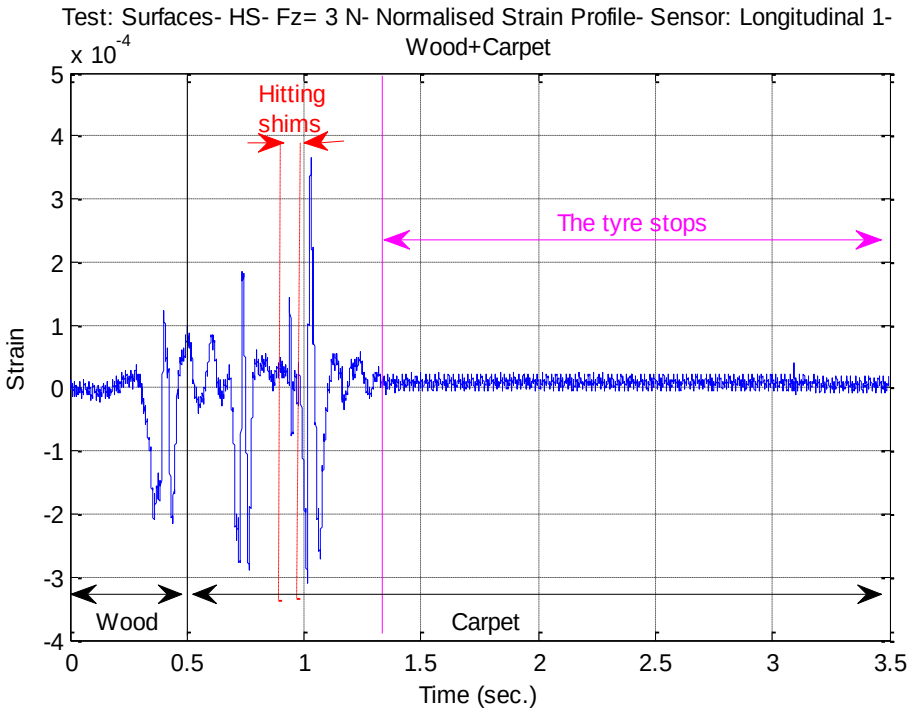

(b) Sensor: Longitudinal 1.

Figure 6.1: Using the strain sensors' readings to identify moving from wood to carpet (HS = High Speed (12.20 rad./sec. = 116.50 RPM), F_z = 3 N).

The readings of the current sensor showed a measurement change at the point where the tyre started rotating on the second surface. Starting from this point, the current value increased as seen in Figure 6.2. This shows that the tyre motor needed to pull more current in order to be able to move over the carpet, which has rough texture compared to the initial traversed surface (wood).

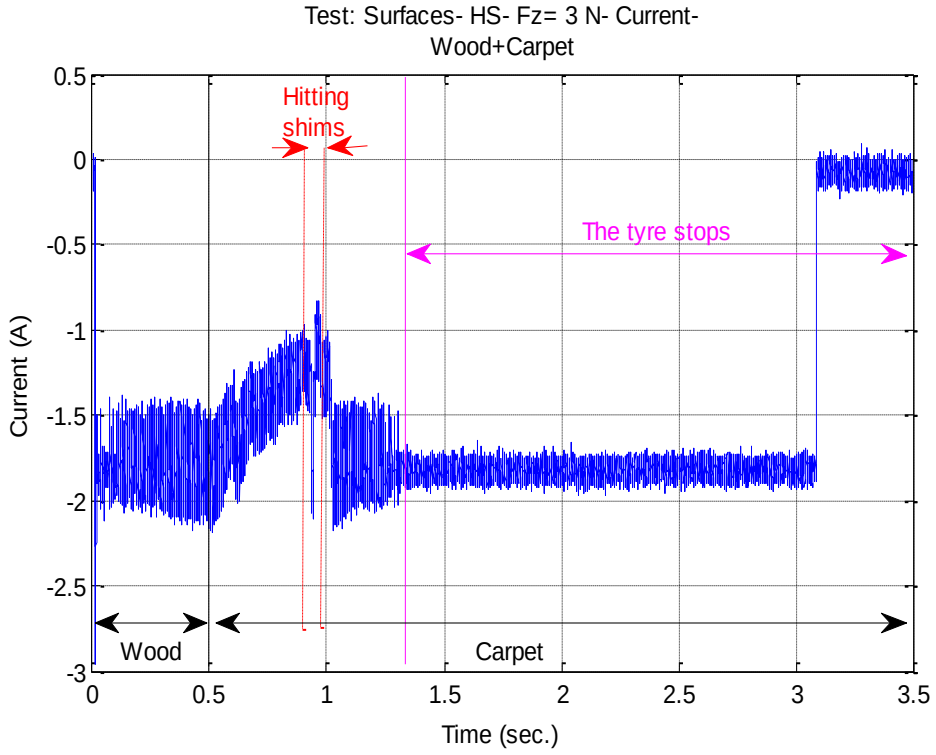

Figure 6.2: Verifying the results obtained from the strain sensors for moving from wood to carpet using the current sensor's reading
(HS = High Speed (12.20 rad./sec. = 116.50 RPM), F_z = 3 N).

The sensors' readings in the (wood + dirt) case are shown in Figure 6.3. Distorted strain profile was generated while moving on the dirt as compared to the wave shape resulted from moving on the wood. This difference was caused by the uneven surface of the dirt and the presence of gravel at some points. Therefore, the shape of the strain waveforms gives some indications about the nature of the traversed surface. Smooth waveforms are obtained with smooth surfaces whereas irregular waveforms correspond to travelling rough surfaces.

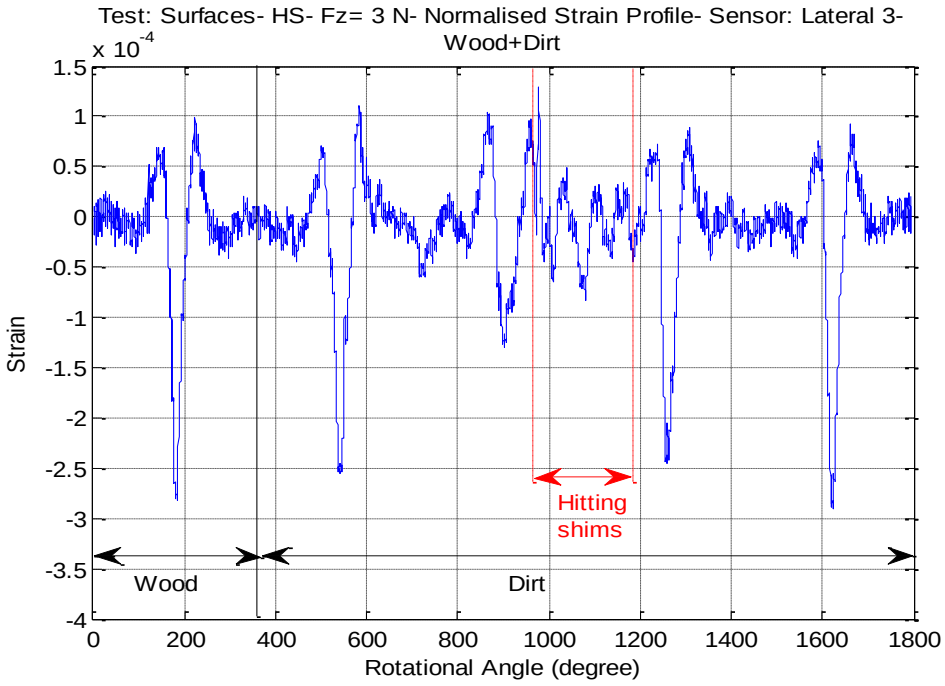

(a) Sensor: Lateral 3.

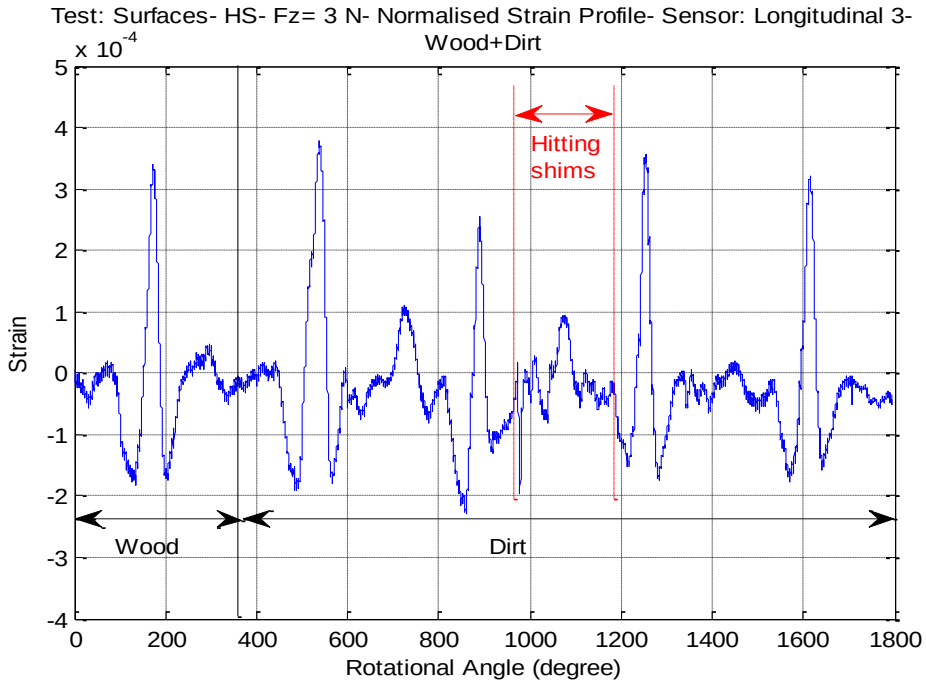

(b) Sensor: Longitudinal 3.

Figure 6.3: Using the strain sensors' readings to identify moving from wood to dirt (HS = High Speed (12.20 rad./sec. = 116.50 RPM), F_z = 3 N).

The effect of moving on the dirt on the strain measurements was examined in another test. The full track on the rig was covered with vinyl. The second half of this vinyl was then coated with the dirt. Figure 6.4 illustrates that the same observation and conclusion mentioned for the (wood + dirt) applied to the readings of the (vinyl + dirt) case. In addition, the presence of a big stone in the dirt caused a different waveform shape in the second revolution when compared to the first revolution.

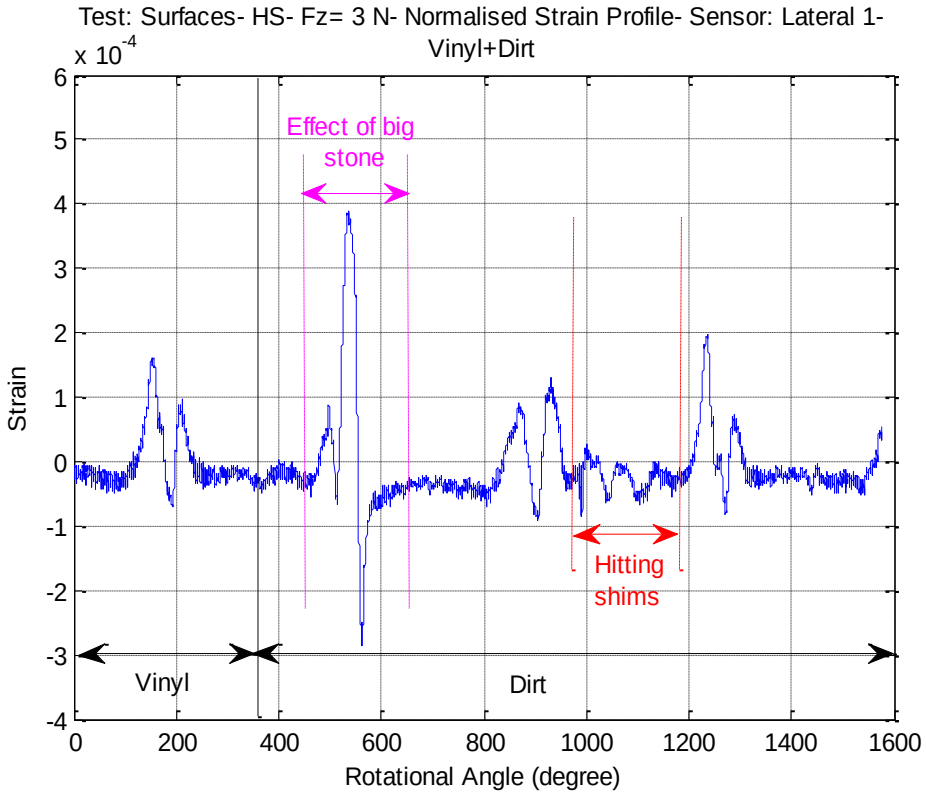

(a) Sensor: Lateral 1.

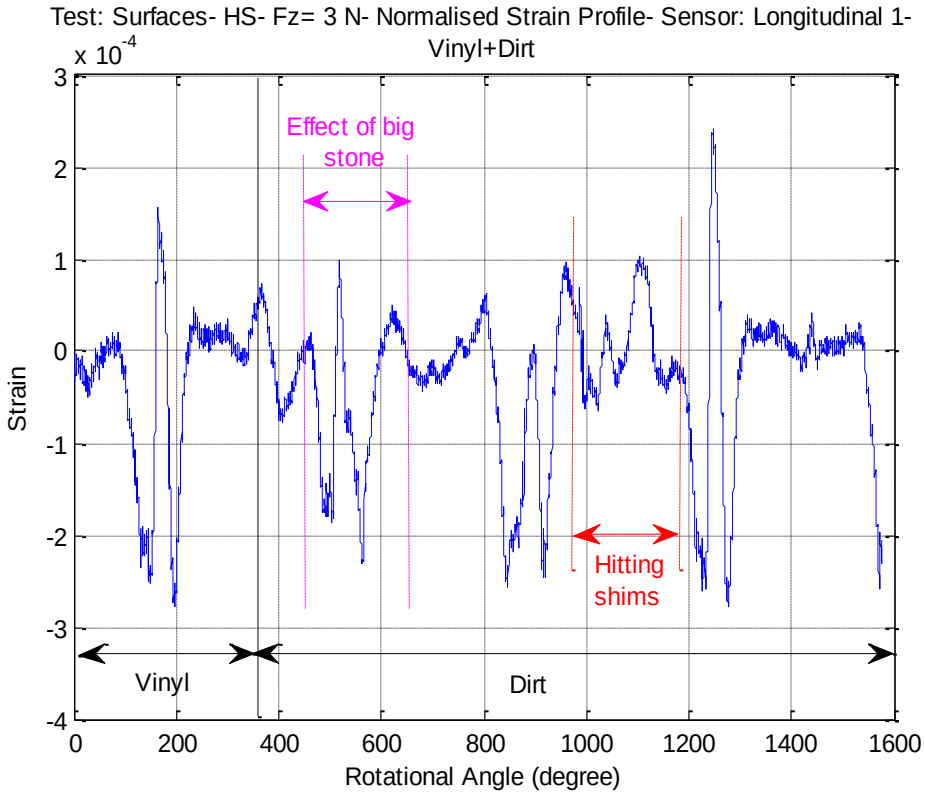

(b) Sensor: Longitudinal 1.

Figure 6.4: Using the strain sensors' readings to identify moving from vinyl to dirt (HS = High Speed (12.20 rad./sec. = 116.50 RPM), F_z = 3 N).

6.2 Identifying smooth surfaces

To test the smooth surfaces, the second half of the track was covered with vinyl or glass. The third tested surface was plastic. As presented in Section 3.3.6, the plastic sample was thick and therefore it was placed on the full track. Figure 6.5 presents the sensors' readings for the (wood + vinyl) case. The second surface (vinyl) had a texture that was not greatly different from the control surface (wood); consequently, there was a very small change in the strain value between the first and second cycles in the strain profiles. Likewise, small stain variations were observed for the other smooth surfaces.

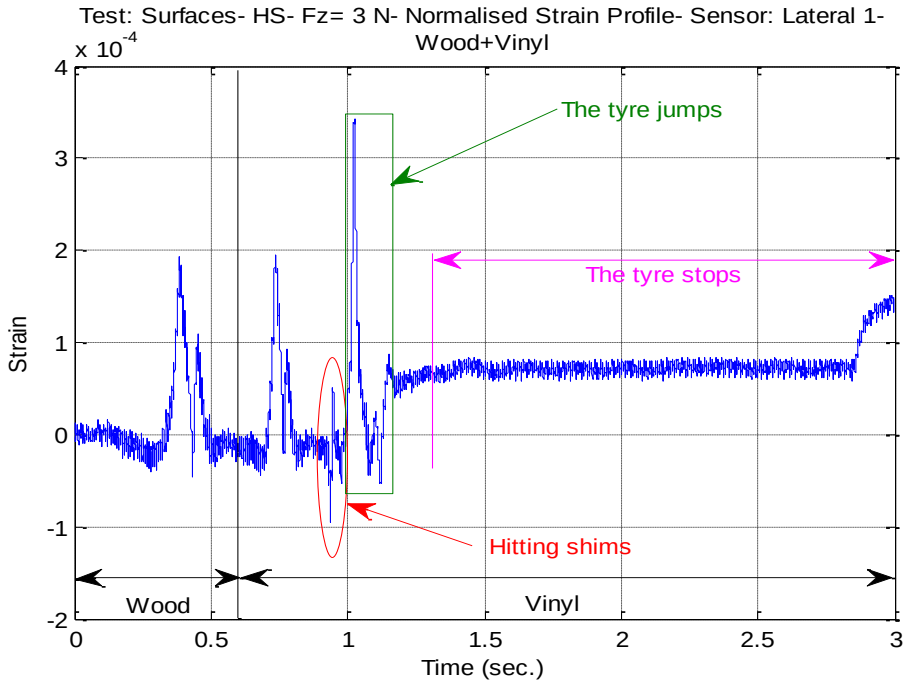

(a) Sensor: Lateral 1.

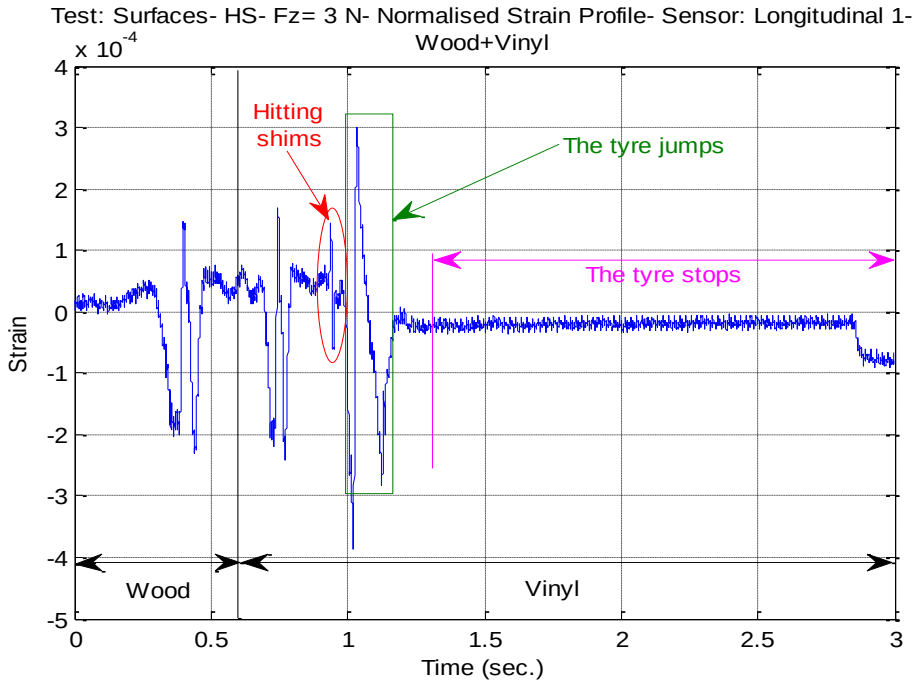

(b) Sensor: Longitudinal 1.

Figure 6.5: Using the strain sensors' readings to identify moving from wood to vinyl (HS = High Speed (12.20 rad./sec. = 116.50 RPM), F_z = 3 N).

It is worthwhile mentioning that the value of the strain peak for the third cycle in Figure 6.5 is higher than the value of the corresponding peak in the first two cycles. This third cycle represents the first spinning cycle after the cart hit the shims at the end of the rail. After inspecting the video of this test, it was found that the reason for this sharp increase in the peak's value is that the tyre jumped then fell strongly after the cart hit the shims.

The value of the strain peak at the centre of the contact patch was used to calculate the percentage of strain change when moving from the control surface (wood) to the second surface. For the second surface, the strain peak for the first cycle was used. Table 6.2 shows that this percentage differs in accordance with the nature of the traversed surface. It also shows that the value is much higher for the rough surfaces.

Table 6.2: Percentage values of the strain change caused by moving on different surfaces.

Surface	**Strain Change (%)**
Wood to Carpet	52.13
Wood to Dirt	51.20
Wood to Grass	24.98
Wood to Glass	3.22
Wood to Plastic	1.98
Wood to Vinyl	1.73

Lastly, it should be mentioned that identifying liquid surfaces using the reading of the in-tyre sensors was also investigated. The same material was used for the full track for this investigation. Three control surfaces were tested: wood, vinyl, and plastic. The second half of these surfaces was coated with liquid. This means that the tyre completed the first revolution on the control surface and the other cycles on the control surface coated with the liquid. Figure 6.6 shows the results of these tests. It is seen that there were no significant strain changes produced when the tyre moves over a liquid

surface. This is observed by comparing the first two cycles in the strain profiles shown in Figure 6.6. The first cycle represents the strains while travelling on the first surface (control surface) whereas the second cycle is for traversing the control surface with the liquid. The two cycles are similar in waveform shapes. This means that the tyre was compressing or stretching in a similar manner and at the same points in the two cases. In addition, the percentage of change in the strain values was less than 1 %. Hence, it is concluded that the strain sensors cannot differentiate between traversing the liquid and traversing a different surface.

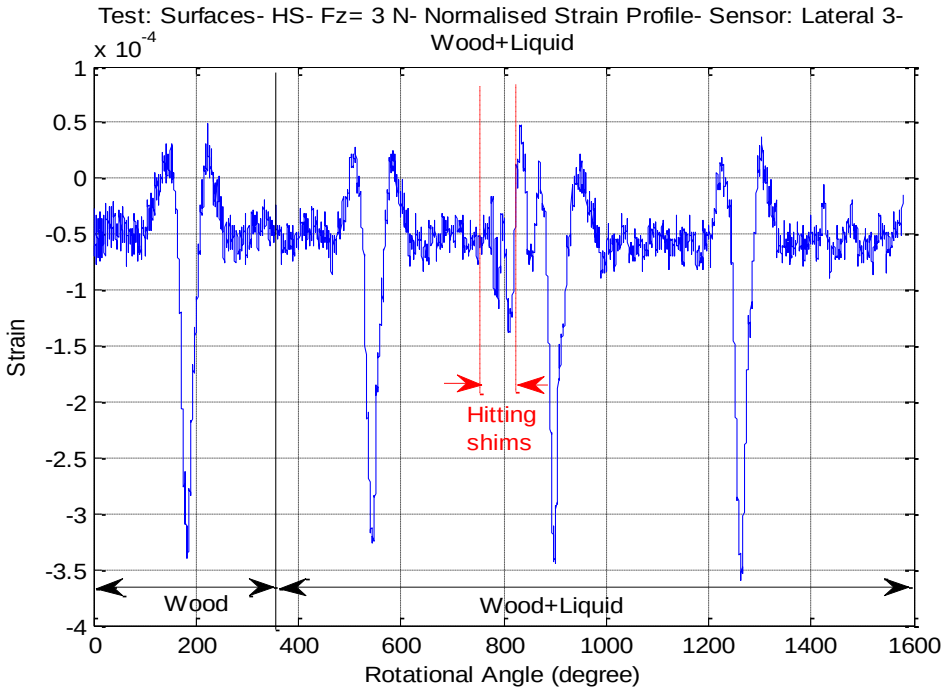

(a) Wood to wood + liquid.

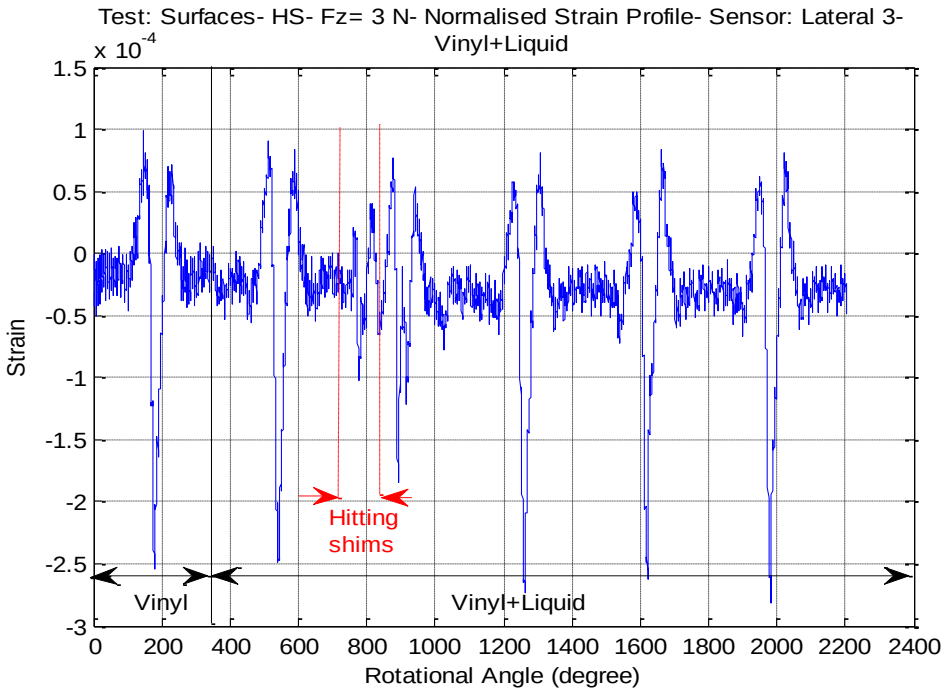

(b) Vinyl to vinyl + liquid.

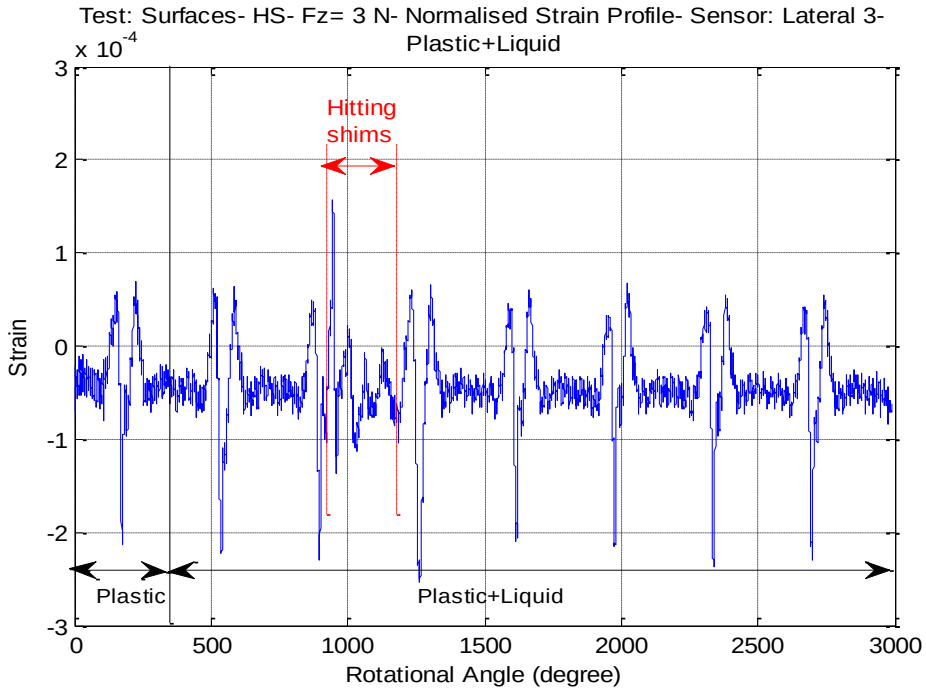

(c) Plastic to Plastic+ Liquid.

Figure 6.6: Strain profiles when the tyre moves from the control surface to control surface+ liquid (HS = High Speed (12.20 rad./sec. = 116.50 RPM), F_z = 3 N).

6.3 Using the frequency content of the strain waveforms to identify surfaces

In this section, the frequency content of the in-tyre strain waveforms is investigated to determine if it can be used to identify the contact surfaces. For this purpose, the frequency distribution is examined to identify changes that are related to traversing different surfaces. The effects of the tyre angular velocity and the wheel load on the frequency content of the waveforms are also analysed.

It is expected that the same frequency in the strain waves emerges each time the tyre travels a particular surface. Figure 6.7 presents the frequency magnitude spectrum for various surfaces tested in the dynamic tests under the same angular velocity and wheel load. The term bouncing cycles will be used in this section to refer to the cycles of the strain wave that resulted from the bouncing of the tyre after the cart hit the shims at the track's end. For each surface, the frequency components resulted from several normal cycles and bouncing cycles are overlapped.

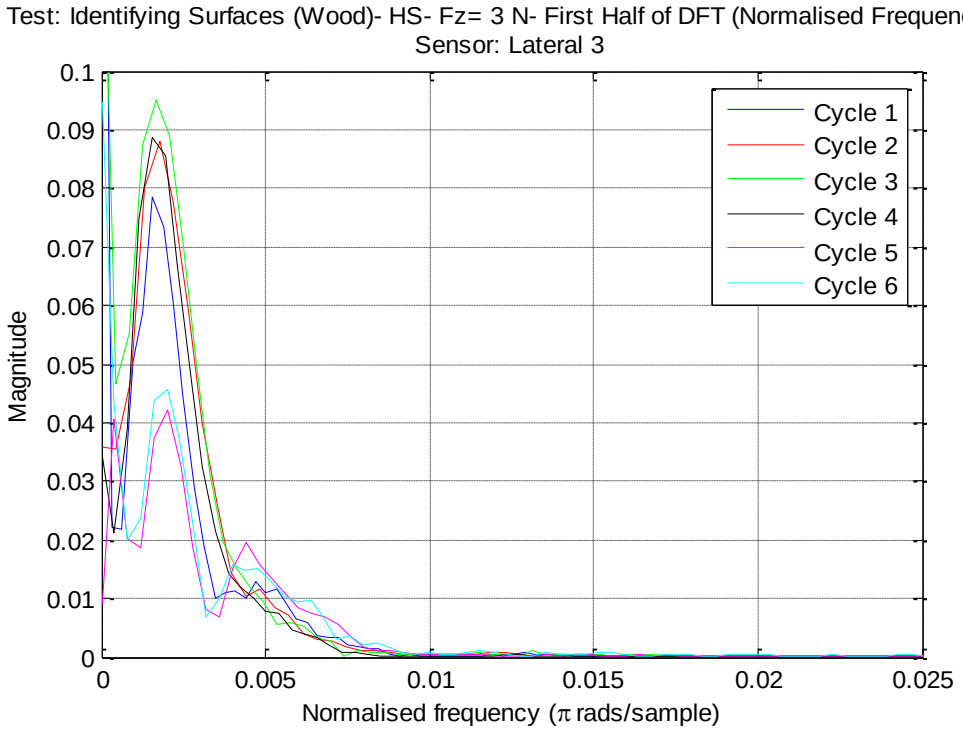

(a) Wood.

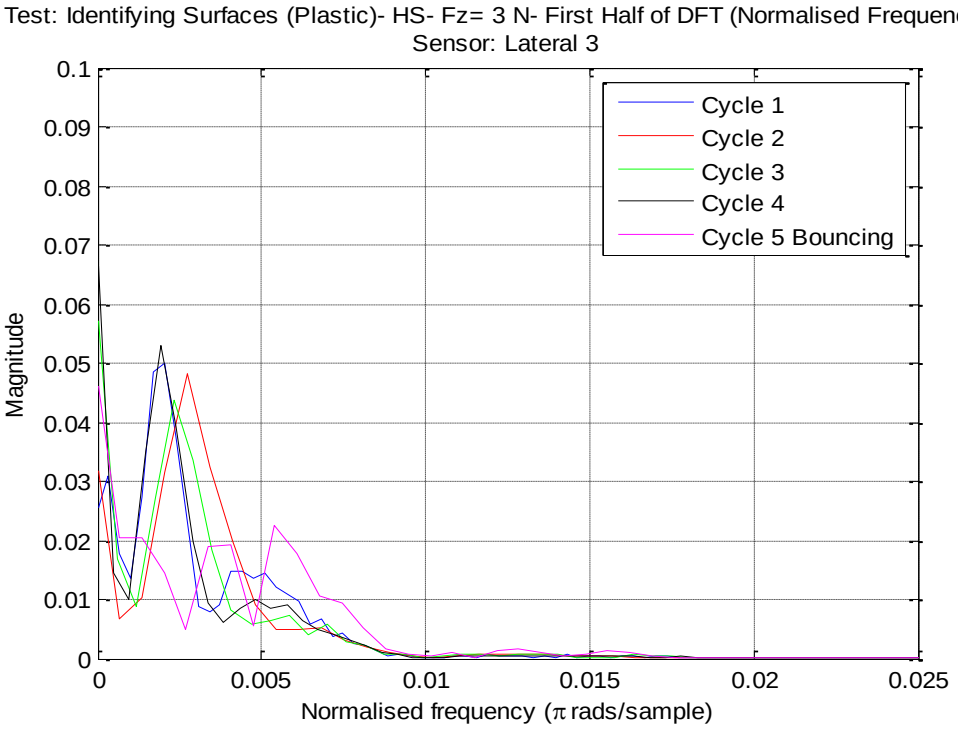

(b) Plastic.

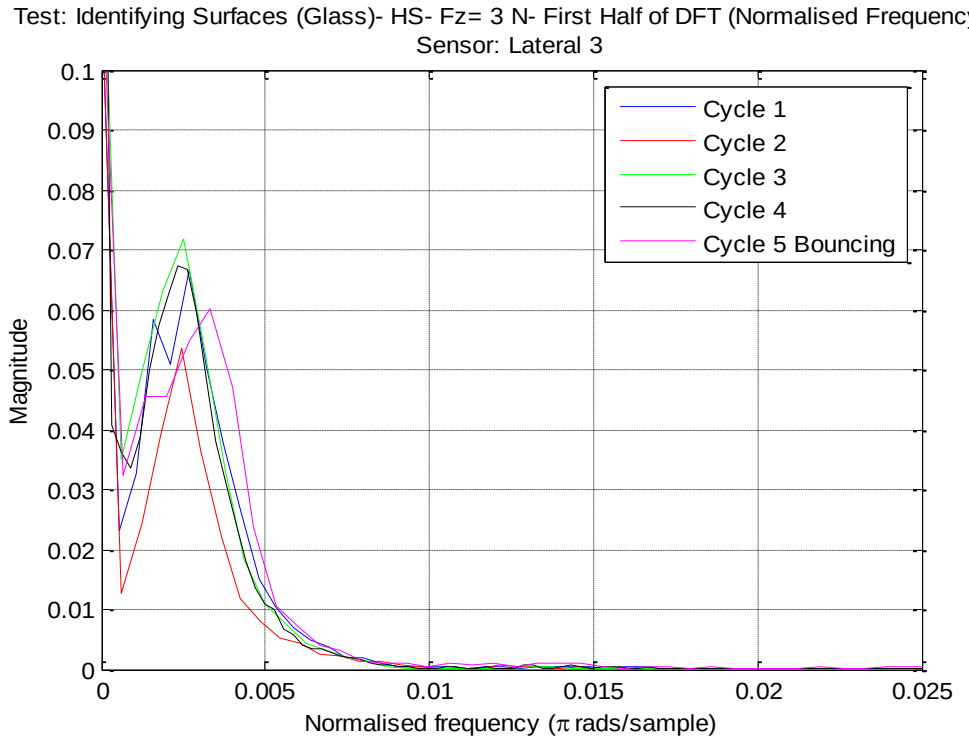

(c) Glass.

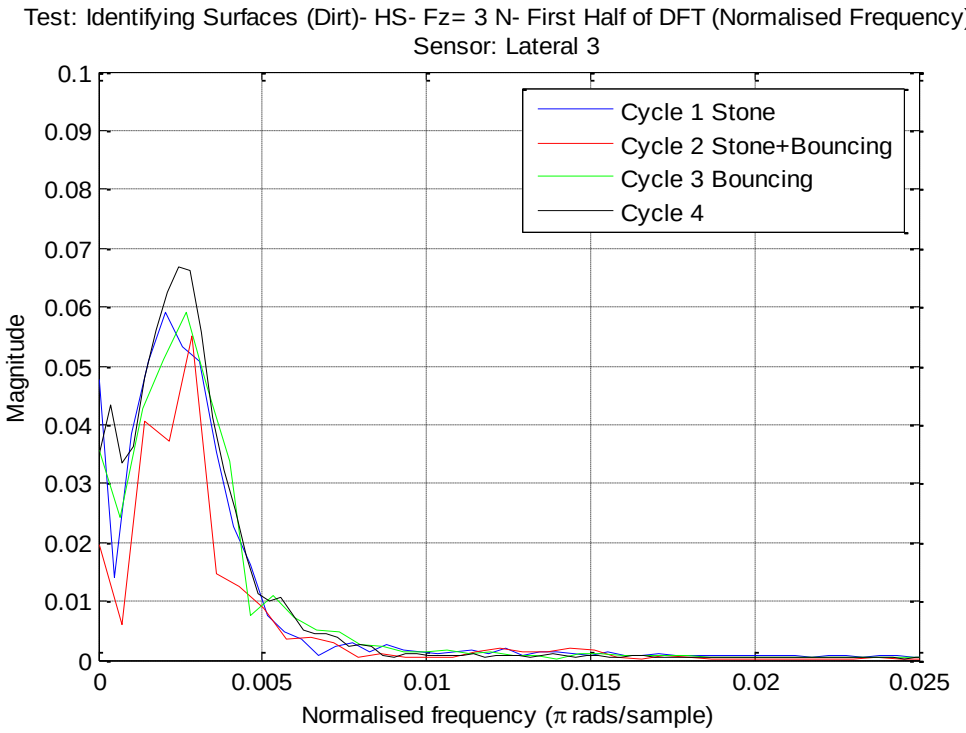

(d) Dirt.

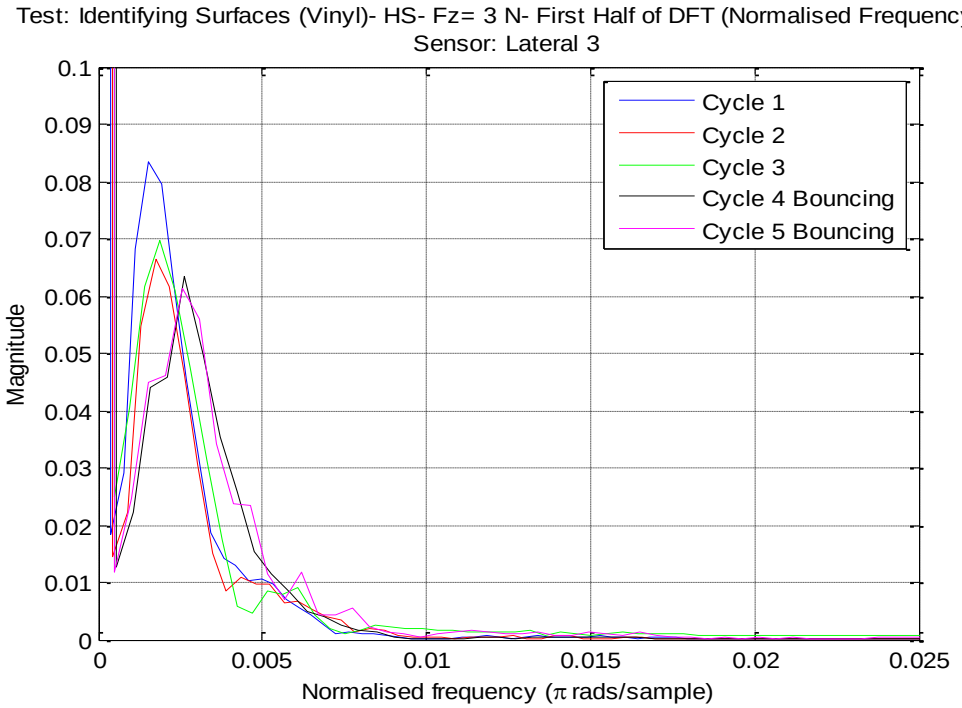

(e) Vinyl.

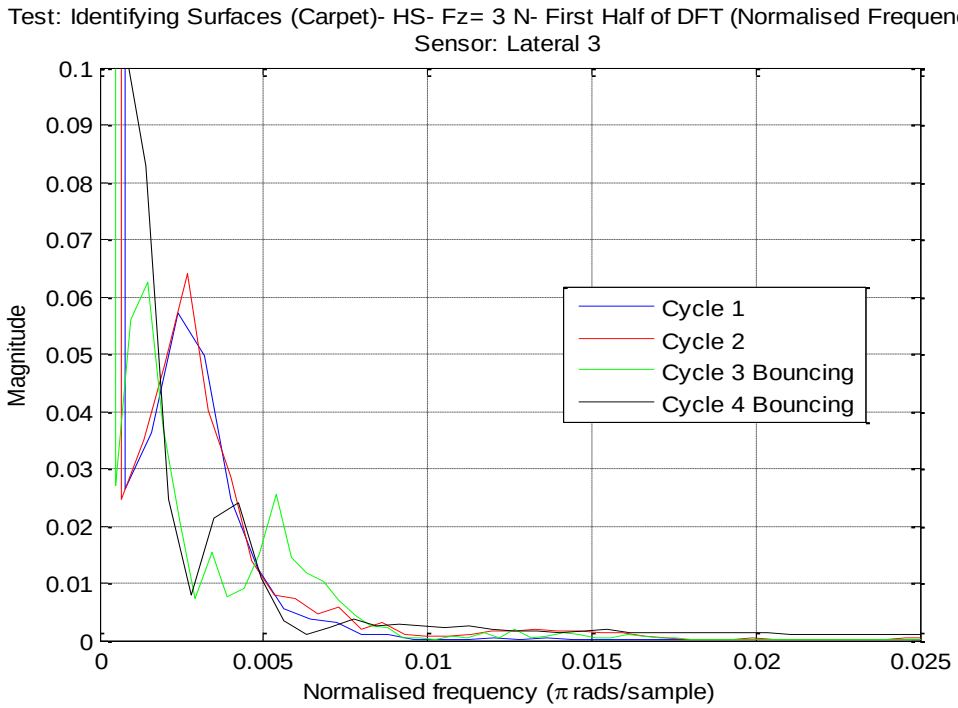

(f) Carpet.

Figure 6.7: Frequency magnitude spectrum for several normal and bouncing cycles in different surfaces (The bouncing cycles are the strain cycles that result from the bouncing of the tyre after the cart hits the shims at the track's end).
(Sensor: Lateral 3, HS = High Speed (12.20 rad./sec. = 116.50 RPM), F_z = 3 N).

For the normal cycles (no-bouncing cycles), it can be seen that a similar pattern for the fundamental frequency is identified for each surface. In addition, when comparing the frequency spectrum for the different surfaces, it is observed that there was only a slight shift in the average frequency value of the dominant frequency. The average change of frequency for the presented surfaces was 1.62×10^{-4}. On the other hand, the difference in the average magnitude of this frequency was greater and more noticeable. The average change of magnitude for the surfaces was 7.10×10^{-3}. Therefore, it can be concluded that it is possible to identify traversing different surfaces using the frequency spectrum of the in-tyre strain profiles. This is achieved by detecting a specific magnitude of the fundamental frequency components in this spectrum.

It should also be mentioned that these initial results showed that the frequency contents could not clearly reflect traversing rough or smooth surfaces. As shown in Table 6.3, there was an inconsistent change in the frequency spectrum for the surfaces. On the

contrary, the change in the strain values was consistent and indicated traversing rough or smooth surfaces as presented in Table 6.2. Thus, to make conclusive decisions about the feasibility of using the frequency spectrum of the strain profiles for surface identification, a deeper analysis should be conducted. This analysis requires performing tests with several more surfaces, more tyre's revolutions on each surface, and more data samples. These tests and analyses are among the main aspects of future work.

Table 6.3: Frequency content for different surfaces (normal (no-bouncing) cycles).

Surfaces	**Average Frequency ($\pi\ rads/sample$)**	**Average Magnitude**	**Percentage of Frequency Change (Compared to Wood) (%)**	**Percentage of Magnitude Change (Compared to Wood) (%)**
Carpet	0.002529	0.06058	44.78	16.79
Dirt	0.002251	0.06302	28.86	13.44
Glass	0.002482	0.06486	42.09	10.91
Plastic	0.002257	0.03789	29.23	47.95
Vinyl	0.001715	0.07322	1.803	0.5723

It was shown in some of the dynamic tests that the tyre's cart hit the shims at the end of the track on the bench-top rig. Depending on the tyre's rotational speed and the nature of the contact surface, this action caused the cart to reverse for a distance while the tyre bounced and rotated before stopping completely. It was also shown that the in-tyre strain sensors were able to detect unusual strain readings in such cases and, thereby, identify these incidents. The frequency profiles resulting in these cases are analysed to determine whether they can provide indications that the tyre rotations are unusual. As presented in Figure 6.7, this was performed by comparing the frequency

magnitude spectrum of the strain cycles for usual rotations against bouncing rotations on the tested surfaces. It can be seen that the bouncing cycles produced different frequency curves. Table 6.4 presents the frequency content for the bouncing cycles for the surfaces. By comparing Table 6.3 and Table 6.4, it is seen that the fundamental frequency component in the bouncing cycles had a higher frequency and a less magnitude. In addition, in surfaces where the tyre made more than one bouncing cycle, it can be observed that there was no constant trend in the frequency content of the bouncing cycles. This is expected since these bouncing incidents were irregular and caused a different change in the tyre rotations in terms of angular speed and strain values for each cycle. Hence, for the vinyl case (Figure 6.7e), the frequency spectrum resulted from two bouncing cycles reflected a similar shape for the frequency curve. In addition, Table 6.4 shows that these two cycles had very close frequency and magnitude values for the dominant frequency element. Conversely, for the carpet case (Figure 6.7f), the frequency curves for two bouncing cycles were different in shape. It is also observed that the value of the frequency and magnitude of the fundamental frequency component in these two cycles differed considerably.

Table 6.4: Frequency content for different surfaces (bouncing cycles).

Surfaces	**Frequency (π rads/sample)**		**Magnitude**	
	Cycle 1	**Cycle 2**	**Cycle 1**	**Cycle 2**
Carpet	0.001462	0.004215	0.06244	0.02418
Dirt	0.002877	0.002661	0.05519	0.05922
Glass	0.003321		0.06012	
Plastic	0.005405		0.02235	
Vinyl	0.002648	0.002581	0.06333	0.06144

To examine the effect of the tyre's rotational speed on the frequency spectrum of the strain waveforms on a particular surface, the frequency content resulting from applying different angular velocities under the same wheel load and for the same surface was

investigated. Figure 6.8 shows that the shape of the frequency curves was similar for the individual speed levels. In addition, the value of the frequency and magnitude for the dominant frequency was almost the same for the cycles in each of the speed levels. This means that the frequency profiles of the strain waveforms can be utilised to estimate the angular velocity of the tyre. To explain, the values of the frequency and magnitude for the dominant frequency components that appear with a specific operating condition for the tyre can be used to build a lookup table. This operating condition includes the traversed surface, the angular velocity, and the wheel load. This table can then be used to determine the tyre's velocity based on the corresponding frequency outputs. This estimation for the velocity using the frequency content of the in-tyre strain reading can be used to compensate or correct the encoder readings. The frequency content of the in-tyre sensors can provide indications about the contact surface; therefore, it can complement the encoder readings.

The last point about Figure 6.8 is that as the tyre's angular velocity increased, the fundamental frequency component became higher in frequency and lower in magnitude.

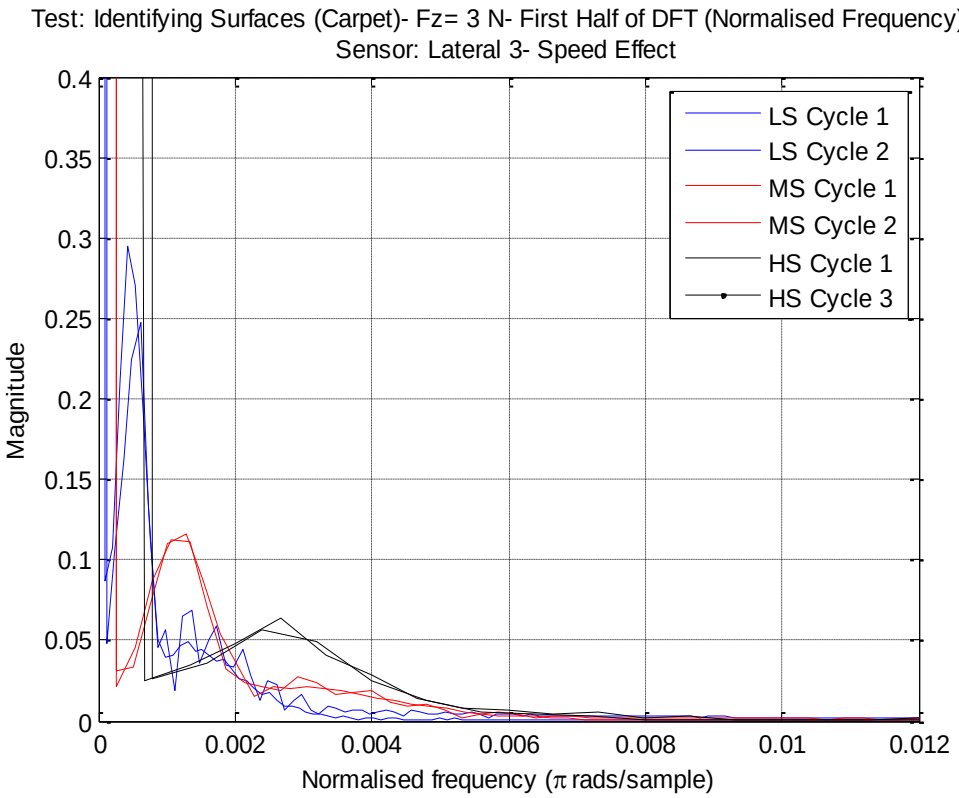

Figure 6.8: Effect of the rotational speed on the frequency magnitude spectrum on a surface (carpet)

(Sensor: Lateral 3, LS = Low Speed (3.50 rad./sec. = 33.42 RPM),

MS = Medium Speed (6.65 rad./sec. = 63.50 RPM),

HS = High Speed (12.20 rad./sec. = 116.50 RPM), F_z = 3 N).

Identifying the effect of the wheel load is studied by comparing the frequency profiles of the strain waveforms generated when the tyre moved on the same surface and with the same speed. Figure 6.9 presents the frequency curves of the tyre's strain revolutions for four values of the vertical load. The change in both the frequency and magnitude of the dominant frequency component was small. However, the change in the frequency value was more observable.

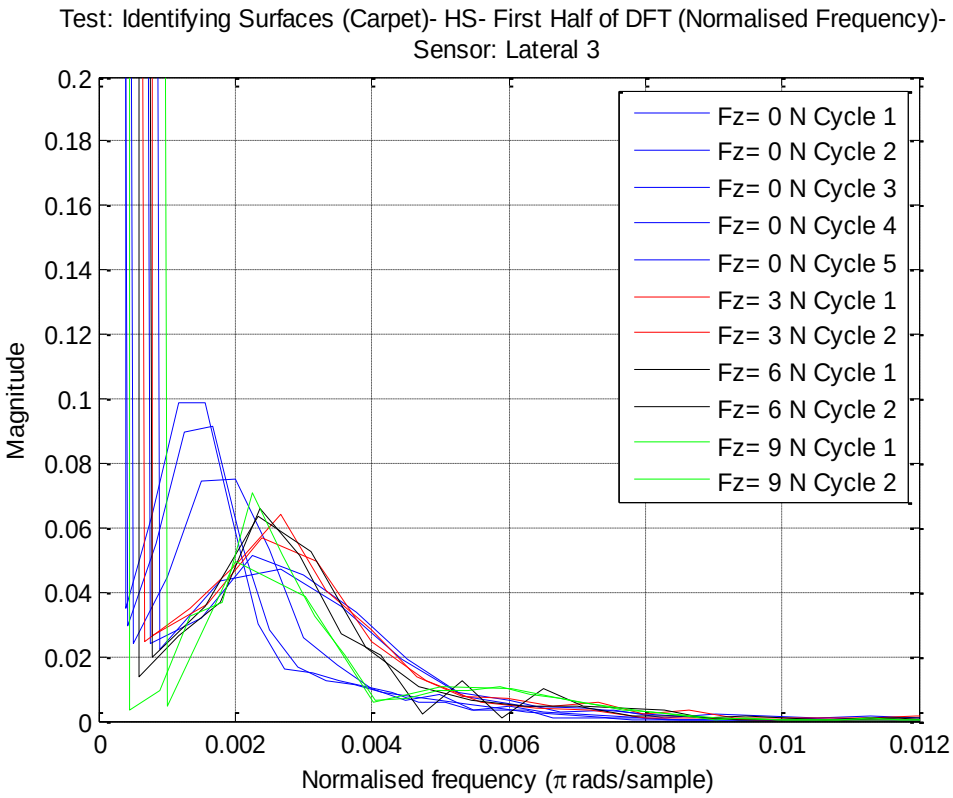

Figure 6.9: Effect of the vertical force on the frequency magnitude spectrum on a surface (carpet) (HS = High Speed (12.20 rad./sec. = 116.50 RPM)).

6.4 Summary

This chapter has investigated exploiting the in-tyre strain profiles for surface identification. For this investigation, dynamic tests were conducted on the second rig where several contact surfaces were examined. The following points summarise the analysis of the strain measurements:

- The strain profiles could be used to identify traversing the rough surfaces. The strain values were higher on the rough surfaces as compared to the control surface (wood) on the rig. This increase in the strain implied that the tyre experienced higher deformations in order to continue rotating on these high-grip surfaces. The minimum percentage of strain change for the rough surfaces was 24.98 %. This conclusion was confirmed by observing the readings of the motor's current sensor.

- The strain measurements could not clearly reflect traversing the smooth surfaces. As compared to the control surface, only a small increase in the strain value was noticed when the tyre moved over the smooth surfaces. The similar texture for the control and the smooth surfaces caused this slight strain change. The maximum percentage of strain change for the smooth surfaces was 3.22 %.

- The strain sensors could not indicate passing over the liquid surfaces. The strain waveforms resulted from crossing the liquid surfaces were similar in shape and strain values to the waveforms generated with the control surface. The percentage of the strain change was less than 1 %.

- The shape of the strain profiles reflected some aspects of the texture of the traversed surfaces. When the tyre moved over smooth surfaces such as vinyl, smooth waveforms were collected. Conversely, distorted waveforms were generated when the tyre traversed the rough surfaces especially the uneven and inconsistent dirt surface.

- The analysis of the frequency content of the strain waveforms showed that the frequency spectrum was the same for the wave cycles in each tested surface. In addition, the magnitude of the dominant frequency can be used as an indication of traversing different surfaces. Furthermore, the analysis demonstrated a difference in the frequency curves for the normal and bouncing wave cycles. However, it was suggested that extensive tests are required to develop a profound analysis of the frequency distributions for the in-tyre strain waveforms.

To conclude, the results presented in this chapter suggested that the strain measurements can indicate traversing rough surfaces. This tactile information can be integrated with the visual data to develop accurate surface identification systems. The role of the tactile data in such systems would be overcoming the flaws of the visual sensors. For example, the tactile data are more reliable in the case of adverse illumination conditions. It is also useful if there is a difficulty in capturing the real surface that holds the weight of the vehicle such as in the presence of grass on the dirt surface. A detailed discussion on the advantages of using tactile data from the in-tyre sensors for surface identification was presented in Section 1.3.

Chapter 7

Force, Contact Patch, Angular Velocity, and Camber Angle Estimation

This chapter investigates the relationships between the in-tyre strain measurements and the tyre's mechanical parameters. The strain readings are analysed to extract features that are used to determine the tyre's basic properties. These features are utilised to estimate the tyre's forces in three directions, the contact patch length and centre, the angular velocity, and the camber angle.

It was concluded from the literature review that the in-tyre strain measurements of the non-pressurised tyres have not been previously modelled. As mentioned in Section 4.4, the strain profiles of the non-pressurised tyres used in this work were found to be similar to the profiles of the pneumatic car tyres. Therefore, the models that were presented in the literature to relate the strain measurements to the mechanical properties for the pneumatic car tyres are employed for the non-pressurised tyres in this chapter.

Results from both the static and dynamic tests are utilised to investigate the strain changes in response to the changes in the applied vertical and longitudinal forces. The dynamic tests' data are employed to establish important relationships that link the strain characteristics and features to the tyre forces, contact patch, angular velocity, and camber angle under different wheel loads and different velocities.

The sensors' data were collected from the experiments presented in Chapter 3. Table 7.1 below shows the sections of Chapter 7 and the sections where the associated experimental work was explained in Chapter 3.

Table 7.1: Linking the sections in Chapter 7 to the corresponding sections that described the experimental setup and tests in Chapter 3.

Sections in Chapter 7	**Associated sections that explained the experimental setup and tests' description in Chapter 3**
7.1 Force estimation	3.2.3 Static tests to detect slip and construct strain profiles + 3.3.3 Vertical load tests + 3.3.2 Angular velocity tests
7.2 Contact patch estimation	3.3.2 Angular velocity tests + 3.3.3 Vertical load tests
7.3 Angular velocity estimation	3.3.2 Angular velocity tests + 3.3.3 Vertical load tests
7.4 Camber angle estimation	3.3.5 Camber angle tests

7.1 Force estimation

The static tests provided the opportunity to study the strain changes resulted from applying vertical and longitudinal forces at individual angular positions for the tyre used herein. The effect of increasing the longitudinal forces on the tyre's strain profiles is shown in Figure 7.1. The figure presents the readings for the sensors called lateral 1 and longitudinal 1. Similar results were obtained from the other sensors. In this figure, it is seen that there was a high degree of consistency in the shape of the strain profiles resulting from the progressively applied longitudinal forces.

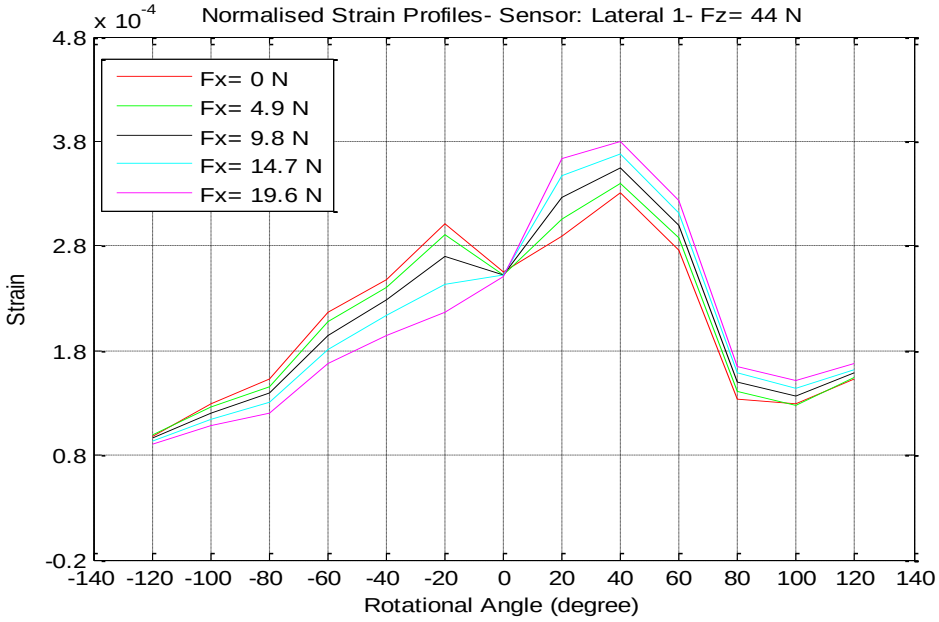

(a) Sensor: Lateral 1.

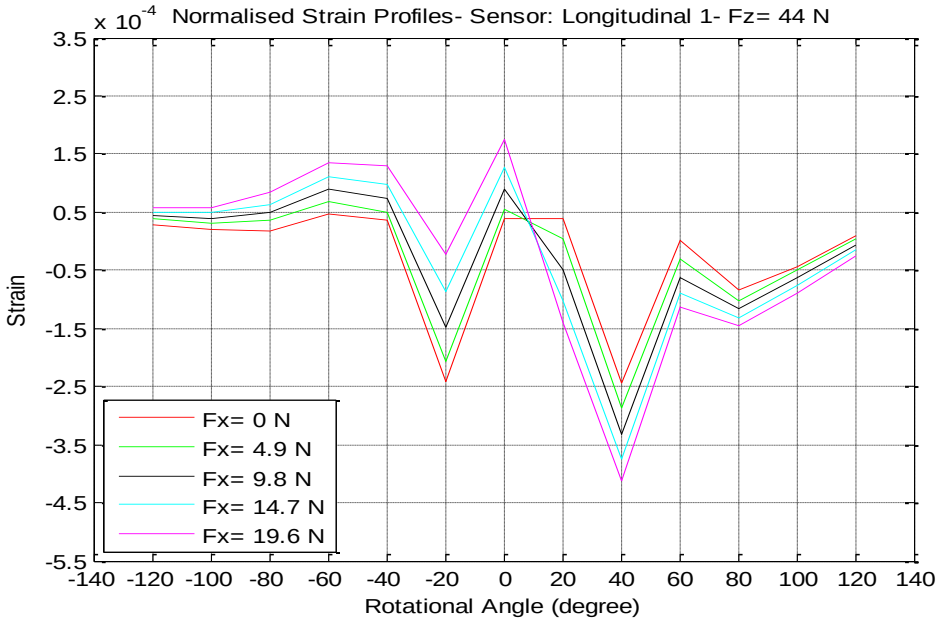

(b) Sensor: Longitudinal 1.

Figure 7.1: Effect of the longitudinal force on the strain profiles (F_z = 44 N).

For the lateral sensor in Figure 7.1a, increasing the longitudinal force led to a decrease in the strain at the negative angles and an increase in the strain at the positive angles. The exact opposite of the previous observations applied to the measurements of the longitudinal sensor presented in Figure 7.1b. As the longitudinal force increased, the

strain increased in the negative angles and decreased in the positive angles. This point was discussed in Section 4.1.1 when examining the trend of the relationships between the longitudinal load and the strain measurements at the angular positions.

The effect of increasing the vertical force on the strain waveforms is shown in Figure 7.2. For a lateral sensor (Figure 7.2a), an upward shift in strain profiles resulted from increasing the vertical force. Conversely, for a longitudinal sensor (Figure 7.2b), increasing the value of the vertical force led to a downward shift for the strain waveform. Similar observations about the effect of the vertical force on the in-tyre strain measurements were reported for pneumatic car tyres (Matsuzaki & Todoroki 2008a; Yang 2011).

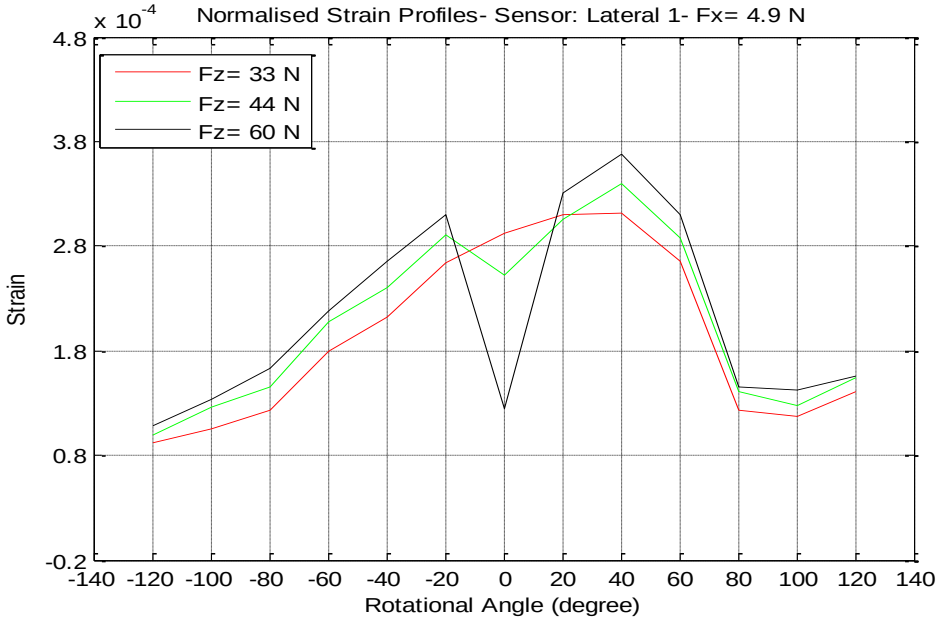

(a) Sensor: Lateral 1.

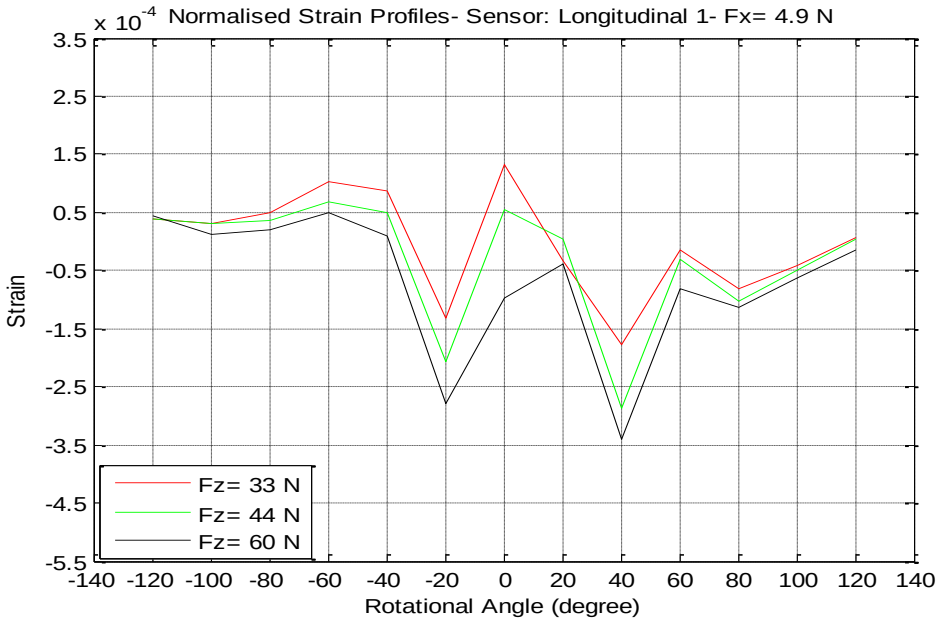

(b) Sensor: Longitudinal 1.

Figure 7.2: Effect of the vertical force on the strain profiles (F_x = 4.9 N).

The effect of the applied forces is closely investigated by examining the strain measurements at the angular positions. Figure 7.3 shows an example of the relationship between the longitudinal force (F_x) and the strain at a constant value of the vertical force (F_z) at some of the tested angular positions. Figure 7.4 shows an example of the relationship between F_z and the strain at a constant value of F_x at some of the tested angular positions. It can be seen in these figures that the sensors' readings demonstrated a linear relationship between the applied force, longitudinal or vertical, and the strain values. In addition, the graphs show that the lines representing the relationships are evenly spaced and close to each other, which indicates a consistent performance for the sensors.

The variation in the strain values at the different angles is related to the different distances between the sensor angular position and the point at which the force is applied to the tyre, which is the contact patch centre. Therefore, Figure 7.3 and Figure 7.4 show that as the sensors became closer to the contact patch, the slope of the lines became steeper. This is seen in the angles 40°, 20°, -20°, and -40° in the figures. This is because the strain at the points near the contact patch was higher. Consequently,

increasing the applied force resulted in larger changes in the strain at these points as compared to the angles far from the contact patch.

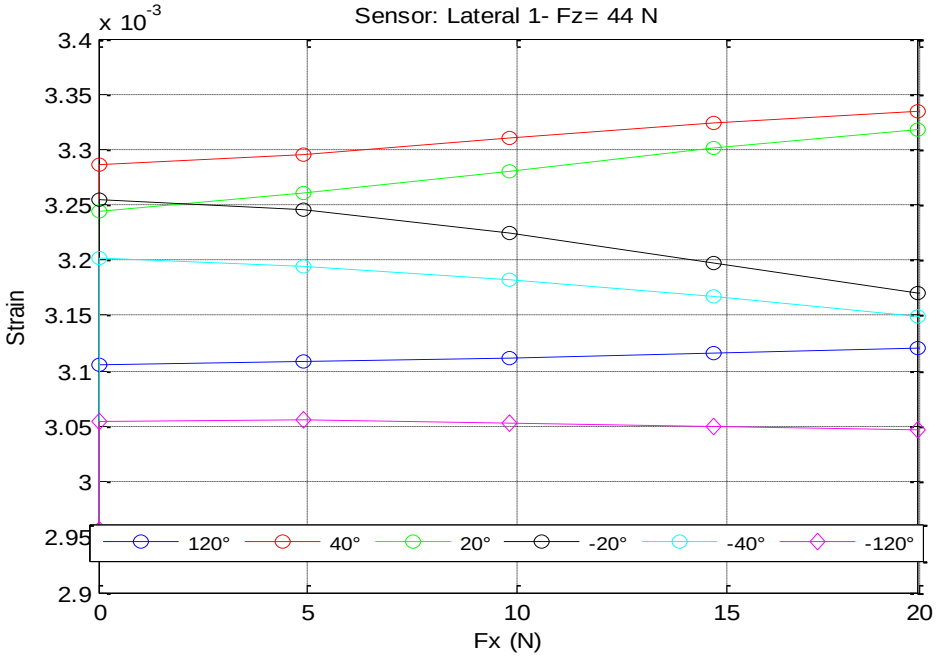

(a) Sensor: Lateral 1.

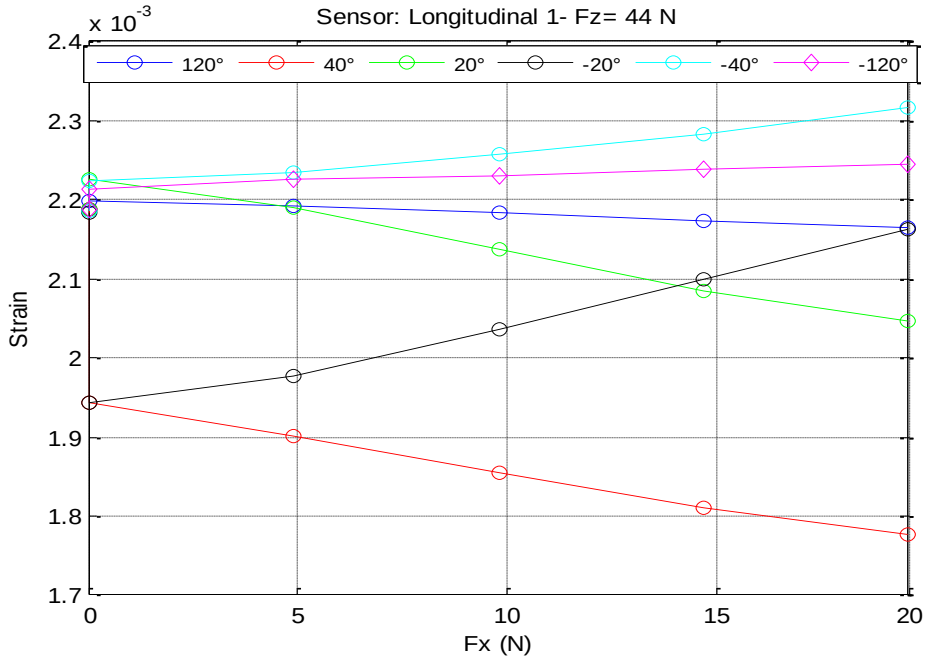

(b) Sensor: Longitudinal 1.

Figure 7.3: Strain versus F_x at some tested angles (F_z = 44 N).

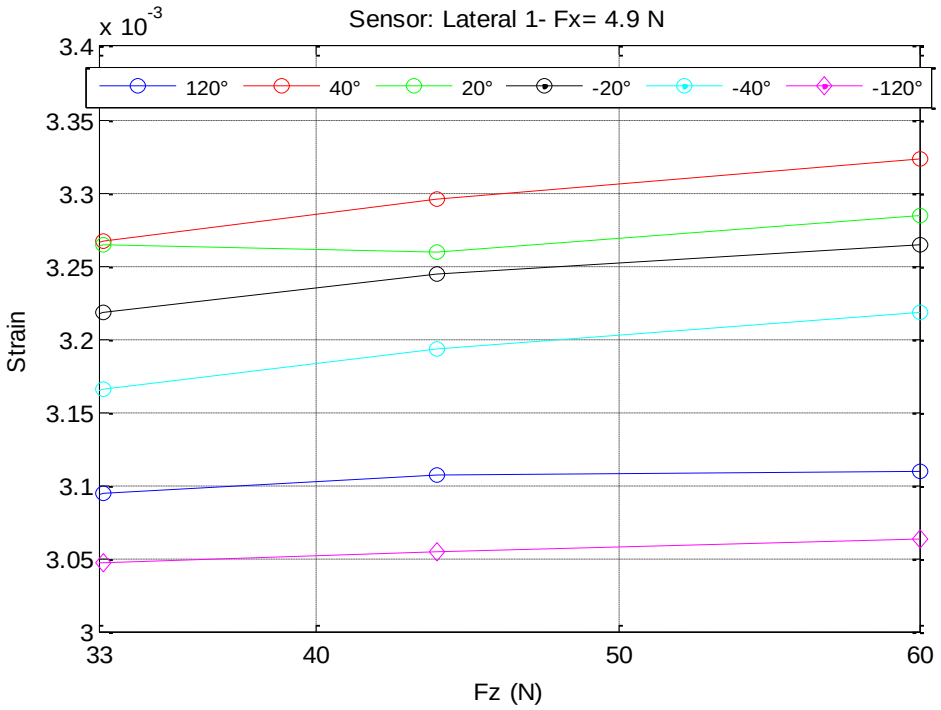

(a) Sensor: Lateral 1.

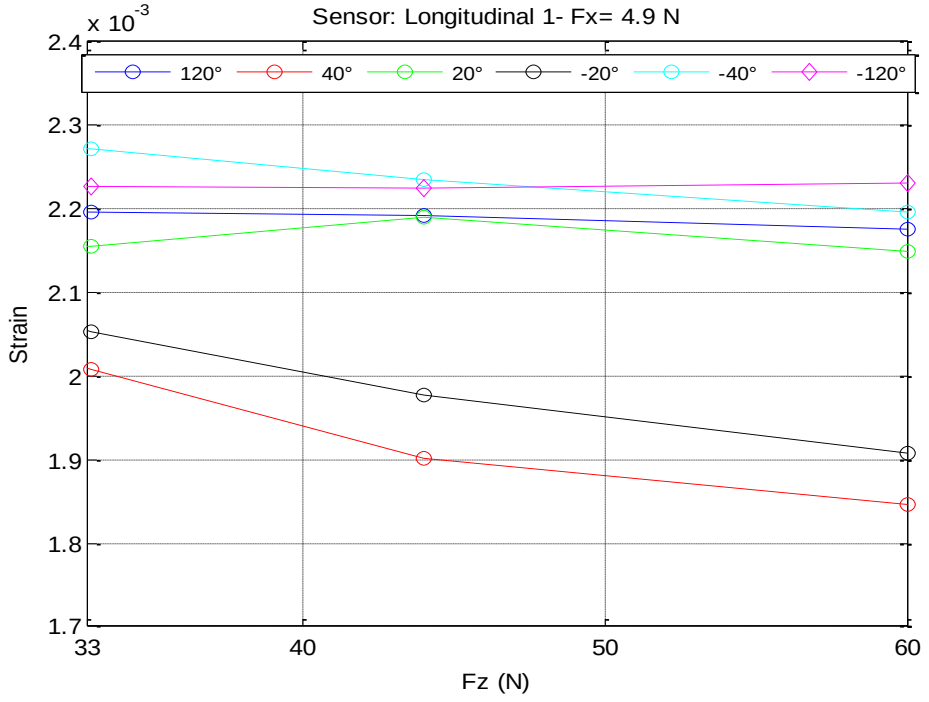

(b) Sensor: Longitudinal 1.

Figure 7.4: Strain versus F_z at some tested angles (F_x = 4.9 N).

In the following, more relationships are constructed using the strain data extracted from the profiles generated through the dynamic tests since they provide more continuous readings. Firstly, Figure 7.5 shows that increasing the applied vertical load caused an increase in the lateral tensile strains (Figure 7.5a) and in the longitudinal compressive strains (Figure 7.5b).

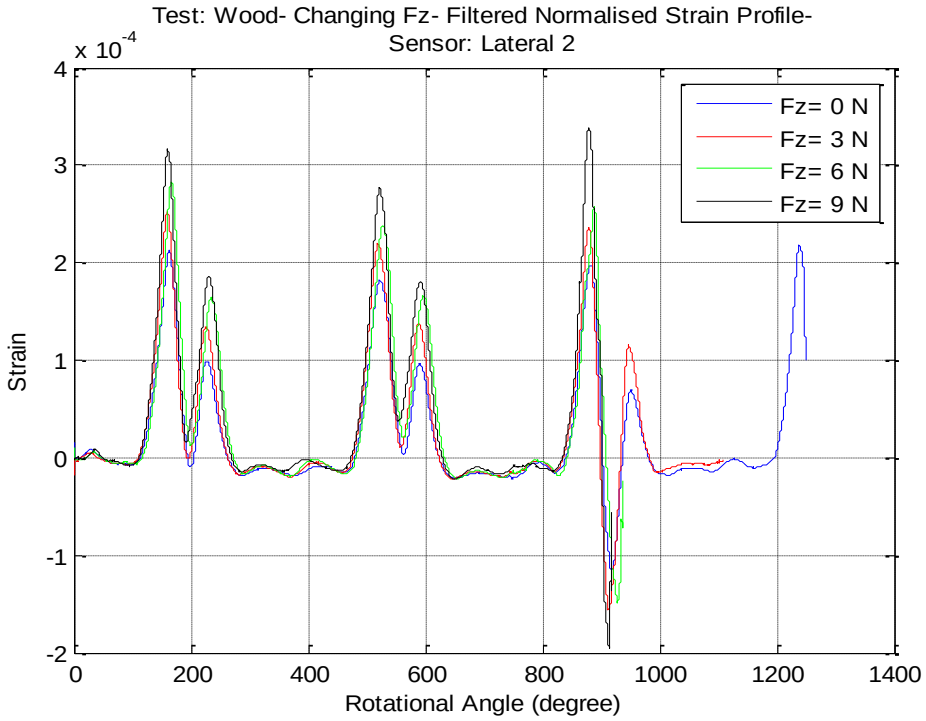

(a) Sensor: Lateral 2.

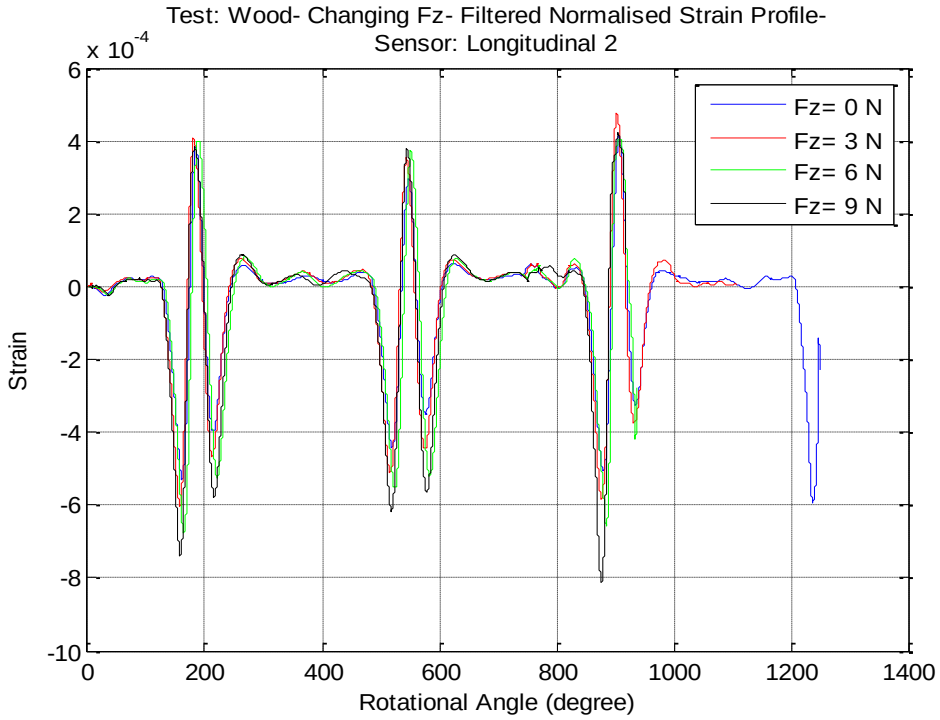

(b) Sensor: Longitudinal 2.

Figure 7.5: Smoothed strain profiles for the sensors for applied vertical forces (HS = High Speed (12.20 rad./sec. = 116.50 RPM)).

From the strain curves presented in Figure 7.5, the average value of the two longitudinal compressive strain peaks or the average value of the two lateral tensile strain peaks was used to extract an equation to estimate the vertical load as shown in Figure 7.6. Similar to the pneumatic car tyres used by other researchers, a second order polynomial represents the relationships between the average strain and the vertical load for the non-pressurised tyres used in this research (Yang 2011; Yang et al. 2013).

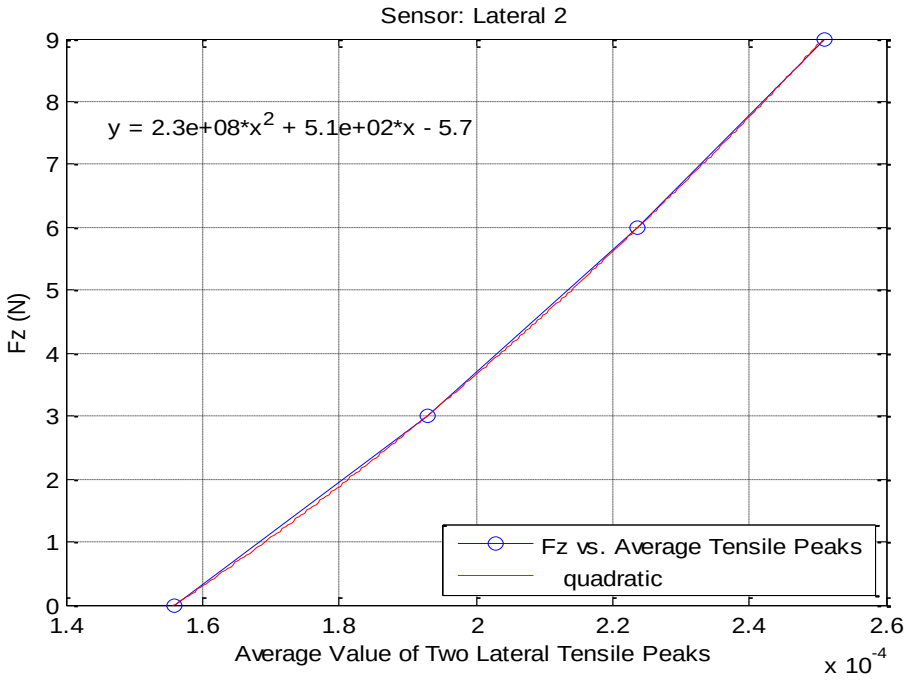

(a) Sensor: Lateral 2.

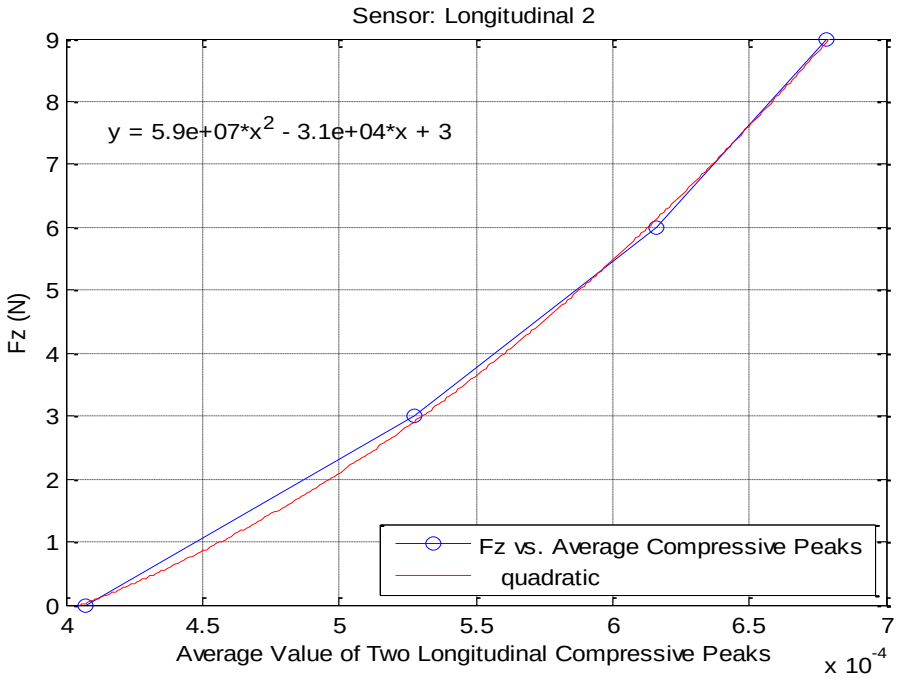

(b) Sensor: Longitudinal 2.

Figure 7.6: Relationship between the average value of the two strain peaks and vertical forces (HS = High Speed (12.20 rad./sec. = 116.50 RPM)).

The longitudinal (braking/traction) force (F_x) applied on the tyre can also be estimated utilising strain characteristic from the waveforms of the in-tyre strain sensors. As mentioned in Section 4.2.1, the values of the front and rear strain peaks differed as a result of the traction torque working on the tyre. This strain variation was caused by the effect of the longitudinal force. Figure 7.7 shows the front and rear strain peaks in the readings of the strain sensors.

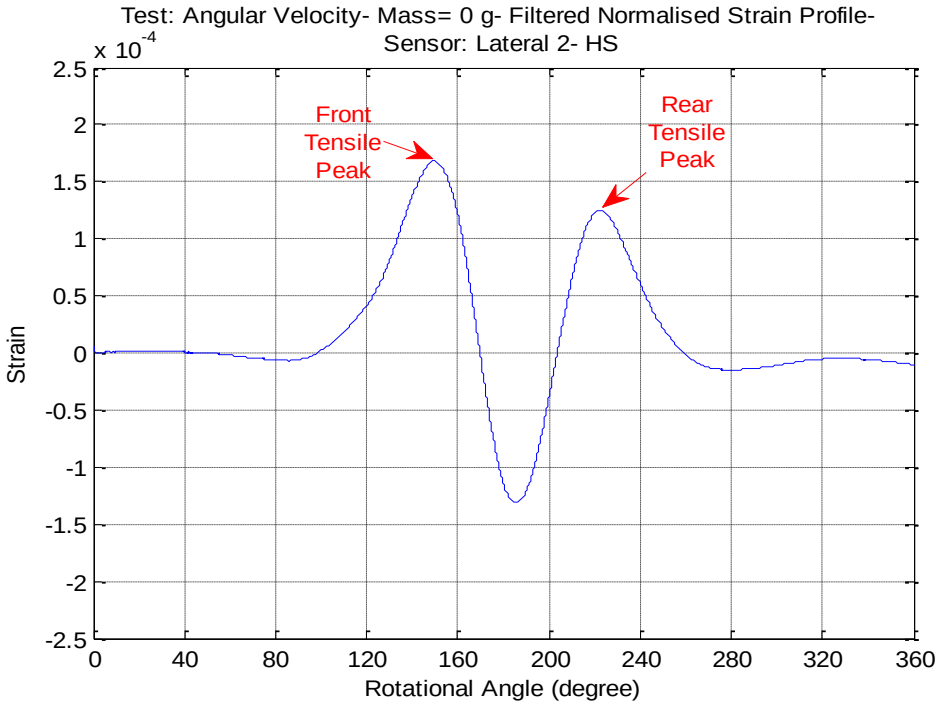

(a) Tensile strain peaks in the readings of a lateral sensor.

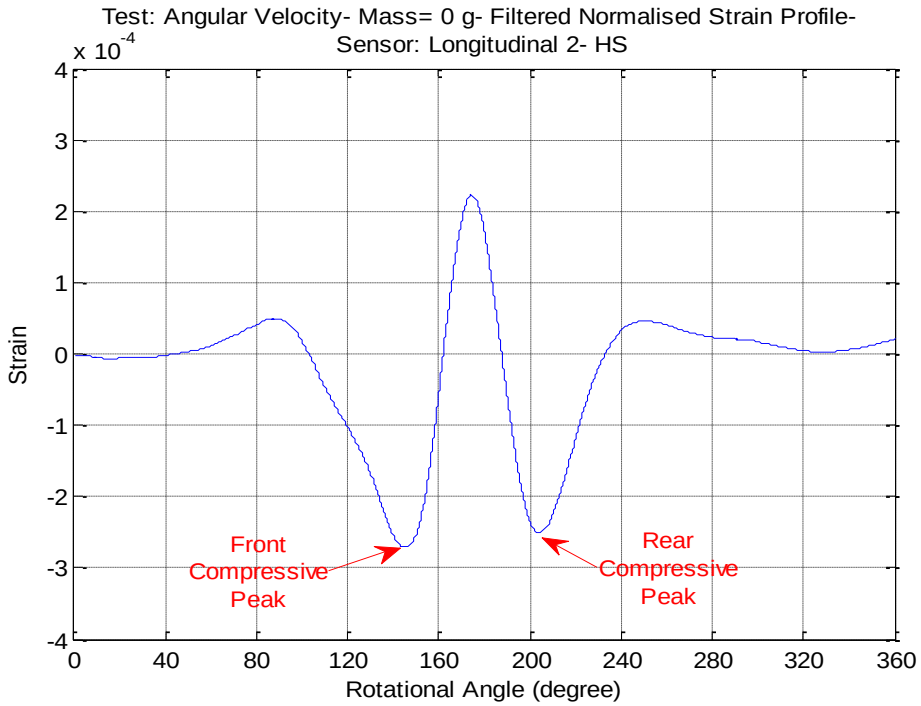

(b) Compressive strain peaks in the readings of a longitudinal sensor.

Figure 7.7: Front and rear strain peaks in the sensors' readings
(HS = High Speed (12.20 rad./sec. = 116.50 RPM), F_z = 0 N).

The simplified low-budget bench-top rig used in the dynamic tests was not equipped with a braking/traction mechanism to change the longitudinal force. As an alternative solution, it was expected that changing the tyre angular velocity by increasing the voltage to the motor would cause a change in the longitudinal force according to Equations 4.3 and 4.4. Figure 7.8 shows the values of the longitudinal force resulted from increasing the angular velocity.

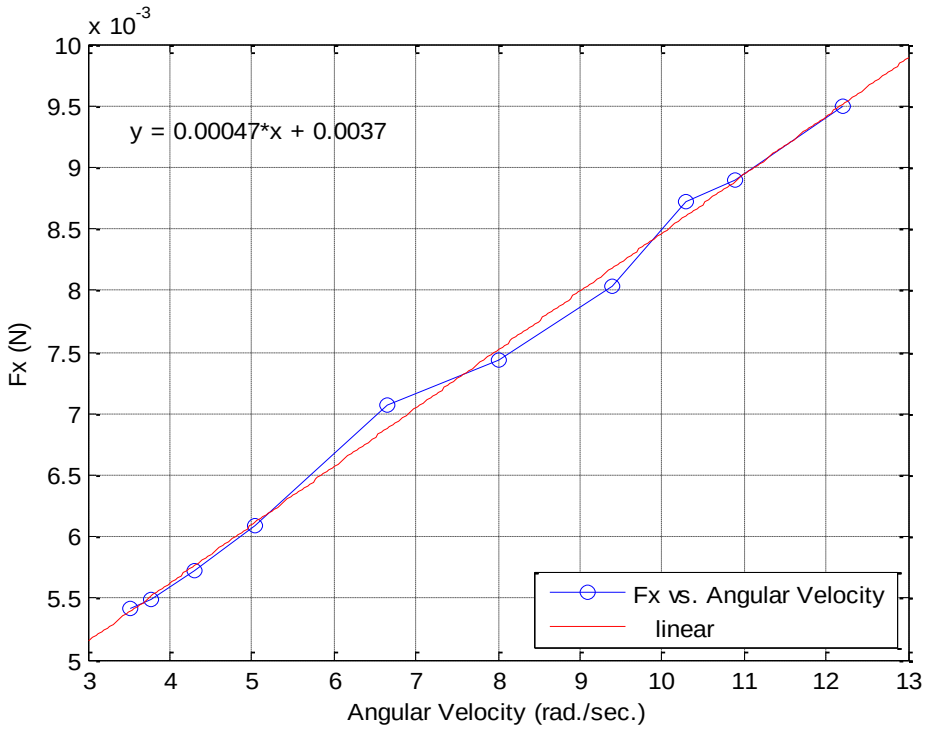

Figure 7.8: Relationship between the tyre angular velocity and the longitudinal force (F_z = 0 N).

The ratio of the front to the rear tensile lateral strain peak is used to find the longitudinal force (Yang 2011). Figure 7.9a presents the relationship between the lateral tensile strain peak ratio for a lateral sensor and the longitudinal force in the speeds' tests. From Figure 7.8 and Figure 7.9a, it is seen that as the tyre speed increased, the longitudinal force increased and the peak ratio decreased. Likewise, the longitudinal compressive strain peak ratio of the front to rear peaks in a longitudinal strain sensor can be used to estimate the longitudinal force. Figure 7.9b illustrates the relationship between the longitudinal compressive strain peak ratio and the longitudinal force. It is shown in Figure 7.8 and Figure 7.9b that as the tyre speed increased, the longitudinal force and the peak ratio increased.

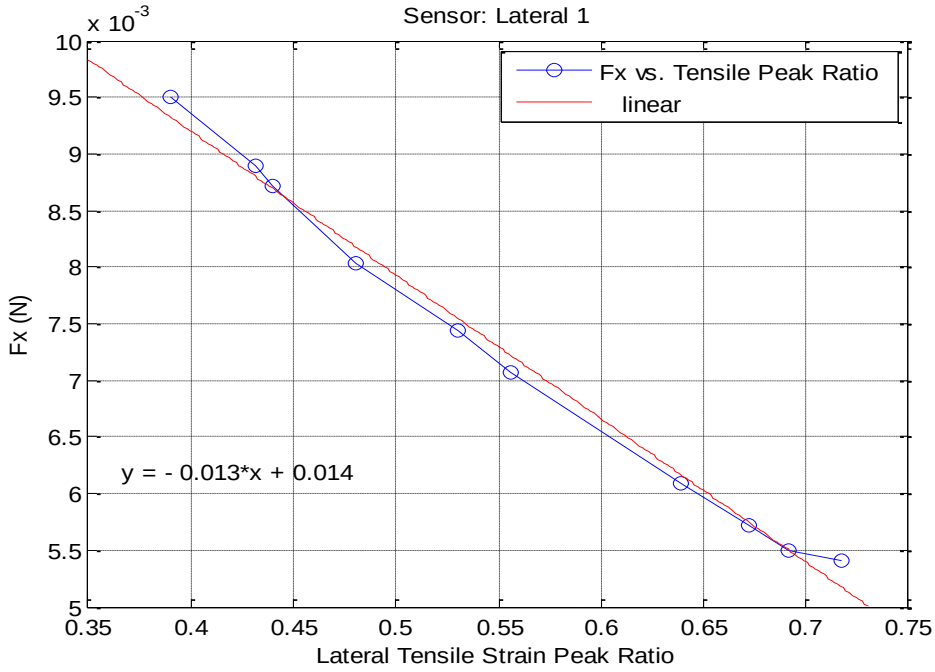

(a) Sensor: Lateral 1.

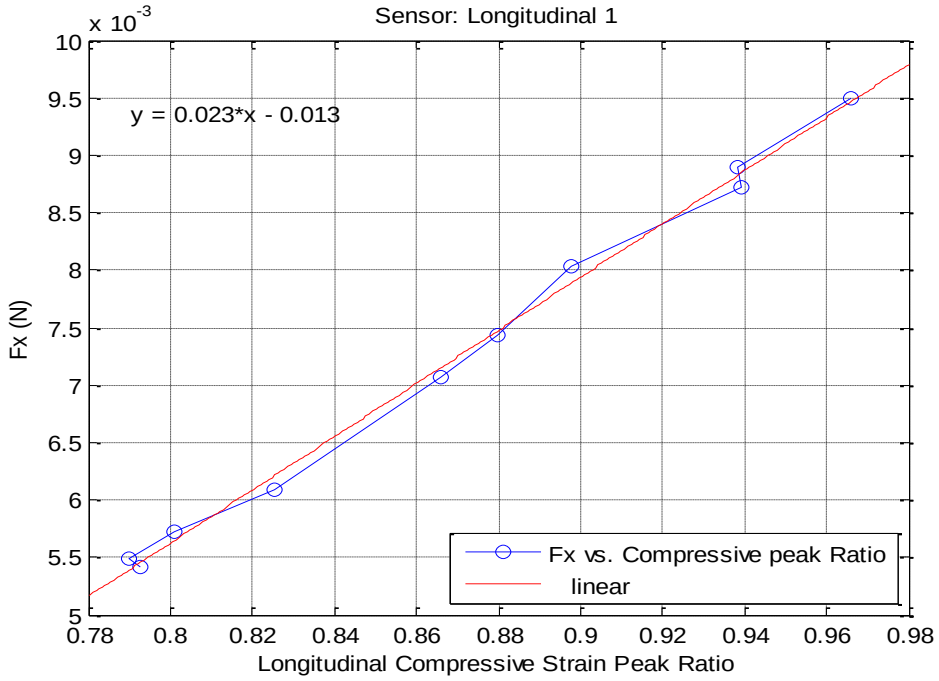

(b) Sensor: Longitudinal 1.

Figure 7.9: Relationship between the strain peak ratio and the longitudinal force ($F_z = 0$ N).

It is worthwhile mentioning that the strain measurements of the tyre's inner surface can also be used to estimate the lateral force (cornering force, steering force) during cornering (steering). In this situation, the lateral strain distribution in the contact patch becomes asymmetrical. This property can be utilised to estimate the tyre lateral force using the strain readings from the two side lateral sensors since they are placed at the contact patch edges across the tyre width. Thus, the variation in the lateral tensile strain peak ratio between the two side lateral sensors can be used as an indication for a variation in the lateral force applied on the tyre (Yang 2011). Although the current setup of the bench-top rig is supposed to produce a straight-line movement and thereby there are no lateral forces on the tyre, this tensile peak ratio can still be used to identify changes in the lateral force caused by the tyre's working conditions. For instance, lateral forces may be caused by mechanical vibrations in the rig that can lead to a sudden short-time lateral movement for the tyre, a slip angle, or a camber angle. It was possible to test the effect of the mechanical vibrations and the presence of a camber angle with the current setup of the rig. To study the effect of the mechanical vibrations on the lateral strain of the tyre, Figure 7.10a shows the lateral tensile strain peak ratio between the two side lateral sensors in each of the speed tests. The ratio increased as the speed in the test increased. It can be said that as the tyre rotational speed increased, more mechanical vibrations are generated in the rig which in turn caused a lateral movement for the tyre. Hence, the lateral tensile strain peak ratio between the two side lateral sensors increased in the speed tests. The effect of the presence of a camber angle will be shown later.

Similarly, the longitudinal compressive strain peak ratio between the two side longitudinal sensors can be related to the lateral force. Figure 7.10b demonstrates this relationship for the speed tests. It agrees with the conclusions drawn for the figure of lateral strains for the two side lateral sensors.

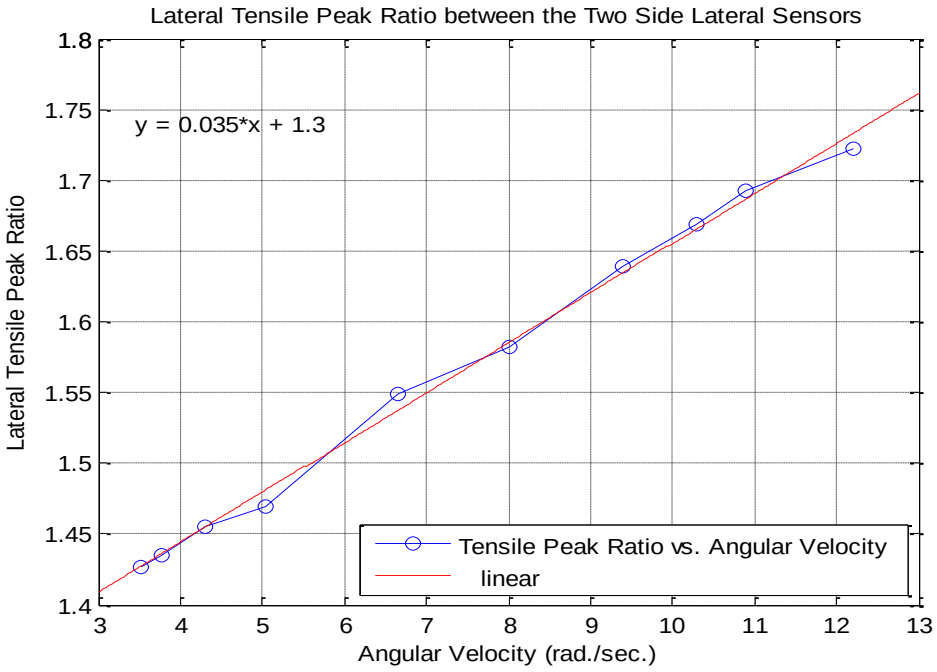

(a) The two side lateral sensors.

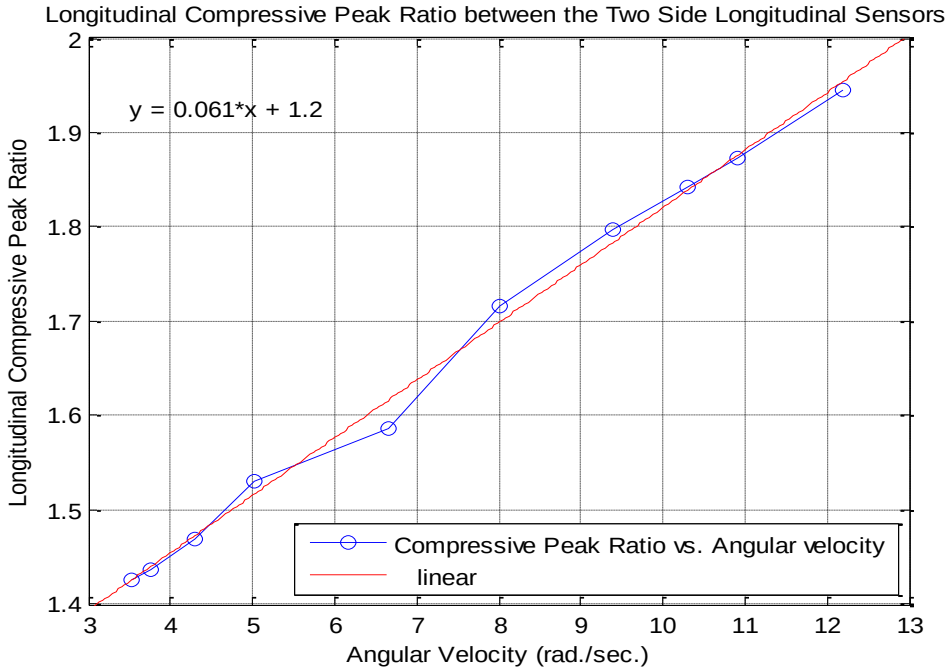

(b) The two side longitudinal sensors.

Figure 7.10: Strain peak ratio between the two side sensors in the speeds' tests ($F_z = 0$ N).

The influence of the vertical load on the lateral force is examined using the strain peak ratio between the two side sensors. Figure 7.11 shows the effect of increasing the vertical load on the ratio of the strain peaks between the two side sensors for the lateral and longitudinal sensors respectively. It indicates that as the vertical load increased, the ratio that corresponded to the lateral force decreased. This means that higher wheel loads provided more grip for the tyre; therefore, the effect of the lateral force decreased.

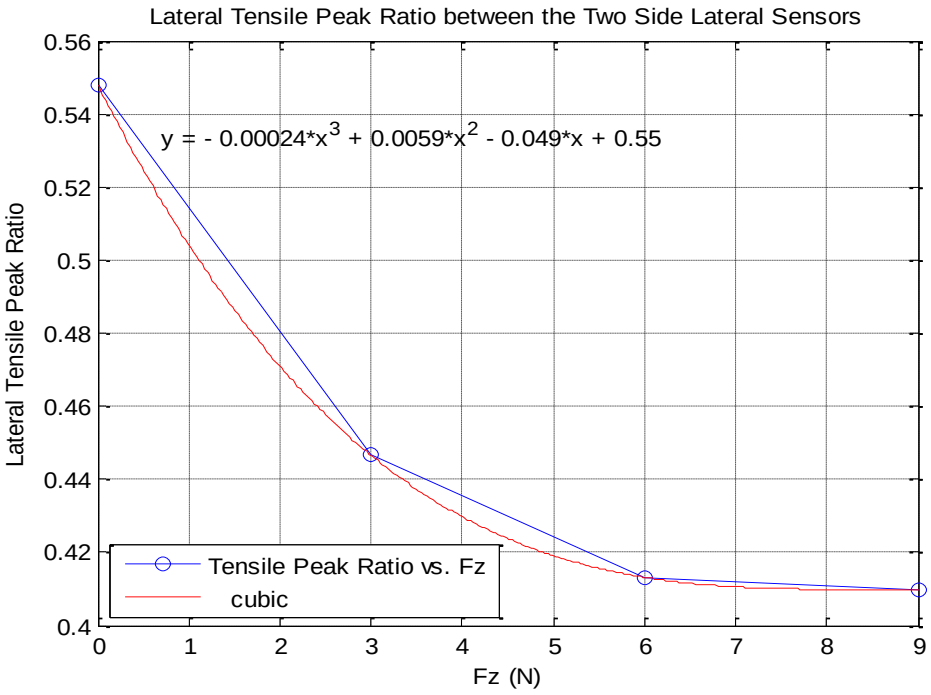

(a) The two side lateral sensors.

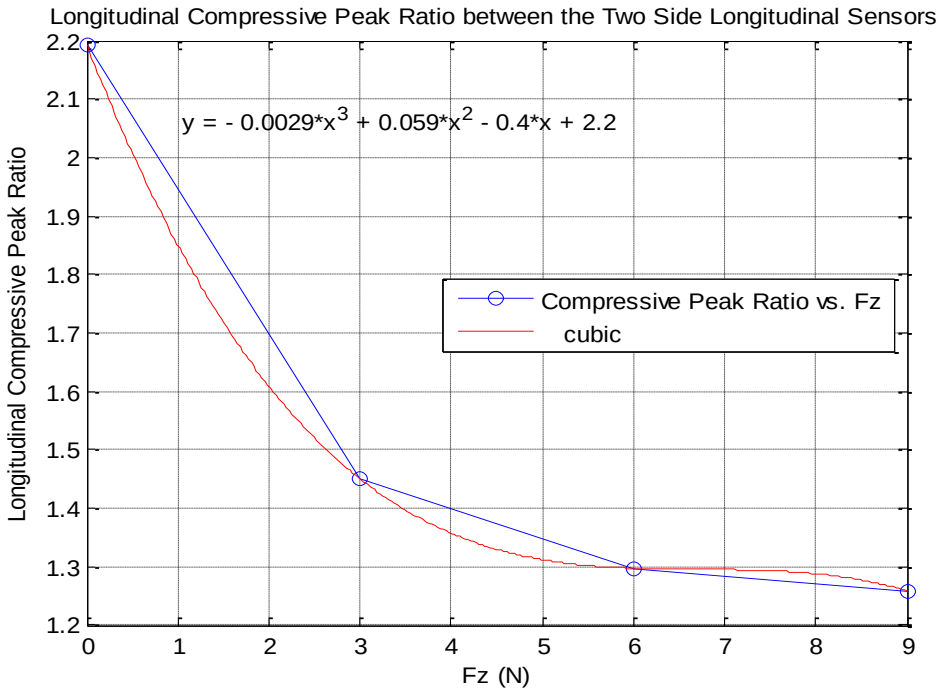

(b) The two side longitudinal sensors.

Figure 7.11: Relationship between the strain peak ratio between the two side sensors and vertical force (HS = High Speed (12.20 rad./sec. = 116.50 RPM)).

7.2 Contact patch estimation

The individual cycles in the filtered first derivative of the strain waveforms obtained from the dynamic tests were used to find the contact patch length and centre. Figure 7.12 shows one of these cycles. As seen in the figure, the cycle of the waveform contains a maximum positive peak and a maximum negative peak. These two peaks represent the points on the tyre with the highest strain rate in a single tyre rotation. In other words, they appear at the positions of the contact patch edges (Matsuzaki & Todoroki 2008a). Thus, the contact patch length and centre can be calculated by finding the distance between these two peaks.

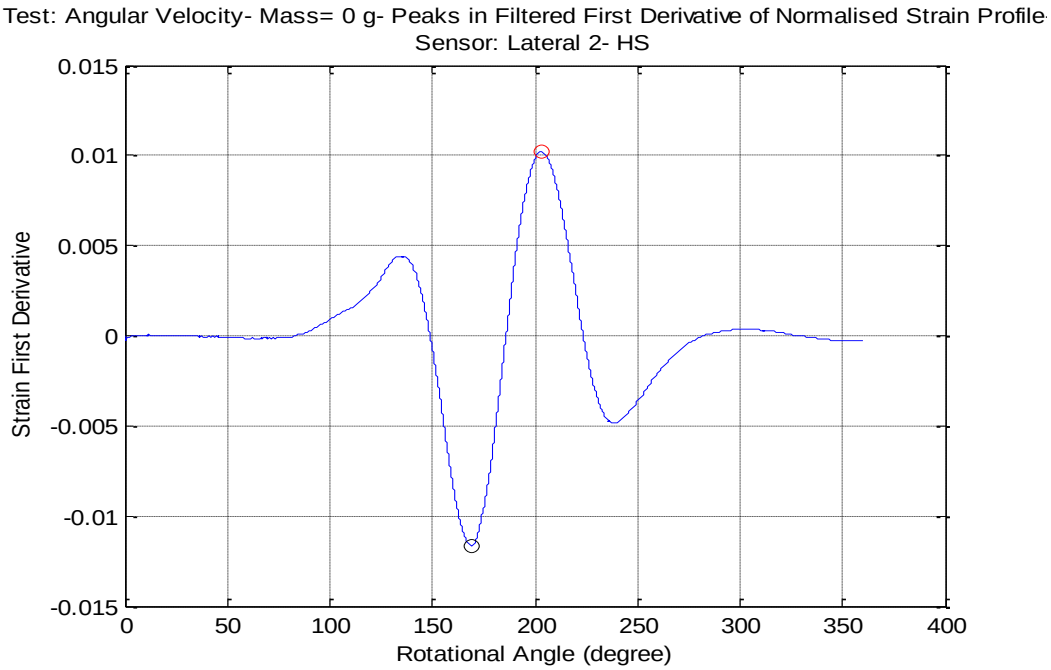

(a) Lateral sensor.

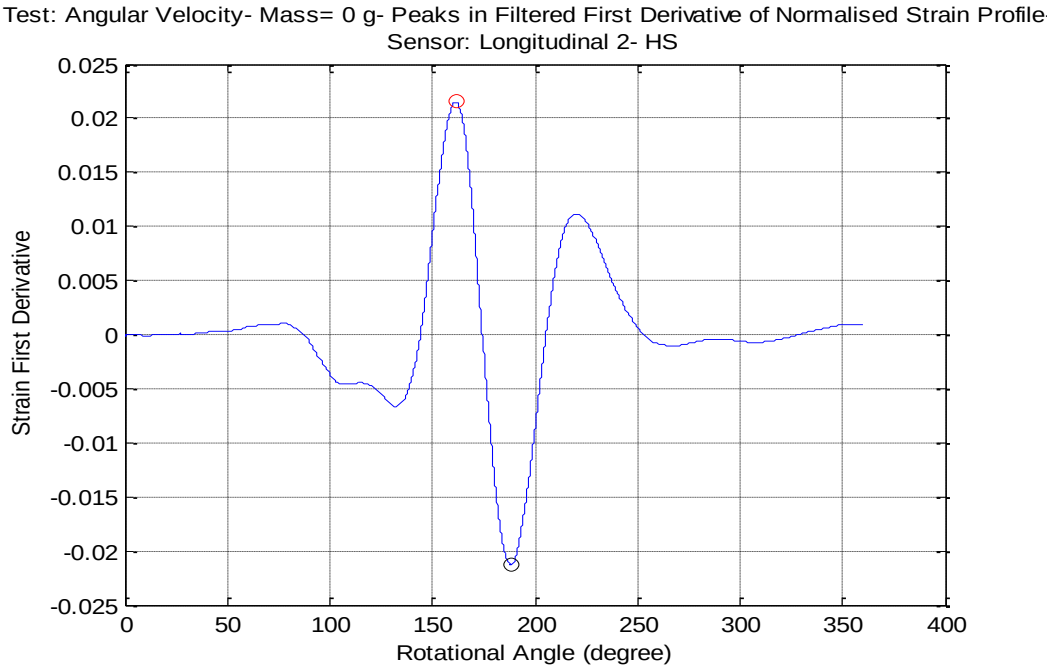

(b) Longitudinal sensor.

Figure 7.12: Finding the contact patch edges using first derivatives of strain profiles (HS = High Speed (12.20 rad./sec. = 116.50 RPM), F_z = 0 N).

Before discussing the contact patch estimation using the strain measurements, it should be stated that the shape of the contact patch for the tyres used herein was irregular. More details about the footprint of these tyres were presented in Section 3.1.2.

Consequently, each sensor provided a relatively different estimation for the contact patch according to its position. Figure 7.13 shows the footprint taken when the tyre was at a standstill on the rig used in the dynamic tests. The figure illustrates the non-uniform contact patch shape of the tyre used in this research.

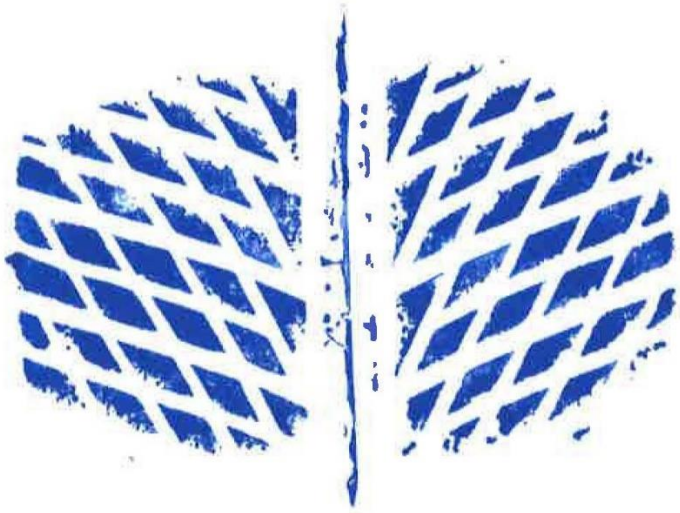

Figure 7.13: Footprint of the tyre used in the dynamic tests (F_z = 9 N).

Firstly, to compare the length of the contact patch under different rotational velocities, Figure 7.14 shows the time required to traverse the contact patches calculated from the sensors' readings in the speed tests. As the speed increased, this time decreased. The difference in the time measured by each sensor was a result of the different mounting positions.

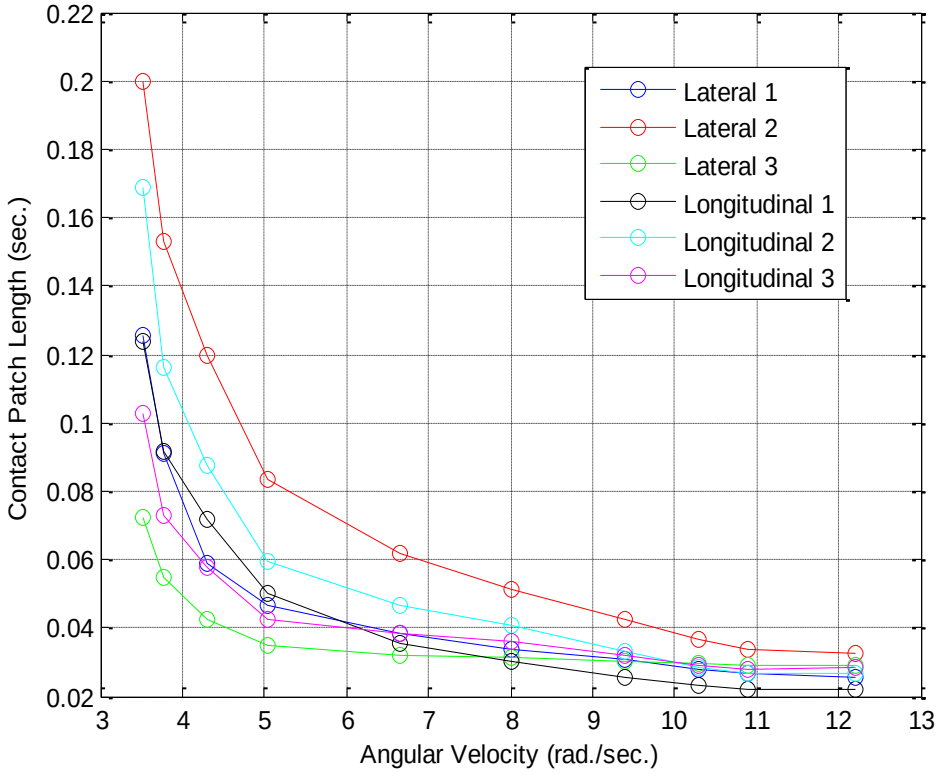

Figure 7.14: Time to traverse the contact patch length calculated using the readings of each sensor in the speeds' tests (F_z = 0 N).

The effect of the wheel load (F_z) on the patch length is examined secondly. With increasing wheel load, the tyre deformations within the contact patch become bigger and thereby the length of the contact patch increases (Matsuzaki & Todoroki 2008a). Figure 7.15 presents the relation between F_z and the contact patch length. For the lateral sensor (Figure 7.15a), this relationship cannot be approximated with a linear fitting. Figure 7.15b illustrates that the longitudinal sensor's reading reflected a positive linear proportionality between the wheel load and the contact patch length. Therefore, it can be concluded that the longitudinal sensors produced better estimations for the length of the contact patch. This is because the longitudinal sensors stretch in a parallel direction with respect to the contact patch length.

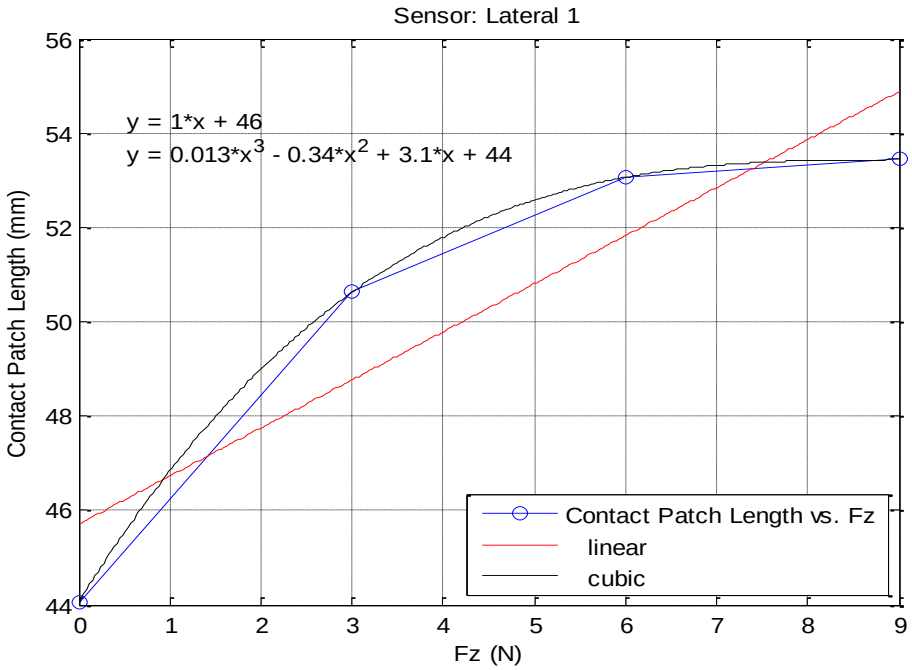

(a) Sensor: Lateral 1.

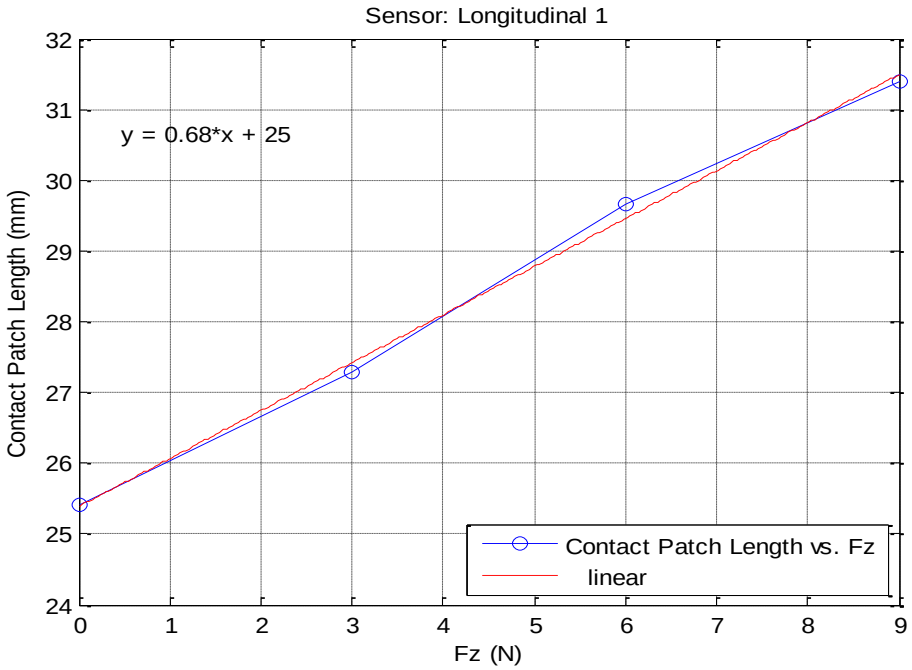

(b) Sensor: Longitudinal 1.

Figure 7.15: Relationship between the contact patch length and wheel load (HS = High Speed (12.20 rad./sec. = 116.50 RPM)).

Another consequence of the increase in the wheel load is the decrease in the tyre effective radius because the centre of the wheel becomes lower. The effective radius that corresponds to the applied wheel load was found using image processing for screenshots from videos of the tests. The effective radius was measured in several rotations where it was found that the values were very close. The average of these values was calculated to represent the effective radius for the exerted wheel load. Figure 7.16 presents the relationship between the applied wheel load and the tyre effective radius.

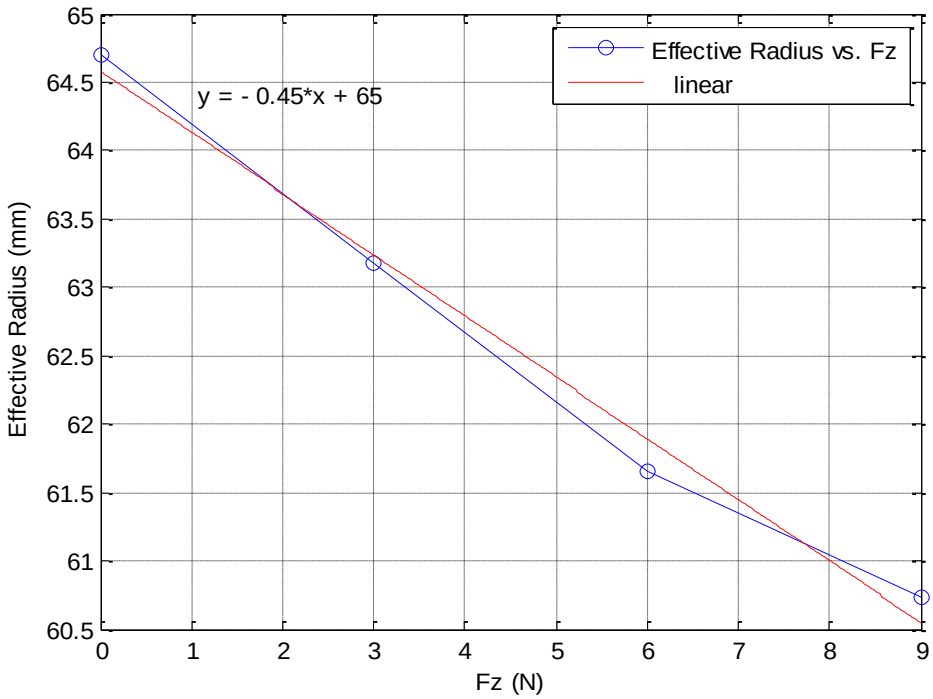

Figure 7.16: Relationship between the tyre effective radius and wheel load (HS = High Speed (12.20 rad./sec. = 116.50 RPM)).

From the previous two figures, it can be concluded that there is a relationship between the contact patch length and the tyre effective radius (Matsuzaki & Todoroki 2008a). As shown in Figure 7.17, as the contact patch length increased, the effective radius decreased. The relationship between the effective radius and the patch length extracted from the strain readings of the longitudinal sensor (Figure 7.17b) presents a linear proportionality as in the case of the pneumatic car tyres (Matsuzaki 2007).

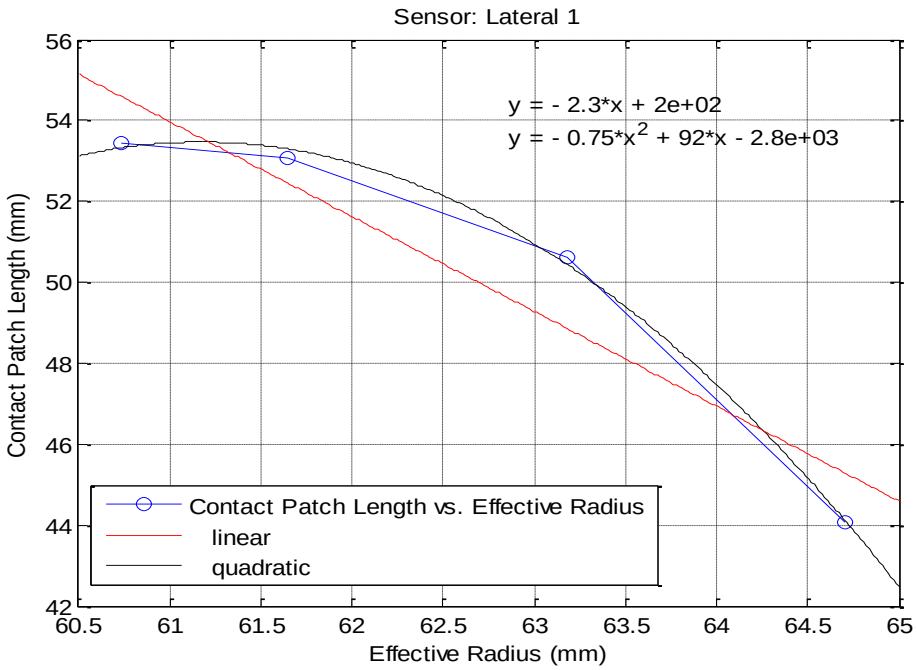

(a) Sensor: Lateral 1.

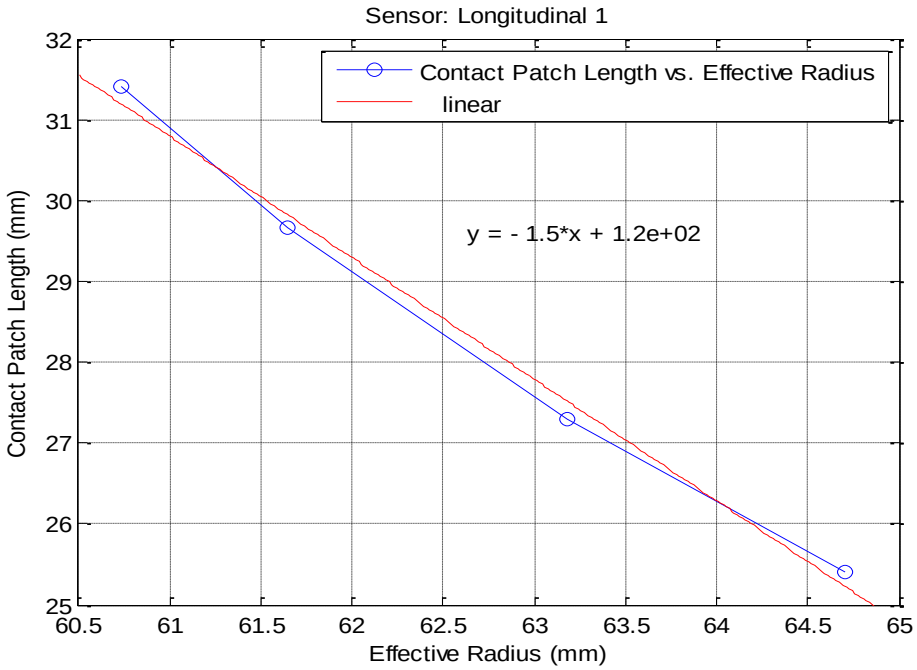

(b) Sensor: Longitudinal 1.

Figure 7.17: Relationship between the contact patch length and tyre effective radius (HS = High Speed (12.20 rad./sec. = 116.50 RPM)).

Lastly, it is stated that the longitudinal force (F_x) is related to the shift in the angular position of the contact patch centre (Savaresi et al. 2008). This relationship was tested in this research using the estimations of the contact patch centre under different values of the longitudinal force. Figure 7.18 shows a linear relationship between the contact centre position detected by a lateral or a longitudinal strain sensor and the longitudinal force.

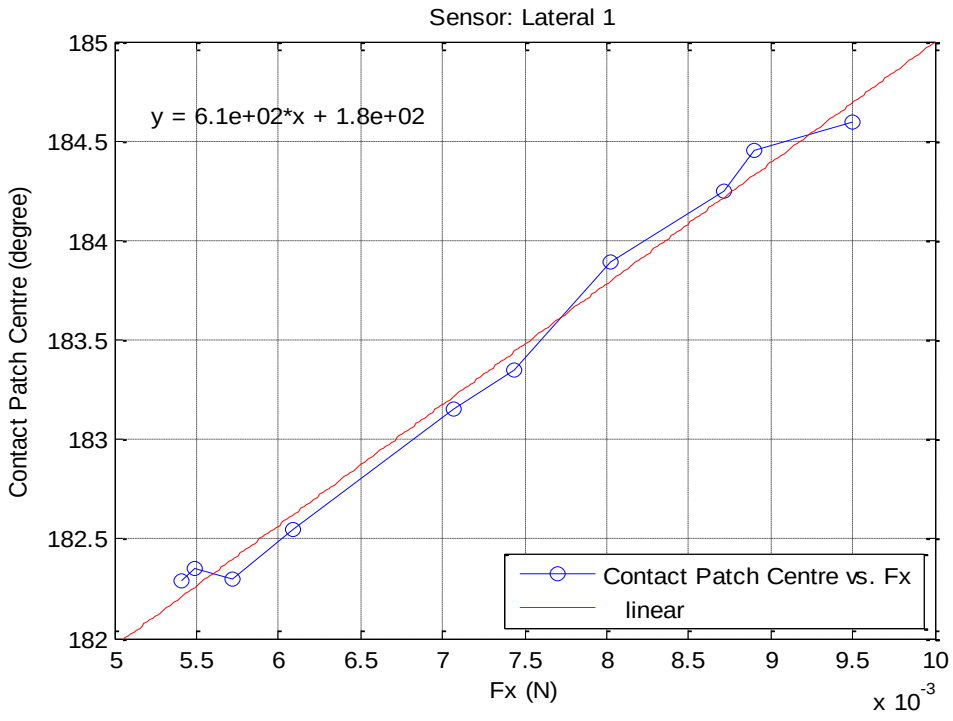

(a) Sensor: Lateral 1.

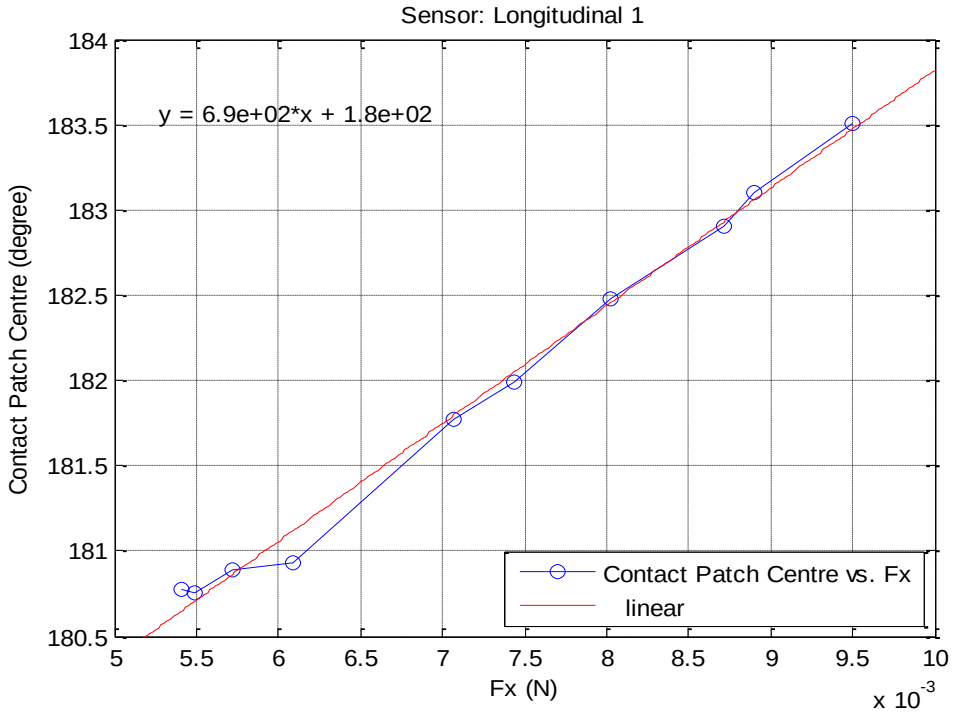

(b) Sensor: Longitudinal 1.

Figure 7.18: Relationship between the contact patch centre and longitudinal force in the speeds' tests (F_z = 0 N).

7.3 Angular velocity estimation

This section investigates the relationship between the tyre angular velocity and the in-tyre strain measurements. Figure 7.19 compares three representative waveforms of strain data resulted from applying low, medium, and high speed. It can be seen that as the speed increased, the waveform became narrower. In other words, when higher speeds were applied, more wave cycles were produced during a particular period of time and thus the waveforms appeared as if they were contracted.

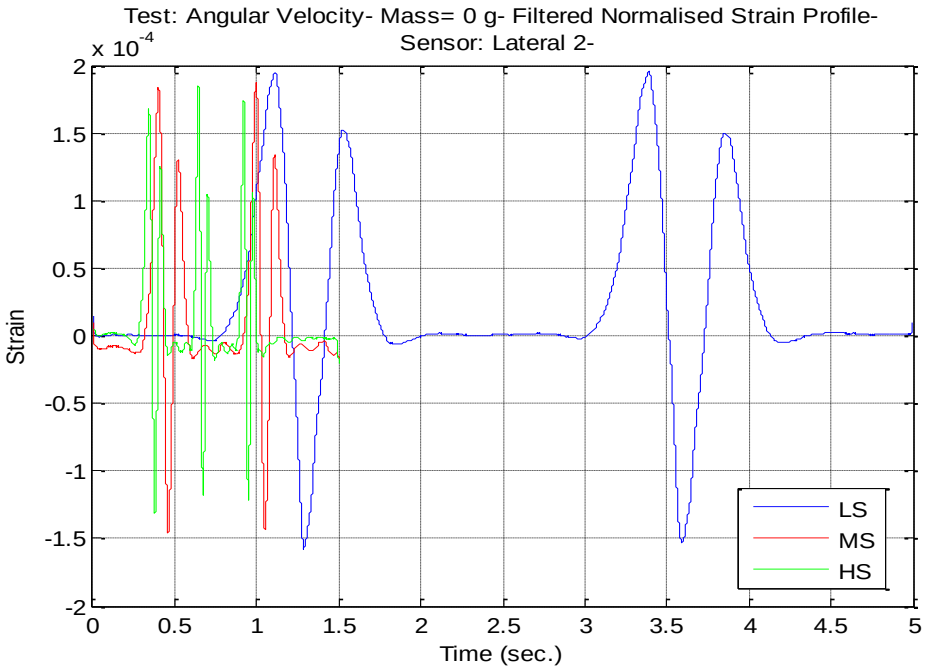

(a) Sensor: Lateral 2.

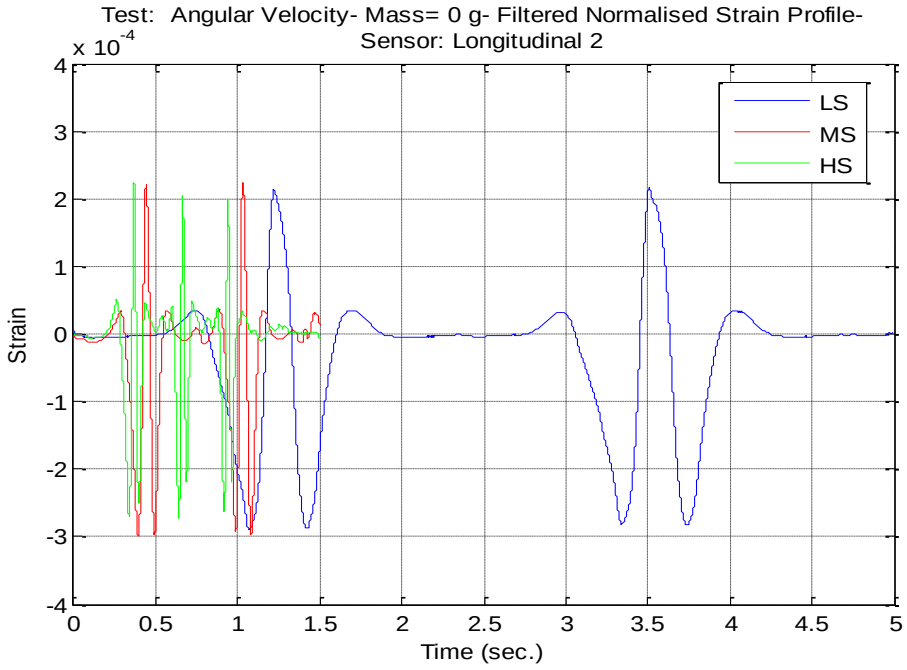

(b) Sensor: Longitudinal 2.

Figure 7.19: Comparing sensors' readings for low, medium, and high speeds (LS = Low Speed (3.50 rad./sec. = 33.42 RPM), MS = Medium Speed (6.65 rad./sec. = 63.50 RPM), HS = High Speed (12.20 rad./sec. = 116.50 RPM), F_z = 0 N).

To compare the waveform shapes, the strain profiles are plotted with respect to the rotational angle (Figure 7.20). The figure shows that the waveform shapes were consistent and that the strain peaked at almost the same angular positions under the three speed's levels.

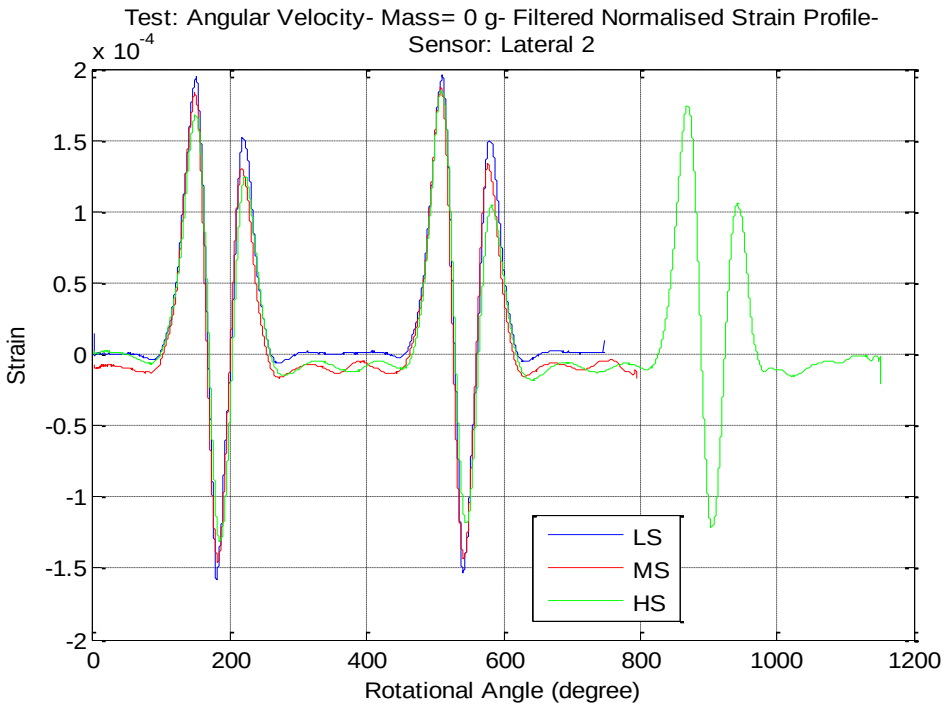

(a) Sensor: Lateral 2.

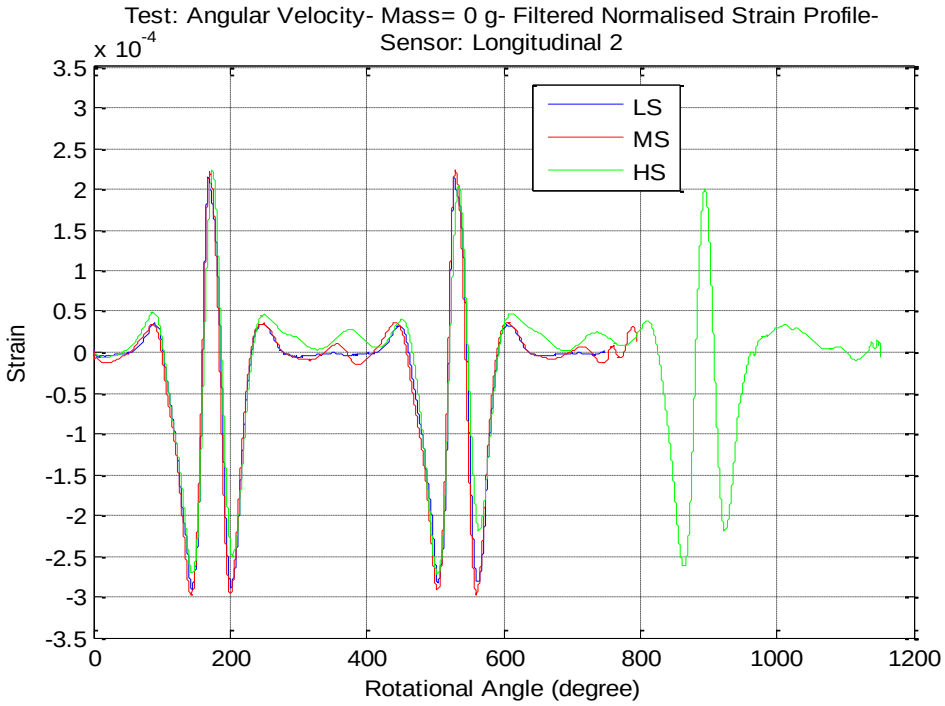

(b) Sensor: Longitudinal 2.

Figure 7.20: Filtered sensors' readings with respect to tyre rotational angle

(LS = Low Speed (3.50 rad./sec. = 33.42 RPM),

MS = Medium Speed (6.65 rad./sec. = 63.50 RPM),

HS = High Speed (12.20 rad./sec. = 116.50 RPM), F_z = 0 N).

One of the advantages of mounting a strain sensor inside a tyre is that the tyre angular velocity can be calculated from the strain readings without the need for other sensors. The revolution time can be found using the time history of the strain readings. This time can be utilised to determine the tyre's angular velocity (Yang 2011). The benefit of using the in-tyre strain sensor instead of the encoder to find the angular velocity is that the strain sensor will continue to record the readings in case the tyre motor stops but the tyre continues to spin before coming to a complete stop. Such a situation can occur if the motor stalls while the tyre is rotating on a low-friction surface. Thus, more information about the tyre's movement can be obtained using the in-tyre sensors.

Figure 7.21 compares the tyre angular velocity estimated from the in-tyre strain sensors and from the encoder. It shows that the strain sensors were able to determine the velocity with a sufficient degree of agreement with the encoder readings where the error was 3.98 %. The figure also demonstrates a nonlinear relationship between the tyre angular velocity and the time of the revolution.

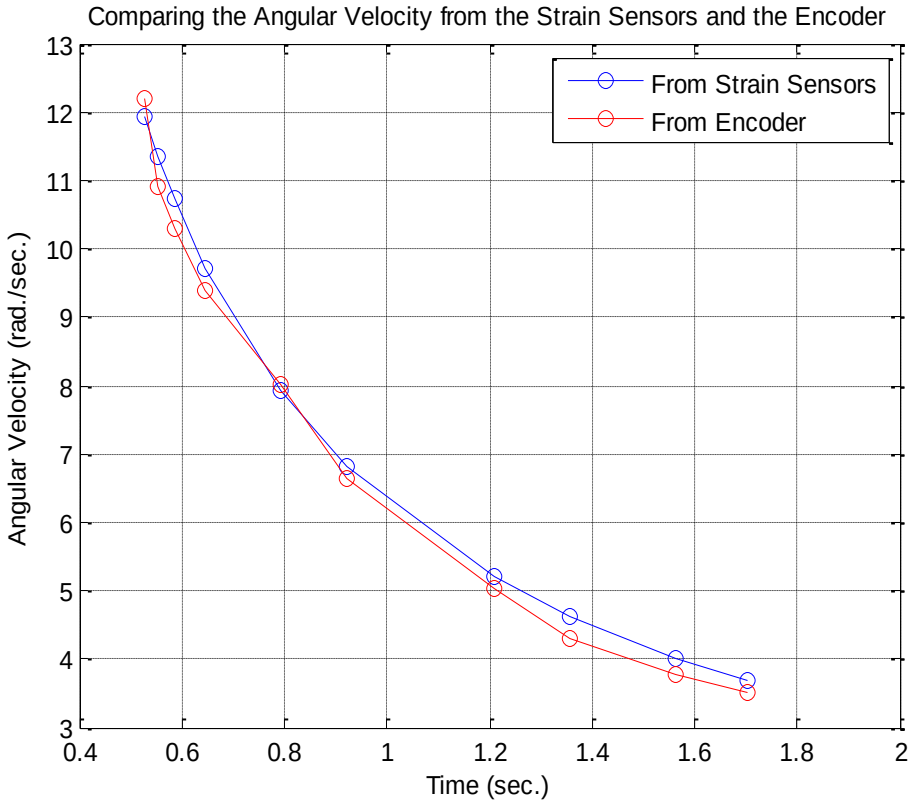

Figure 7.21: Comparing the angular velocity obtained from the strain sensors and the encoder (F_z = 0 N).

The effect of the vertical load on the angular velocity is examined by conducting a number of tests where the angular velocity was fixed and the wheel load was increased. Figure 7.22 shows that the time required to complete one tyre revolution increased as the vertical load applied to the tyre increased. This means that increasing the wheel load resulted in decreasing the tyre angular velocity as illustrated in Figure 7.23. Figure 7.23 indicates that the measurements of the in-tyre strain sensors can be utilised to build an accurate relationship between the wheel load and the tyre angular velocity. Such a relationship can be used to design an efficient speed control system for robots.

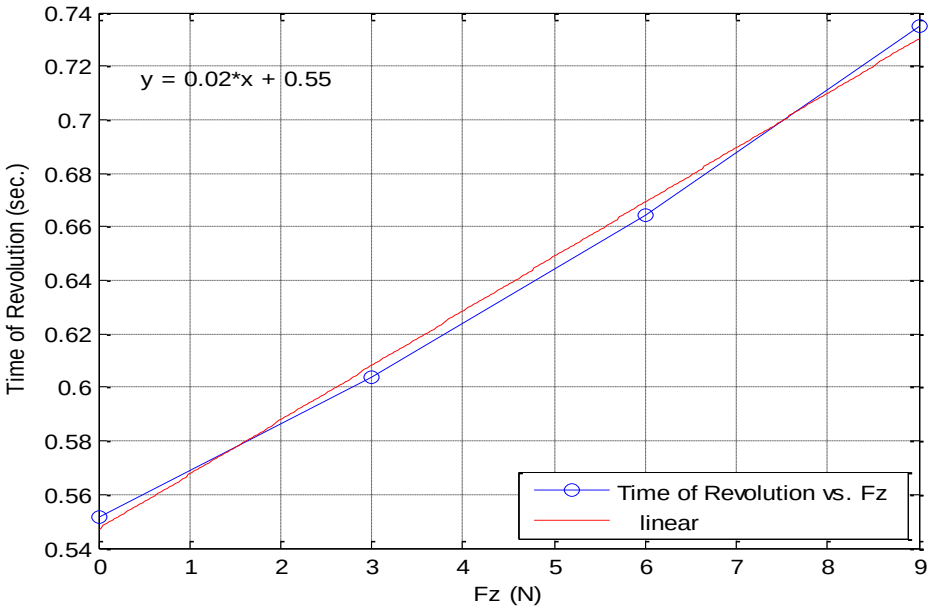

Figure 7.22: Relationship between vertical force and time of revolution (HS = High Speed (12.20 rad./sec. = 116.50 RPM)).

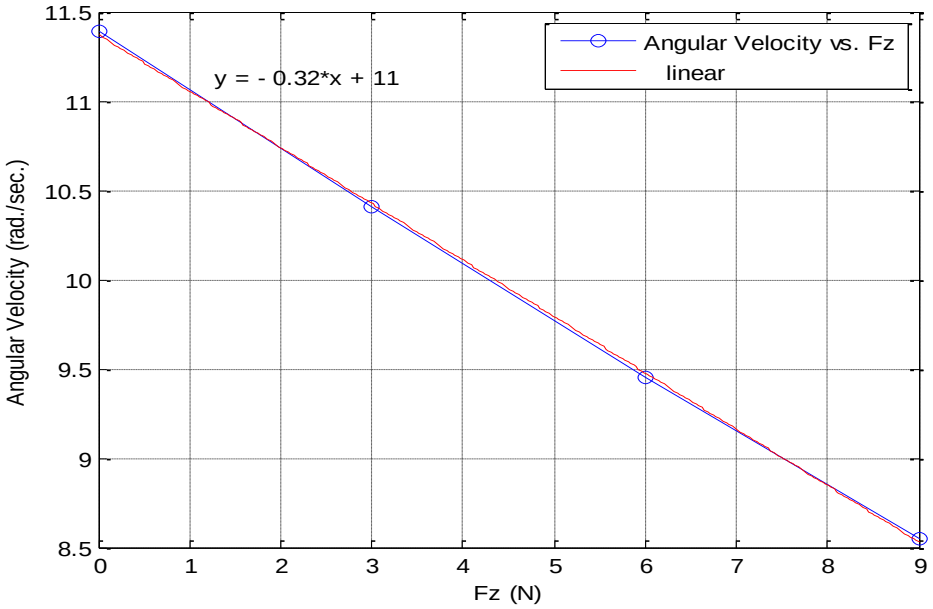

Figure 7.23: Relationship between vertical force and angular velocity (HS = High Speed (12.20 rad./sec. = 116.50 RPM)).

A last note about the tyre angular velocity in the dynamic tests is that a small change in the velocity was observed between some of the runs although the supply voltage was set to the same value. This change was caused by the motor that might operate at a slightly different speed during some runs. Figure 7.24 illustrates this point by comparing the angular velocity of two tests. It can be concluded from this figure that the tyre in Test 1 was rotating faster. To clarify, it was found from the video of these tests that during, for example, 0.15 sec., the tyre in Test 1 travelled 221.87 mm whereas it travelled 192.56 mm in Test 2. Consequently, a small horizontal shift in the rotational angles appeared when comparing the strain profiles obtained from these two tests as shown in Figure 7.25.

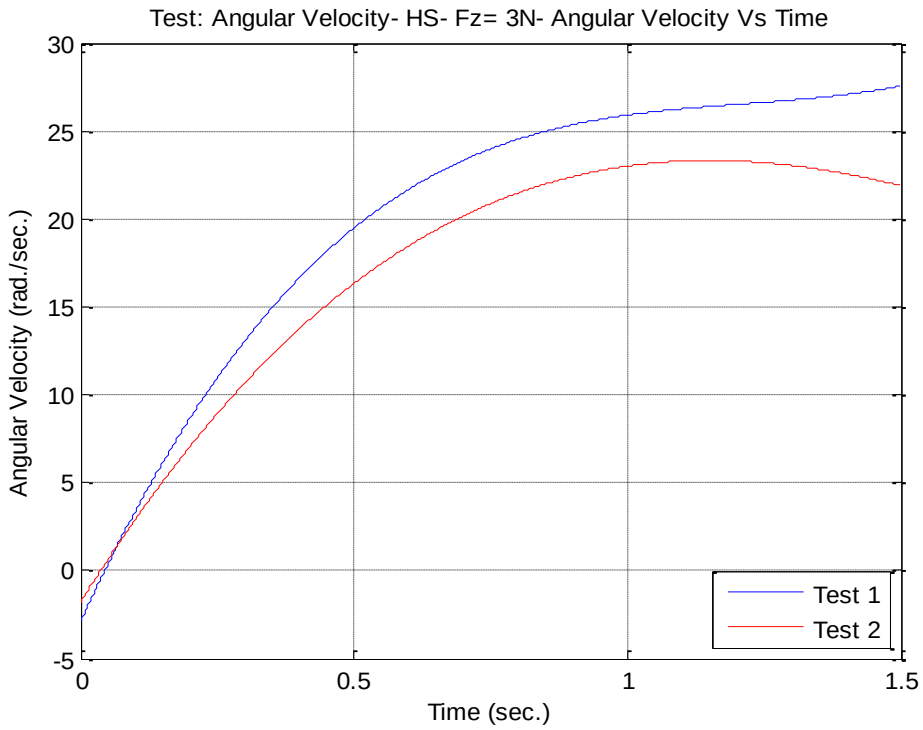

Figure 7.24: Comparing the angular velocity for two tests under the same initial voltage and vertical load (HS = High Speed (12.20 rad./sec. = 116.50 RPM), F_z = 3 N).

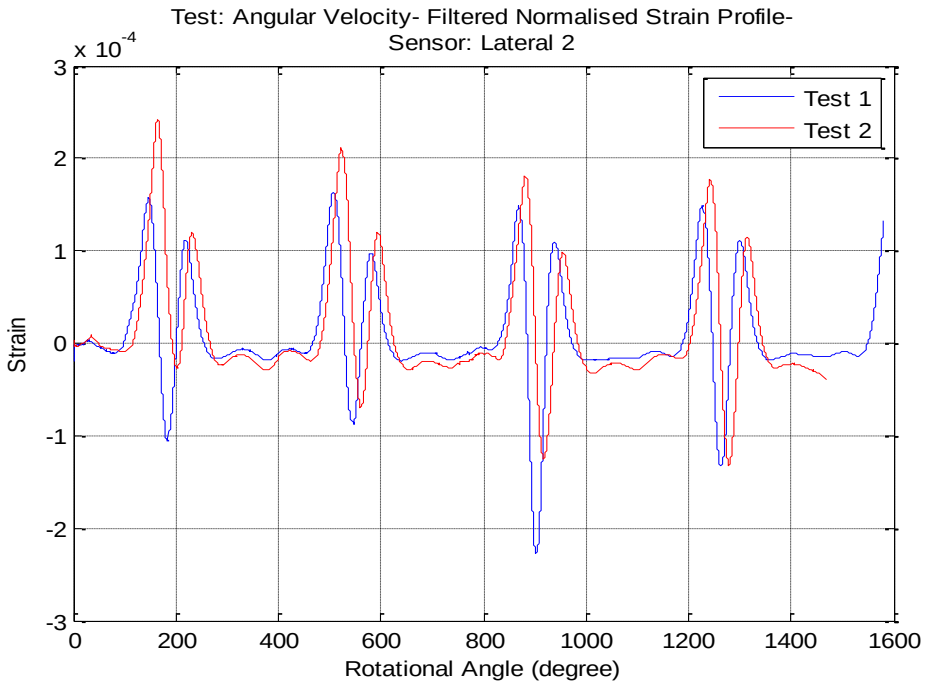

(a) Sensor: Lateral 2.

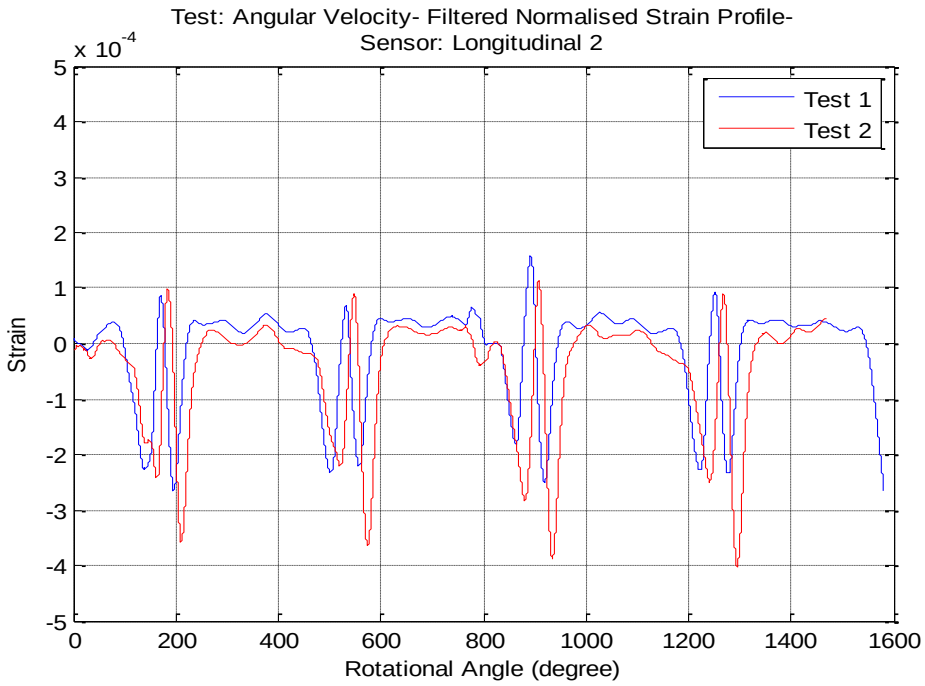

(b) Sensor: Longitudinal 2.

Figure 7.25: Comparing the strain readings from two tests under the same initial voltage and vertical load (HS = High Speed (12.20 rad./sec. = 116.50 RPM), F_z = 3 N).

7.4 Camber angle estimation

The relationship between the camber angle and the strain measurements of the in-tyre sensors is examined. The lateral strain measurements can be used to identify changes in the camber angle of the tyre. Figure 7.26 compares the lateral strain readings acquired by one lateral sensor under no-camber (Camber Angle = 0°) against different camber angles. It is seen that the strain values were higher in the camber cases. The figure also shows that as the value of the camber angle increased, the strain increased because the tyre became more pressed against the road.

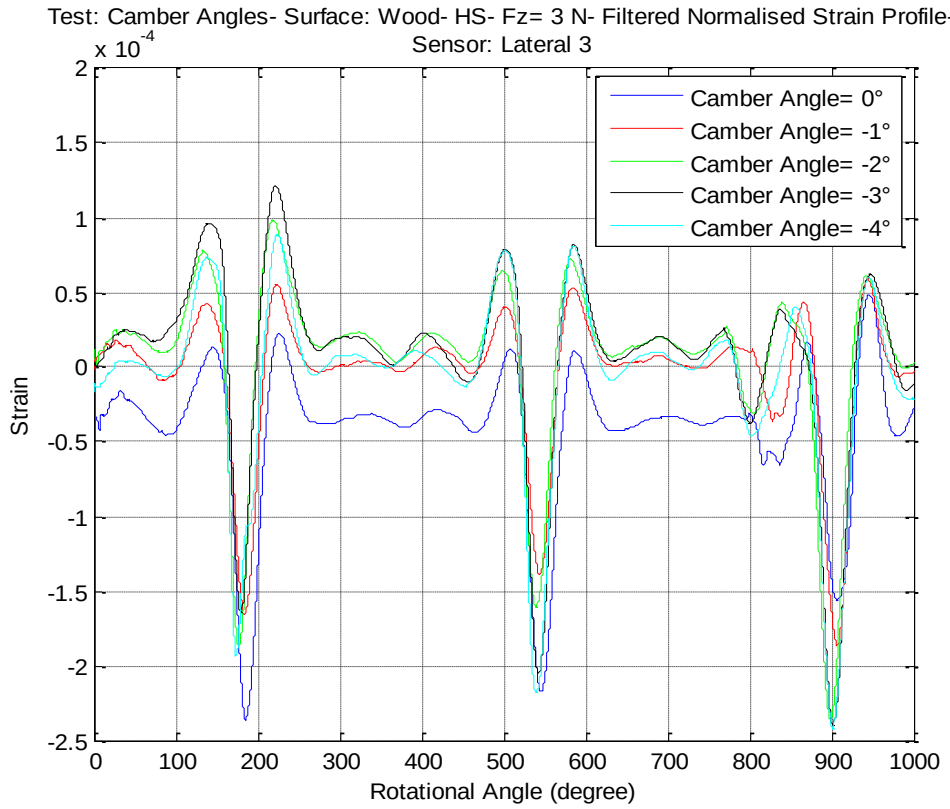

Figure 7.26: Lateral strain profiles obtained from a lateral sensor under different camber angles (Sensor: Lateral 3,
HS = High Speed (12.20 rad./sec. = 116.50 RPM), F_z = 3 N).

The relationship between the strain and the camber angle is illustrated by observing the average value of the two lateral tensile peaks from a lateral sensor at the different camber angles (Figure 7.27). This figure shows that the average value increased in almost a linear manner in response to the increase in the camber angles.

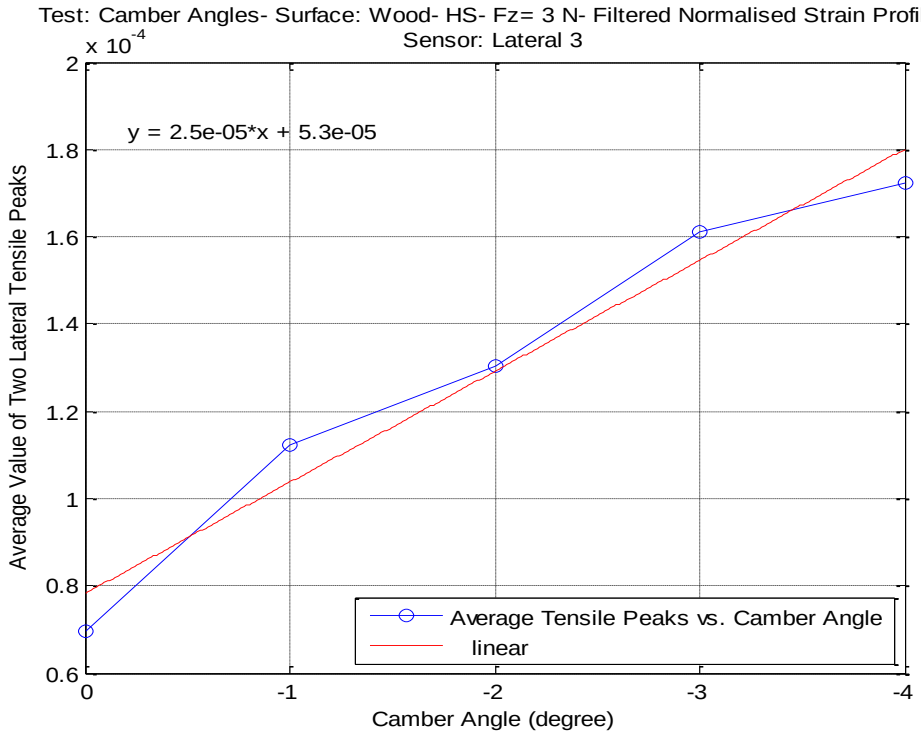

Figure 7.27: Average value of the two lateral tensile peaks for a lateral sensor (Lateral 3) at different camber angles
(HS = High Speed (12.20 rad./sec. = 116.50 RPM), F_z = 3 N).

Since introducing a camber angle causes the tyre to incline, the measured strain values are different across the width of the contact patch. As shown in Figure 7.28, since the side sensor named Lateral 1 was on the pressed side of the tyre, the strain readings obtained from this sensor were higher than the readings provided by the lateral sensor located on the opposite side of the tyre, i.e., Lateral 3.

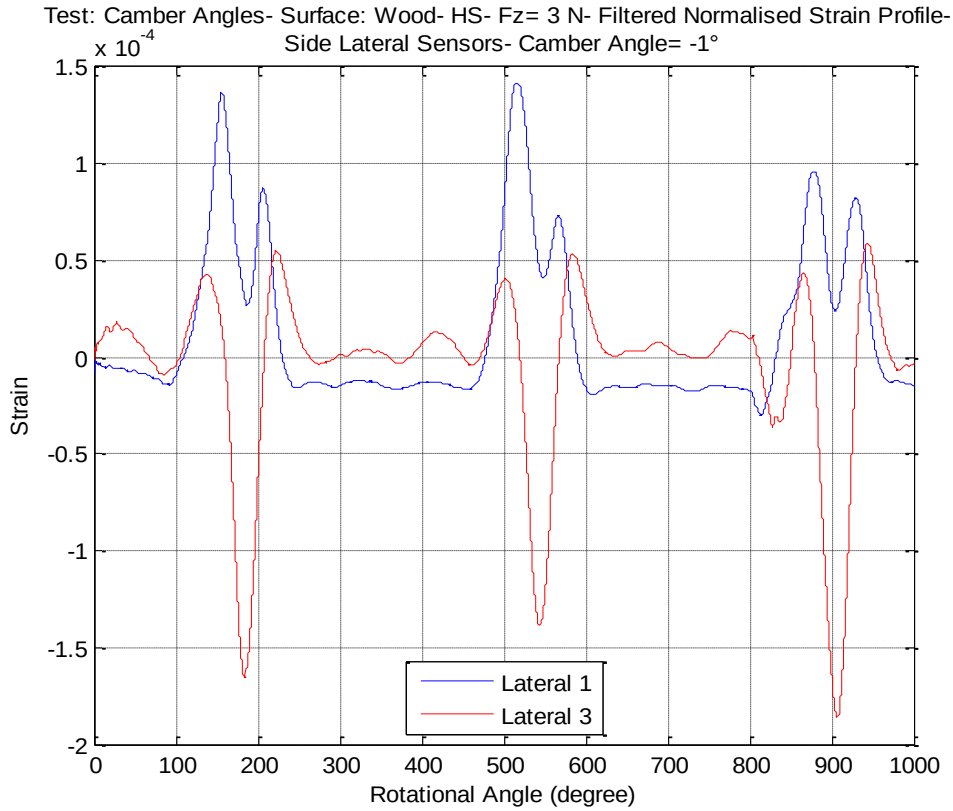

Figure 7.28: Comparing the readings of the two side lateral sensors when applying a camber angle (HS = High Speed (12.20 rad./sec. = 116.50 RPM), F_z = 3 N).

Thus, the effect of the camber angle can be observed by comparing the readings of the side lateral strain sensors as they were expected to show the maximum and minimum strains. The ratio of the lateral tensile strain peaks between the two side lateral sensors was used for this comparison (Yang 2011). Figure 7.29 illustrates that as the camber angle increased, the lateral tensile ratio increased.

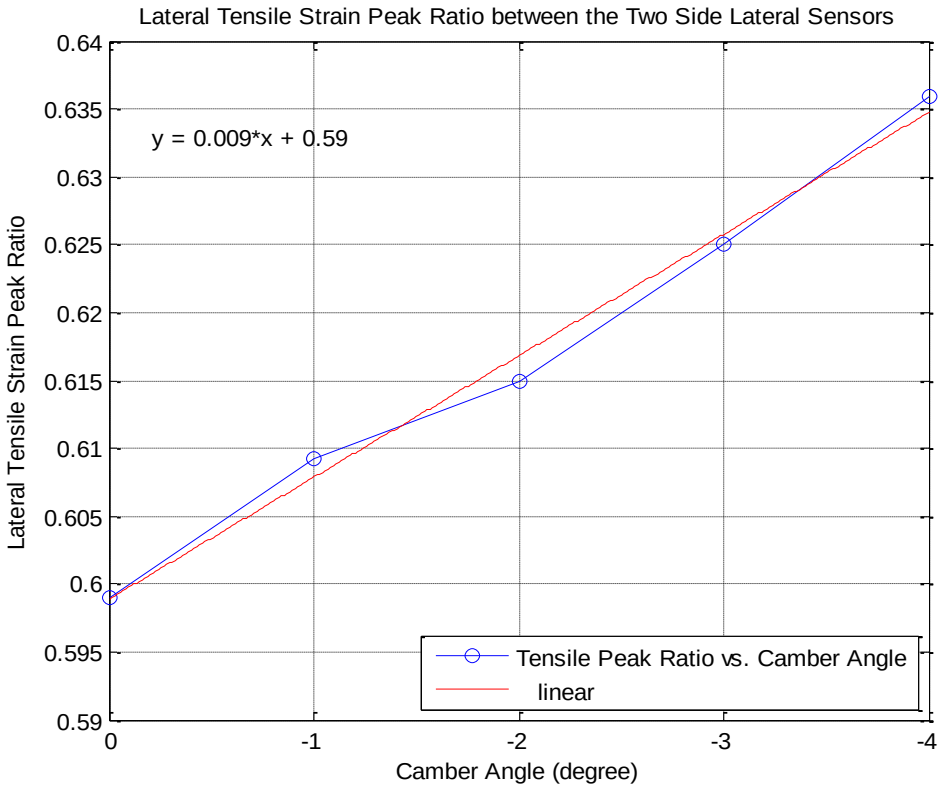

Figure 7.29: Lateral tensile strain peak ratio between the two side lateral sensors at different camber angles (HS = High Speed (12.20 rad./sec. = 116.50 RPM), F_z = 3 N).

7.5 Summary

In this chapter, the tyre's forces, contact patch, angular velocity, and camber angle were extracted from the in-tyre strain measurements. The estimation of these variables utilising the direct measurements from the tyre-ground interface can result in building reliable control systems.

It was concluded in Sections 4.1.2 and 4.2.1 that the strain profiles for the small non-pressurised tyres are similar to those of pneumatic car tyres. As a result, most of the models used by other researchers to describe the strain waveforms of pneumatic car tyres were utilised in this chapter for the non-pressurised tyres. In general, these can be divided into two main models as shown in Figure 7.30. The first model depends on relating features from the strain profiles to the tyre's mechanical properties. It uses the time history of the strain waveform to estimate the tyre's angular velocity. It also uses the strain peaks at the contact patch edges in the strain profiles to estimate the forces in three directions and the camber angle. The second model describes the tyre's parameters using the contact patch variables. The contact patch is identified by locating the angular positions of the contact patch edges. These positions are found by determining the two points with the highest strain rate in the time differential of the strain profiles. Using these positions, the contact patch length and centre can be calculated. The contact patch length is related to the vertical force and effective radius whereas the shift in the patch centre is linked to the longitudinal force.

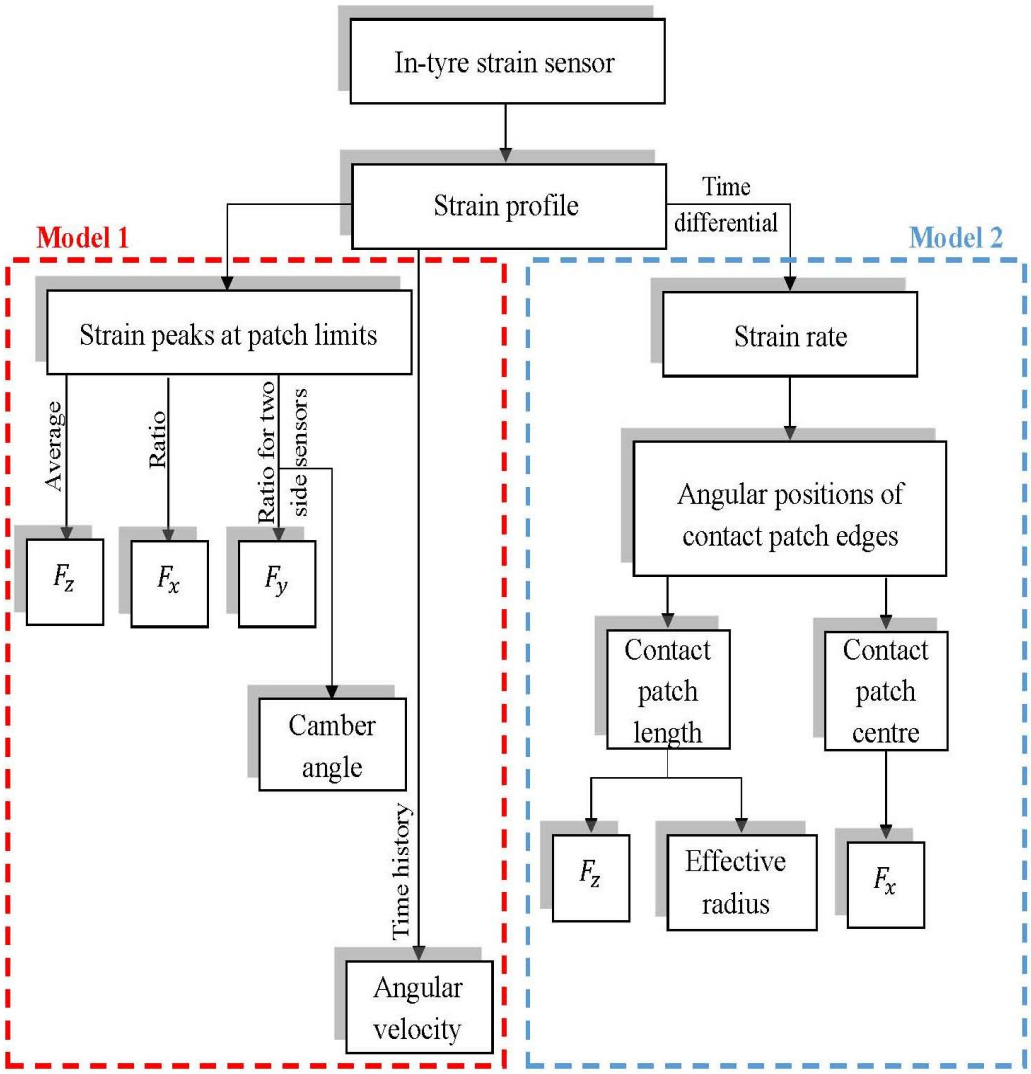

Figure 7.30: Models used in Chapter 7 to extract the tyre's properties from the in-tyre strain measurements.

The relationships presented in this chapter illustrated that the two models can be used for non-pressurised tyres. However, the strain change that resulted from changing a particular variable was not perfectly consistent in some of these relationships. This inconsistency was caused by the occurrence of unexpected deformations for this type of tyres. For this reason, a few points deviated from the model used to describe these relationships. Therefore, the curve of the relationships was irregular when compared to the approximation model used to describe it.

Chapter 8

Conclusions and Future Work

This thesis has investigated the feasibility of equipping small non-pressurised tyres that are widely used for small mobile robots with sensing capabilities. This research has also explored some of the benefits of using an in-tyre strain-sensing system in small mobile robots. The measurements of the in-tyre strain sensors were used to derive features that correspond to the tyre's working condition, surrounding environment, and mechanical properties.

This chapter shows the achievement of the research objectives, presents the research findings, and suggests developments for future work.

8.1 Achievement of the research objectives

This section discusses the achievement of the objectives that were set in Section 1.7.

Objective 1: Identify an appropriate sensing method, choosing suitable sensors, and suggesting the best design for the sensor system for small non-pressurised tyres.

The requirements for designing a low-cost sensing system inside small non-pressurised tyres were presented in Section 1.1. The in-tyre sensing methods were presented in Section 2.1. After examining the sensing methods in terms of satisfying these requirements, strain sensing utilising a flexible sensor was found to be the best

solution for a low-cost sensing system for the tyre used in this work. This system was capable of providing the information required for the applications presented in this thesis. Low cost here refers to sensors of the order of $100 AUD.

To identify possible sensors for the system, a preliminary study of the different available types and technologies of tactile sensors was conducted. In this study, the advantages and disadvantages of each sensor were taken into consideration (Dahiya et al. 2010; Yousef et al. 2011; Girão et al. 2013; Lucarotti et al. 2013). Special attention was given to the sensors that have already been used in the field of intelligent tyres. The reason is that these were found to be the closest to this research in terms of installation and measured quantities. Additionally, the sensors must fulfil the requirements for building a sensing system inside a small non-pressurised tyre. These requirements are low cost and complexity, availability, compatibility with the tyre's material, and small size. It was concluded that the standard resistive strain gauges successfully meet all these specifications. Developing a new tyre sensing system was indispensable to reach the specific research objectives. The sensors' type, number, and configuration were determined according to the type of the tyre used in this work and the targeted applications. More details about the selection of the sensing method and the sensors were given in Sections 2.4 and 2.5.

To suggest a suitable design for the sensory system for the particular tyre used herein, footprint tests were conducted using a compression machine (Chapter 3). These tests helped in studying the contact patch in terms of its shape as well as the effect of changing the vertical force on varying its shape and size. From the results of these tests, it was decided to place the sensor system in an area that corresponds to the smallest possible footprint. The best positions to place the sensors were decided according to the shape of this footprint and the available space inside this area. With this placement, it is ensured that all the sensors are located inside the contact patch under all possible loading conditions. Other conditions were placed so that the sensor design can fulfil the research objectives. Most importantly, it must be able to capture strain measurements in both longitudinal and lateral directions. The reason for that was to cover the possible cases of tyre's straight-line steady state rolling, braking, traction, and turning. In addition, the design should use the minimum number of required sensors and allow placing the sensors in the desired positions. Considering these

factors, a sensor system design was determined and implemented. This design consisted of six strain gauges placed on the inner surface of the tyre. Three strain sensors were mounted in the tyre's longitudinal direction to measure the longitudinal strains while another three sensors were placed in the tyre's lateral direction to measure the lateral strains.

Achieving this objective led to correctly collecting the in-tyre measurements for the non-pressurised tyre used herein. More details are given in Point 1 in Section 8.2.

Objective 2: Build low-cost testing platforms to acquire the data in static and dynamic tests.

The commercial tyre-testing rigs that are utilised for conducting research on tyres are designed for pneumatic car tyres. These rigs are bulky and expensive. In addition, a large number of these rigs adopt a car tyre rotating on a drum. This configuration can generate unrealistic readings when investigating tyre sensors. It does not produce the actual shape of the contact patch when the tyre rotates over the ordinary flat road (Erdogan 2009). Therefore, the lack of testing equipment for small non-pressurised tyres had necessitated building custom-designed test beds within a low budget to collect the data in this work. To achieve this, two small-scale bench-top rigs were built using low-cost materials (Chapter 3). The first rig was specially designed to conduct static experiments. It served three purposes. First, verify that the sensor system was providing acceptable readings. This indicated the suitability of the materials utilised for the manufacturing, the success of the installation steps, and the efficiency of the DAQ system. Second, study the responses of the strain sensors to changing the vertical force, the longitudinal force, and the angular position. Third, construct strain profiles by collecting the readings at different angles. Utilising the results of the static tests, a second rig was built to perform dynamic tests. This rig provided the opportunity to examine the in-tyre strain profiles for a rotating tyre moving along a track. This means that the tyre rolling speed was added to the variables that can be tested with this rig. It also means that more realistic situations could be tested with this rig since the tyre can have both angular and linear motions. The rig also allowed testing the effect

of changing the contact surface on the sensors' measurements. The contact surface was changed by placing different surfaces on the rig's board.

Accomplishing this objective resulted in providing the testing platforms required to examine the sensor design through static and dynamic tests. It helped in achieving Objectives 4 and 5. The sensors' readings obtained from the tests on the two rigs were employed to derive the findings presented in Section 8.2.

Objective 3: Extract features from the in-tyre strain measurements to detect slip/spin, identify obstacles, differentiate surfaces, and to estimate the forces, contact patch variables, tyre's angular velocity, and the tyre's camber angle.

The measurements acquired from both the longitudinal and the lateral in-tyre strain sensors were utilised in this thesis (Chapter 5, Chapter 6, and Chapter 7). Table 8.1 illustrates the extracted strain features that were employed to estimate the tyre's operating conditions. The outcomes of utilising these features are discussed in Points 2, 3, 5, and 6 in Section 8.2.

Table 8.1: Extracted strain features to estimate the tyre's operating conditions.

Application/Estimated characteristic	**Extracted strain feature**
Slip detection	Oscillations between a steady state limit and a saturation limit in the strain readings.
Spin detection	A distinctive part in the strain waveforms that corresponds to hitting the shims at the end of the track in the dynamic tests. The spin was indirectly identified by observing the number of tyre's revolutions relative to this distinctive part.
Obstacle detection	Sharp variation in the strain waveform and the strain values.
Surface identification (surface roughness)	Increase in strain values and/or irregular strain waveform.
F_z	Average value of the two tensile peaks in the lateral strain profiles or average value of the two compressive peaks in the longitudinal strain profiles.
F_x	Ratio of front to rear tensile peak in a lateral sensor's reading or ratio of front to rear compressive peak in a longitudinal sensor's reading.
F_y	Ratio of tensile strain peaks between the two side lateral sensors or ratio of compressive strain peaks between the two side longitudinal sensors.
Contact patch length and centre	Distance between two peaks in the time derivative of the strain waveforms.
Angular velocity	Cycle period from the time history of the strain waves.
Camber angle	Ratio of tensile peaks between the two side lateral sensors.

Objective 4: Conduct static tests to determine whether the sensors' readings can indicate slip incidents. A second reason for carrying out the static tests is to build a comprehensive understanding about the sensors' response by constructing strain profiles for different values of vertical and longitudinal forces.

A set of static tests was conducted to examine the sensors' response during slip incidents (Chapter 3). To induce slip, a relative motion was created between the tyre and the contacting surface. This was done on the first rig by gradually pushing the slide over the surface of the stationary tyre by applying longitudinal forces at constant time increments. In each of these tests, the tyre was fixed at a certain angle, a constant vertical force was applied, and the value of the longitudinal force was changed by increasing the number of rotations of the bolt from 0 to 15 rotations in steps of 1 rotation. A fixed time was left before applying each rotation.

To construct the strain profiles for different values of vertical and longitudinal forces, the strain readings at a particular value of vertical and longitudinal forces were collected from the tests of different angular positions. These static tests were repeated for 13 angular positions, from 120° to -120° in steps of 20°, with three values of vertical force, F_z = 33 N, 44 N, and 60 N, in each angle. After that, the relationship between the longitudinal load and the strain at a specific vertical load was plotted for each of the 13 angular positions for the six strain gauges. Then, the value of the strain at the same longitudinal load in the linear part of the relationship was extracted from all the graphs. The maximum number of F_x values that could be found in the linear part of the relationships for one value of F_z was 8 (F_x = 0 N, 4.9 N, 9.8 N, 14.7 N, 19.6 N, 24.5 N, 29.4 N, and 34.3 N). The number of $F_z - F_x$ combinations was 19. The total number of strain profiles for the six strain sensors was 107. The strain profiles obtained from these static tests were analysed to gain a better understanding of the sensors' responses as well as to implement some parts of the processing algorithms as was presented in Sections 4.1, 4.3, 5.1, and 7.1. Thus, meeting this objective helped in studying the strain variations at the individual angular positions, identifying the slip, and examining the strain profiles. The corresponding findings are detailed in Points 1, 3, and 5 in Section 8.2.

Objective 5: Conduct dynamic tests to evaluate the performance of the in-tyre strain sensors in the case of a rotating tyre. The readings that are collected in these dynamic tests will be utilised to investigate the possibility of detecting spin, identifying obstacles, differentiating surfaces, and estimating the forces, contact patch variables, angular velocity, and camber angle.

A high number of dynamic tests were carried out on the second bench-top rig (Chapter 3). The tested variables were the tyre's angular velocity, the vertical load, the contact surface, and the camber angle. The tyre's rotational speed was changed by increasing the supply voltage to the motor. Ten values of speed, ranging from 3.50 rad./sec. to 12.20 rad./sec., were examined by incrementally increasing the supply voltage to the motor from 2 V to 11 V with a step of 1 V. For clarity in comparisons, three representatives of these speed values were mostly presented in this thesis, low, medium, and high. With regard to the vertical load, ten values were tested, from 0 N to 9 N with a 1 N increment. Again, for comparison reasons, only four of these values were mostly shown, 0 N, 3 N, 6 N, and 9 N. In terms of the contact surfaces, twelve combinations of different surfaces were used in the tests; wood, wood+ liquid, wood+ dirt, wood+ glass, wood+ (glass+ liquid), wood+ vinyl, vinyl+ liquid, vinyl+ dirt, wood+ carpet, wood+ grass, plastic, and plastic+ liquid. The workflow in these tests was to place a contact surface, apply a constant wheel load, and perform multiple runs wherein the speed was successively increased. Lastly, a group of tests was conducted to investigate the effect of changing the tyre's camber angle. Five camber angles were created by adjusting the height of the shims that support the rail. Fulfilling this objective resulted in determining the sensors' potential in identifying spin, obstacles, and surfaces. It also made it possible to estimate the tyre's mechanical properties. This was achieved through relating the strain measurements to the forces, contact patch parameters, the angular speed, and the camber angle. The findings extracted as a consequence of accomplishing this objective are highlighted throughout the points in Section 8.2.

8.2 Research findings

1) This research has shown that it is possible to capture the strain profiles of non-pressurised tyres with standard low-cost strain sensors. The readings of the strain gauges successfully reflected the changes in the applied vertical and longitudinal forces, angular velocities, contacting surfaces, and camber angles as discussed in the following points:

- The measurements of all the sensors demonstrated a linear relationship between the applied vertical or longitudinal forces and the resulting strain values (Section 7.1). The lines representing these relationships at different sensors' angular positions were close to each other, which indicates a consistent performance of the sensors. Considering the waveforms of the strain profiles, no previous work has described the strain variations for small non-pressurised tyres. Therefore, the strain profiles in this research are compared to those of pneumatic car tyres. Similar features are observed in the strain waveforms of the two types of tyres in terms of the strain variations in both the longitudinal and the lateral strain profiles. Slight changes in the strain readings were noticed in the angles far from the contact patch. On the contrary, the variations in the measured strain became more significant in the vicinity of the contact patch. The profiles also indicated that the tyre was stretching at some of the rotational angles whereas it was compressing at other angles. For the longitudinal strain profiles, compressive peaks appeared at the edges of the contact patch while a tensile peak existed at the centre of the patch. The lateral strain profiles exhibited an opposite trend. To clarify, tensile peaks were noticed at the contact patch edges whereas a compressive peak was seen at the patch centre. Furthermore, the time differential of the strain profiles for the non-pressurised tyre was also similar to that of pneumatic car tyres. Two peaks per revolution appeared in the strain derivative for the two types of tyres. These peaks represented the strain rate at the contact patch edges.

- In terms of the angular velocity, the time history of the strain measurements showed that the waveforms corresponded to the rotational speed of the tyre.

As the rolling speed increased, the strain profiles contracted, i.e., more wave cycles appeared within a specific time interval as compared to strain profiles of lower speeds (Section 7.3).

- Regarding the contact surface, two features in the measurements indicated that the sensors could sense the surface. These features were the strain value and the waveform shape. For example, higher strain values were obtained when crossing a rough surface (Figure 6.1) and distorted stain waves were collected when traversing uneven surface (Figure 6.3).

- Lastly, when camber angles were introduced, the readings of the two side lateral sensors showed that there was a variation in the strain values at the sides of the tyre's contact patch (Section 7.4). This is because the tyre was tilted across the width of the contact patch; therefore, the magnitude of the lateral strain was higher at one side.

2) As discussed in point 1 above, a high degree of similarity was observed when comparing the strain profiles of the small non-pressurised tyres used in this research and the pneumatic car tyres. This similarity suggested that it is possible to employ the strain models used for the pressurised car tyres to address the strain measurements of the small non-pressurised tyres. These models relate the strain features extracted from the in-tyre measurements to the mechanical properties. They were used in this thesis (Chapter 7) to estimate the tyre forces, the contact patch length and centre, the angular velocity, and the camber angle. As presented in Section 7.5, there are two strain models. The first model utilises features extracted from the original strain profiles whereas the second model uses characteristics from the time derivative of the strain profiles as shown in Figure 7.30. It was illustrated in Chapter 7 that the two models can be utilised for the non-pressurised tyres used in this work. A degree of divergence was observed between these strain models and their corresponding approximation models at a few points in some of the relationships. This was the effect of the unexpected deformations of this type of tyres on the performance of these strain models.

3) The research showed that the in-tyre strain information can indicate slip/spin incidents, obstacles' presences, and traversing different surfaces. In more details:

- Slip incidents were identified statically by examining the relationship between the applied longitudinal force and the resulting strain (Chapter 5). The slip incidents caused oscillations of the strain readings between two limits. These oscillations appeared in the relationships of all the sensors and in all the static tests where different vertical forces, longitudinal forces, and sensors' angular positions were tested. Hence, promising results were obtained because they indicated that the sensors can detect slip with a consistent performance. Spin incidents were indirectly identified by locating a distinctive part in the strain waveforms that corresponded to hitting the shims exist at the end of the track in the dynamic tests (Chapter 5). If there were more than two wave cycles before this part, it meant that the tyre spun before reaching the shims. In this case, the strain readings from the end of the second wave cycle to the identified part represented the spinning region. Similarly, all the strain readings after this part reflected additional rotations before the tyre came to a complete stop.

- In terms of detecting obstacles using the strain measurements, the waveforms evidently included a distinctive part when obstacles impacted the tyre (Chapter 5). For instance, an oscillation in the strain readings was seen when the cart hit the shims because the tyre bounced up and down. Likewise, a sharp variation in the strain waveform and the strain values was noticed when the tyre passed over a big stone (Figure 6.4).

- As for surface identification, the in-tyre strain readings can indicate moving over rough surfaces such as fake grass, soil, and loop-pile carpet (Chapter 6). The dynamic tests showed that the tyre needed to work harder under the same wheel load to traverse these high-grip surfaces as compared to the control surface (wood). As a result, the strain values were higher. The percentages of change in the strain values for these surfaces were 24.98 %, 51.20 %, and 52.13 %, respectively. On the other hand, there were no clear indications in

the measurements that the tyre was traversing smooth or liquid surfaces. These surfaces did not induce large strain variations, as demonstrated in Figure 6.5 and Figure 6.6. The percentage of strain change was between 1.73 % - 3.22 % for smooth surfaces and less than 1 % for liquid surfaces.

4) The readings of the motor's current sensor were used as ground truth to validate three of the observations that were concluded from the in-tyre sensors. Firstly, in the variable-speed tests presented in Section 5.2.3, the gradual increase in the strain's values within the transit phase from low to high speeds (Figure 5.17) corresponded to a similar change in the current sensor's readings (Figure 5.14). During this transit phase, the tyre's tread blocks were stretching/compressing to higher levels to help the tyre avoid slipping; consequently, the current and strain sensors showed an increase in their measurements. Secondly, when the traversed contact surface changed from a smooth to a rough surface as shown in Section 6.1, the strain sensors showed significant variations in their readings (Figure 6.1). These variations included a notable change (an additional peak) at the point where the tyre stepped on the second surface and a subsequent gradual increase in the strain values as the tyre ran on this surface. These strain variations implied that the tyre was putting more effort to continue its movement on the rough surface. The same changes were also recorded by the current sensor (Figure 6.2). Thirdly, when the cart hit the shims at the track's end, a sudden spike appeared in the strain reading as shown in Figure 6.1, Section 6.1. Similarly, a spike appeared at the same point in the measurements of the current sensor, Figure 6.2, Section 6.1.

5) Three observations in this thesis suggest that increasing the vertical load on the tyre provides more grip. Firstly, it was noticed in Section 5.1 that as the vertical load (F_z) increased, the longitudinal load (F_x) that was required to induce the tyre slip increased. Secondly, it was seen in Section 5.2.2 that increasing F_z led to delaying the spin phase after hitting the shims and decreasing the spins of the tyre. Thirdly, it was shown in Section 7.1 that higher F_z reduced the effect of the lateral forces on the tyre. On the other hand, there was a trade-off between the grip that resulted from increasing the vertical load and running the tyre with the maximum specified speed. To explain, it was observed in Section 7.3 that increasing F_z caused a decrease in the set rolling speed. The effect of increasing the vertical load on the

angular velocity can be estimated from the in-tyre strain measurements as illustrated in Figure 7.23. The estimation of this effect can be used to adjust the control system accordingly.

6) The strain profiles obtained from both the longitudinal sensors and the lateral sensors were utilised in this thesis. The results presented in Chapter 5, Chapter 6, and Chapter 7 showed that the strain features extracted from both the longitudinal and the lateral sensors provided acceptable and similar estimations. There were only two exceptions. First, it was shown in Section 5.2.3 that the readings of the sensor called Lateral 2 did not provide clear variations to show that the cart hit the shims. Due to the tread pattern on the tyre's outer surface, the lateral orientation of this sensor did not allow it to correctly indicate the strain caused by the shock of hitting the shims. Therefore, the measurements of this sensor cannot be used for accurate spin and obstacle detection. The other exception was presented in Section 7.2. The longitudinal sensors were more accurate in demonstrating the relationship between the vertical force and the contact patch length. This is because the longitudinal sensors stretch in a parallel direction with respect to the contact patch length.

7) The encoder readings were used as ground truth to validate the angular velocity estimations from the in-tyre strain sensors. Figure 7.21 demonstrated that the angular velocity measurements obtained from the strain sensors and the encoder were closely correlated where the error was 3.98 %.

Based on these findings, it can be concluded that the research presented in this thesis has successfully addressed the research questions presented in Section 1.6 and met the objectives listed in Section 1.7.

8.3 Future work

8.3.1 Improvements for the sensor-system design

- With the sensor system design implemented in this work, the strain measurements were acquired as one strain wave per tyre revolution. To increase the data update rate, the same design can be placed on different angles on the tyre circumference, for instance, 120°, 0°, and -120°. Such a placement would provide more updated sensing of the road. This is useful for accurately identifying slip incidents, detecting obstacles, and indicating a change in the traversed surface. When this new arrangement of sensors experiences these situations, it is more likely that a sensor is located in the vicinity of the contact patch. In addition, it is possible to utilise the average of the strain readings collected from the different points on the tyre circumference. This results in more accurate estimations for the tyre mechanical properties. As another close modification, the sensor design can be bonded at different angles with a lateral offset. This sensors' configuration can be particularly useful in improving the estimations of the tyre's properties that are caused by the lateral deformations. For instance, the lateral slip, the lateral force, the slip angle, and the camber angle.

- This research has confirmed that the strain measurements of the tyre tread contain a significant amount of information. To improve the estimation models, the tread measurements can be complemented by strain measurements of the tyre sidewall. One of the potential advantages of using sidewall strains is that it can help in decomposing the combined effects that result in the cases of tyre's coupled deflections (Yang 2011). However, it is a big challenge to directly measure the sidewall strain for small tyres because of the small size of the sidewall. One possible solution for this issue is to design a miniature version of the sensor presented by Erdogan (2009). Such a sensor depends on sensing the bending motion of a PVDF-based cantilever. This cantilever will be fixed at one end to the tyre edge near the rim and will be connected at the

other end to a cylindrical element that is attached to the tyre inner surface. Thus, this sensor measures only the lateral sidewall deflections.

8.3.2 Improvements for the experimental procedure

- A number of modifications can be introduced to the rig used in the dynamic tests to allow examining more parameters. First, adding a braking/traction mechanism to change the longitudinal force. In addition, designing a mechanical setup that enables the testing of the cornering (turning) condition by changing the tyre's slip angle. For example, the tyre's cart can be made of two layers. The upper layer holds the tyre and can swivel on the lower layer in the horizontal plane. Different slip angles can be tested by aligning the upper layer with an angle with respect to the direction of the tyre's travel. To create this angle, the two layers will be clamped together using screws at specified holes. Lastly, the test rig will be instrumented with load cells to measure the applied vertical, longitudinal, and lateral forces.

- Different foam's densities can be used inside the tyre and the resulting tyre pressure can be measured. To investigate this variable using the same in-tyre strain sensors, the difficulties of inserting the rim in the tyre-foam assembly without damaging the sensors must be overcome. A feasible solution is to design a dividable rim that consists of individual parts. These parts can be combined after inserting them in the tyre.

- Measuring the tyre's temperature especially in high-speed tests. It is suggested that increasing the tyre's rotational speeds may increase the sensors' errors because of the expected increase in the tyre's temperature.

- Building another rig based on a tyre rotating around a pole. Such a rig will provide two main opportunities. First, obtaining more tyre revolutions.

Secondly, studying the more complex, combined longitudinal-lateral slip conditions and the corresponding tyre's mechanical properties.

8.3.3 Improvements for the data analysis

- Most importantly, modifying the estimation models by adding parameters that account for the properties of the non-pressurised rubber tyres. These parameters can be concluded from, for example, a finite element analysis for the tyre under different working conditions, such as temperature, forces, slip, etc.

- Using other features in the strain signals to identify the slip and spin incidents. For instance, the frequency content of the strain waveforms can be analysed to extract information about the occurrence of the slip and spin.

- To present more realistic estimation models of the tyre's properties, intelligent algorithms such as the artificial neural network or fuzzy logic can be used. It is expected that such algorithms will be more efficient in processing the data of the in-tyre sensors in real-life situations.

- After modifying the rig to test different slip angles, the contact length ratio calculated from the two side lateral sensors can be used to estimate the slip angle of the tyre.

- After testing different foam inserts, the in-tyre strain data can be used to extract a model that relates between the strain and the pressure.

- Taking the effects of temperature on the strain measurements into account. This leads to link the in-tyre strain readings to the tyre mechanical properties with accurate models.

After considering the suggestions presented in Section 8.3, the in-tyre sensing system can be tested on a real mobile robot. It is worth mentioning that the literature has reported the emergence of three challenges when developing a complete intelligent tyre system. These are the types of sensors (these were investigated in this work), methods of data transmission from inside the tyre to the processing unit, and sources of power supply to feed the in-tyre sensors and the transmission modules. More details about the last two points are covered in, for instance, the review paper of Matsuzaki and Todoroki (2008b). The latter two issues need to be addressed for advanced future work so that the in-tyre sensing system and the developed estimation algorithms can be used for a rotating tyre. There are two suggestions. Using a slip ring and a portable data collection module to access the data from the in-tyre strain gauges used in this thesis. Alternatively, if online monitoring of tyre deformations is the target, then a wireless strain sensor such as the one proposed by Matsuzaki and Todoroki (2007) can be employed. In this case, to provide power to the sensors and to the wireless transmitter, batteries or an energy harvesting method can be used.

8.4 Applications

The following points present some potential applications of the sensing system and the estimation methods utilised in this research:

- The applications of the in-tyre strain measurements investigated in this thesis are beneficial to both the robotic and the automotive field. Wheel slip detection, surface identification, obstacle recognising, and tyres' mechanical properties estimation are a shared concern and could result in improvements in both fields. In robotics, they will result in introducing mobile robots that are greatly sensitive to the surrounding environment. It will also enhance the autonomous capabilities of mobile robots to navigate unstructured environments at a high speed (Sidek & Sarkar 2013). In addition, in the context of machine learning, they can bring about optimum exploiting of robot batteries. This can be achieved if the derived results are used to employ more efficient manoeuvres and control strategies. As a result, it is ensured that the

mobile robot will be able to complete its planned tasks with a consistent performance. For road vehicles, they can provide a more comprehensive and updated knowledge of the immediate condition of the traversed surface as well as the tyre's current working condition in unknown environments. This is a pivotal factor in improving road safety. In the framework of active safety systems, real-time estimation of these variables will result in reducing the number of car accidents and traffic injuries.

- The measurements of the in-tyre sensors can correct or compensate for the odometric inaccuracies in cases of wheel slip/spin. For instance, when these incidents occur, the controller will ignore the encoders' readings and rely upon the in-tyre strain measurements. This in turn produces more efficient localisation and navigation algorithms.

References

Anderson, R & Bevly, DM 2004, 'Estimation of slip angles using a model based estimator and gps', *Proceedings of the 2004 American Control Conference* IEEE, Boston, Massachusetts, pp. 2122-7.

Angelova, A, Matthies, L, Helmick, D, Sibley, G & Perona, P 2006, 'Learning to predict slip for ground robots', *Proceedings of the 2006 IEEE International Conference on Robotics and Automation (ICRA 2006)* IEEE, Orlando, Florida, pp. 3324-31.

APOLLO Consortium 2003, *Intelligent tyre systems-State of the art and potential technologies,* International Journal of Control, Automation and Systems, APOLLO Deliverable D7 for Project IST-2001-34372, Technical Research Centre of Finland (VTT).

Armstrong, EG, Sandu, C & Taheri, S 2015, 'Investigation into use of piezoelectric sensors in a wheeled robot tire for surface characterization', *Journal of Terramechanics*, vol. 62, pp. 75-90.

Baffet, G, Charara, A & Lechner, D 2009, 'Estimation of vehicle sideslip, tire force and wheel cornering stiffness', *Control Engineering Practice,* vol. 17, no. 11, pp. 1255-64.

Bevly, DM, Gerdes, JC, Wilson, C & Zhang, G 2000, 'The use of GPS based velocity measurements for improved vehicle state estimation', *Proceedings of the American Control Conference* IEEE, Chicago, Illinois, pp. 2538-42.

Braghin, F, Brusarosco, M, Cheli, F, Cigada, A, Manzoni, S & Mancosu, F 2006, 'Measurement of contact forces and patch features by means of accelerometers fixed

inside the tire to improve future car active control', *Vehicle System Dynamics*, vol. 44, no. sup1, pp. 3-13.

Breuer, B, Bartz, M, Karlheinz, B, Gruber, S, Semsch, M, Strothjohann, T & Xie, C 2000, 'The mechatronic vehicle corner of Darmstadt University of technology-interaction and cooperation of a sensor tire, new low-energy disc brake and smart wheel suspension', *Proceedings of the International Federation of Societies of Automobile Engineering (FISITA'00)*, Seoul, Korea, pp. 1-7.

Brooks, C, Iagnemma, K & Dubowsky, S 2005, 'Vibration-based terrain analysis for mobile robots', *Proceedings of the 2005 IEEE International Conference on Robotics and Automation (ICRA 2005)* IEEE, Barcelona, Spain, pp. 3415-20.

Brooks, CA & Iagnemma, K 2005, 'Vibration-based terrain classification for planetary exploration rovers', *IEEE Transactions on Robotics*, vol. 21, no. 6, pp. 1185-91.

Changfang Chen, F, Yingmin Jia, F & Matsuno, F 2013, 'Wheel slip estimation based on real-time identification of tire-road friction conditions', *2013 American Control Conference (ACC)*: *Proceedings of the 2013 American Control Conference (ACC)* IEEE, Washington, DC, USA, pp. 2815-20.

Chankyu, L, Hedrick, K & Kyongsu, Y 2004, 'Real-time slip-based estimation of maximum tire-road friction coefficient', *IEEE/ASME transactions on mechatronics*, vol. 9, no. 2, pp. 454-8.

Cheli, F, Ivone, D & Sabbioni, E 2014, 'Effect of cornering forces measurement on real-time estimation of tyre-road friction coefficient, vehicle sideslip angle and road bank angle', *12th International Symposium on Advanced Vehicle Control (AVEC'14)*, pp. 285-93.

Collins, EG & Coyle, EJ 2008, 'Vibration-based terrain classification using surface profile input frequency responses', *2008 IEEE International Conference on Robotics and Automation (ICRA 2008)* IEEE, Pasadena, CA, USA, pp. 3276-83.

D'Alessandro, V, Melzi, S, Sbrosi, M & Brusarosco, M 2012, 'Phenomenological analysis of hydroplaning through intelligent tyres', *Vehicle System Dynamics*, vol. 50, no. sup1, pp. 3-18.

Dahiya, RS, Metta, G, Valle, M & Sandini, G 2010, 'Tactile sensing—from humans to humanoids', *IEEE Transactions on Robotics*, vol. 26, no. 1, pp. 1-20.

Daily, R & Bevly, DM 2004, 'The use of GPS for vehicle stability control systems', *IEEE transactions on industrial electronics*, vol. 51, no. 2, pp. 270-7.

Daimler, C 2005, *Apollo intelligent tyre for accident-free traffic*, IST-2001-34372, Eur. Comm. Inform. Society Tec.

Dao, DV, Sugiyama, S & Hirai, S 2011, 'Development and analysis of a sliding tactile soft fingertip embedded with a microforce/moment sensor', *IEEE Transactions on Robotics*, vol. 27, no. 3, pp. 411-24.

Erdogan, G 2009, 'New sensors and estimation systems for the measurement of tire-road friction coefficient and tire slip variables', PhD thesis, University of Minnesota.

Erdogan, G, Alexander, L & Rajamani, R 2011, 'Estimation of tire-road friction coefficient using a novel wireless piezoelectric tire sensor', *Sensors Journal, IEEE*, vol. 11, no. 2, pp. 267-79.

Ergen, SC, Sangiovanni-Vincentelli, A, Sun, X, Tebano, R, Alalusi, S, Audisio, G & Sabatini, M 2009, 'The tire as an intelligent sensor', *IEEE Transactions on Computer-Aided Design of Integrated Circuits and Systems*, vol. 28, no. 7, pp. 941-55.

Farrell, J & Barth, M 1999, *The global positioning system and inertial navigation*, McGraw-Hill, New York.

Giguere, P & Dudek, G 2011, 'A simple tactile probe for surface identification by mobile robots', *IEEE Transactions on Robotics*, vol. 27, no. 3, pp. 534-44.

Gillespie, TD 1992, *Fundamentals of vehicle dynamics* , Society of Automotive Engineers Inc, Warrendale, PA.

Girão, PS, Ramos, PMP, Postolache, O & Miguel Dias Pereira, J 2013, 'Tactile sensors for robotic applications', *Measurement*, vol. 46, no. 3, pp. 1257-71.

Gobbi, M, Mastinu, G & Rocca, G 2010, 'A smart wheel for improving the active safety of road vehicles', *Proceedings of the ASME 2010 International Design*

Engineering Technical Conferences & Computers and Information in Engineering Conference, American Society of Mechanical Engineers, Montreal, Quebec, Canada, August 15-18, pp. 331-44.

Green, R 2011, 'A non-contact method for sensing tire contact patch deformation using a monocular vision system and speckled image tracking', Master thesis, Auburn University.

Gustafsson, F 1997, 'Slip-based tire-road friction estimation', *Automatica*, vol. 33, no. 6, pp. 1087-99.

Halatci, I, Brooks, CA & Iagnemma, K 2008, 'A study of visual and tactile terrain classification and classifier fusion for planetary exploration rovers', *Robotica*, vol. 26, no. 06, pp. 767-79.

Heewon, C & Jae-Bok, S 2013, 'Slippage detection and pose recovery for upward-looking camera-based SLAM using optical flow', *2013 13th International Conference on Control, Automation and Systems (ICCAS 2013)*, Kimdaejung Convention Center, Gwangju, Korea, October 20-23, pp. 1108-13.

Helmick, DM, Cheng, Y, Clouse, DS, Bajracharya, M, Matthies, LH & Roumeliotis, SI 2005, 'Slip compensation for a Mars rover', *2005 IEEE/RSJ International Conference on Intelligent Robots and Systems*, IEEE, Edmonton, Alta., Canada, August 2-6, pp. 2806-13.

Holweg, E, Hoeve, H, Jongkind, W, Marconi, L, Melchiorri, C & Bonivento, C 1996, 'Slip detection by tactile sensors: algorithms and experimental results', *Proceedings of the 1996 IEEE International Conference on Robotics and Automation* IEEE, Minneapolis, Minnesota, April, pp. 3234-9.

Hong, S, Erdogan, G, Hedrick, K & Borrelli, F 2013, 'Tyre–road friction coefficient estimation based on tyre sensors and lateral tyre deflection: modelling, simulations and experiments', *Vehicle System Dynamics*, vol. 51, no. 5, pp. 627-47.

Iizuka, K, Sasaki, T, Yamano, M & Kubota, T 2014, 'Development of grousers with a tactile sensor for wheels of lunar exploration rovers to measure sinkage', *Int J Adv Robot Syst*, vol. 11, pp. 1-7.

Ise, T, Higuchi, M & Tachiya, H 2013, 'Development of a tactile sensor to measure tire friction coefficients in arbitrary directions', *Journal ref: International Journal of Automation Technology*, vol. 7, no. 3, pp. 359-66.

Ise, T, Higuchi, M, Suzuki, Y & Tachiya, H 2017, 'Measurement on friction coefficients of tire grounding surface in arbitrary directions under high-load', *Experimental Mechanics*, vol. 57, no. 9, pp. 1383-93.

Jayakumar, P, Melanz, D, MacLennan, J, Gorsich, D, Senatore, C & Iagnemma, K 2014, 'Scalability of classical terramechanics models for lightweight vehicle applications incorporating stochastic modeling and uncertainty propagation', *Journal of Terramechanics*, vol. 54, pp. 37-57.

Jazar, RN 2017, 'Tire dynamics', in *Vehicle Dynamics*, Springer, Boston, USA, pp. 3-114.

Ju, J, Kim, D-M & Kim, K 2012, 'Flexible cellular solid spokes of a non-pneumatic tire', *Composite Structures*, vol. 94, no. 8, pp. 2285-95.

Jung, J, Lee, H-K & Myung, H 2013, 'Slip compensation of mobile robots using SVM and IMM', in *Robot Intelligence Technology and Applications 2012*, Springer, Berlin, Heidelberg, pp. 5-12.

Jwo, D-J, Yang, C-F, Chuang, C-H & Lee, T-Y 2013, 'Performance enhancement for ultra-tight GPS/INS integration using a fuzzy adaptive strong tracking unscented Kalman filter', *Nonlinear Dynamics*, vol. 73, no. 1-2, pp. 377-95.

Kaneko, K, Kanehiro, F, Kajita, S, Morisawa, M, Fujiwara, K, Harada, K & Hirukawa, H 2005, 'Slip observer for walking on a low friction floor', *2005 IEEE/RSJ International Conference on Intelligent Robots and Systems*, IEEE, Edmonton, Alta., Canada, August 2-6, pp. 634-40.

Kawamura, T, Inaguma, N, Nejigane, K, Tani, K & Yamada, H 2013, 'Measurement of slip, force and deformation using hybrid tactile sensor system for robot hand gripping an object', *International Journal of Advanced Robotic Systems*, vol. 10, pp. 1-8.

Khaleghian, S & Taheri, S 2017, 'Terrain classification using intelligent tire', *Journal of Terramechanics*, vol. 71, pp. 15-24.

Klomp, M, Gao, Y & Bruzelius, F 2014, 'Longitudinal velocity and road slope estimation in hybrid electric vehicles employing early detection of excessive wheel slip', *Vehicle System Dynamics*, vol. 52, no. sup1, pp. 172-88.

Krebs, A, Thueer, T, Carrasco, E, Siegwart, RY, Siegwart, RY & Siegwart, RY 2008, 'Towards torque control of the CRAB rover', *Proceedings of the 9th International Symposium on Artificial Intelligence, Robotics and Automation in Space (iSAIRAS)*, Eidgenössische Technische Hochschule Zürich, Autonomous Systems Lab, Los Angeles, USA.

Krebs, A, Risch, F, Thueer, T, Maye, J, Pradalier, C & Siegwart, R 2010, 'Rover control based on an optimal torque distribution-Application to 6 motorized wheels passive rover', *The 2010 IEEE/RSJ International Conference on Intelligent Robots and Systems*, IEEE, Taipei, Taiwan, October 18-22, pp. 4372-7.

Krier, D, Zanardo, GS & del Re, L 2014, 'A PCA-based modeling approach for estimation of road-tire forces by in-tire accelerometers', *IFAC Proceedings Volumes*, vol. 47, no. 3, pp. 12029-34.

Lamon, P & Siegwart, R 2005, 'Wheel torque control in rough terrain-modeling and simulation', *Proceedings of the 2005 IEEE International Conference on Robotics and Automation (ICRA 2005)*, IEEE, Barcelona, Spain, April, pp. 867-72.

Lauria, M, Piguet, Y & Siegwart, R 2002, 'Octopus-an autonomous wheeled climbing robot', *Proceedings of the Fifth International Conference on Climbing and Walking Robots*, Citeseer, Bury St Edmunds and London, UK.

Lee, H & Taheri, S 2017, 'Intelligent tires? A review of tire characterization literature', *IEEE Intelligent Transportation Systems Magazine*, vol. 9, no. 2, pp. 114-35.

Lincoln, LS & Bamberg, SJM 2010, 'Insole sensor system for real-time detection of biped slip', *32nd Annual International Conference of the IEEE EMBS*, IEEE, Buenos Aires, Argentina, August 31 - September 4, pp. 1449-52.

Lucarotti, C, Oddo, CM, Vitiello, N & Carrozza, MC 2013, 'Synthetic and bio-artificial tactile sensing: A review', *Sensors (Basel)*, vol. 13, no. 2, pp. 1435-66.

Magori, V, Magori, VR & Seitz, N 1998, 'On-line determination of tyre deformation, a novel sensor principle', *Proceedings of IEEE Ultrasonics Symposium*, IEEE, Sendai, Japan, pp. 485-8.

Manduchi, R, Castano, A, Talukder, A & Matthies, L 2005, 'Obstacle detection and terrain classification for autonomous off-road navigation', *Autonomous Robots*, vol. 18, no. 1, pp. 81-102.

Matsuzaki, R 2007, 'A study on intelligent tires based on measurement of tire deformation', Doctor of Engineering thesis, Tokyo Institute of Technology.

Matsuzaki, R & Todoroki, A 2005, 'Wireless strain monitoring of tires using electrical capacitance changes with an oscillating circuit', *Sensors and Actuators A: physical*, vol. 119, no. 2, pp. 323-31.

Matsuzaki, R & Todoroki, A 2006, 'Passive wireless strain monitoring of actual tire using capacitance–resistance change and multiple spectral features', *Sensors and Actuators A: physical*, vol. 126, no. 2, pp. 277-86.

Matsuzaki, R & Todoroki, A 2007, 'Wireless flexible capacitive sensor based on ultra-flexible epoxy resin for strain measurement of automobile tires', *Sensors and Actuators A: physical*, vol. 140, no. 1, pp. 32-42.

Matsuzaki, R & Todoroki, A 2008a, 'Intelligent tires based on measurement of tire deformation', *Journal of solid mechanics and Materials engineering*, vol. 2, no. 2, pp. 269-80.

Matsuzaki, R & Todoroki, A 2008b, 'Wireless monitoring of automobile tires for intelligent tires', *Sensors (Basel)*, vol. 8, no. 12, pp. 8123-38.

Matsuzaki, R, Kamai, K & Seki, R 2014, 'Intelligent tires for identifying coefficient of friction of tire/road contact surfaces using three-axis accelerometer', *Smart Materials and Structures*, vol. 24, no. 2, p. 025010.

Matsuzaki, R, Keating, T, Todoroki, A & Hiraoka, N 2008, 'Rubber-based strain sensor fabricated using photolithography for intelligent tires', *Sensors and Actuators A: physical*, vol. 148, no. 1, pp. 1-9.

Matsuzaki, R, Hiraoka, N, Todoroki, A & Mizutani, Y 2010, 'Analysis of applied load estimation using strain for intelligent tires', *Journal of solid mechanics and Materials engineering*, vol. 4, no. 10, pp. 1496-510.

Matsuzaki, R, Hiraoka, N, Todoroki, A & Mizutani, Y 2012, 'Strain monitoring and applied load estimation for the development of intelligent tires using a single wireless CCD camera', *Journal of solid mechanics and Materials engineering*, vol. 6, no. 9, pp. 935-49.

Melchiorri, C 2000, 'Slip detection and control using tactile and force sensors', *IEEE/ASME transactions on mechatronics*, vol. 5, no. 3, pp. 235-43.

Miller, SL, Youngberg, B, Millie, A, Schweizer, P & Gerdes, JC 2001, 'Calculating longitudinal wheel slip and tire parameters using GPS velocity', *Proceedings of the American Control Conference*, IEEE, Arlington, VA, June 25-27, pp. 1800-5.

Moffitt, RD, Bland, SM, Sunny, MR & Kapania, RK 2009, 'Sensor technologies for direct health monitoring of tires', in *Encyclopedia of Structural Health Monitoring*, John Wiley Sons, Ltd., USA, pp. 1-7.

Muller, S, Uchanski, M & Hedrick, K 2003, 'Estimation of the maximum tire-road friction coefficient', *Journal of dynamic systems, measurement, and control*, vol. 125, no. 4, pp. 607-17.

Nagatani, K, Ikeda, A, Sato, K & Yoshida, K 2009, 'Accurate estimation of drawbar pull of wheeled mobile robots traversing sandy terrain using built-in force sensor array wheel', *The 2009 IEEE/RSJ International Conference on Intelligent Robots and Systems*, IEEE, St. Louis, USA, October 11-15, pp. 2373-8.

Nam, K, Oh, S, Fujimoto, H & Hori, Y 2013, 'Estimation of sideslip and roll angles of electric vehicles using lateral tire force sensors through RLS and Kalman filter approaches', *IEEE transactions on industrial electronics*, vol. 60, no. 3, pp. 988-1000.

Naranjo, SD, Sandu, C, Taheri, S & Taheri, S 2014, 'Experimental testing of an off-road instrumented tire on soft soil', *Journal of Terramechanics*, vol. 56, pp. 119-37.

Niskanen, A & Tuononen, AJ 2015, 'Three three-axis IEPE accelerometers on the inner liner of a tire for finding the tire-road friction potential indicators', *Sensors (Basel)*, vol. 15, no. 8, pp. 19251-63.

Niskanen, AJ & Tuononen, AJ 2014, 'Three 3-axis accelerometers fixed inside the tyre for studying contact patch deformations in wet conditions', *Vehicle System Dynamics*, vol. 52, no. sup1, pp. 287-98.

Ojeda, L, Reina, G & Borenstein, J 2004, 'Experimental results from FLEXnav: An expert rule-based dead-reckoning system for Mars rovers', *2004 IEEE Aerospace Conference Proceedings*, IEEE, Big Sky, MT, March 6–13, pp. 816-25.

Ojeda, L, Cruz, D, Reina, G & Borenstein, J 2006, 'Current-based slippage detection and odometry correction for mobile robots and planetary rovers', *IEEE Transactions on Robotics*, vol. 22, no. 2, pp. 366-78.

Pacejka, HB 2005, *Tyre and vehicle dynamics*, 2nd edn, Butterworth-Heinemann, Oxford.

Palmer, M, Boyd, C, McManus, J & Meller, S 2002, 'Wireless smart-tires for road friction measurement and self state determination', *43rd AIAA/ASME/ASCE/AHS/ASC Structures, Structural Dynamics, and Materials Conference*, Denver, Colorado, April 22-25, p. 1548.

Park, B, Kim, J & Lee, J 2012, 'Terrain feature extraction and classification for mobile robots utilizing contact sensors on rough terrain', *Procedia Engineering*, vol. 41, pp. 846-53.

Piyabongkarn, D, Rajamani, R, Grogg, JA & Lew, JY 2009, 'Development and experimental evaluation of a slip angle estimator for vehicle stability control', *IEEE Transactions on control systems technology*, vol. 17, no. 1, pp. 78-88.

Pohl, A, Steindl, R & Reindl, L 1999, 'The "intelligent tire" utilizing passive SAW sensors measurement of tire friction', *IEEE Transactions on Instrumentation and Measurement*, vol. 48, no. 6, pp. 1041-6.

Ray, LR, Brande, DC & Lever, JH 2009, 'Estimation of net traction for differential-steered wheeled robots', *Journal of Terramechanics*, vol. 46, no. 3, pp. 75-87.

Reina, G, Ojeda, L, Milella, A & Borenstein, J 2006, 'Wheel slippage and sinkage detection for planetary rovers', *IEEE/ASME transactions on mechatronics*, vol. 11, no. 2, pp. 185-95.

Reina, G, Ishigami, G, Nagatani, K & Yoshida, K 2008, 'Vision-based estimation of slip angle for mobile robots and planetary rovers', *Proceedings of the IEEE InternationalConference on Robotics and Automation (ICRA 2008)*, IEEE, Pasadena, California, May, pp. 486-91.

Ryu, J, Rossetter, EJ & Gerdes, JC 2002, 'Vehicle sideslip and roll parameter estimation using GPS', *Proceedings of the AVEC International Symposium on Advanced Vehicle Control*, Hiroshima, Japan, pp. 373-80.

Salycheva, A 2004, 'Medium accuracy INS/GPS integration in various GPS environments', masters thesis, University of Calgary, Calgary, Canada.

Savaresi, SM, Tanelli, M, Langthaler, P & Del Re, L 2008, 'New regressors for the direct identification of tire deformation in road vehicles via “in-tire” accelerometers', *IEEE Transactions on control systems technology*, vol. 16, no. 4, pp. 769-80.

Senatore, C & Iagnemma, K 2014, 'Analysis of stress distributions under lightweight wheeled vehicles', *Journal of Terramechanics*, vol. 51, pp. 1-17.

Senatore, C, Wulfmeier, M, MacLennan, J, Jayakumar, P & Iagnemma, K 2012, 'Investigation of stress and failure in granular soils for lightweight robotic vehicle applications', *2012 NDIA Ground Vehicle Systems Engineering and Technology Symposium Modeling & Simulation, Testing and Validation (MSTV) Mini-symposium*, DTIC Document, Michigan, August 14-16.

Sergio, M, Manaresi, N, Tartagni, M, Guerrieri, R & Canegallo, R 2003, 'On road tire deformation measurement system using a capacitive-resistive sensor', *Smart Materials and Structures*, vol. 15, no. 6, pp. 1059-63.

Shirafuji, S & Hosoda, K 2014, 'Detection and prevention of slip using sensors with different properties embedded in elastic artificial skin on the basis of previous experience', *Robotics and Autonomous Systems*, vol. 62, no. 1, pp. 46-52.

Sidek, N & Sarkar, N 2013, 'Exploiting wheel slips of mobile robots to improve navigation performance', *Advanced Robotics*, vol. 27, no. 8, pp. 627-39.

Singh, KB, Arat, MA & Taheri, S 2012, 'Enhancement of collision mitigation braking system performance through real-time estimation of tire-road friction coefficient by means of smart tires', *SAE International journal of passenger cars-electronic and electrical systems*, vol. 5, no. 2012-01-2014, pp. 607-24.

Song, X, Seneviratne, L & Althoefer, K 2009, 'A vision based wheel slip estimation technique for mining vehicles', *IFAC Proceedings Volumes*, vol. 42, no. 23, pp. 179-84.

Song, X, Song, Z, Seneviratne, LD & Althoefer, K 2008, 'Optical flow-based slip and velocity estimation technique for unmanned skid-steered vehicles', *2008 IEEE/RSJ International Conference on Intelligent Robots and Systems*, IEEE, Acropolis Convention Center, Nice, France, September 22-26, pp. 101-6.

Sutoh, M, Ito, T, Nagatani, K & Yoshida, K 2010, 'Influence evaluation of wheel surface profile on traversability of planetary rovers', *Proceedings of IEEE/SICE International Symposium on System Integration*, IEEE, pp. 67-72.

Teshigawara, S, Tadakuma, K, Ming, A, Ishikawa, M & Shimojo, M 2010, 'High sensitivity initial slip sensor for dexterous grasp', *2010 IEEE International Conference on Robotics and Automation (ICRA 2010)*, IEEE, Anchorage Convention District, Anchorage, Alaska, USA, May 3-8 pp. 4867-72.

Todoroki, A, Miyatani, S & Shimamura, Y 2003a, 'Wireless strain monitoring using electrical capacitance change of tire: part I—with oscillating circuit', *Smart Materials and Structures*, vol. 12, no. 3, p. 403.

Todoroki, A, Miyatani, S & Shimamura, Y 2003b, 'Wireless strain monitoring using electrical capacitance change of tire: part II—passive', *Smart Materials and Structures*, vol. 12, no. 3, p. 410.

Tuononen, A 2009, 'Optical position detection to measure tyre carcass deflections and implementation for vehicle state estimation', Doctoral thesis, Helsinki University of Technology.

Tuononen, A & Hartikainen, L 2008, 'Optical position detection sensor to measure tyre carcass deflections in aquaplaning', *International Journal of Vehicle Systems Modelling and Testing*, vol. 3, no. 3, pp. 189-97.

Tuononen, AJ 2008, 'Optical position detection to measure tyre carcass deflections', *Vehicle System Dynamics*, vol. 46, no. 6, pp. 471-81.

Wada, M, Yoon, KS & Hashimoto, H 2000, 'High accuracy road vehicle state estimation using extended Kalman filter', *2000 IEEE Intelligent Transportation Systems*, IEEE, Dearborn (MI), USA, October l-3, pp. 282-7.

Wang, Y, Wang, S, Tan, R & Jiang, Y 2012, 'Adaptive control method for path tracking of wheeled mobile robot considering parameter changes', *International Journal of Advanced Mechatronic Systems*, vol. 4, no. 1, pp. 41-9.

Ward, CC & Iagnemma, K 2007, 'Classification-based wheel slip detection and detector fusion for outdoor mobile robots', *2007 IEEE International Conference on Robotics and Automation (ICRA 2007)*, Citeseer, Roma, Italy, April 10-14, pp. 2730-5.

Ward, CC & Iagnemma, K 2008, 'A dynamic-model-based wheel slip detector for mobile robots on outdoor terrain', *IEEE Transactions on Robotics*, vol. 24, no. 4, pp. 821-31.

Xiong, Y & Tuononen, A 2014, 'A laser-based sensor system for tire tread deformation measurement', *Measurement Science and Technology*, vol. 25, no. 11, p. 115103.

Xu, B, Pradalier, C, Krebs, A, Siegwart, R & Sun, F 2011, 'Composite control based on optimal torque control and adaptive Kriging control for the CRAB rover', *2011*

IEEE International Conference on Robotics and Automation (ICRA 2011) IEEE, Shanghai International Conference Center, Shanghai, China, May 9-13 pp. 1752-7.

Yang, X 2011, 'Finite element analysis and experimental investigation of tyre characteristics for developing strain-based intelligent tyre system', PhD thesis, University of Birmingham.

Yang, X, Olatunbosun, O, Ramos, DG-P & Bolarinwa, E 2013, 'Experimental investigation of tire dynamic strain characteristics for developing strain-based intelligent tire system', *SAE International Journal of Passenger Cars-Mechanical Systems*, vol. 6, no. 2013-01-0633, pp. 97-108.

Yi, J 2008, 'A piezo-sensor-based "smart tire" system for mobile robots and vehicles', *IEEE/ASME transactions on mechatronics*, vol. 13, no. 1, pp. 95-103.

Yi, J & Tseng, EH 2008, 'A "smart tire" system for tire/road friction estimation', *ASME 2008 Dynamic Systems and Control Conference*, American Society of Mechanical Engineers, Ann Arbor, Michigan, USA, October 20–22, pp. 1293-300.

Yi, J, Zhang, J, Song, D & Jayasuriya, S 2007, 'IMU-based localization and slip estimation for skid-steered mobile robots', *Proceedings of the 2007 IEEE/RSJ International Conference on Intelligent Robots and Systems*, IEEE, San Diego, CA, USA, October 29 - Nov 2, pp. 2845-50.

Yi, J, Wang, H, Zhang, J, Song, D, Jayasuriya, S & Liu, J 2009, 'Kinematic modeling and analysis of skid-steered mobile robots with applications to low-cost inertial-measurement-unit-based motion estimation', *IEEE Transactions on Robotics*, vol. 25, no. 5, pp. 1087-97.

Yousef, H, Boukallel, M & Althoefer, K 2011, 'Tactile sensing for dexterous in-hand manipulation in robotics—a review', *Sensors and Actuators A: physical*, vol. 167, no. 2, pp. 171-87.

Zhang, X 2003, 'Integration of GPS with a medium accuracy IMU for metre-level positioning', Master thesis, University of Calgary.

Zhang, X & Liu, R 2012, 'Slip detection by array-type pressure sensor for a grasp task', *2012 IEEE International Conference on Mechatronics and Automation (ICMA)* IEEE, Chengdu, China, August 5-8, pp. 2198-202.

Zhang, Y 2014, 'Modeling and control of single-track vehicles: a human-machine-environment interactions perspective', PhD thesis, Rutgers University-Graduate School-New Brunswick.

Zhang, Y, Yi, J & Liu, T 2013, 'Embedded flexible force sensor for in-situ tire–road interaction measurements', *IEEE SENSORS JOURNAL*, vol. 13, no. 5, pp. 1756-65.

Zhang, Y, Allen, AW, Yi, J & Liu, T 2012, 'Understanding tire/road stick-slip interactions with embedded rubber force sensors', *2012 IEEE/ASME International Conference on Advanced Intelligent Mechatronics (AIM)* IEEE, Kachsiung, Taiwan, July 11-14, pp. 550-5.

Associated Publications

Lutfi, AFL, Low, T & Maxwell, A 2018, 'A preliminary evaluation of static tests to detect slip using tyre strain sensing system in robotic platforms', *2018 15th International Conference on Control, Automation, Robotics and Vision (ICARCV)*, IEEE, Singapore, Singapore, November 18-21, pp. 1400-7.

(The work in this paper is presented in Chapter 3, Chapter 4, and Chapter 5).

Lutfi, AFL, Low, T & Maxwell, A 2018, 'Designing and initial testing of a tyre strain sensing system to estimate slip in robotic platforms'. *Proceedings of the 2018 Australasian Conference on Robotics and Automation (ACRA2018)*, Lincoln University, Lincoln, Canterbury, New Zealand, December 4-6.

(The work in this paper is presented in Chapter 3, Chapter 4, and Chapter 7).